

**Lehrstuhl für Computation in Engineering  
Fakultät für Bauingenieur- und Vermessungswesen  
Technische Universität München**

## **Introduction to Building Performance Modeling and Simulation**

A basic introduction to modeling and numerical simulation  
of the energy and thermal quality performance of buildings  
using a geometry based zone model

Bei der Fakultät für Bauingenieur- und Vermessungswesen der Technischen Universität München zur Erlangung der Lehrbefähigung für das Fach "Computational Building Physics" eingereichte

## **Habilitationsschrift**

vorgelegt von

Dr.-Ing. Christoph Alban van Treeck

### **Gutachter:**

Univ.-Prof. Dr. rer.nat. Ernst Rank  
Univ.-Prof. Dr.-Ing. Gerd Hauser  
Univ.-Prof. Dr. Ir. Jan Hensen

Tag der Einreichung:  
12.02.2010



# **Introduction to Building Performance Modeling and Simulation**

A basic introduction to modeling and numerical simulation  
of the energy and thermal quality performance of buildings  
using a geometry based zone model

Christoph Alban van Treeck

February 12, 2010



---

# Contents

<b>1</b>	<b>Introduction</b>	<b>9</b>
1.1	What is building performance simulation? . . . . .	9
1.2	The simulation community and its communication channels . . . . .	11
1.3	Scales and levels in building simulation . . . . .	12
1.4	A short historical review . . . . .	14
1.5	Available simulation software and tools . . . . .	16
1.6	References and further reading . . . . .	17
<b>2</b>	<b>Energy efficient building design</b>	<b>20</b>
2.1	Energy consumption and energy scenarios . . . . .	20
2.2	The Energy Performance of Buildings Directive . . . . .	23
2.3	The building life cycle . . . . .	24
2.4	Tools for the early design stages . . . . .	25
2.5	Lessons learned? . . . . .	26
2.6	Active and passive components and measures . . . . .	29
2.6.1	Measures related to ventilation, radiation and thermal capacity . . . . .	30
2.6.2	Measures related to insulation, thermal capacity and phase changes . . . . .	33
2.6.3	Active and plant components . . . . .	35
2.7	References . . . . .	38
<b>3</b>	<b>Heat balances and energy flow paths</b>	<b>43</b>
3.1	Basic heat transfer mechanisms . . . . .	43
3.2	Steady-state heat transfer through walls . . . . .	44
3.3	The (h,x) psychrometric chart by Mollier . . . . .	45
3.4	Basic heat balances . . . . .	47
3.5	Energy flow paths and causal effects . . . . .	50
3.5.1	Heat transfer through walls . . . . .	50
3.5.2	Heat transfer through windows . . . . .	52
3.5.3	Whole zone . . . . .	53
3.6	A sample model according to VDI Standard 6020 . . . . .	53
3.7	Steady-state monthly and annual balances . . . . .	56
3.7.1	Winter case . . . . .	57
3.7.2	Summer case . . . . .	59
3.8	References . . . . .	60

<b>4 Transition and boundary conditions in simulation</b>	<b>63</b>
4.1 Transition conditions to the external environment . . . . .	63
4.1.1 Weather data . . . . .	63
4.1.2 External pressure and temperature distribution . . . . .	67
4.1.3 Heat transfer by forced convection . . . . .	72
4.1.4 Soil temperature . . . . .	73
4.2 Transition conditions to the internal environment . . . . .	74
4.2.1 Room air flow characteristics . . . . .	74
4.2.2 Internal convective heat transfer coefficients . . . . .	78
4.2.3 Internal heat gains and user behavior . . . . .	79
4.3 Impacts of the urban environment and the climate change . . . . .	80
4.4 References . . . . .	81
<b>5 Geometric modeling</b>	<b>86</b>
5.1 The geometric model: A key element in building simulation . . . . .	86
5.2 Basic geometric representation of objects . . . . .	87
5.2.1 Direct representation schemes . . . . .	88
5.2.2 Indirect representation schemes . . . . .	89
5.3 Integration and interoperability . . . . .	90
5.3.1 Building information modeling (BIM) . . . . .	90
5.3.2 Data exchange and interoperability . . . . .	91
5.3.3 Integration of building performance simulation . . . . .	92
5.4 A geometric model with minimum semantics using hexahedral elements . . . . .	92
5.5 References . . . . .	95
<b>6 Heat conduction in solids</b>	<b>98</b>
6.1 The Fourier heat equation . . . . .	98
6.2 Finite difference discretization in space and time . . . . .	99
6.2.1 Numerical discretization . . . . .	99
6.2.2 Forward, backward and central differences . . . . .	100
6.2.3 Convergence analysis for steady-state conditions . . . . .	102
6.3 Forward Euler time integration . . . . .	103
6.3.1 First order time discretization . . . . .	103
6.3.2 Stability criteria . . . . .	103
6.3.3 Example: Explicit solution . . . . .	105
6.4 Backward Euler time integration . . . . .	107
6.4.1 First order time discretization . . . . .	107
6.4.2 Example: Implicit solution . . . . .	108
6.5 Other time integration methods . . . . .	109
6.6 References . . . . .	109
<b>7 Internal radiation processes</b>	<b>111</b>
7.1 Radiative heat exchange between surfaces . . . . .	111
7.1.1 Blackbody emissive power . . . . .	111
7.1.2 Grey, diffuse surfaces . . . . .	112
7.1.3 Surface energy balance . . . . .	113

---

7.1.4	View factor definition . . . . .	114
7.1.5	Net radiation method . . . . .	116
7.1.6	View factors for finite surfaces . . . . .	117
7.2	Numerical solution techniques . . . . .	118
7.2.1	Analytical, numerical and sampling methods . . . . .	118
7.2.2	Numerical determination of view factors . . . . .	120
7.2.3	Accuracy and computational effort . . . . .	123
7.2.4	Numerical approximation of the integral equation . . . . .	126
7.2.5	Solving the equation set by LU decomposition . . . . .	126
7.2.6	Example: View factors for the VDI 6020 sample room . . . . .	128
7.3	References . . . . .	129
<b>8</b>	<b>Solar radiation processes</b>	<b>131</b>
8.1	Required quantities and definitions . . . . .	131
8.2	The solar spectrum . . . . .	132
8.3	Position of the sun in the sky . . . . .	134
8.3.1	Local position and orientation of the building model . . . . .	134
8.3.2	Solar time and hour angle . . . . .	136
8.3.3	Solar declination . . . . .	137
8.3.4	Solar zenith and elevation angle . . . . .	137
8.3.5	Surface incidence angle . . . . .	137
8.3.6	Solar azimuth angle . . . . .	138
8.3.7	Sun trajectory expressed with spherical coordinates . . . . .	138
8.4	Solar irradiation to arbitrarily tilted surface . . . . .	138
8.4.1	Transformation of beam radiation . . . . .	138
8.4.2	Transformation of diffuse radiation . . . . .	138
8.4.3	Absorption at opaque surfaces . . . . .	139
8.4.4	Example . . . . .	140
8.5	Shading analysis . . . . .	142
8.6	Internal distribution of shortwave radiation . . . . .	143
8.6.1	Simplified methods . . . . .	143
8.6.2	A raytracing algorithm for tracking beam radiation . . . . .	144
8.6.3	Daylight analysis . . . . .	149
8.7	External radiative heat exchange . . . . .	150
8.8	References . . . . .	151
<b>9</b>	<b>Optical and thermal properties of windows</b>	<b>153</b>
9.1	Heat transfer through multi-layered glazings . . . . .	153
9.1.1	Structure of a glazing system . . . . .	153
9.1.2	The different domains and their interaction . . . . .	154
9.1.3	The total window heat transfer coefficient . . . . .	155
9.1.4	Daylight transmittance versus solar heat gains . . . . .	157
9.2	Solar optical properties: A simplified model . . . . .	158
9.2.1	Transmittance by reflection losses considered . . . . .	159
9.2.2	Transmittance by absorption losses considered . . . . .	160
9.2.3	Transmittance-absorptance product . . . . .	160

9.2.4 Secondary heat gains due to solar absorption (half-stack) . . . . .	161
9.3 Example . . . . .	162
9.4 Overall optical properties of multi-layered glazings . . . . .	165
9.4.1 Recursive calculation of the overall optical properties . . . . .	165
9.4.2 Selective transmittance through coated glazings . . . . .	166
9.5 Professional software packages . . . . .	169
9.6 References . . . . .	170
<b>10 The zone model</b>	<b>172</b>
10.1 Zone-based modeling . . . . .	172
10.2 Assembling the energy matrix equation . . . . .	173
10.2.1 Energy conservation . . . . .	173
10.2.2 Heat conduction within solid components . . . . .	176
10.2.3 Room air energy balance equation . . . . .	177
10.2.4 Surface heat balance equations . . . . .	178
10.3 Structure of the energy matrix equation . . . . .	180
10.3.1 The energy matrix equation . . . . .	180
10.3.2 Solving the energy matrix equation . . . . .	181
10.4 The overall solution algorithm . . . . .	182
10.5 Time discretization convergence analysis . . . . .	182
10.6 References . . . . .	184
<b>11 Modeling air flows in buildings</b>	<b>187</b>
11.1 The nodal network method . . . . .	187
11.1.1 Artificial air pressure nodal network . . . . .	187
11.1.2 The Bernoulli equation . . . . .	188
11.1.3 Mass conservation . . . . .	189
11.2 Iterative solution by a Newton-Raphson method . . . . .	190
11.3 Coupling with the thermal zone model . . . . .	191
11.4 Outlook: Computational fluid dynamics (CFD) . . . . .	192
11.5 References . . . . .	193
<b>12 Validation and benchmarking</b>	<b>196</b>
12.1 Benchmark tests in the literature . . . . .	196
12.2 The BESTEST energy simulation test and diagnostic method . . . . .	197
12.3 VDI Standard 6020 benchmark application . . . . .	197
12.3.1 Transient responses during 60 day period . . . . .	198
12.3.2 Plant performance for solar radiation and zero capacity . . . . .	199
12.3.3 Annual heating and cooling performance . . . . .	201
12.4 References . . . . .	204
<b>13 Thermal quality performance assessment in buildings</b>	<b>206</b>
13.1 Indoor thermal quality performance prediction . . . . .	206
13.2 The energy balance equation . . . . .	209
13.3 Human thermoregulation in detail . . . . .	209
13.3.1 Regulation mechanisms and thermal stimuli . . . . .	209

---

13.3.2 Human thermoregulation models . . . . .	211
13.3.3 The model of Fiala . . . . .	211
13.4 Conditions for thermal comfort . . . . .	213
13.4.1 What is thermal comfort? . . . . .	213
13.4.2 Linking temperature sensation and comfort . . . . .	214
13.4.3 Environmental and personal parameters affecting comfort . . . . .	216
13.5 Prediction of thermal comfort . . . . .	217
13.5.1 Uniform and steady state conditions . . . . .	217
13.5.2 Local thermal comfort for conditions near thermal neutrality . . . . .	220
13.5.3 Inhomogeneous and transient conditions . . . . .	221
13.5.4 People's expectation and behavioral adaptation . . . . .	224
13.5.5 Overheating risk prediction . . . . .	225
13.6 Ergonomics of the thermal environment in buildings . . . . .	225
13.6.1 Static comfort envelopes . . . . .	226
13.6.2 ASHRAE summer and winter comfort zones . . . . .	227
13.6.3 Adaptive comfort guidelines . . . . .	228
13.6.4 Long-term thermal quality performance . . . . .	230
13.7 References . . . . .	231
<b>14 Application examples</b>	<b>240</b>
14.1 Applications in building performance simulation . . . . .	240
14.1.1 Thermal comfort analysis using a multizone model . . . . .	241
14.1.2 Local draught risk analysis using CFD . . . . .	244
14.1.3 Local and dynamic comfort analysis using a human model . . . . .	245
14.2 Thermal flow analysis in an aircraft cabin . . . . .	249
14.3 References . . . . .	250
<b>15 Some future trends and aspects in building simulation</b>	<b>253</b>
15.1 Simulation, integration and modeling trends . . . . .	253
15.1.1 Multi-physics simulation . . . . .	253
15.1.2 Integrated product data management . . . . .	253
15.1.3 Equation-based modeling . . . . .	254
15.2 Computational steering – a new trend? . . . . .	255
15.2.1 What is computational steering? . . . . .	255
15.2.2 Application scenarios . . . . .	256
15.3 References . . . . .	257



# Abstract

The book on hand provides a basic introduction to the modeling and to the numerical simulation of the energy performance and the thermal quality performance of buildings. It is the conceptual idea to explain the physical background and the numerical techniques which form part of the core of building performance simulation. The knowledge is provided with minimum semantics in terms of creating the particular modules of a geometry-based thermal multizone model step by step. The book addresses students at the graduate or PhD level.

At the beginning, a short historical review is given, the different scales and levels in building simulation are explained, and the related simulation community and its communication channels are introduced. Motivated by the European Energy Performance of Buildings Directive, we provide an overview of the energy efficient building design including a few examples for active and passive measures towards sustainable building design. Prior to introducing numerical techniques, a general picture is drawn of the relevant heat balances and energy flow paths in a building. Using a static balancing approach, a calculation example is given for a sample building model. External and internal boundary conditions are summarized, including the weather data acquisition, the pressure and temperature distribution at the building surface, heat transfer coefficients for free and forced convection, as well as the impacts of the urban environment and the climate change to the prediction methods.

Detailed material is provided on how to numerically calculate the respective heat and mass flows in a building. This includes heat conduction in solids, internal long wave radiation processes, solar radiation, and optical and thermal properties of windows. Numerical techniques are introduced, such as finite difference methods, numerical integration to calculate view factors, the radiosity method, and a simplified raytracing algorithm. A zone model finally integrates the respective multi physics heat transfer into a single model. Air flows between spaces are treated by a nodal network method. A geometric model thereby forms the basis of the discussed discretization methods. We therefore recapitulate the basic geometrical representation of objects and explain the issue of integration in terms of linking building information modeling and building performance simulation. Validation tests are performed with the developed model in terms of the VDI 6020/6007 benchmark definitions.

For the thermal quality performance assessment, information is provided on the human energy balance and thermoregulation, the conditions for thermal comfort, the relevant prediction methods for both steady state uniform and inhomogeneous transient conditions, models to include peoples' expectation and behavioral adaptation, and the relevant comfort envelopes and calculation methods. Examples clarify the application of the respective models in simulation.

# Nomenclature

## Declaration of variables and expressions

Variable	SI-Unit	Description
$\alpha$	[%]	absorptance (glazing)
$\alpha$	[%]	absorption coefficient (walls)
$\alpha$	[%]	aerodynamic surface roughness coefficient
$\alpha$	[ $m^2/s$ ]	thermal diffusivity
$\alpha_s$	[rad] or [ $^\circ$ ]	solar elevation angle
$A$	[ $m^2$ ]	surface area
$dA$	[ $m^2$ ]	differential surface element
$\beta$	[ $1/K$ ]	thermal (volume) expansion coefficient
$\beta$	[rad] or [ $^\circ$ ]	surface slope angle
$b_{sky}$	[—]	sky coverage
$c$ or $c_p$	[ $J/(kg\ K)$ ]	specific heat capacity
$C$	[ $J/(m^2\ K)$ ]	overall heat capacity
$c_{eff}$	[ $Wh/(m^2K)$ ]	overall effective thermal capacity
$c_p$	[—]	dynamic wind pressure coefficient
$c_0$	[ $m/s$ ]	speed of light in vacuum ( $2.998 \cdot 10^8\ m/s$ )
$C_d$	[—]	flow resistance coefficient
$\delta$	[ $m$ ]	boundary layer thickness
$\delta$	[rad] or [ $^\circ$ ]	solar declination angle
$\Delta$	[ $m$ ]	optical retardation (path difference)
$d_p$	[—]	discretization error
$DR$	[%]	draught risk
$\varepsilon$	[%]	surface emissivity
$\varepsilon_{sky}$	[—]	long wave sky emissivity
$\eta$	[—]	utilization factor
$e$	[%]	relative error
$E$	[ $W/m^2$ ]	emissive power
$E_{b\lambda}$	[ $W/m^2$ ]	blackbody emissive power
$E_b$	[ $W/m^2$ ]	total blackbody emissive power
$f$	[%]	frame portion
$F$	[—]	view factor (shape factor)
$F_c$	[—]	shading system reduction factor
$f_{cl}$	[—]	clothing factor

Variable	SI-Unit	Description
$Fo$	[—]	Fourier number
$\gamma$	[—]	ratio between heat sources and sinks
$\gamma$	[rad] or [°]	azimuth angle
$\gamma_s$	[rad] or [°]	solar azimuth angle
$g$	[ $m/s^2$ ]	acceleration due to gravity
$g$	[%]	solar heat gain coefficient (SHGC)
$Gr$	[—]	Grashof number
$h$	[ $kJ/kg$ ]	enthalpy
$h$	[ $W/(m^2 K)$ ]	heat transfer coefficient
$h$	[ $J s$ ]	Planck constant ( $6.626 \cdot 10^{-34} Js$ )
$h$	[ $m$ ]	glazing thickness
$H$	[ $W/K$ ]	specific heat transfer
$H$	[ $W/m^2$ ]	irradiation
$\Delta H$	[ $W$ ]	enthalpy change
$i$	[—]	used as identifier and running variable
$I_\lambda$	[ $W/m^2$ ]	spectral radiative intensity
$I$	[ $W/m^2$ ]	total radiative intensity
$I_{cl}$	[ $(m^2 K)/W$ ]	clothing insulation
$J$	[ $W/m^2$ ]	radiosity
$k$	[ $J/K$ ]	Boltzmann constant ( $1.3806 \cdot 10^{-23} J/K$ )
$k_d$	[—]	flow coefficient
$K$	[ $1/m$ ]	extinction coefficient
$K_{i,j}$	[ $W/K$ ]	equivalent thermal resistance
$\lambda$	[ $W/(m K)$ ]	thermal conductance
$\lambda$	[nm], [ $\mu m$ ]	wave length
$\Lambda$	[ $W/(m^2 K)$ ]	(equivalent) thermal resistance
$L$	[ $m$ ]	characteristic length scale
$L_{local}$	[rad] or [°]	site longitude
$L_{std}$	[rad] or [°]	local standard meridian
$LTSV$	[—]	local thermal sensation vote
$\mu$	[ $kg/(sm)$ ]	dynamic viscosity
$\dot{m}$	[ $m^3/s$ ]	mass flow rate
$M$	[ $W$ ]	metabolic heat
$\nu$	[ $m^2/s$ ]	kinematic viscosity
$\nu$	[ $1/s$ ]	photon frequency
$n$	[ $1/h$ ]	air change rate
$n$	[—]	refractive index
$N_i()$	[—]	shape function
$Nu$	[—]	Nusselt number
$\varphi$	[%]	relative air humidity
$\varphi$	[rad] or [°]	solar incidence angle w.r.t. surface normal
$\phi$	[rad] or [°]	site latitude
$\Psi_g$	[ $W/(mK)$ ]	linear heat transfer coefficient
$p$	[ $Pa$ ] = [ $N/m^2$ ]	pressure
$P$	[ $Pa$ ] = [ $N/m^2$ ]	total pressure
$p_a$	[ $Pa$ ] = [ $N/m^2$ ]	water vapor pressure

Variable	SI-Unit	Description
$p_d$	[Pa] = [N/m <sup>2</sup> ]	dynamic wind pressure
$p_s$	[Pa] = [N/m <sup>2</sup> ]	static wind pressure
$Pr$	[—]	Prandtl number
$PMV$	[—]	predicted mean vote
$PPD$	[%]	predicted percentage of dissatisfied (people)
$q$	[W/m <sup>2</sup> ]	heat flux density ( $q = \dot{Q}/A$ )
$\dot{Q}$	[J/s] = [W]	heat flux
$Q$	[J] = [W · s]	heat quantity
$\rho$	[%]	reflectivity
$\rho_L$	[%]	daylight reflectivity
$\varrho$	[kg/m <sup>3</sup> ])	density
$r$	[%]	reflection (unpolarized radiation)
$R$	[(m <sup>2</sup> K)/W]	heat resistance
$R$	[—]	horizontal radiation transformation factor
$Ra$	[—]	Rayleigh number
$Re$	[—]	Reynolds number
$R_i$	[J/(kg K)]	special gas constant for air
$\sigma$	[W/(m <sup>2</sup> K <sup>4</sup> )]	Stefan-Boltzmann constant ( $5.67051 \cdot 10^8 W/(m^2K^4)$ )
$s$	[m]	spatial distance
$s$	[—]	selectivity (glazing)
$\tau$	[h]	time constant
$\tau$	[%]	transmissivity (glazing)
$\tau_L$	[%]	daylight transmissivity
$\theta$ or $\theta_z$	[rad] or [°]	zenith angle
$\vartheta$	[°C] or [K]	temperature
$t$	[s], [h], [d], [a]	time ( $1a = 365d = 8760h$ )
$t_{sol}$	[h]	solar time
$\Delta t$	[s]	time step size
$T$	[°C] or [K]	temperature
$\bar{T}$	[°C] or [K]	mean temperature
$\Delta T$	[°C] or [K]	temperature difference
$Tu$	[%]	degree of turbulence
$u$	[m/s]	flow speed, velocity
$U$	[W/(m <sup>2</sup> K)]	overall heat transfer coefficient
$U_f$	[W/(m <sup>2</sup> K)]	heat transfer coefficient of the frame
$U_g$	[W/(m <sup>2</sup> K)]	heat transfer coefficient of the glazing
$U_t$	[W/(m <sup>2</sup> K)]	total window heat transfer coefficient
$V$	[m <sup>3</sup> ]	volume
$w$	[—]	weighting coefficient (Gaussian quadrature)
$W$	[W]	mechanically conducted work
$x$	[g/kg]	absolute air humidity
$\Delta x$	[m]	spatial distance
$z$	[m]	height
$Z()$	[min]	equation of time
$\omega$	[rad]	hour angle
$\omega$	[—]	relaxation coefficient

## Declaration of superscripts

Superscript	Description
$c$	convective
$r$	radiative
$c,r$	combined convective and radiative
$(n)$	current (known) discrete time step
$(n+1)$	future (unknown) discrete time step
$(t)$	current (known) time row
$(t+\Delta t)$	future (unknown) time row

## Declaration of subscripts

Subscript	Description
$\alpha$	due to absorption
$air$	air
$amb$	ambient
$beam$	beam (radiation)
$bl$	blood
$c$	convective
$c,r$	combined convective and radiative
$cl$	clothing
$comf$	comfort
$cond$	conductive
$conv$	convective
$crit$	critical
$d$	dynamic
$diff$	diffuse (radiation)
$dry$	dry (sensible)
$eff$	effective
$env$	environment
$eq$	equivalent
$ew$	exponentially weighted
$ext$	external
$fsky$	fictitious sky (temperature)
$global$	global (beam and diffuse)
$half$	half stack
$hy$	hypothalamus
$\infty$	infinity
$I$	internal

Subscript	Description
<i>inf</i>	infiltration
<i>ins</i>	inside
<i>int</i>	internal
$\lambda$	spectral
<i>lw</i>	long wave
<i>m</i>	mean
<i>met</i>	meteorological
<i>old</i>	old value (of preceding time step)
<i>op</i>	operative (temperature)
<i>out</i>	outside
$\varphi$	angular dependency
$\parallel$	parallel
$\perp$	perpendicular
<i>r</i>	radiative
<i>ref</i>	reference
<i>resp</i>	respiration
<i>rfl</i>	reflection
<i>rm</i>	running mean
<i>s</i>	static
<i>S</i>	solar
<i>sk</i>	skin
<i>surf</i>	surface
<i>sw</i>	short wave
<i>T</i>	transmission
<i>T,earth</i>	transmission to earth
<i>tot</i>	total
<i>V</i>	ventilation, infiltration
<i>vent</i>	ventilation
<i>wd</i>	working day (schedule)
<i>we</i>	weekend (schedule)
<i>win</i>	window

# Preface

In 1997 I became "infected" with the virus of building performance simulation during my work at the Fraunhofer Institute for Solar Energy Systems in Freiburg, Germany. In the subsequent twelve years, during a good time at my former affiliation, the institute for Computation in Engineering at the Technische Universität München, I studied the related subsystems such as geometrical and building information modeling, advanced numerical algorithms, and computational fluid dynamics. A number of colleagues influenced me on this way.

Since 2005, I provide a lecture and exercise course on the subject. The first version of this course – its debut – emerged for a workshop within the European ATHENS program in November 2005. Since that time this course has been integrated into the regular course of studies within the Faculty for Civil Engineering, and into the Master's program *ClimaDesign* of the Faculty for Architecture at the Technische Universität München. Likewise, within a Master's program at the Augsburg University of Applied Sciences the course has been given. It is thereby a challenging idea to close the still persisting gap in the course of studies in civil engineering concerning the topic of building energy simulation. Traditionally, the latter is taught within the field of mechanical engineering or is subject to the work of physicists or "numerically talented" architects while civil engineering places more emphasis on the computational mechanics sector.

Following a number of discussions with PhD students at conferences, international workshops and according to the feedback received at visits of other departments, I observe that in many cases PhD candidates start working with powerful simulation tools without having a profound knowledge of the insides and the various interdependencies. The book is therefore designed as an introduction into the topic of building energy simulation including the prediction of the indoor thermal quality performance and addresses students at the graduate or PhD level working in the respective field.

The intention of the material on hand aims not at replacing existing textbooks such as for example the comprehensive book of JOE CLARKE on *Energy simulation in building design* or the book of CHRIS UNDERWOOD ET AL. on *Modeling methods for energy in buildings* which I would both like to recommend for further reading. In order to understand the numerical techniques implemented in building simulation software, it is the conceptual idea to develop a thermal multizone simulation prototype as used in today's building simulation software tools step by step with minimum semantics – but including a detailed geometric model.

In my first ATHENS courses students developed a single-zone prototype with the computer

algebra software MapleV. Although being a powerful tool, the main simulation time loop produces "spaghetti-code" which is not easy to read. With this experience, we merged the Maple code to the Matlab/Simulink tool and saw that – with a completely reviewed data structure for the geometric model – the set of functions produces numerous files, which may not be advantageous in terms of didactics. Based on these observations, we finally decided to use an object-oriented class hierarchy in C++ for the model. In my opinion, however, a new and promising trend is the equation based multi-physics modeling, such as the models of the MODELICA environment, which emerged during the last years. These models are very powerful, if combined with interactive graphical programming environments.

The concept of providing a practical introduction is similar to the book on *Numerical simulation in fluid dynamics* of MICHAEL GRIEBEL ET AL., which inspired me a lot. The reader shall become familiar with the theoretical background, the mathematical models and the related discretization methods. The reader shall accordingly be "straining at the leash" to develop his or her own code... This is, in my opinion, the best way to really understand the mathematical, numerical and physical background of the respective models. On the other hand, the beginner should be aware, that modern software packages are based on hundreds of man-years work or more – it does accordingly make not any sense to create a new simulation tool from scratch. However, in case you may feel this "prickle", the concept behaves as intended. If not please feel free to send your comments and suggestions!

I would like to express my sincere gratitude (in alphabetical order) to Martin Egger, Jérôme Frisch, Wolfram Haupt, Gerd Hauser, Gerhard Hausladen, Jan Hensen, Sebastian Herkel, François Hillion, Manfred Krafczyk, Sylvain Lauret, Petra Liedl, Christoph Nytsch-Geusen, Gunter Pültz, Ernst Rank, Darren Robinson, Tobias Schrag, Rudi Schwab, Iris Schweinfurth, Jonas Tölke, Christian Waldhoff, and others for their professional comments, suggestions and the material provided.

Last but not least, I am more than grateful to my family for their endless support and love, who endured losing their husband, son and dad for several months in series.

Kammlach, August 27, 2009

Christoph van Treeck  
*treeck@ibp.fraunhofer.de*

# Chapter 1

## Introduction

### 1.1 What is building performance simulation?

Building performance simulation offers an efficient aid towards sustainable development of building and operation of buildings – a tool for estimating the energy use and operating cost of residential and commercial buildings and for a thorough investigation of dynamic effects like the energy demand for cooling and heating of a building, the temperature distribution in rooms and inside components, the various heat flows through a building's fabric including inter-zonal air flows, the assessment of the occupant's level of thermal comfort, the interaction of the power plant system with the building including control, or the use of daylight. Various modeling approaches and methods exist in order to address these issues.

One distinguishes between

- *energy balancing approaches*, e.g. monthly or annual heat balances,
- *building component models* for the simulation if steady state or transient heat and moisture transport in 1D, 2D, or 3D,
- *single or multizone models* for predicting the energy use for space heating and cooling,
- *HVAC<sup>1</sup> and building control models* for calculating the energy use for water heating and additional energy etc.,
- *daylight simulation (daylighting)*,
- *detailed numerical methods* for computing heat and mass transfer including radiation with a high resolution in space and time,
- and *life cycle assessment (LCA)* methods for estimating the resource requirements of buildings in terms of primary energy usage (and treatment of waste materials).

This book focusses on the introduction to thermal multizone models and simplified models for calculating the air exchange between zones and the environment.

---

<sup>1</sup>Heating, ventilation and air-conditioning (HVAC)

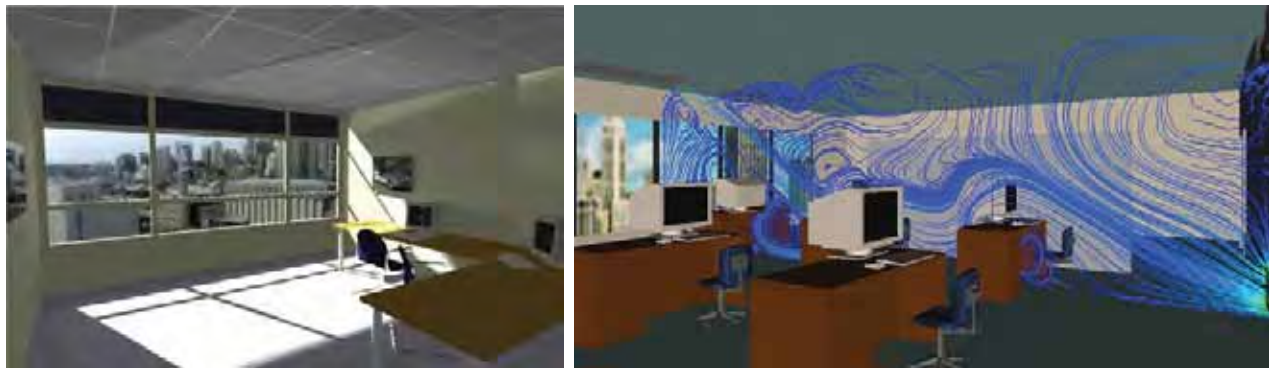


*Figure 1.1:* Daylighting analysis (courtesy of Fraunhofer ISE, Freiburg) and indoor air flow analysis. The CFD results [17] show the air flow induced by in- and outlets of an HVAC system. Streamlines of the 3D simulation are visualized on a 2D plane, colors indicate different flow velocities.

Numerical building simulation tools were traditionally developed and applied by mechanical engineers and building physicists. Nowadays the topic continues its success in the disciplines of civil engineering and architectural engineering. At the present time a new generation of engineers is emerging – in charge of supporting the process of sustainable building design and operation by providing consultancy work with the help of building performance simulation. The latter approach is required as the dynamic behavior of a building and its users cannot be captured by simplified calculation methods. New and existing buildings make great demands on the indoor thermal quality performance and the energy consumption. Building performance simulation supports planning reliability in the energy efficient building design and renovation planning.

A problem building simulation engineers are facing is the persisting sequential workflow in the planning process which focusses on the issues of architectural design (aesthetics, lay-out, etc.) and structural design in the initial stage of a project. Besides the installation of HVAC components according to the demands, sustainable concepts require *passive measures* in order to utilize environmental sources, to protect from undesired loads and to limit the demands for cooling and heating. The heat and cooling *delivery* is a second step.

The more a building and its envelope reacts to the outside climate conditions the less technology, and energy, is required in order to achieve a comfortable indoor climate. This requires an in-depth knowledge of the environmental potential of the respective climate zone. Simulation provides means to examine the interrelations between the design variables and to assess uncertainties in order to find a stable, feasible and optimal solution.

## 1.2 The simulation community and its communication channels

A number of engineers, researchers and practitioners specialized in the field of building performance simulation are organized in the *International Building Performance Simulation Association (IBPSA)*, see [www.ibpsa.org](http://www.ibpsa.org) for details. When IBPSA was established in 1987 after a number of international symposia on the use of computers for environmental engineering related to buildings (first in 1971) [18], the association defined the ambitious mission to "advance and promote the science and technology of building performance simulation in order to improve the design, construction, operation, maintenance and deconstruction of new and existing buildings worldwide" (IBPSA 1987, [15]). Over the years a number of regional affiliates have been established where the interested is kindly invited to join. IBPSA-World organizes the international conference series *Building Simulation*, the web site offers access to its proceedings (currently membership is free).

Other societies and organizations are the *Federation of European Heating and Air-conditioning Associations - Rehva* ([www.rehva.com](http://www.rehva.com)) and its daughter organizations, such as the *Chartered Institution of Building Services Engineers* ([www.cibse.org](http://www.cibse.org)), the *American Society of Heating, Refrigeration and Air-Conditioning – ASHRAE* ([www.ashrae.org](http://www.ashrae.org)), and architectural associations such as the *Royal Institute of British Architects - RIBA* ([www.architecture.com](http://www.architecture.com)).

A number of mailing lists are available in the internet. For example, *BLDG-SIM* is a tool independent mailing list for users of building energy simulation programs. Details may be found at <http://lists.onebuilding.org/listinfo.cgi/bldg-sim-onebuilding.org>. Further lists are provided by software developers and vendors for their respective products.

Major scientific journals addressing building performance simulation are

- *Journal of Building Performance Simulation* (official journal of IBPSA by Taylor&Francis)
- *ASHRAE Journal* and *ASHRAE Transactions* (American Society of Heating, Refrigerating and Air-Conditioning Engineers)
- *Energy and Buildings* (Elsevier)
- *Building and Environment* (Elsevier)
- *Solar Energy* (Elsevier)
- *Building Simulation* (Tsinghua Press, co-published with Springer)
- *Indoor and Built Environment* (Sage Publications)
- *Lighting Research and Technology* (Sage Publications)
- *Heat and Mass Transfer* (Springer)
- *International Journal of Heat and Mass Transfer* (Elsevier)

and others.

### 1.3 Scales and levels in building simulation

Building performance simulation can be characterized as a multi-scale and multi-level problem. The simulation *scales* range from seconds to years in time and from millimeters to kilometers in space. The various *levels* in simulation range from the environment and building surroundings, i.e. the issue of atmospheric and urban modeling including building aerodynamics, over the point of view of individual building zones and the building fabric in terms of multi-layered structures up to the occupant's level considering user behavior, temperature sensation, thermal comfort perception and human thermoregulation.

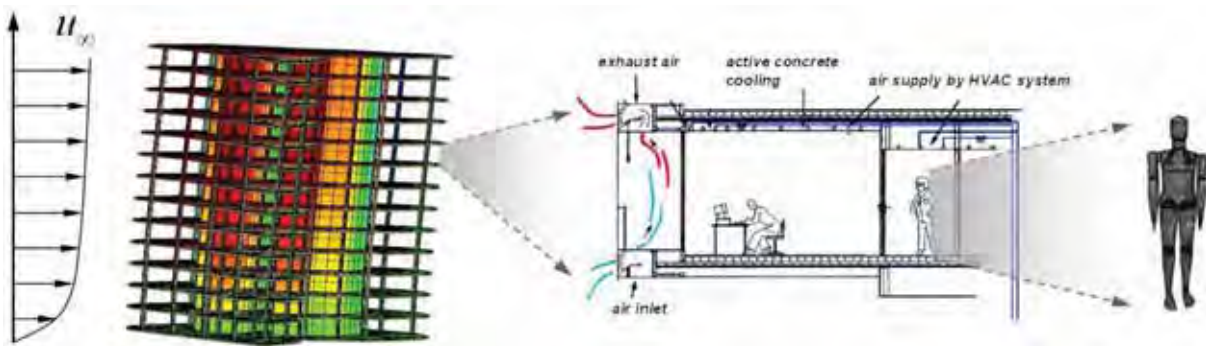


Figure 1.2: The various levels in simulation: Environment – whole building – single zone – occupant.

In order to properly describe the heat transfer mechanisms between a building and its environment detailed knowledge of the ambient climate is required such as the incident solar radiation, the ambient temperature, the air humidity, the sky coverage, or the static and dynamic wind pressure along the facade. The facade plays a key role as the relevant interface.

The granularity of a thermal analysis is determined by the spatiotemporal resolution ( $\Delta x, \Delta t$ ) of the balancing or modeling approach. The methods can be characterized as

- steady-state heat balances (coarse level),  $\delta T/\delta t = 0$ ,
- dynamic multizone models,  $\delta T/\delta t \neq 0$ , and
- computational methods modeling fluid flow, radiative heat transfer and heat conduction in detail (fine level).

Coupled approaches exist in order to bridge the gap between the scales and levels.

*Static balance approaches* for assessing the energy consumption of a building make use of monthly or annual heat balances with degree days as weighting function. Heating and cooling demands are determined by approximating transmission and infiltration losses, solar and internal heat gains. Transient effects such as the heat storage capability may be estimated in the form of lump-sum factors as provided in standards. Local spatiotemporal effects such as daily temperature variations cannot be captured, static balances are therefore indicative of global causalities for a building as a whole.

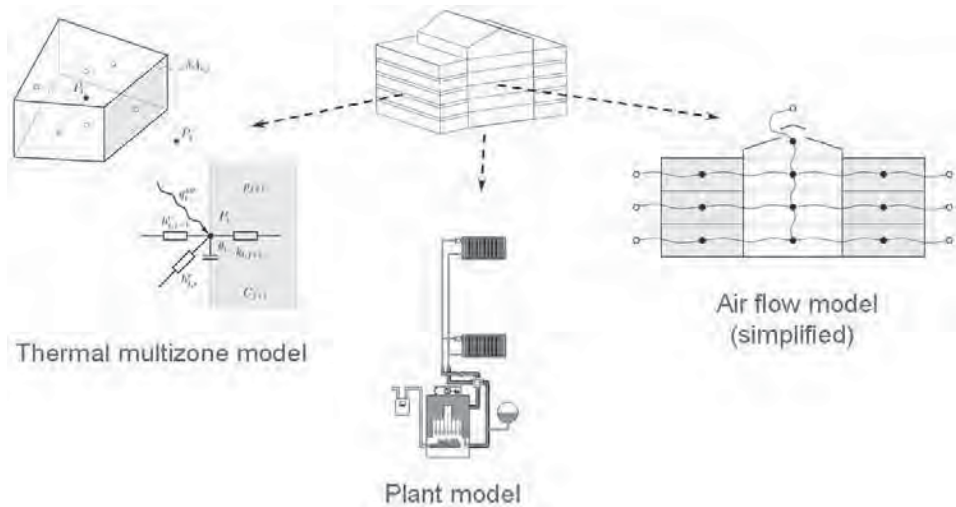


Figure 1.3: Interaction between thermal multizone model, plant model and simplified air flow model.

Whole building energy performance simulation on an annual basis with a temporal resolution from seconds to hours restricts the spatial resolution to a rough zonal discretization. *Thermal multizone models* are usually based on an anisotropic finite volume (FV) conservation approach [6]. The physical problem is transformed into a set of conservation equations for energy and mass which are then integrated at successive time-steps in response to ambient climate, occupant and control system influences. Energy balances involve short and long wave radiation processes, transient heat conduction through the structure, surface convection and enthalpy changes. Heat flux through the structure is thereby approximated in a one-dimensional form for each component. The discretization generally leads to a set of nonlinear equations with unknown temperatures to be solved at each time-step. Mass flow rates between different zones, each represented by either a single node or a few nodes, are computed using an artificial nodal network with pressure values as unknowns. The resulting nonlinear equation set is

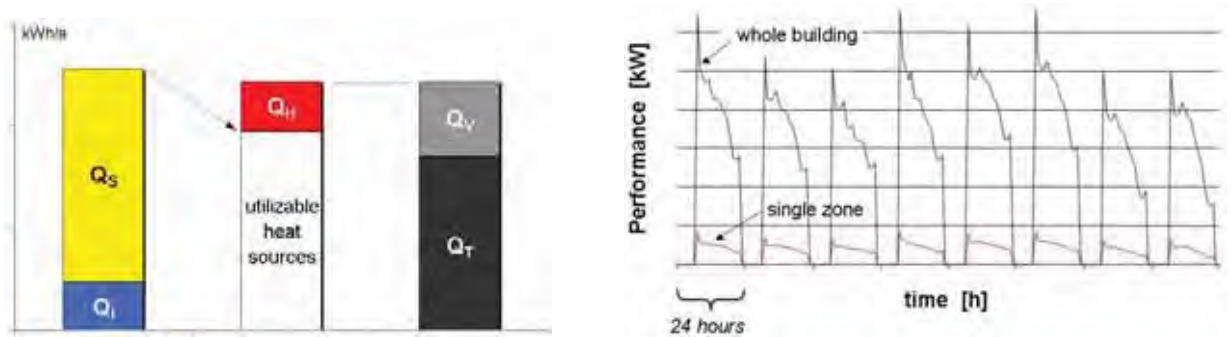


Figure 1.4: Static annual balance versus time dependent performance variations computed with a thermal multizone model. In the left hand picture, sources (solar and internal heat gains) and sinks (infiltration, ventilation and transmission losses) are accumulated. The heating demand results from the difference between sinks and (utilizable) sources. The right hand side shows the heat performance as single quantity both for a single zone and for the whole building for the period of eight days, for example [29].

simultaneously coupled with the aforementioned thermal network. Both sets have to be solved iteratively. For an office building, for example, it is usual to obtain equation sets with a few hundred to thousand unknowns to be solved for each time-step.

*Computational fluid dynamics (CFD)* on the other hand is a high-resolution technique for resolving complex flow patterns such as indoor air flows. A CFD model requires a geometrical model as input for creating a mesh model of the respective scene; a thermal multizone may provide realistic boundary conditions for such simulations. After the usually (expensive engineering) time consuming preprocessing step and simulation phase, results are analyzed in a subsequent postprocessing step in order to reduce, visualize, integrate and interpret the data. As typical problem sizes range from a few thousand up to several million degrees of freedom, a CFD analysis is limited to single zones and short time intervals – a whole year building performance simulation is thus not feasible with CFD. Further care must be taken of the treatment of the near wall flow domain and the capabilities of the applied model concerning turbulence, transient effects and (adaptive) mesh refinement. The reasonable application of CFD requires profound knowledge in fluid dynamics and thermodynamics [10].

In practice, the simulation resolution and accuracy depends on the data availability and the level-of-detail of the respective model. For example, in the early design phase of a building information may be available on the location, the shape of the building (e.g. U-shaped building with glazed courtyard), the floorage and the intended type of use (office building, school, hospital). With this little knowledge only minor predictions are possible. If, at a later stage, further details are known such as the overall layout, the type of the building envelope, the construction materials and the type of HVAC system to be applied, a detailed thermal analysis would be feasible. Initial information obtained by a dynamic multizone model on an hourly basis may then provide a suggestive decision basis, a further refined model including a plant model would restrict the simulation to even smaller time-steps.

In simulation practice also the visualization of simulation results is an important aspect. The expressiveness of results varies according to the level of detail. At a coarse level, for example, significant details may not be visible while at a fine level the mere flood of data must be condensed in order to extract and interpret the relevant quantities.

## 1.4 A short historical review

Building energy simulation has been developed throughout the past decades in the context of energy efficient building design, taking considerable advantage of improvements in efficient numerical algorithms. First computer applications started in the early 1960s with simplified hour by hour simulation of heat and moisture processes [18] replacing more and more graphical methods for solving the mathematical equations. One of the first papers on the use of the finite difference method on digital computers was published by KUSUDA [19] in 1964. In these early days, emphasis was placed on improving physical and empirical models for heat and moisture transfer considering different conditions of weather and building use as calculations were based on analytical formulations and simplified assumptions with a weak coupling between calculation steps [6]. Consulting engineers initially concentrated on computerized

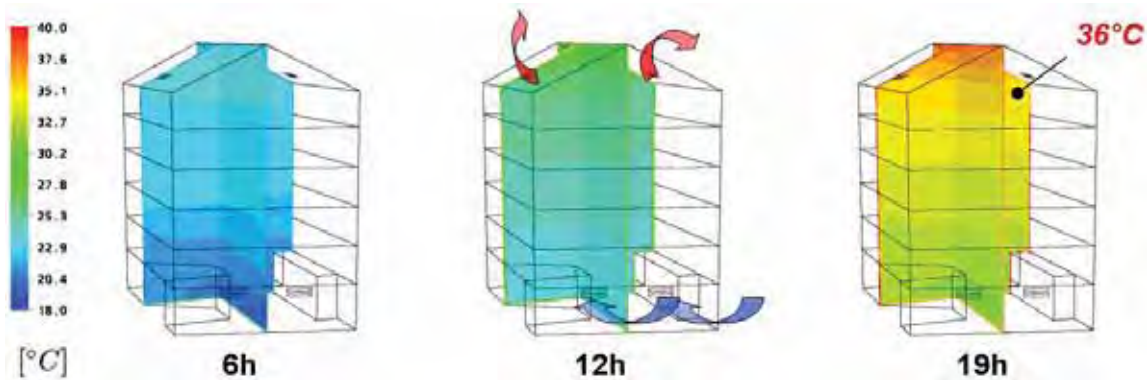


*Figure 1.5:* Ventilation study of a building with inner courtyard for a hot summer day [14, 30, 32]. For this study, a thermal multizone and a CFD model were coupled in order to obtain realistic boundary conditions for the CFD. The results (temperature plot using slice planes) indicate a thermal stratification with maximum temperatures in the late afternoons.

HVAC calculations based on quasi steady state models assuming ideal control systems without set point deviations.

In order to reduce the complexity and to lessen the computational load, STEPHENSON and MITALAS introduced the thermal response factor method (Z-transfer functions) for accurately predicting transient heat conduction through multi-layered wall components [22]. The method is based on a Laplace transfer domain analysis for solving the time delayed heat storage effect by a convolution scheme and allows to compute the respective Fourier coefficients prior to the thermal analysis in order to save computing time during the simulation (also described in [6]). The method can also be applied to room cooling load calculations. A drawback of the elegant method is its restriction to one-dimensional heat transfer problems. It is thus not applicable to capture 2D or 3D effects (only for constant heat transfer coefficients)).

Related to building simulation, since the late 1960s a number of models and correlations were published in order to empirically address convective heat transfer or concerning simplified numerical models for radiative heat transfer or shadow calculation. Based on tracer gas experiments, for example, correlations were found between the infiltration air change rate and the wind speed and temperature difference as driving forces [1, 18]. GERTIS ET AL. [9] present a summary on the state-of-the-art of calculation methods in these days. With the introduction of indices relating the level of comfort perception FANGER is a well known pioneer in the field of thermal comfort analysis [7]. Also first ideas on modeling human thermoregulation emerged during that time such as the multi-segment model of STOLWIJK [27] or the two-node model of GAGGE [8].

Many of the simulation codes have their roots in the early 1970s [11, 12, 24, 26]. Multizone simulation models make use of a numerical approximation of a mathematical model representing energy flow paths and their interactions having space and time as the only independent variables. With the so-called integrated modeling approach which emerged in the 1980s, thermal, visual and acoustic effects of performance were considered at the same time [6, 30]. In the 1980s, also first ISO activities were published which addressed the comparison between different simulation programs [2].

Today, the availability of powerful hardware allows a detailed treatment of physical processes within acceptable simulation time. Simulations such as computational fluid dynamics (CFD), finite element (FEM) based approaches or multizone building models, for example, are thereby state-of-the-art tools. A further increase of performance is obtained when the computational code is implemented on parallel hardware architectures. It should be noted that the direct numerical simulation of all the scales and levels at the same time still is and will persist a "Grand Challenge" for the next decade(s). Among the major problems of the application of detailed simulation tools such as CFD are the engineering costs associated with the effort for setting up numerical models and the complexity of mesh generation which restricts the application of such tools. Building performance simulation will always be a compromise between accuracy, computational efficiency and modeling effort.

The next generation of simulation software will therefore have to support a state-of-the-art *integrated* building design process providing links to building information models (BIM) and CAD models in the sense of supporting *interoperability* [30] and should behave like a *generic* and *model-adaptive* multi-physics simulation tool.

## 1.5 Available simulation software and tools

The various software tools in the respective context of building performance simulation are summarized in the *Building Energy Software Tools Directory* of the US Department of Energy, see [www.eere.energy.gov/buildings/tools\\_directory](http://www.eere.energy.gov/buildings/tools_directory). The directory provides information on tools for evaluating energy efficiency, renewable energy, and sustainability in buildings including a short description and information concerning expertise required, users, audience, in-and output, strengths and weaknesses, technical contact, and licensing issues.

Among the most frequently used tools are for example:

- **ESP-r** has been developed since 1974 by the Department of Mechanical Engineering of the University of Strathclyde (UK) and is available under GPL license. The code is based on a finite volume conservation approach and comprises a central project manager providing the simulator itself, support databases, performance assessment tools and links to other applications for CAD, visualization and report generation.  
Link: <http://www.esru.strath.ac.uk>

- **TRNSYS** by the Solar Energy Laboratory of the University of Wisconsin (USA) is a modular energy simulation program including a graphical interface, a simulation engine, and a library of components that range from building models to HVAC equipment and others. TRNSYS is very flexible but requires sufficient experience. Also a "light" version is available.

Link: <http://sel.me.wisc.edu/trnsys>

- **EnergyPlus** of the US Department of Energy (USA) emerged from the building energy simulation programs BLAST and DOE-2 and is a multizone simulation program supporting airflow, electric power simulation and others. E+ provides an interface to the

IFC standard for exchanging geometry with CAD programs. The DesignBuilder tool (developed in the UK) is linked with E+ for rapidly creating volume models and zones. Links: <http://www.energyplus.gov> and <http://www.designbuilder.co.uk>

- **IDA Indoor Climate and Energy (ICE)** by the Swedish company EQUA Simulation AB is a new generation tool for simulation of thermal comfort, indoor air quality and energy consumption in buildings. Its mathematical models are described in terms of equations in a formal language, the neutral model format (NMF) and in terms of the MODELICA language [23]. IDA ICE provides an interface to the IFC [5].  
Link: <http://www.equa.se>
- <Virtual Environment> of Integrated Environmental Solutions (IES <VE>) is an integrated system for building performance assessment. It provides a link to BIM tools such as Autodesk REVIT and Google SketchUp.  
Link: <http://www.iesve.com>
- **TAS** is a software package by Environmental Design Solutions Limited (UK) for the thermal analysis of buildings including a 3D modeler, a thermal/energy analysis module and a systems/controls simulator, etc.  
Link: <http://www.edsl.net>

## 1.6 References and further reading

- [1] P.R. Achenbach and C.W. Coblenz. Field measurement of air infiltration in ten electrically heated houses. *ASHRAE Transactions*, 69:306–358, 1963.
- [2] L. Agnoletto, E. Danter, K. Gertis, G. Hauser, G. Johannesson, A. Sachi, and A. Verhoeven. The non-steady state thermal behaviour of a building. H. 24, Forschungsberichte aus dem Fachbereich Bauwesen der Universität – Gesamthochschule Essen, 1984.
- [3] G. Augenbroe and Hensen J., editors. *Building Simulation 2003*. Proceedings of the 8th International IBPSA Conference, August 11-14, Eindhoven, The Netherlands, International Building Performance Simulation Association, 2003.
- [4] I. Bryn and P.A. Schiefloe (editors). Atrium models for the analysis of thermal comfort and energy use. Report of Task 12, Project A.3, Atrium Model Development, International Energy Agency (IEA), 1996.
- [5] buildingSMART. Industry Alliance for Interoperability (IAI), 2009. <http://www.buildingsmart.de>.
- [6] J.A. Clarke. *Energy simulation in building design*. Butterworth-Heinemann, 2nd edition, 2001.
- [7] P.O. Fanger, J. Ostergaard, O. Olesen, T. Madsen, and Lund. The effect on man's comfort of a uniform air flow from different directions. *ASHRAE Transactions*, 80:142–157, 1974.
- [8] A. Gagge. Rational temp. indices of man's thermal env. and their use with a 2-node model of his temp. reg. *Fed. Proc.*, 32:1572–1582, 1973.

- [9] K. Gertis and G. Hauser. Instationäre Berechnungsverfahren für den sommerlichen Wärmeschutz im Hochbau – Eine zusammenfassende Darstellung aufgrund des vorliegenden Schrifttums. *Berichte aus der Bauforschung*, Verlag Ernst & Sohn, 103, 1975.
- [10] M. Griebel, T. Neunhoeffer, and T. Dornseifer. *Numerical Simulation in Fluid Dynamics: A Practical Introduction*. Siam Monographs on Mathematical Modeling and Computation, 1997.
- [11] F. Haferland, W. Heindl, and H. Fuchs. Ein Verfahren zur Ermittlung des wärmetechnischen Verhaltens ganzer Gebäude unter periodischen Belastungen. *Berichte aus der Bauforschung*, 99, 1975.
- [12] G. Hauser. *Rechnerische Vorherbestimmungen des Wärmeverhaltens großer Bauten*. PhD thesis, Universität Stuttgart, 1977.
- [13] G. Hausladen, K. Kippenberg, and J. Oeltzen. Kontext Bauphysik, Komplexität als Konzept. In D. Danner, F.H. Dassler, and J. Krause, editors, *Die klima-aktive Fassade*, pages 30–39. AIT Edition Intelligente Architektur, 1999.
- [14] P. Heiselberg, S. Murakami, and C.-A. (editors) Roulet. Ventilation of large spaces in buildings. Report of Annex 26, Energy Efficient Ventilation of Large Enclosures, International Energy Agency (IEA), 1998.
- [15] International Building Performance Simulation Association (IBPSA). <http://www.ibpsa.org>.
- [16] R. Koenigsdorff and van Treeck C., editors. *BauSIM2006 Tagungsband Energieeffizienz von Gebäuden und Behaglichkeit in Räumen*. Erste deutsch-österreichische IBPSA Konferenz, 9.-11. Oktober, TU München, IBPSA Germany, 2006.
- [17] S. Kühner. *Virtual Reality basierte Analyse und interaktive Steuerung von Strömungssimulationen im Bauingenieurwesen*. PhD thesis, Department for Computation in Engineering, Technische Universität München, 2003.
- [18] T. Kusuda. Building environment simulation before desk top computers in the usa through a personal memory. *Energy and Buildings*, 33(4):291–302, 2001.
- [19] T. Kusuda and P.R. Achenbach. Numerical analysis of the thermal environment of occupied underground space with finite cover using a digital computer. *ASHRAE Journal*, 69:99–109, 1964.
- [20] R. Lamberts, C.O.R. Negrao, and Hensen J., editors. *Building Simulation 2001*. 7th International IBPSA Conference, August 13-15, Rio de Janeiro, Brazil, International Building Performance Simulation Association, 2001.
- [21] A. Malkawi and Augenbroe G. (eds.). *Advanced Building Simulation*. Spon Press, New York, 2004.
- [22] G.P. Mitalas and D.G. Stephenson. Calculation of heat conduction transfer functions for multi-layer slabs. *ASHRAE annual meeting, Washington D.C.*, 1971.

- [23] MODELICA. Modelica Association, 2009. <http://www.modelica.org>.
- [24] L. Rouvel. Berechnung des wärmotechnischen Verhaltens von Räumen bei dynamischen Wärmelasten. *Brennstoff-Wärme-Kraft*, 24(6):245–262, 1972.
- [25] E.-R. Schramek. *Taschenbuch für Heizung und Klimatechnik*. Oldenbourg Industrieverlag München, 73. edition, 2007.
- [26] J.E. Seem. *Modeling of heat transfer in buildings*. PhD thesis, Solar Energy Laboratory, University of Wisconsin Madison, 1987.
- [27] J.A.J. Stolwijk. A mathematical model of physiological temperature regulation in man. Contractor report NASA CR-1855, National Aeronautics and Space Administration, Washington D.C., 1971.
- [28] C. Underwood and F. W. H. Yik. *Modelling methods for energy in buildings*. Blackwell Publishing, Oxford, 2004.
- [29] C. van Treeck. *Numerische Bestimmung der Transmissionswärmeverluste durch Wärmebrücken in der dynamischen Gebäudesimulation am Beispiel eines hochwärmegedämmten Mehrfamilienhauses*. Diploma thesis, Fraunhofer-Institute for Solar Energy Systems (ISE), Freiburg, 1997.
- [30] C. van Treeck. *Gebäudemodell-basierte Simulation von Raumluftströmungen*. PhD thesis, Technische Universität München, 2004.
- [31] C. van Treeck. *Lecture notes in Building Energy Simulation*. Department for Computation in Engineering, Technische Universität München, 2005–2008.
- [32] C. Waldhoff, B. Lenzen, T. Schrag, C. van Treeck, M.M. Gonzalez, and Nytsch-Geusen C. Vergleich thermischer und strömungsmechanischer Simulation von grossen verglasten Räumen. In *TSE Otti, Staffelstein*, 2004.
- [33] J.P. Waltz. *Computerized building energy simulation handbook*. The Fairmont Press Inc., Lilburn, GA, 1999.

# Chapter 2

## Energy efficient building design

### 2.1 Energy consumption and energy scenarios

During the past decades legislation put considerable effort into reducing the total energy consumption of buildings and thus to countervail greenhouse gas emissions. The building sector significantly contributes to the overall primary energy consumption and waste production. Most of this portion is used for heating, cooling, air-conditioning, lighting, utilization, and hot water supply. Another part is required for the production and transport of building materials and components. These demands are mainly supplied by consuming nonrenewable energy resources.

The building sector offers the largest single potential for energy efficiency [6], especially in the passive solar energy domain. Measures to reduce the primary energy consumption are

- decreasing the demands,
- increasing the efficiency for energy production, supply and transformation,
- improving the operation of buildings and
- enhancing the use of renewable energy.

Figure 2.1 shows the total primary energy demand in Germany for the year 2006, for example, for the four sectors industry, households, trade & commerce and transport and for the respective domains of information and communication (ICT), lighting, mechanical energy, space heating and heat required for processes according to [51]. Thereby the space heating of households dominates the overall heating expenses, for the industrial sector it is the process heat. The transport sector contributes significantly to the balance with more than one third. Following [51], petroleum based energy sources (heating oil and fuel) contribute with 40% to the final energy, petroleum gas and electricity with 27% and 20%, respectively. With respect to the final energy, approximately just 50% can be finally utilized as effective energy. The example clearly demonstrates the saving potentials in both the industrial and private sectors and the need for intensifying the use of renewable energy resources in order to reduce greenhouse gas emissions.

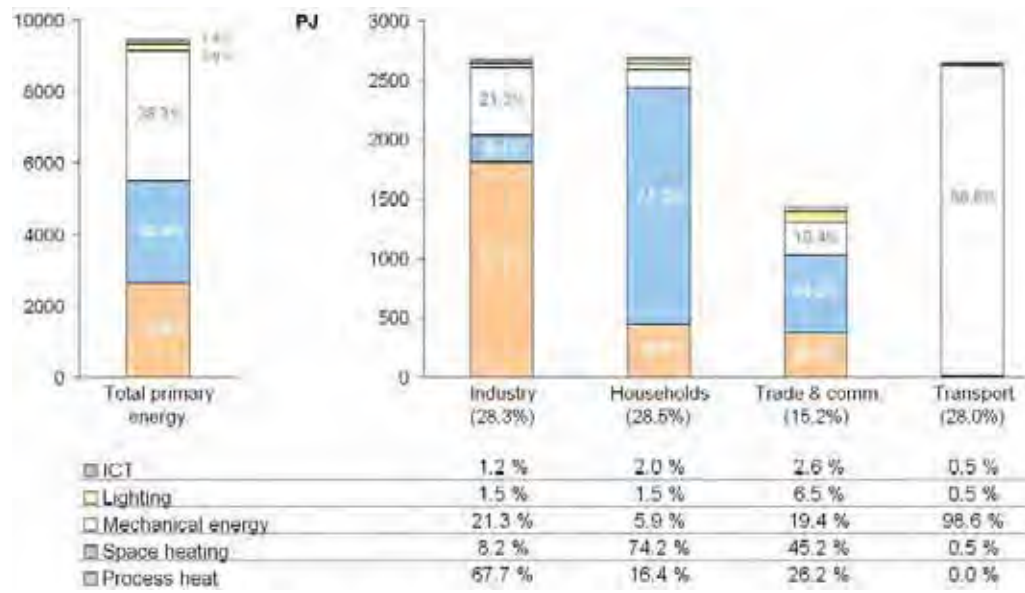


Figure 2.1: Primary energy demand in Germany (2006) with respect to different sectors and domains. The left hand side shows the cumulated quantities of all four sectors. Adapted from [51].

The World Energy Outlook 2006 of the *International Energy Agency (IEA)*<sup>1</sup> starts by summarizing the central message from the preceding documents with the following statement:

*"The energy future which we are creating is unsustainable. If we continue as before, the energy supply to meet the needs of the world economy over the next twenty-five years is too vulnerable to failure arising from under-investment, environmental catastrophe or sudden supply interruption."* [33]

In its reference scenario IEA predicts an increase of the global energy-related carbon-dioxide emissions by 55% between 2004 and 2030 where developing countries account for over 70%. Governmental action can thereby alter this trend [33]. If no actions are performed, the energy-related carbon-dioxide emissions, cf. Figure 2.2, grow faster than the primary energy use.

In the so-called alternative policy scenario which accounts for the case if countries were to adopt all of their considered policies the world primary energy demand could decrease by 10% compared to the reference scenario. This requires enhancing the use of renewable energy resources such as geothermal resources, biowaste power, solar thermal and photovoltaic power, hydrogen power, hydraulic power and off- and onshore wind power generation, as well as the use of passive solar energy in buildings or the use of efficient systems for the energy conversion such as CHP generation plants<sup>2</sup>. Figure 2.3 shows the development of the world energy demand for the two scenarios and for different primary energy supplies.

<sup>1</sup>Body within the framework of the Organization for Economic Co-operation and Development (OECD).

<sup>2</sup>combined heat and power generation (cogeneration)

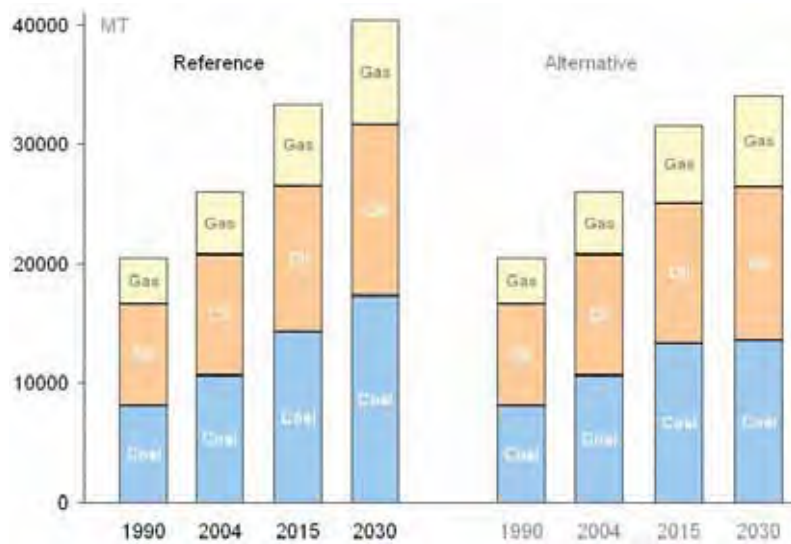


Figure 2.2: Development of the carbon-dioxide emissions for both scenarios. In the reference scenario current settings and political decisions remain unchanged. Adapted from [33].

The potential for using renewable resources thereby differs from country to country. In some countries, for example, geothermic resources are available close to the surface, other countries possess high potentials for hydroelectric power production. In the global picture of the IEA also nuclear power may contribute to reducing the  $CO_2$  emissions. The latter is very controversially discussed in the public because of the high long-term risks associated with the technology.

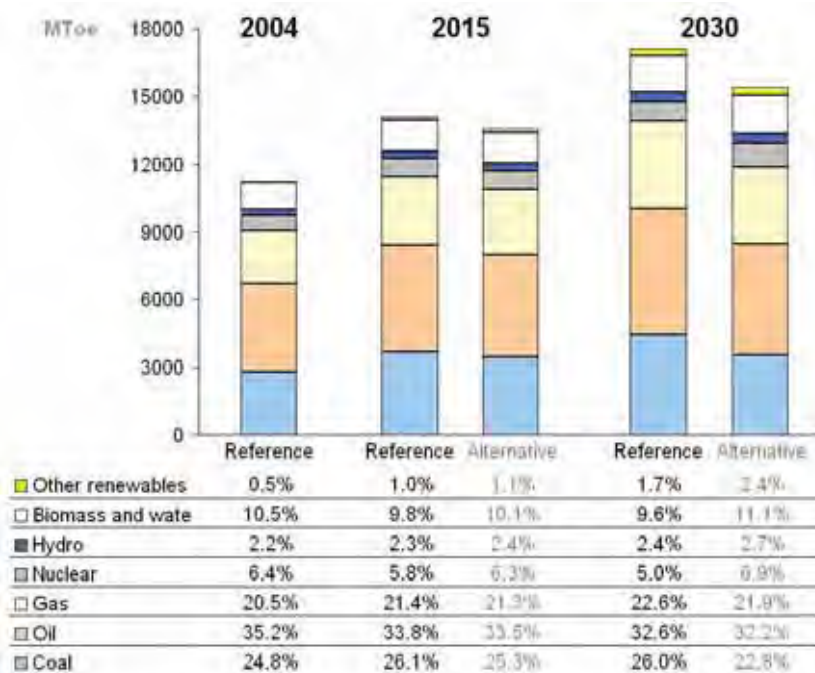


Figure 2.3: Different scenarios of the IEA World Energy Outlook 2006 for the development of primary energy supplies. Adapted from [33].

## 2.2 The Energy Performance of Buildings Directive

The European *Energy Performance of Buildings Directive (EPBD)* which was established in 2002 by the European Parliament and the European Council targets at reducing the primary energy demand of buildings [13]. The directive claims general calculation procedures to assess building energy efficiency and demands the implementation of minimum efficiency requirements for new and existing buildings (refurbishment of large buildings). Buildings are considered as an integrated system together with the installed plant systems and also the preceding processes in the energy supply and power generation are taken into account. The directive goes beyond balancing annual heating demands as a single performance indicator which is insufficient for non-residential buildings. *Energy passes* serve as a further descriptive measure for evaluating the energy efficiency which becomes relevant if a building owner or user changes. Another issue is the regular inspection of heating and air-conditioning systems. The European countries themselves transfer the EPBD into national codes and standards. For an overview it is referred to the diagram published in the EN Standard 15251 [11]. In Germany, for example, the Energieeinsparverordnung (EnEV) [12] defines the energetic requirements and other standards such as the DIN 18599 [9] the respective calculation methods.

In the residential building sector the low energy or passive building standard recently demonstrated the saving potentials. According to the definition of FEIST [14], a passive building restricts the annual heating demand to  $15\text{kWh}/(\text{m}^2\text{a})$  or less. Residential and non-residential buildings thereby require different optimization strategies as the using conditions diverge.

For non-residential buildings the electrical energy requirements significantly contribute to the total primary energy demand in terms of air-conditioning, lighting, utilization and active cooling. The energy efficiency of non-residential buildings can be improved

- by applying a high thermal insulation standard as well as solar shading devices in combination with improvements in the use of daylight,
- by activating the thermal mass of a building for passive cooling,
- by using heat recovery ventilation systems in winter,
- by enabling users to naturally ventilate rooms and spaces in summer and
- by reducing the internal loads.

Further decreasing the electrical power consumption contributes to save primary energy while the increased efficiency of the equipment again helps to reduce the thermal loads of the building. The latter is also important in terms of the thermal insulation. The requirements for active cooling can be further reduced if fully glazed facades are avoided, see section 2.5. Extra costs may become available for improving the efficiency if, in turn, expenses are saved for the HVAC installation, for example if the active cooling becomes obsolete. In the recent years, some projects demonstrated that non-residential buildings can be operated with less than  $40\text{kWh}/(\text{m}^2\text{a})$  primary energy for space heating, lighting, and air-conditioning (with respect to the net base area) [26, 32, 49].

In addition to the simulation which supports the planning phase also *monitoring* the energy consumption during the operation is an important task, also with respect to the facility management. Comparable to the instruction manual of a car, simple operating guidelines and user documentations could support building users in the configuration of the building automation systems. Cyclically monitoring the energy efficiency helps to operate a building as intended by the energy concept and thus to improve the overall performance [45].

## 2.3 The building life cycle

The holistic evaluation of the ecological impact of a building on the environment goes beyond the purely energetic view during the utilization phase of the building and is further based on the consideration of primary energy requirements and pollutants emitted during the construction, maintenance, refurbishment and demolition phases of a building. Figure 2.4 shows the different phases of the building life cycle from the design up to the deconstruction.

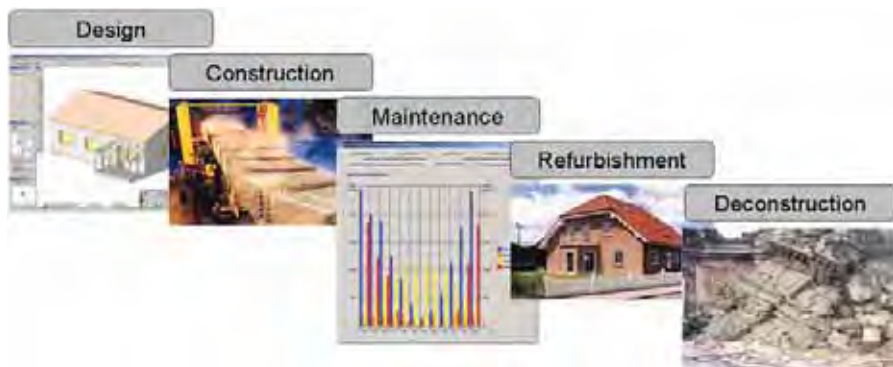


Figure 2.4: Phases of the building life cycle from design and construction up to deconstruction.

After a few years of operation the primary energy demand for heating, cooling and hot water supply exceeds the amount of the primary energy required for the construction as shown for the cumulated energy demand (CED) [15] on the right hand chart of Figure 2.5 for a non-residential building. On the other hand, the choice of components used for the construction has significant influence on the ecological impact assessment of a building. The contribution of the utilization energy with respect to some of the impact potentials, such as the eutrophication or the acidification potential of the whole building, may differ from (and in some cases might even undershoot) the contribution of the energy required for the building phase [61]. Hence, the emission of pollutants should be considered in addition to the energetic parameters in order to find an optimal solution in terms of the environment.

Standardized *life cycle assessment (LCA)* methods such as the ISO Standard 14040 [8] address this issue. Computer-aided methods can thereby support the integrated planning process by providing tools for drawing up a viable estimate of the ecological costs in the early stages of the design process. Figure 2.5 displays the results of a life cycle impact assessment obtained by a software prototype which is linked with a building information model in order to gather the data required for the inventory analysis and to compute energy required for heating and

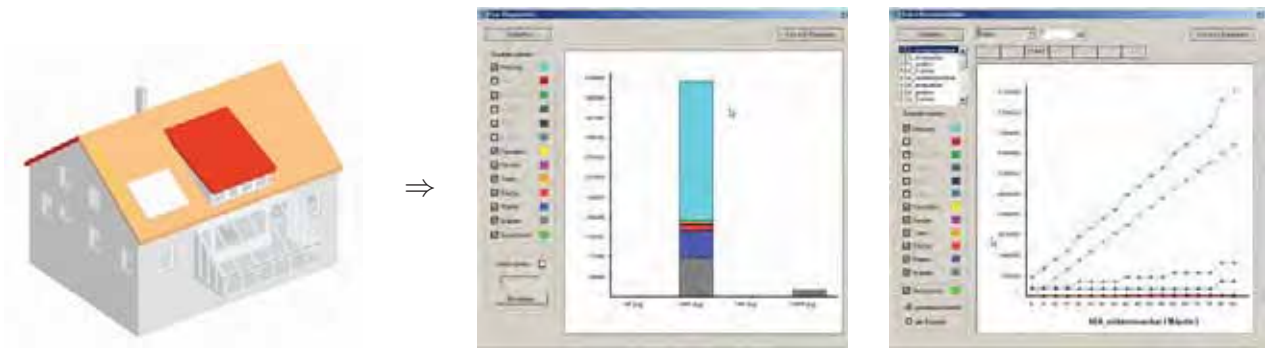


Figure 2.5: CAD integrated life cycle assessment of a residential building [41, 61].

cooling with a static balance approach. The relevant data such as the individual emissions of the building components are accessed from a central type catalogue provided by an internet database server [41, 61]. The software supports calculating balances with respect to different assessment methods such as the cumulated energy demand (CED) [15], the CML method [30], or the Ecoindicator95 method [19]. Starting with an inventory analysis the environmental impact is thereby separately assessed for the various areas such as the greenhouse effect or the carbon dioxide emissions. With a digital building product model, all the mass-, area- and volume-related properties can be efficiently collected and updated if the model is changed. The overall ecological impact can be quantified by finally aggregating the individual effects and weighting their respective influences in order to form a single ecological index [50].

In summary, *sustainability* in terms of building design and operation accordingly means to minimize the impact to the environment by minimizing the consumption of resources and energy, i.e. to minimize the increase of entropy in a thermodynamic sense as indicated by GERTIS et al. [18]. In the recent years, a number of methods for the sustainability assessment have been internationally discussed. In Germany, these methods are implemented in terms of the *Deutsches Gütesiegel für Nachhaltiges Bauen* by the German Sustainable Building Council (Deutsche Gesellschaft für nachhaltiges Bauen, DGNB) and the Federal Ministry of Transport, Building and Urban Development (BMVBS), in the UK the *BREEAM* system [4] is established, in the United States the *LEED Green Building Rating System* [53], in Australia the *Green Star* [20] and in Japan the *CASBEE* system [34].

## 2.4 Tools for the early design stages

In the early conceptual design stage of a project the simulation of the building performance is not feasible as detailed information such as the building geometry is yet absent. Coarse methods, monthly or annual balances which will be discussed in Chapter 3, may give first hints of the feasibility of a concept. Recently, a number of suggestions have been published in order to support decisions for the further planning process by providing guidelines and tools for a sustainable design.

HAUSLADEN ET AL. published a guideline for qualitatively predicting the indoor climate and the energy efficiency of non-residential buildings by pointing out the influences and inter-

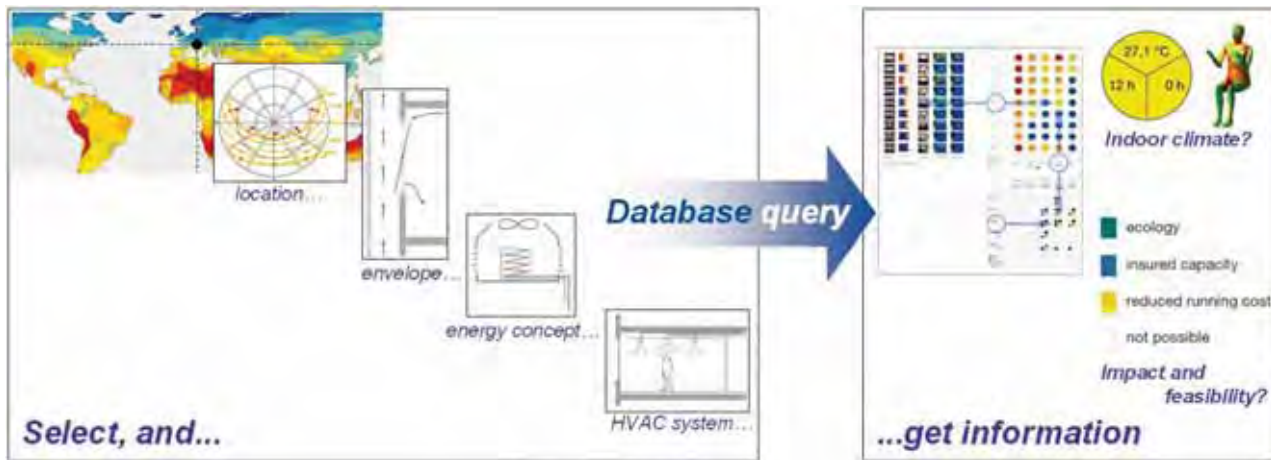


Figure 2.6: Guideline for planning buildings in different climate zones. Tool for pointing out the interplay between design variables with location dependent performance indicators considering indoor climate, thermal and visual comfort and energy requirements [29, 28, 38].

relationships between the individual design variables [29, 28]. The facade plays a key role in these considerations, since the window area, solar protection measures and the choice of materials exert a significant influence on the room climate. The interactions between the ambient climate, site specific conditions, the energy concept and the room climate become visible in the sense of a case-dependent sensitivity analysis. In order to exhaust the energetic and economic saving potentials, energy consumption and costs are addressed for the whole building life cycle including the construction and maintenance phases. As shown in Figure 2.6 the interrelations are displayed in a descriptive matrix-wise manner indicating the impact and feasibility of a concept. Performance indicators summarize indoor climate, thermal and visual comfort and energy requirements.

Another example is the *MIT Design Advisor* developed by URBAN ET AL. [52]. The tool is targeted for non-technical users and enables architects for rapid energy simulation of early-stage building designs. Basic parameters such as location, orientation, window size, type and insulation are selected from a single-page graphical interface. The tool dynamically computes the energy consumption and thermal comfort in real-time using integrated models for heating, cooling, and lighting.

## 2.5 Lessons learned?

The preceding sections covered the topics energy efficiency and savings in the primary energy consumption. The present section would like to address the issue of using large glazed facades and spaces in the design which became very popular over the past decades. People often associate the term *modern glass architecture* with the adjectives transparent, dynamic, precise, progressive or innovative. Historically, in the 1930s inexperience with the new glass material revealed the problems related with these constructions such as overheating in summer and uncomfortable cold conditions in winter. Figure 2.7 gives some examples of the well known Bauhaus architects Gropius and Le Corbusier.



*Figure 2.7:* From left to right: The Fagus factory building and the Bauhaus building in Dessau (Walter Gropius). Source: Wikipedia.

Even today the design of highly glazed buildings is a challenging task. The feasibility of a concept including a fully transparent facade depends on a number of parameters and should be carefully investigated by an integrated design team. Aesthetical reasons should not be the sole driving force in the architectural design. For example, some ventilation concepts adapt a double skin facade in order to make use of the natural pressure distribution along the surface. As the pressure distribution strongly depends on the atmospheric boundary layer and the surroundings such concepts imply uncertainties.

Double facades can be an instrument for noise control and – to some extent and given the limitations discussed by GERTIS ET AL. [17] – for supporting natural ventilation to counter-vail the so-called sick building syndrome [37] in tall commercial buildings. From the building physics point of view double skin facades shall improve the thermal properties of a facade including transparency and illumination. However, the investment costs of double skin facades exceed the costs for common curtain walls and these systems imply further collateral costs for operation and maintenance [36]. As commercial buildings significantly differ from residential buildings in terms of internal heat gains, a primary design intention is the reduction of the

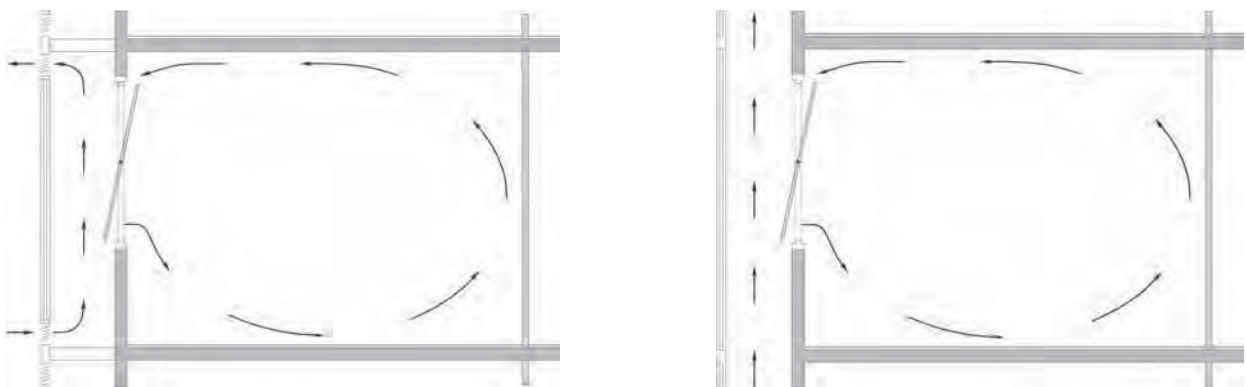


*Figure 2.8:* Air flow scheme for different double facade systems. Left hand side: Floor-wise separated system, right hand side: curtain wall double facade with chimney effect [40, 55].



*Figure 2.9:* In [10] described buildings concerning user comfort. From left to right: RWE Tower (1996), a "prototype for natural ventilation" ... with 2.1MW cooling plant installed. ARAG building (2000) with solar chimney for 7 floors each, disastrous primary energy demand of about  $700\text{kWh}/\text{m}^2$ . Commercial building (1996) with single pane heat protection glazing, mechanical ventilation without air-conditioning; according to [10]  $38^\circ\text{C}$  measured inside at 4th floor during ambient temperature of  $26^\circ\text{C}$ .

cooling loads.

Did people learn from the early lessons? Critical authors relate the modern architecture to *rapidly pre- and overheating buildings that have to be ventilated and cooled and that are real-time controlled by computers* [10]. Buildings with large glazed facades imply a *technically very complex effort for solving problems that conceptually emerge in the first place* [17]. Solar buildings may also be characterized as some kind of robots equipped with technology and sensors – comparable with *buildings in an intensive care unit* [59].

For commercial buildings performance characteristics are usually not available in the public. If so, the primary energy demand may reach a devastating magnitude. It is not unusual, that summer indoor air temperatures exceeded the ambient temperatures. Due to shading devices, the transparent facade may not prevent the extensive use of electrical light: even at clear sky conditions electrical lighting may become necessary as roller blinds remain closed in order to shade most of the incident solar radiation.

Another example is the Düsseldorfer Stadttor which has a double skin facade with an integrated courtyard and a remarkable structural design. According to [42] the natural pressure distribution contributes to the ventilation concept. The external part of the facade consists of a single-pane glazing, the inner part of an insulation glazing. In the 1.4m space between a high-performance reflecting roller blind is installed; air in- and outlets are arranged alternatingly along the facade. On a congress in 1995 [42], the concept was introduced as *brand-new air-conditioning technology. Hitherto required fully climatisation would become almost dispensable. The revolutionary construction would be able to partially replace conventional air-conditioning technology*. In reality, the air inlets are taking in the air heated by the upward facing facade boundary layer flow, the building is equipped with cooling slabs, uses evaporative cooling and

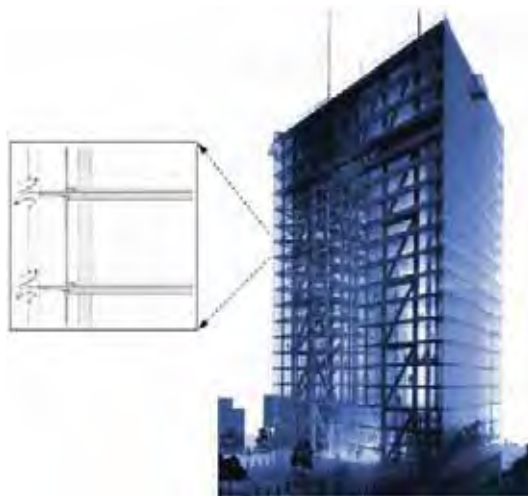


Figure 2.10: Düsseldorfer Stadttor, architects Petzinka, Pink and Partner [42]. The detail shows the floor-wise air inlets.

several additional equipment, details and specifications unknown. In 2003, the architect stated that he would *refrain from building fully glazed buildings in the future again* [10].

*Lessons learned?* The examples indicate that the advantages claimed by manufacturing companies and by some architects in terms of thermal properties, ventilation, transparency and modern design hide some of the relevant problems. These problems are overheating in summer [24], sound and smell transmission through the facade corridor as well as fire protection issues. Simulation provides a means for a thorough investigation of these effects in order to avoid the mentioned problems.

## 2.6 Active and passive components and measures

A sustainable building concept requires the consideration of a number of systems, components and materials and their interdependencies. One distinguishes between passive and active measures influencing the thermal behavior. Also the use of daylight for lighting is an important issue which interacts with the other measures. Passive systems require no or at least very low additional energy resources for their operation. Examples are glazed spaces integrated into the energy concept for preheating air in winter [25]. For example, HAUSER [23] quantifies the effect of such passive energy concepts. Active energy systems are components or control elements for hot water or electric power supply. Using active and passive solar cooling it is principally possible to design office buildings in central Europe without conventional active cooling devices. In the following section, some of the active and passive measures and components will be briefly introduced which are relevant for a thermal building model. Emphasize is placed on the passive measures. For further reading it is referred to [3, 16, 23, 28, 29, 58, 57], for example, and the references given in Section 2.7.

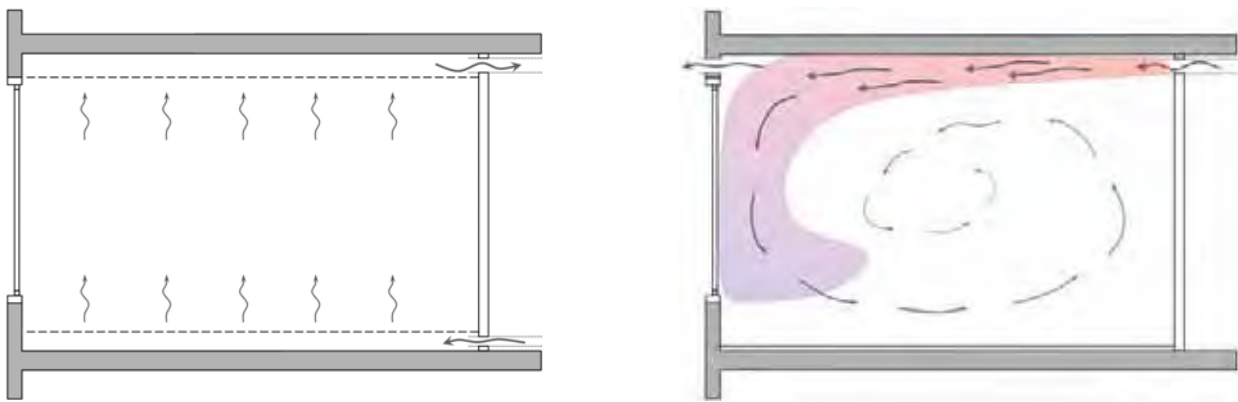


Figure 2.11: Left: Displacement flow in a space in the ideal case with a laminar flow and no mixing of the air layer. Right: Entrainment flow, here as driven cavity flow type with intensive mixing of the air.

### 2.6.1 Measures related to ventilation, radiation and thermal capacity

In order to access the available potential for passive cooling and heat recovery different concepts are available. Most of them make use of the building's thermal mass and use convective or radiative heat transfer mechanisms between components and occupants.

**Mechanical ventilation strategies.** Mechanical or natural ventilation is essential for fresh air supply and pollution control in order to sustain the required indoor air quality. Thermal comfort is thereby an important issue in both cases such as minimizing the draught risk or avoiding overheating. Controlled ventilation systems can help to reduce undesired infiltration losses and are usually applied in non-residential buildings. For the mechanical ventilation it is distinguished between different methods for routing the air flow inside rooms as shown in Figure 2.11: In the case of *displacement flow*, air is moved in a piston or plug-type motion in space [2]. Ideally the flow is of laminar type and the room air is not mixed in order to efficiently remove the used or contaminated air. If the inlet air temperature is lower than the room air and if the air inlets are located at the bottom, fresh air is accumulated in some kind of bubble. For realizing an *entrainment flow* type, ceiling-based supply air diffusers are commonly used for distributing and mixing the inlet air. As the air is effectively mixed, the temperature level of the inlet air may significantly differ from the room air. The latter is not possible in the case of displacement flow.

For the whole building different air duct concepts are feasible in order to make use of solar heat gains or to support passive cooling. The systems are characterized by the type of air supply, air handling unit and preconditioning, and the type of heat recovery. The concept may be adapted over the seasons in order to respond to altered circumstances. In order to avoid air-conditioning solely by convection and thus large air intakes, ventilation and air-conditioning are usually treated in a separate manner [2, 47].

*Air preconditioning with glazed spaces.* Fresh air may be provided via the facade (see also Figure 2.8) or via an inner courtyard which is connected to the building for pre-heating in

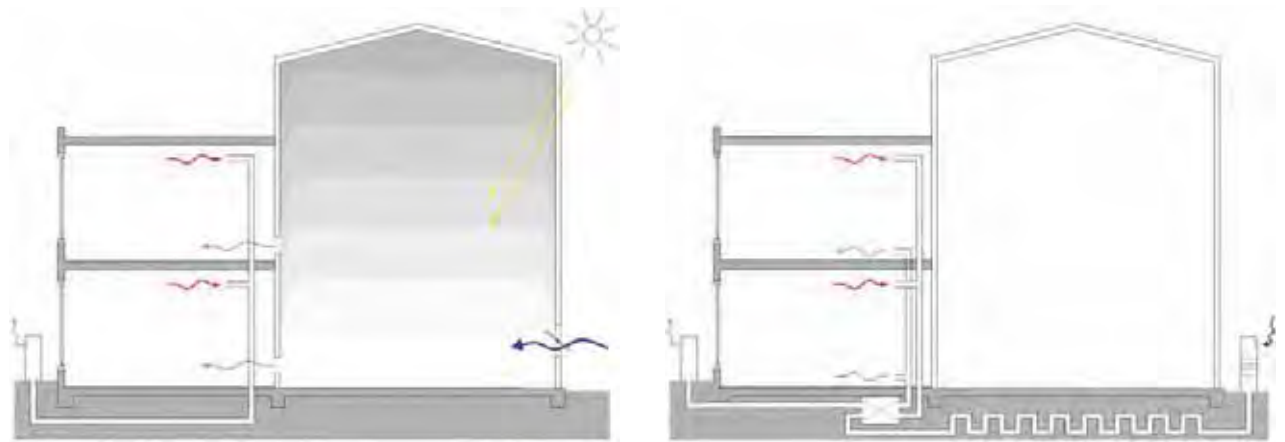


*Figure 2.12:* Different types of air duct systems in buildings. Left: Fresh air supply using an inner courtyard for preheating in winter and mechanical ventilation for the exhaust air. Right: Building with central air handling unit with heat recovery and soil air duct system for preheating/cooling of the air.

winter as depicted in Figure 2.12. For the latter concept a high air quality is required within the atrium. The supply and return air is transported with air duct systems. The installation effort thereby depends on the type of energy concept – in the most expensive way both air streams are directed to a central air handling unit. If, for example, the exhaust air is directed through the facade, the accumulated heat in the facade layer can be decreased in order to avoid overheating.

*Heat recovery.* In a mechanical ventilation system the exhaust air heat can be used by heat recovery. Centralized as well as local peripheral heat recovery systems are available. The system can be further enhanced by adding adiabatic cooling or by connecting with a soil air duct system for pre-heating or cooling the ambient air. If the air streams are not coupled with a central air handling unit and the exhaust air is directed through an inner courtyard, the heat recovery can be realized with the help of a heat pump [28].

*Soil air duct systems.* For passive cooling, the thermal capacity of the earth can be utilized with the help of a soil duct system [7]. The simplest form is an air duct system for air preconditioning, i.e. for pre-heating the ambient air in winter and (pre-)cooling in summer as the mean earth temperature remains nearly constant around  $10^{\circ}\text{C}$  over the seasons in 3 meters depth – or follows at least a flat sinusoidal function. Most important is the installation of appropriate filtering devices in order to prevent the accumulation of organic material in the pipe.

**Natural ventilation strategies.** The air change through windows or facade elements is driven by temperature and pressure gradients between the in- and outside [1] as shown on the left hand side of Figure 2.13 [55]. Figure 2.13 also illustrates the ventilation intensity related to the temperature difference for a single room according to PÜLTZ [46]. The ventilation intensity thereby depends on the room aspect ratio and the local position of the openings. MAAS [39] quantified the relation between temperature difference and volumetric flow rate by experiments. The development of the air age over time can be visualized in 3D by a fluid flow

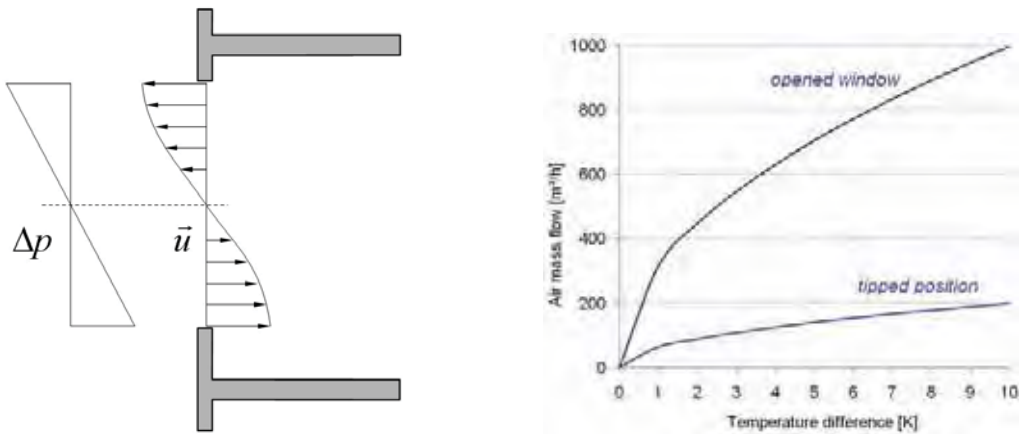


Figure 2.13: Left hand side: Bidirectional air exchange. Right hand side: Mass exchange related to the temperature difference between in- and outside for open and tipped window [1, 46].

simulation using an additional transport equation for the air age. It is referred to [2, 48].

Naturally ventilated buildings support users with a high level of user control and may prevent the effects of the sick or tight building syndrome [31, 47]. Adaptive thermal comfort guidelines thereby consider the adaptation of people to their surroundings in order to reduce physiological strain in terms of conscious actions (clothing, activity level, ventilation) and unconscious actions (shivering or sweating). The subject will be detailed in Chapter 13.

**Night ventilation.** With its high internal heat gains due to technical equipment, in non-residential buildings the thermal mass plays an important role. During the day the thermal capacity is able to store some of these gains whereas in the night period heat can be discharged by ventilation. The effectiveness is determined by the heat conductivity, capacity and density of the respective materials, the accessible indoor surface areas and the ambient temperature variations. The facade system has accordingly to technically support the ventilation strategy.

**Embedded pipe systems.** Besides the passive measure of night ventilation the thermal

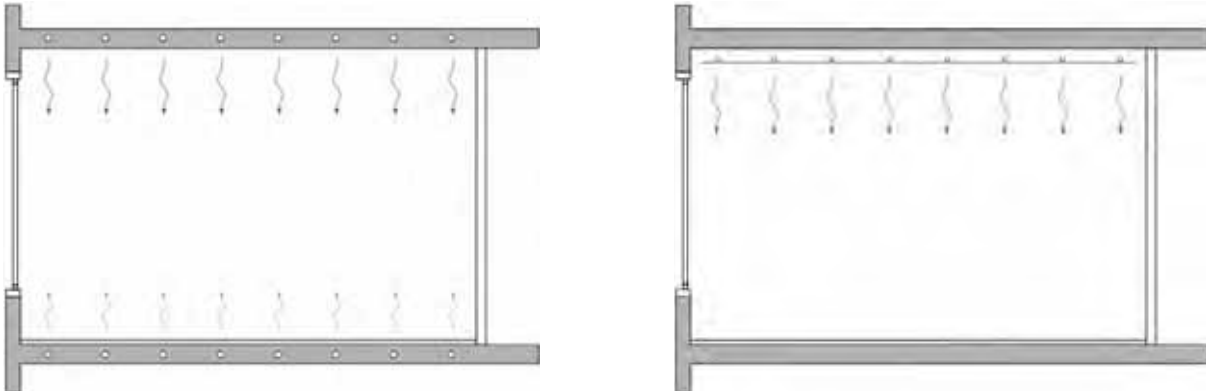


Figure 2.14: Left: Embedded pipe system in the massive ceiling. Right: Cooling panels installed below the ceiling.

mass can be activated by embedding water-bearing pipe systems into massive components such as the ceiling or the floor. The system shows a very inert behavior with a time delayed answer which can be used to compensate performance peaks. The realization of the system is cost effective. However, the ceiling should not be covered with additional materials such as sound absorbing elements which counteract the mode of operation.

**Cooling/heating panels.** In contrast, cooling (or heating) panels installed at the ceiling are a frequently used technique in office buildings. To prevent condensation the system usually comes along with a mechanical ventilation. As the thermal mass of the building is not directly activated the response time is much faster. In both of the latter cases the heat exchange is mainly due to radiative heat transfer. As the effective heat exchanging surface is large, low differences are feasible between room temperature and the cooling/heating water which allows for making use of regenerative energy sources.

## 2.6.2 Measures related to insulation, thermal capacity and phase changes

In the past decades a number of innovative systems and insulation materials have been developed such as translucent insulation materials (TIM), phase change materials (PCM), vacuum insulation panels (VIP), high performance glazings and high performance frame systems, and, as a new trend, vacuum insulation glazings [43, 60]. The physical correlations and casual heat fluxes through the building facade will be generally discussed in Chapter 3.

**Translucent insulation materials (TIM)** combine high energy transmission with good insulation properties [22, 44]. The comb or capillary structure, cf. Figure 2.18, enables a high transmission of solar radiation with multiple reflections towards a black absorber installed at the massive wall surface. The thin material has a low solar absorption and low heat conductance, it suppresses convective heat transfer by its comb structure, and can be further optimized with respect to the longwave exchange by adjusting the geometric aspect ratio [56].

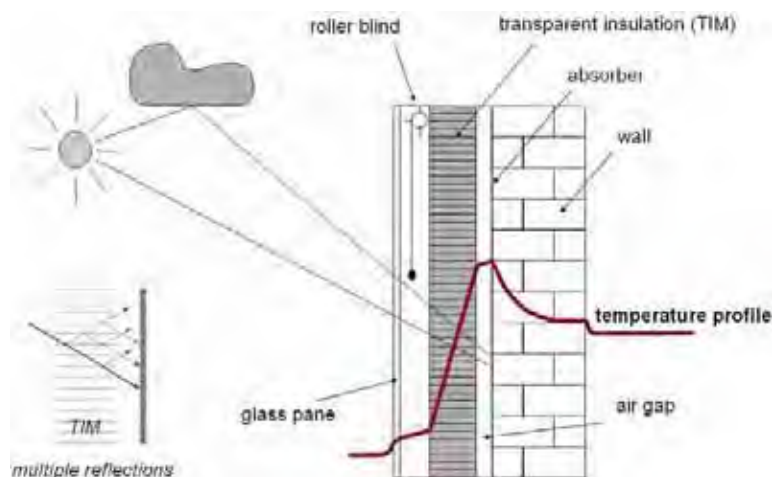


Figure 2.15: Basic configuration of a transparent insulation material (TIM) [54].

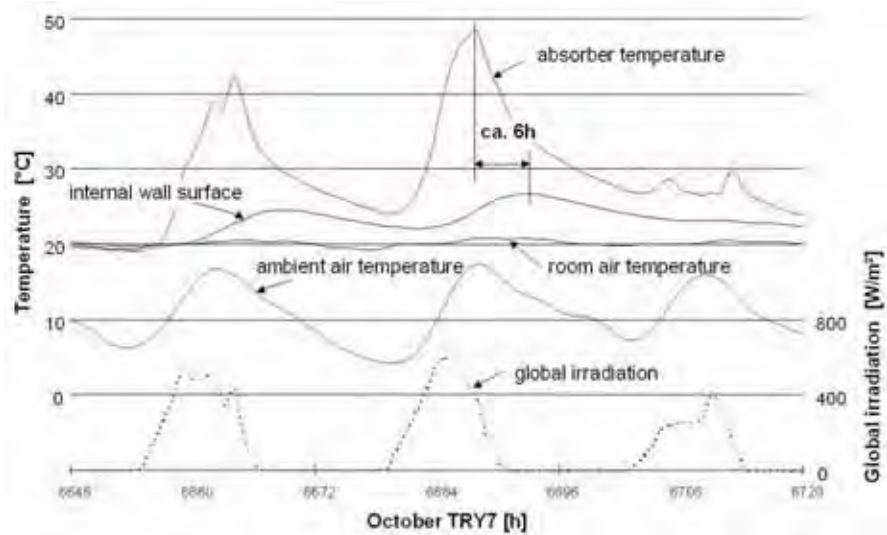


Figure 2.16: Results of TRNSYS simulation of a wall with transparent insulation material (TIM) for the period of three days [54]. The time dependent temperature distribution at the inner wall surface shows a characteristic time delay of  $\approx 6\text{h}$  to the absorber maximum.

TIM can also be directly integrated into the facade system as a light scattering medium. The time dependent temperature distribution at the inner wall surface of a TIM wall shows a characteristic time shift of approximately 6h to the maximum absorber temperature which is related to the irradiation [54] as shown in Figure 2.16. It thus enables a time delayed usage of solar energy with the inner wall as large radiator. In summer, a shading device is essential. The structure must be protected from environmental dirt and dust. TIM is well suited for buildings requiring heating during the transition periods.

**Phase change materials (PCM)** make use of latent thermal storage where the heat capacity is increased within a well defined temperature interval. PCM help to reduce seasonal

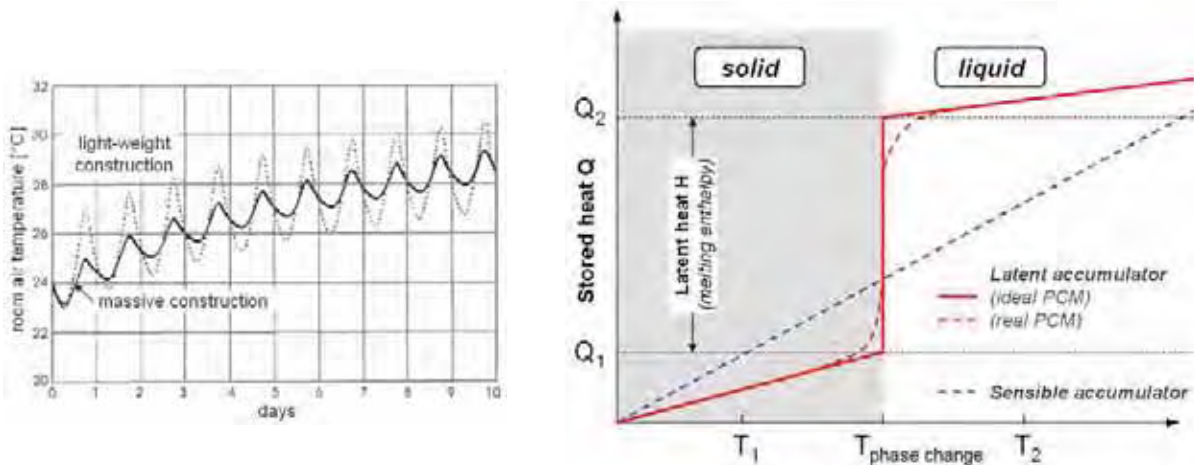
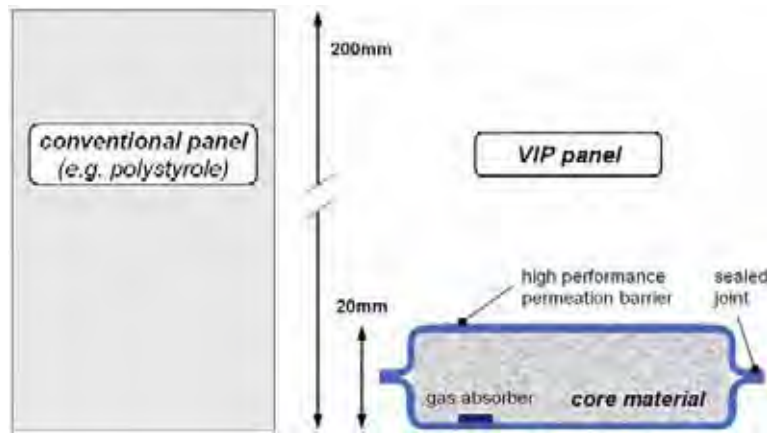


Figure 2.17: Left: Comparison of a light-weight and a massive structure for a hot summer period according to [21]. Right: Ideal PCM material compared with sensible heat storage [27].



*Figure 2.18:* Comparing the thickness of a conventional insulation with a vacuum insulation panel (VIP). For the same thermal properties theoretically a size ratio of 1:10 is feasible.

overheating and are especially well suited for light-weight constructions. The left hand side of Figure 2.17, for example, compares the room air temperatures of a massive with a light-weight building as shown by HAUSER ET AL. in [27]. As a key effect of PCM, the thermal mass of a light-weight building construction is increased within a typical range of temperatures during a hot summer period only. Within this period, the thermal mass is comparable to that of a massive construction [35].

On the right hand side of Figure 2.17 the effect of latent heat storage is compared to the sensible heat storage. Charging a medium by the latter sensible effect goes along with a proportional increase in temperature where the gaseous state remains unchanged. In the ideal case of latent heat storage during the phase change (here from solid to fluid) at a defined temperature level thermal energy is stored without changing the temperature. In real PCM materials the effect takes place in a specific temperature range. The discharge process works the other way round where enthalpy is released. Compound elements are for example build on a paraffine basis and can be combined with gypsum. The melting point ranges typically from  $24^{\circ}\text{C}$  to  $26^{\circ}\text{C}$ .

**Vacuum insulation panels (VIP)** are an innovative insulation technique for reducing the insulation thickness (theoretically) by a factor of five to ten. The core of a VIP consists of a porous medium which is evacuated within a gas-proof barrier film as envelope. By evacuating an insulation material, heat transmission can be further reduced as the gas conduction contributes up to 80% to the heat transfer. As protection of the VIP and connections at the boundaries yield additional losses, composite foam-VIP materials have been developed recently, also in order to minimize heat bridge effects which are "tolerated" in practice. Because of its slim design, VIP are advantageous for renovating existing buildings, for example if the insulation shall be placed at the interior side of a wall [43].

### 2.6.3 Active and plant components

**Air handling unit.** The air handling unit of a heating, ventilation and air-conditioning

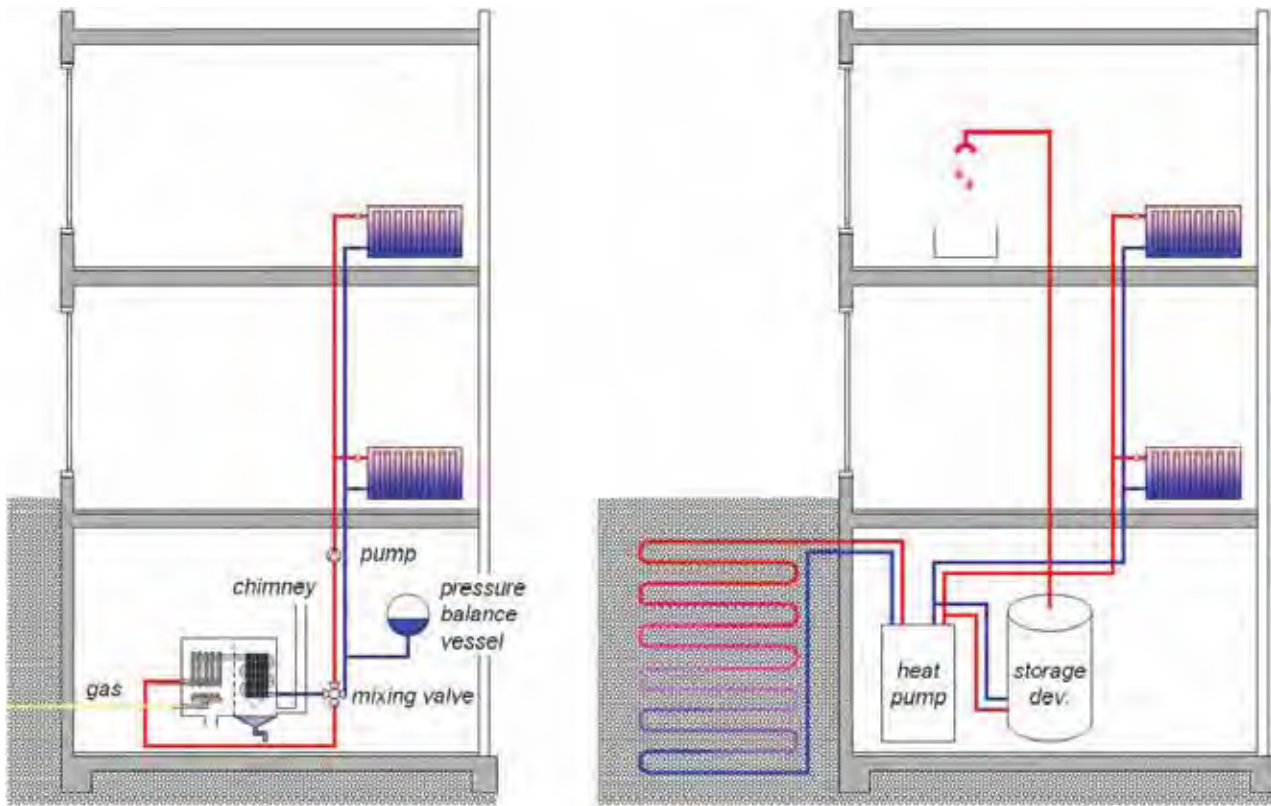


Figure 2.19: Condensing boiler within the heating system of a building and building with heat pump using the earth as heat exchanging medium. For explanations see text.

(HVAC) device consists of various components for changing the thermodynamic state of the air. This includes one or more fans and filters and devices for heating and cooling, humidification and dehumidification, and for heat recovery [2, 47]. Within the duct system sound absorbing devices are necessary. Air-conditioning by sole convection involves large air mass flow rates. The flow rates exceed in this case the air change rates that are required for maintaining the air quality due to hygienical aspects. Ventilation and air-conditioning can be therefore treated separately by using water bearing systems for space heating or cooling. For more details it is referred to [2, 47].

**Heating system.** The heating system consists of a heat producing unit, a storage system and a pipe network. For space heating usually boiler, heat pumps or long-distance heat supply systems are applied. *Low-temperature boiler* operate at a flexible preliminary temperature around  $40^{\circ}\text{C}$  and are fueled with oil or gas. With the low preliminary temperature large heat exchanging surfaces are required such as floor or flat heating units. With a *condensing boiler* the energy source (usually gas) can be used beyond its calorific value. The system makes use of latent heat by condensing the water vapor of the exhaust gas. The hot exhaust gas is cooled with the return water until condensation occurs. Therefore the temperature of the return water must remain below the dew point temperature. Afterwards the water is heated by the gas flame. The degree of effectiveness can reach up to 107% with respect to the lower calorific value of the fuel. The basic principle is depicted in Figure 2.19.

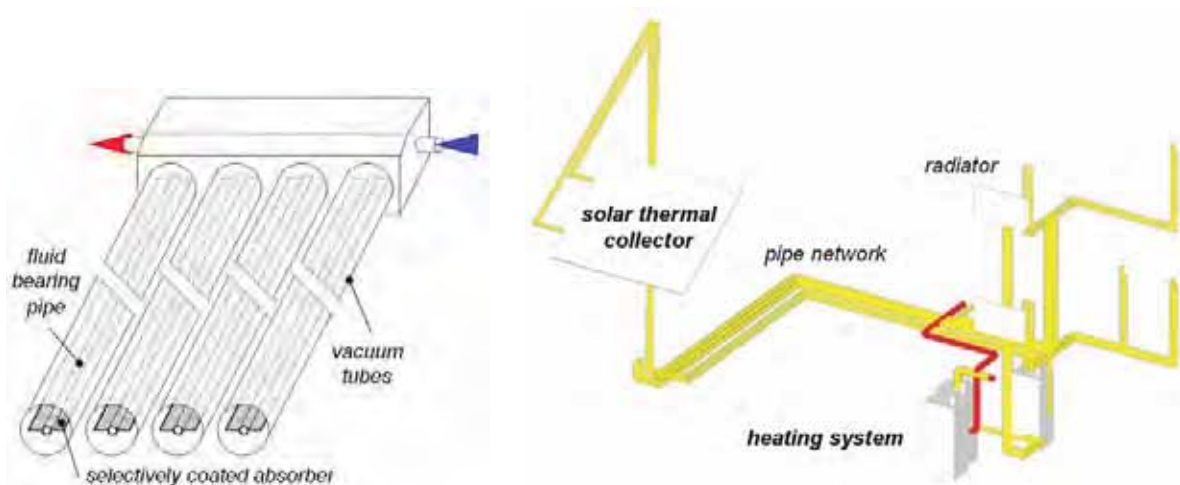


Figure 2.20: Left: Basic configuration of a solar vacuum collector. Right: CAD model of an integrated solar power plant for a residential building (drawn with Autodesk RoCAD).

A very effective method for energy supply is a *heat pump unit*. A heat pump withdraws energy from the building's environment at a low temperature level and supplies the heat to the heating system at a higher temperature level. The system therefore requires low-temperature heating units. As energy source air, ground water and earth can be used. However, the efficiency of air-based systems is lower due to narrower temperature gradients. In a bivalent configuration a heat pump unit is combined with a heating system in order to support the system in the case of an increased heating demand. A heat pump circuit consists of an evaporator, a compressor, a condenser and an expansion device. The cooling liquid is evaporated at moderate pressure for storing heat from the environment. With mechanical energy the liquid is compressed to a high pressure and temperature level. With the accordingly increased condensation point heat can be transferred to the heating circuit in the condenser at high pressure. The circuit is closed in the expansion device where the liquid is cooled by the pressure drop. The supplied usable energy thereby exceeds the invested electric energy by several times.

In centralized as well as decentralized heat supply systems *combined heat and power (CHP)* generation plants are efficient systems for the conversion of primary energy at a high temperature level. The degree of effectiveness can reach up to 90% if cogeneration can be used for both heating and electrical power supply.

The heating system can be supported by a *solar thermal collector* devices as shown in Figure 2.20 which are especially well suited for heating drinking water and water for domestic use. The best level of effectiveness is obtained with vacuum tube collectors which can generate temperatures up to 70°C above the ambient air temperature.

**Cooling system.** Opposed to the heat pump principle, in the *compression refrigeration* cycle thermal absorption at the condensing unit is used for cooling the cooling supply water. The heat of the condensing unit is transferred to a separate cooling circuit. Compression refrigeration units for cooling require a lot of energy and should thus be avoided in the planning process.

The latter conventional system can be replaced with adsorption or absorption cooling devices. These devices are operated with hot water and can therefore make use of long-distance heat supply systems or waste heat of various sources. *Absorption cooling devices* use a sorption fluid instead of a compressor which absorbs and fluidizes the cooling liquid vapor. By applying heat, both media are separated and fed back to the circuit where the further condensed cooling fluid can absorb the building heat in the vaporizer. In *adsorption cooling devices* gas molecules are accumulated within the matrix of a porous adsorption medium such as silica gel. As the adsorption medium is in solid state, two independent chambers are required for the periodically cooling and desorption cycles where one chamber absorbs the cooling liquid vapor while the other chamber is regenerated [2, 29, 47]. Depending on the supply heat the systems can be used for *solar cooling*.

**Energy storage** is an important issue in terms of using solar energy as the availability of the resource is temporally limited. Recently, a number of innovative storage techniques have been developed such as large seasonal storage devices, latent heat storage devices with phase change materials or thermal-chemical storage devices. With the latter heat can be stored nearly without further losses over a long time period.

## 2.7 References

- [1] F. Allard, M. Santamouris, S. Alvarez, E. Dascalaki, G. Guerracino, E. Maldonado, S. Sciuto, and L. Vandaele. *Natural ventilation in buildings*. James and James, 1998.
- [2] ASHRAE. *Handbook - Fundamentals (SI)*. American Society of Heating, Refrigerating and Air-Conditioning Engineers, 2005.
- [3] N.K. Bansal, G. Hauser, and G. Minke. *Passiv Building Design. A Handbook of Natural Climatic Control*. Elsevier Science B.V., 1994.
- [4] BRE Trust. BREEAM – The BRE Environmental Assessment Method For Buildings Around The World, 2009. <http://www.breeam.org>.
- [5] J.A. Clarke. *Energy simulation in building design*. Butterworth-Heinemann, 2nd edition, 2001.
- [6] European Commission. Energy. <http://ec.europa.eu/energy>.
- [7] G. Dibowski. *Auf Basis umfangreicher Messdatensätze experimentell und numerisch validierte Regeln zur optimierten Auslegung von Luft-Erdwärmetauschern (L-EWT)*. PhD thesis, UUniversitaet Kassel, 2003.
- [8] DIN EN ISO 14040:1997. *Environmental management - Life cycle assessment - Principles and framework*. CEN European Committee for Standardization, 1997.
- [9] DIN V 18599. *Energy efficiency of buildings. Calculation of the net, final and primary energy demand for heating, cooling, ventilation, domestic hot water and lighting*. DIN Deutsches Institut für Normung e.V., Beuth Verlag, 2005.

- [10] W. Eicke-Henning. Glasarchitektur - Lehren aus einem Grossversuch. Hessische Energiespar-Aktion, Institut Wohnen und Umwelt, Darmstadt, 2006.
- [11] EN ISO 15251. *Indoor environmental input parameters for design and assessment of energy performance of buildings addressing indoor air air quality, thermal environment, lighting and acoustics*. 2007.
- [12] Energieeinsparverordnung (EnEV). Verordnung über energieeinsparenden Wärmeschutz und energieeinsparende Anlagentechnik. *Bundesgesetzblatt vom 26. Juli 2007, Teil I*(34):1519–1563, 2007.
- [13] EPBD. *Directive 2002/91/EC of the European Parliament and of the Council of 16 December 2002 on the energy performance of buildings, OJ L 1, 4.1.2003, pp. 65–71*. European Commission, 2003.
- [14] W. Feist. *Passivhäuser in Mitteleuropa*. PhD thesis, Universität Kassel, 1993.
- [15] R. Fritzsche, W. Jenseit, and C. Hochfeld. Methodikfragen bei der Berechnung des kumulierten Energieaufwandes (KEA). Arbeitspapier im Rahmen des uba-FE Vorhabens Nr. 104 01 123, öko-Institut, Darmstadt, 1999.
- [16] K. Gertis. Solarenergienutzung - mit passiven statt mit aktiven Massnahmen. *HLH*, 33(5):169–173, 1982.
- [17] K. Gertis. Sind neue Fassadenentwicklungen bauphysikalisch sinnvoll? Teil 2: Glas-Doppelfassade (GDF). *Bauphysik*, 2:54–66, 1999.
- [18] K. Gertis, G. Hauser, K. Sedlbauer, and W. Sobek. Was bedeutet Platin? zur entwicklung von nachhaltigkeitsbewertungsverfahren. *Bauphysik*, 30(4):244–256, 2008.
- [19] M. Goedkoop. The ecoindicator 95. Final Report, NOH report 9523, Amersfoort, 1995.
- [20] Green Building Council Australia. Green Star, 2009. <http://www.gbcia.org.au/green-star/>.
- [21] G. Hauser. *Rechnerische Vorherbestimmungen des Wärmeverhaltens großer Bauten*. PhD thesis, Universität Stuttgart, 1977.
- [22] G. Hauser. Tragende Außenwände als Wärmespeicher unter Verwendung einer hochwertigen lichtdurchlässigen Wärmedämmung. In *Bericht RKW-Tagung Passive Solararchitektur*, Berlin, 1982.
- [23] G. Hauser. Verglaste Baukörper zur passiven Sonnenenergienutzung. *Bauphysik*, 5(5):147–152, 1983.
- [24] G. Hauser. Sonnenenergienutzung - Temporärer Wärmeschutz - Sommerlicher Wärmeschutz. *Glaswelt*, 37(9):874–880, 1984.
- [25] G. Hauser. Energetische Wirkung einer durchströmten Glasfassade. *TAB*, 20(4):329–338, 1989.

- [26] G. Hauser, J. Kaiser, M. Rösler, and D. Schmidt. Energetische Optimierung, Vermessung und Dokumentation für das Demonstrationsgebäude des Zentrums für Umweltbewusstes Bauen. In *BMWi, Forschungsvorhaben 0335006Z, Abschlussbericht*. <http://www.enob.info>, 2004.
- [27] G. Hauser, C. Kempkes, S. Koch, and S. Schlitzberger. Einsatz von aggregatzustandsändernden Materialien (PCM) in Holzhäusern zur Vermeidung von sommerlichen Überhitzungen. Abschlußbericht zum AiF Forschungsvorhaben 13797, Zentrum für Umweltbewusstes Bauen e.V., Kassel, 2005.
- [28] G. Hausladen, M. de Saldanha, and P. Liedl. *ClimaSkin, Konzepte für Gebäudehüllen, die mit weniger Energie mehr leisten*. Verlag Callwey, München, 2006.
- [29] G. Hausladen, M. de Saldanha, P. Liedl, and Sager. C. *ClimaDesign, Lösungen für Gebäude, die mit weniger Technik mehr können*. Verlag Callwey, München, 2005.
- [30] Heijungs et al. Environmental life cycle assessment of products, guide and backgrounds. Technical report, LCA Centrum voor Milieukunde Leiden (CML), 1992.
- [31] R.T. Hellwig. *Thermische Behaglichkeit – Unterschiede zwischen frei und mechanisch belüfteten Bürogebäuden aus Nutzersicht*. PhD thesis, Technische Universität München, 2005.
- [32] D. Hennings and J. Knissel. *Energieeffiziente Bürogebäude*, volume II. BINE Informationsdienst, Fachinformationszentrum Karlsruhe, Germany, 2000.
- [33] International Energy Agency (IEA). *World Energy Outlook 2006*. OECD/IEA, 2006.
- [34] Japan GreenBuild Council (JaGBC). CASBEE – Comprehensive Assessment System for Building Environmental Efficiency, 2009. <http://www.ibec.or.jp/CASBEE/english/>.
- [35] D. Kalz, J. Pfafferott, P. Schossig, and S. Herkel. Thermoaktive Bauteilsysteme mit integrierten Phasenwechselmaterialien - eine Simulationsstudie. *Bauphysik*, 1:27–32, 2007.
- [36] O. Kornadt, L. Lehmann, and F.J. Zapp. Doppelfassaden: Nutzen und Kosten. *Bauphysik*, 1:10–19, 1999.
- [37] P. Kröling. Sick Building Syndrom: Symptome, Ursachen und Prophylaxe gebäudebedingter Gesundheitsstörungen. *Allergologie*, 21(5):180–191, 1998.
- [38] P. Liedl, C. van Treeck, M. Egger, M. Pfaffinger, P. Tzschetschler, M. Grahovac, E. Rank, G. Hausladen, and U. Wagner. Building, users, climate: Zusammenspiel zwischen Gebäuden, Nutzern, Klima und Energieeffizienz. In *IBPSA-Germany conference BauSIM2008, Sept 8-10*, Universität Kassel, 2008.
- [39] A. Maas. *Experimentelle Quantifizierung des Luftwechsels bei Fensterlüftung*. PhD thesis, Universität Kassel, 1995.
- [40] H.F.O. Müller, C. Nolte, and T. Pasquay. Die Mittel aktiv zu sein, Von der Aufgabenstellung zur Lösung. In D. Danner, F.H. Dassler, and J. Krause, editors, *Die klima-aktive Fassade*, pages 40–113. AIT Edition Intelligente Architektur, 1999.

- [41] F. Neuberg. *Ein Softwarekonzept zur Internet-basierten Simulation des Ressourcenbedarfs von Bauwerken*. PhD thesis, Department for Computation in Engineering, Technische Universität München, 2004.
- [42] C.-H. Petzinka. Düsseldorfer Stadtteil, Glas- und Gebäudetechnologie. In *3. Fachkongress Innovatives Bauen mit Glas*, Bauzentrum München, 1995.
- [43] W. Platzer, C. Stramm, S. Amberg-Schwab, and M. Köhl. Development of innovative insulation systems on the basis of vacuum insulation panels. In EMPA, editor, *7th Int. Vacuum Insulation Symposium 2005*, pages 105–112, Zürich, Switzerland, 2006.
- [44] W.J. Platzer. *Solare Transmission und Wärmetransportmechanismen bei transparenten Wärmedämmmaterialien*. PhD thesis, Albert-Ludwigs-Universität Freiburg, 1988.
- [45] S. Plessner and J. Lang. Gebäude optimieren im laufenden Betrieb. In *Jahrbuch EnBop – Energetische Betriebsoptimierung*. <http://www.enob.info>, 2008.
- [46] G. Pültz. *Bauklimatischer Entwurf für moderne Glasarchitektur, Passive Massnahmen der Energieeinsparung*. Verlag Ernst und Sohn, 2002.
- [47] Recknagel, Sprenger, and Schramek. *Taschenbuch für Heizung, Klima, Technik*. Oldenburg Verlag, München, Wien, 1997/1998.
- [48] W. Richter, J. Seifert, R. Gritzki, and M. Rösler. Bestimmung des realen Luftwechsels bei Fensterlüftung aus energetischer und bauphysikalischer Sicht. Abschlussbericht Bau- und Wohnforschung F2425, Fraunhofer IRB Verlag, ISBN 3-8167-6002-3, 2003.
- [49] SolarBau:MONITOR. Energieeffizienz und Solarenergienutzung im Nichtwohnungsbau - Konzepte und Bauten. <http://www.enob.info>, <http://www.solarbau.de>.
- [50] B. Stahl. *Methodenvergleich und Methodenentwicklung zur Lösung der Bewertungsproblematik in produktbezogenen Ökobilanzen*. PhD thesis, Universität Bremen, 1998.
- [51] P. Tzscheutschler, M. Nickel, I. Wernicke, and H.G. Buttermann. Energy Consumption in Germany, Status 2006: Data, Facts, Comments. *BWK*, 60(3):46–51, 2008.
- [52] B.J. Urban and L.R. Glicksman. The MIT design advisor: A fast, simple building design tool. In R. Koenigsdorff and C. van Treeck, editors, *BauSIM2006, Erste deutsch-österreichische IBPSA Konferenz, 9.-11. Oktober*, TU München, ISBN-13: 978-3-00-019823-6, 2006.
- [53] U.S. Green Building Council. LEED Green Building Rating System, 2009. <http://www.usgbc.org>.
- [54] C. van Treeck. *Numerische Bestimmung der Transmissionswärmeverluste durch Wärmebrücken in der dynamischen Gebäudesimulation am Beispiel eines hochwärmegedämmten Mehrfamilienhauses*. Diploma thesis, Fraunhofer-Institute for Solar Energy Systems (ISE), Freiburg, 1997.
- [55] C. van Treeck. *Gebäudemodell-basierte Simulation von Raumluftströmungen*. PhD thesis, Technische Universität München, 2004.

- [56] K. Voss. Transparente Wärmedämmung - Materialien und Systemtechnik. In OTTI-Technologie-Kolleg, editor, *Transparente Wärmedämmung in der Architektur*, Fraunhofer ISE, Freiburg, 1994.
- [57] K. Voss, G. Löhnert, S. Herkel, A. Wagner, and Wambsgant. *Bürogebäude mit Zukunft*. TÜV-Verlag, Köln, 2005.
- [58] K. Voss, G. Löhnert, and A. Wagner. Energieeinsatz in Bürogebäuden. *Bauphysik*, 2:65–72, 2003.
- [59] A. Wagner. Solares Bauen – Inszenierung in Glas oder energiebewusste Architektur? *Bundesbaublatt, Bauverlag GmbH, Wiesbaden*, 8:571, 1997.
- [60] A. Wagner, S. Herkel, and W. Kohne. *Energieeffiziente Fenster und Verglasungen*. BINE Informationsdienst, Solarpraxis AG, Karlsruhe, 3rd edition, 2007.
- [61] Z. Wassouf, M. Egger, F. Neuberg, C. van Treeck, and E. Rank. Produktmodell basierte Simulation des Ressourcenbedarfs von Bauwerken. *Bauingenieur*, 81(6):251–258, 2006.

# Chapter 3

## Heat balances and energy flow paths

Chapter 1 already introduced the spatiotemporal resolution ( $\Delta x, \Delta t$ ) of the relevant balancing approaches in building simulation. Before dynamic and time dependent models will be treated for the whole building, the following chapter introduces the basic heat transfer mechanisms, casual heat fluxes and the concept of steady-state heat balances. A first monthly and annual balance will be drawn for a sample room.

Transient heat transfer by conduction will be treated in Chapter 6, radiative processes in Chapters 7 and 8 and convective heat transfer in Chapter 4 in more detail as it is relevant for this topic. For further reading it is referred to the text books [2, 3, 15] and [19].

### 3.1 Basic heat transfer mechanisms

Heat transfer in buildings involves the interaction between various domains which are in thermodynamic contact to each other as shown in Figure 3.1. Most of the systems are separated from each other and exchange energy. For example, heat is exchanged by convection between a massive wall and an air layer, the heat transfer between two opposing wall surfaces will additionally involve radiation. Figure 3.2 classifies the heat exchange into heat conduction, convection and radiation [2, 15].

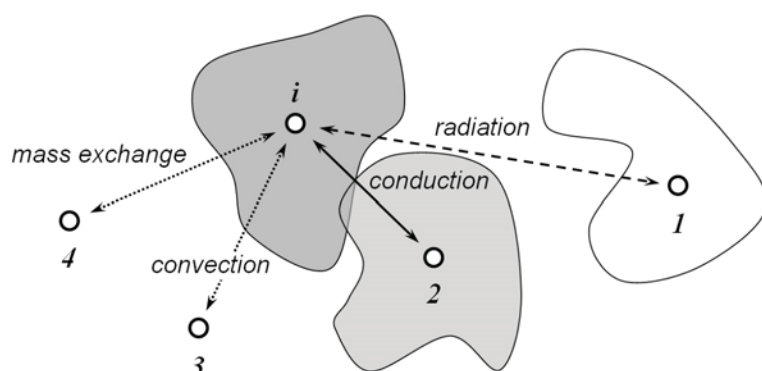


Figure 3.1: Thermodynamic contact of different domains.

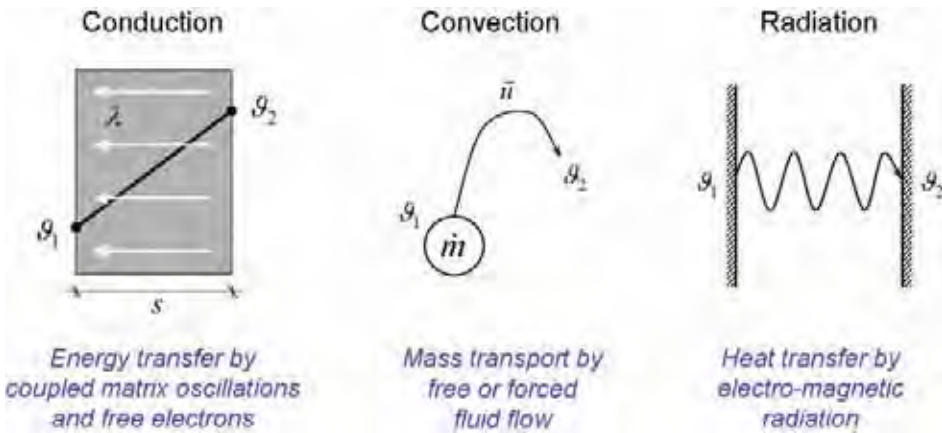


Figure 3.2: The basic heat transfer mechanisms of heat conduction, convection and radiation. Adapted from [15].

According to the principle of irreversibility of the *second law of thermodynamics*, the energy flux between two media has a definite direction and is directed from the higher to the lower temperature level in order to reach equilibrium. Figure 3.3 describes the *Fourier heat equation* as the heat flux density  $q = \dot{Q}/A$  which is induced by a spatial temperature gradient  $\partial T/\partial s$  in direction  $s$  and with the heat conductivity  $\lambda$  as the proportional constant. Molecular heat conduction can be described as heat transfer by coupled matrix oscillations and by charge transport due to free electrons [2, 15].

Heat transfer by convection comes along with mass transport. Depending on the driving forces it is distinguished between free (natural) and forced convection. In building simulation one differs further short-wave from long-wave radiative heat transfer by electro-magnetic radiation. The relevant scales are thereby the emitted solar radiation and the (long-wave) radiative heat transfer between building components.

## 3.2 Steady-state heat transfer through walls

With the heat conductivity  $\lambda_i$  and thickness  $s_i$  of each layer  $i = 1, \dots, n$  of the  $n$ -layered wall component, the overall heat transfer coefficient

$$U = \frac{1}{1/h_{c,r,ins} + \sum s_i/\lambda_i + 1/h_{c,r,amb}} \quad [W/(m^2 K)] \quad (3.1)$$

or the heat resistance

$$R = 1/U \quad [(m^2 K)/W] \quad (3.2)$$

can be calculated. With known values  $\vartheta_{air,ins}$  and  $\vartheta_{air,amb}$  for the indoor and the ambient air temperature the steady-state heat flux through the component is determined by

$$q = U(\vartheta_{air,ins} - \vartheta_{air,amb}) \quad [W/m^2] \quad . \quad (3.3)$$

Depending on the type of boundary layer the values for the combined radiative and conductive internal and ambient heat transfer coefficients can be estimated to  $h_{c,r,ins} \approx 4 \dots 10 \text{ W}/(m^2 K)$

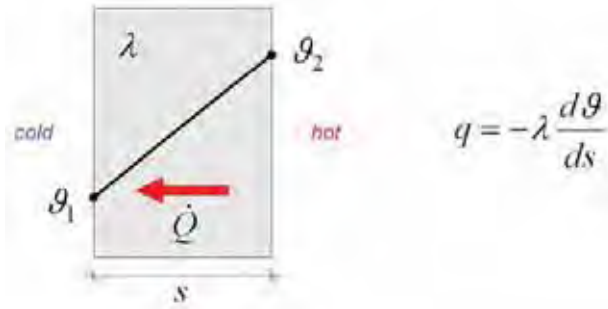


Figure 3.3: Definite direction of the heat flux between two media.

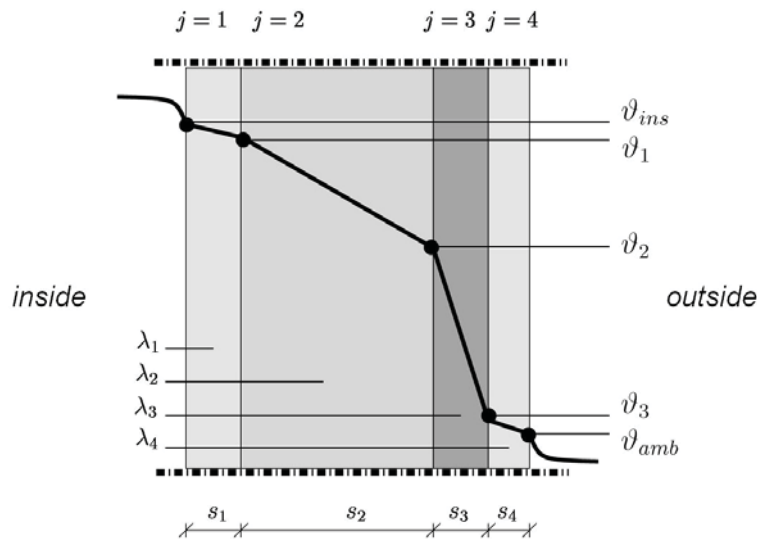


Figure 3.4: Temperature distribution through multi-layered opaque wall component.

and  $h_{c,r,amb} \approx 12...30 \text{ W}/(\text{m}^2\text{K})$ , respectively (see also tables in [4]). At the internal wall surface the temperature is

$$\vartheta_{ins} = \vartheta_{air,ins} - q/h_{c,r,ins}$$

and as the temperature changes by

$$\Delta\vartheta_i = q s_i / \lambda_i$$

in each layer, it is straightforward to compute the temperatures  $\vartheta_i$  at the interface of each layer, for instance using a spreadsheet tool.

### 3.3 The (h,x) psychrometric chart by Mollier

Some of the thermal processes in building simulation considering air-conditioning involve the change of state of the humid air. In order to humidify or dehumidify the air and vapor mixture, the air can be mixed, the enthalpy can be increased or decreased by adding or discharging heat, or moisture can be added or removed, for example by evaporation.

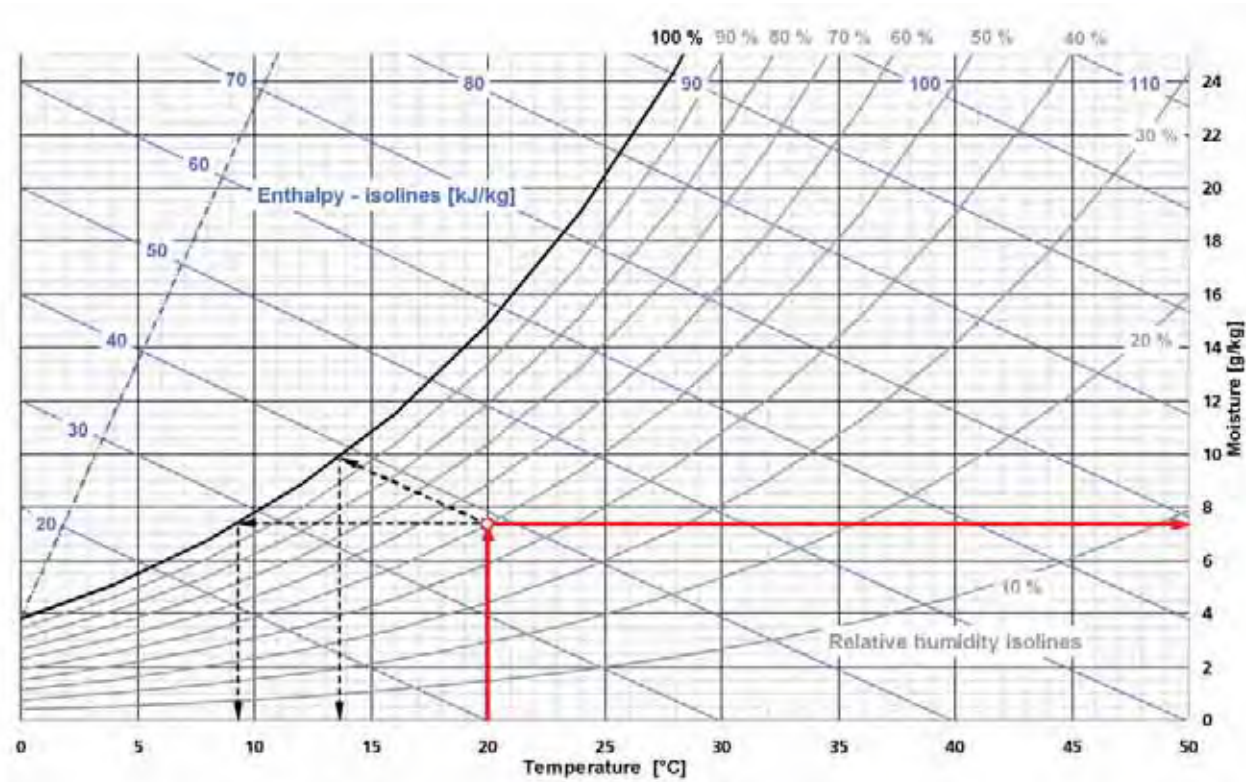


Figure 3.5: The psychrometric chart by MOLLIER, modified from [22] and [26].

The term *absolute air humidity* refers to the ratio of the embodied water vapor mass to the humid air volume. The *relative air humidity*  $\varphi$  corresponds to the partial water vapor pressure divided by the saturation vapor pressure of the water vapor. The absolute air humidity is also expressed as  $x$  in terms of the water vapor mass to the mass of the dry air in [ $g/kg$ ]. With the general gas equation it can be converted into a pressure value [2, 15].

The change of state and its effect can be seen from the psychrometric ( $h, x$ ) chart according to MOLLIER (1923) [22] and the VDI Standard 2067 [26] which is given in Figure 3.5. The  $x$ -axis in the coordinate system corresponds to the temperature  $\vartheta$  [ $^{\circ}C$ ] and the  $y$ -axis to the absolute air humidity  $x$  [ $g/kg$ ] which can be converted to the partial water vapor pressure  $P_D$  [ $mbar$ ]. The curved lines indicate the relative air humidity up to  $\varphi = 100\%$  where saturation occurs. The latter separates the saturated (above) from unsaturated air (below the curve). The dashed inclined axis indicates the enthalpy  $h$  [ $kJ/kg$ ] where the lines orthogonal to the dashed line are isolines of constant enthalpy. The Mollier chart is drawn for a total air pressure of 1000  $mbar$ .

With the diagram, for example, the dew point temperature, air humidity (and vapor pressure) are easily obtained if the temperature and the relative humidity are known [14, 22]. By vertically connecting the temperature ( $20^{\circ}C$ ) from bottom to top with the respective relative humidity (50%), from the intersection point a horizontal line can be drawn for obtaining the *absolute air humidity* ( $7.3g/kg$ ) or an inclined line perpendicular to the enthalpy axis for obtaining the *enthalpy* ( $38.5kJ/kg$ ). Where the horizontal line hits the  $\varphi = 100\%$  saturation

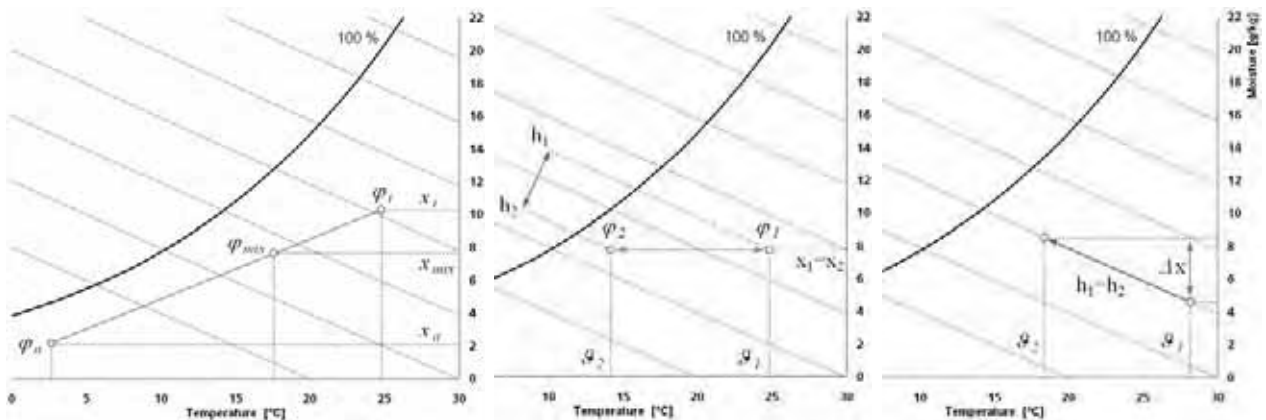


Figure 3.6: Change of the state of air for different settings according to the Mollier chart [14].  
Left: Mixing of cold and warm air. Center: Cooling and heating of a space. Right: Humidification by vaporization/sputtering.

curve, a vertical line can be drawn to the bottom to get the respective *dew point temperature* ( $9.2^\circ\text{C}$ ). From where the inclined line hits the saturation curve, a line can be drawn to read the *wet bulb temperature* ( $13.8^\circ\text{C}$ ).

Figure 3.6 describes the relevant changes of state of the air in a descriptive way. If cold and warm air is mixed, the resulting relative air humidity is obtained on a straight line between both relative humidities with respect to the resulting temperature, cf. left hand side of Figure 3.6. In the case if the air is cooled or heated and if the absolute humidity remains unchanged, the temperature change yields an increase or decrease in the enthalpy as shown in the center of Figure 3.6. On the right hand side the vaporization process is described. If water is sputtered and no additional energy is used the enthalpy remains constant. The latter effect is known as *adiabatic* or *evaporative cooling*.

## 3.4 Basic heat balances

When developing a simulation tool and testing a model heat balances can often lead to the respective source of the problem. Balances are the central concept of all momentum, mass and energy conserving schemes – independent of the considered scale. According to the *first law of thermodynamics* the energy remains constant in a closed system. Within the system the energy is conserved.

$$\sum \dot{Q} = 0 \quad (3.4)$$

If the heat capacity is not considered in the case of steady state conditions, i.e.  $\partial Q / \partial t = 0$ , the heat flux entering a control volume  $\dot{Q}_{in}$  equals the flux leaving the volume  $\dot{Q}_{out}$ ,

$$\dot{Q}_{in} - \dot{Q}_{out} = 0 \quad . \quad (3.5)$$

If the heat capacity is considered, the equation changes to

$$\frac{\partial Q}{\partial t} + \dot{Q}_{in} - \dot{Q}_{out} = 0 \quad . \quad (3.6)$$



Figure 3.7: Control volume heat fluxes if capacity is neglected and if it is taken into account

In Section 3.7, monthly and annual balances will be established for a sample model. As the thermal mass of the building is not considered, local or seasonal effects are not "visible" and must be taken into account by additional lump-sum factors and relations which can be obtained from dynamic simulations, for example, or that are given in standards. Static balances are therefore indicative of global causalities for a building as a whole and can be applied in early stages of the design.

In Figure 3.8 the basic heat fluxes are shown that are relevant in order to draw the energy balance for a building. In particular these are the transmission losses to the environment  $\dot{Q}_T$  and for components in earth contact  $\dot{Q}_{T,earth}$ , ventilation and infiltration losses  $\dot{Q}_V$ , the internal and solar heat gains  $\dot{Q}_I$  and  $\dot{Q}_S$ . As not all of the heat gains can be utilized these gains are reduced by a utilization factor (usually expressed as  $\eta$ ). Losses can be expressed in terms of a temperature dependent quantity [W/K] for multiplication with degree days as weighting function. Integrating these sources and sinks yields the heating demands.

$$Q_{heating} = Q_{sink} - \eta Q_{source} \quad (3.7)$$

The cooling load can be determined from the portion of heat gains that cannot be utilized for space heating as these gains cause overheating [23].

$$Q_{cooling} = (1 - \eta) Q_{source} \quad (3.8)$$

As heat sources and sinks fluctuate temporally and in terms of their magnitude, the heat gain utilization factor  $\eta$  accounts for several effects that are summarized in a time constant which takes into account the overall effective heat capacity in relation to the cooling/discharging potential, and the ratio of heat sources and sinks as well as the temperature fluctuation tolerated by the user [7, 6]. Calculation methods for energy balances are summarized in the standards DIN EN 832 [6], DIN 4108-6 [4], DIN 4701 [5], DIN EN ISO 13790 [9] and DIN

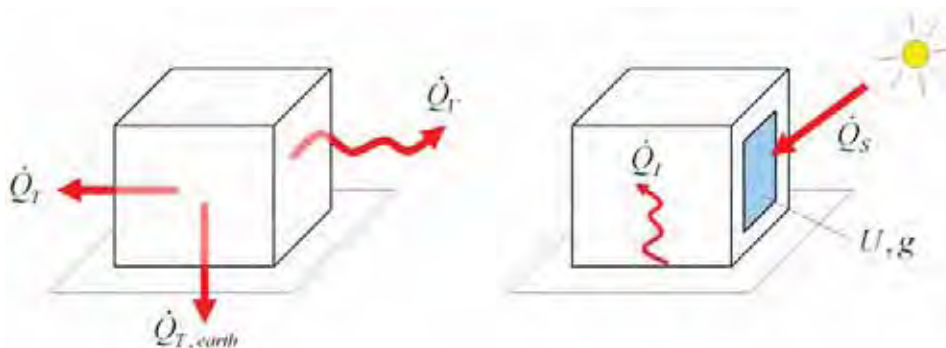


Figure 3.8: Basic heat fluxes relevant in the building energy balance.

18599-2 [7]. The latter is based on a zonal description of the building. The next section will give a calculation example.

Table 3.1 summarizes some of the basic quantities and its units that are relevant in this context. For a detailed list it is referred to the nomenclature.

Quantity	symbol	unit	comment
Heat quantity	$Q$	$[J] = [W \cdot s]$	
Heat flux	$\dot{Q}$	$[J/s] = [W]$	
Heat flux density	$q = \dot{Q}/A$	$[W/m^2]$	
Temperature	$T, \vartheta$	$[K]$ or $^{\circ}C$	$T = 273.15 + \vartheta$
Time	$t$	$[s], [h], [d], [a]$	$1a = 365d = 8760h$
Conductivity	$\lambda$	$[W/(m \cdot K)]$	
Heat capacity	$c$	$[J/(kg \cdot K)]$	(cave if given in $kJ$ )

Table 3.1: Some of the basic quantities and its units.

Figure 3.9 further distinguishes the terms *primary energy*, *final energy* (energy requirements at the building's boundary) and *utilization energy* (effective output) with respect to the total energy efficiency of a building. The primary energy additionally considers the preceding processes with respect to the energy supply, power generation and conversion. The final energy thereby accounts for the total energy which is required by the building plant (HVAC system, domestic water supply, etc.) for maintaining the required indoor air temperatures, for meeting the hot water demands as well as the lighting requirements. The final energy also includes additional demands such as electrical energy requirements of the plant components. For an integrated balance of the utilization energy for heating and cooling it is necessary to take all the associated heat sources and sinks additionally into account. A calculation method according to the EPBD (see 2.2) is given in the DIN Standard 18599 [7].

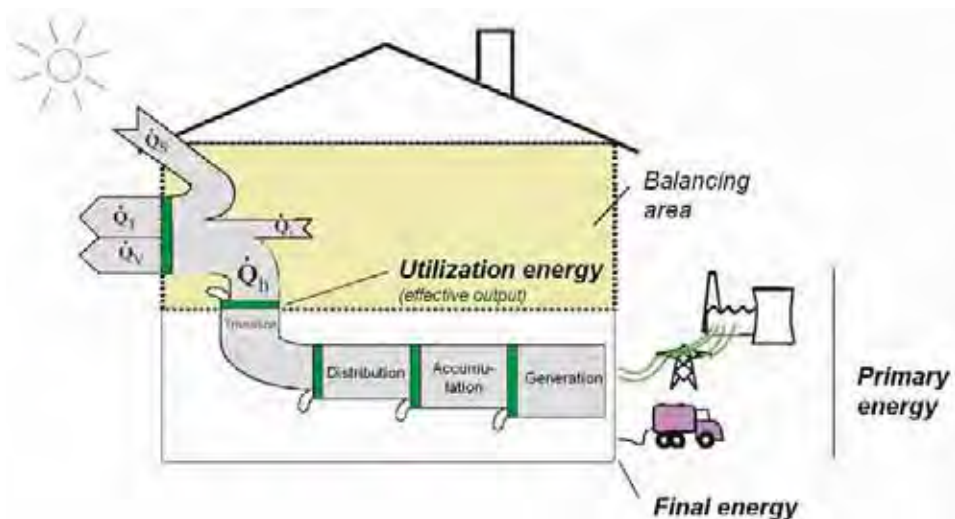


Figure 3.9: Primary energy, final energy and utilization energy. Source: DIN 4701-10 [5].

## 3.5 Energy flow paths and causal effects

Heat transfer in buildings is characterized by various energy flow paths and mutual dependencies which have to be taken into account in order to formulate conservation equations or to establish steady state energy balances. Static and dynamic approaches for balancing sources, sinks and performances involve

- heat conduction through solids,
- convective and radiative heat transfer at surfaces,
- internal heat gains and
- changes in enthalpy which are caused by the air changes between adjacent zones or with the environment.

The inert thermal behavior of a building depends on the interplay of different domains with inherent nonlinear and temperature dependent properties and different frequency characteristics. It is therefore mandatory for a model to preserve the integrity of the system and its components. In most cases the physical behavior can be described by ordinary differential equations or by parabolic differential equations of second order (Fourier heat equation).

### 3.5.1 Heat transfer through walls

The building envelope acts as the interface between the indoor and the ambient climate. The relevant heat transfer mechanisms at the opaque and transparent components of the building envelope are convection, radiation and heat conduction [15].

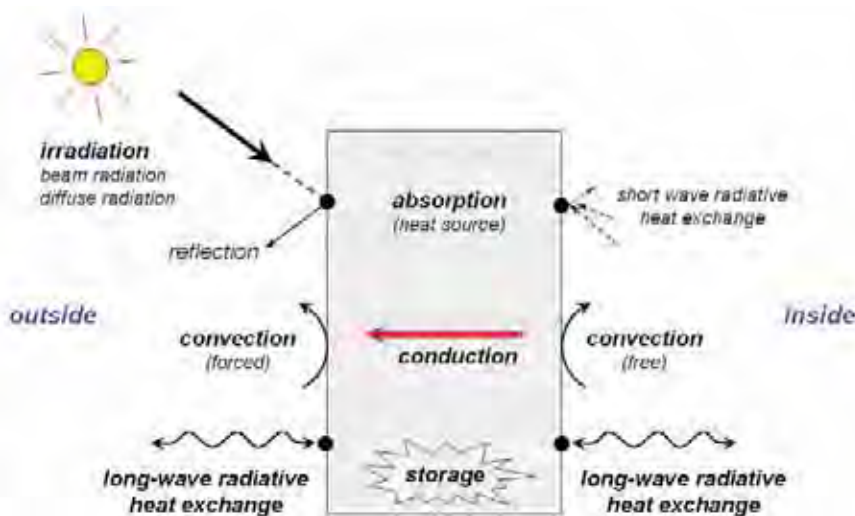


Figure 3.10: Heat transfer mechanisms at a massive wall component.

Weather data are gathered in *test reference years* for specific regions or can be individually created from the *Meteonorm* data base [18] for a specific location, for example. The weather data set quantifies the ambient temperature  $\vartheta_{amb}$ , the mean air velocity, relative air humidity

and it contains values for the beam and diffuse irradiation  $I_{beam}$  and  $I_{diff}$  or for the global irradiation which are given for a plane horizontal surface. By assuming an isotropic sky and with known site location and time, the angle of incidence of the position of the sun can be computed and thus the irradiation values can be transformed with respect to the slope and the orientation of each external building surface [8].

A part of the received global irradiation

$$q_{sw} = \alpha_{sw}(I_{beam} + I_{diff}) \quad (3.9)$$

is absorbed at the opaque surface which locally increases the surface temperature, the other part is reflected. Color and surface specific absorption and reflection coefficients are summarized in standards and text books [2, 4, 15, 19]. A typical value for a painted external opaque wall is  $\alpha_{sw} = 0.7$ . The short wave radiation transmitted through windows is (geometrically) distributed to the internal wall surfaces. This effect strongly influences the thermal behavior of the respective building area as components are locally heated. The multiple reflections of the redistributed short wave radiation may be treated in a lump-sum manner.

The convective heat transfer  $q_{conv}$  is determined by the near wall velocity and temperature boundary layer profile. It is distinguished between free and forced convection depending on the driving forces. In the case of free convection the internal flow is mainly driven by a temperature gradient. Forced convection is due to an imposed velocity by external wind forces or by a mechanical ventilation system. With a linearized heat transfer coefficient  $h_c$  [ $W/(m^2K)$ ] the area specific convective heat transfer can be expressed as

$$q_{conv} = h_c(\vartheta_{air} - \vartheta_{surface}) \quad . \quad (3.10)$$

Empirical correlations for the heat transfer coefficients are summarized in Chapter 4.

For the long wave heat exchange between internal surfaces due to emission (grey body radiation), multiple reflections (diffuse, spectral and mixed) and absorption, the net radiative heat exchange between the surface in question and all the surfaces in visible contact must be calculated simultaneously. The radiative heat flux transferred from a grey body surface element  $i$  to the environment is given by

$$q_{lw,i \rightarrow env} = \varepsilon \sigma (T_{surface}^4 - T_{environment}^4) \quad (3.11)$$

with the emissivity  $\varepsilon$  of the respective surface and the *Stefan-Boltzmann constant*<sup>1</sup>  $\sigma$ . The calculation introduces mathematical complexity due to the nonlinear temperature behavior ( $q \propto T^4$ ) and due to spatial problems. The environment is not uniform but composed of other surfaces and heat is exchanged in both directions and between each surface of a zone. Individual view factors are required for each surface which account for the surface area, the separation distance and the orientation. Also inter-surface obstructions must be taken into consideration. For usual building geometries the radiative heat transfer can be linearized and further simplified at estimable expenses in terms of accuracy. It is referred to Chapter 7.

---

<sup>1</sup> $\sigma = (5.67051 \pm 0.00019)10^{-8}W/(m^2K^4)$  [2]

The long wave radiative heat transfer between external surfaces and the environment  $q_{lw}$  can be computed with the help of a fictitious sky temperature  $T_{fsky}$  according to [8] by

$$q_{lw,amb} = \varepsilon \sigma (T_{fsky}^4 - T_{surface}^4) . \quad (3.12)$$

Within components heat is transferred by transient heat conduction  $q_{cond}$ . Relevant physical properties for each individual wall layer are the heat conductivity  $\lambda[W/(mK)]$ , the density  $\varrho[kg/m^3]$  and the specific heat capacity  $c[J/(kgK)]$ . As shown in Section 3.2 with the overall heat transfer coefficient the steady state heat balance of the transmission losses can be established if constant and homogenous properties are assumed for each layer and if transient effects are neglected. Heat conduction in solids is subject of Chapter 6.

### 3.5.2 Heat transfer through windows

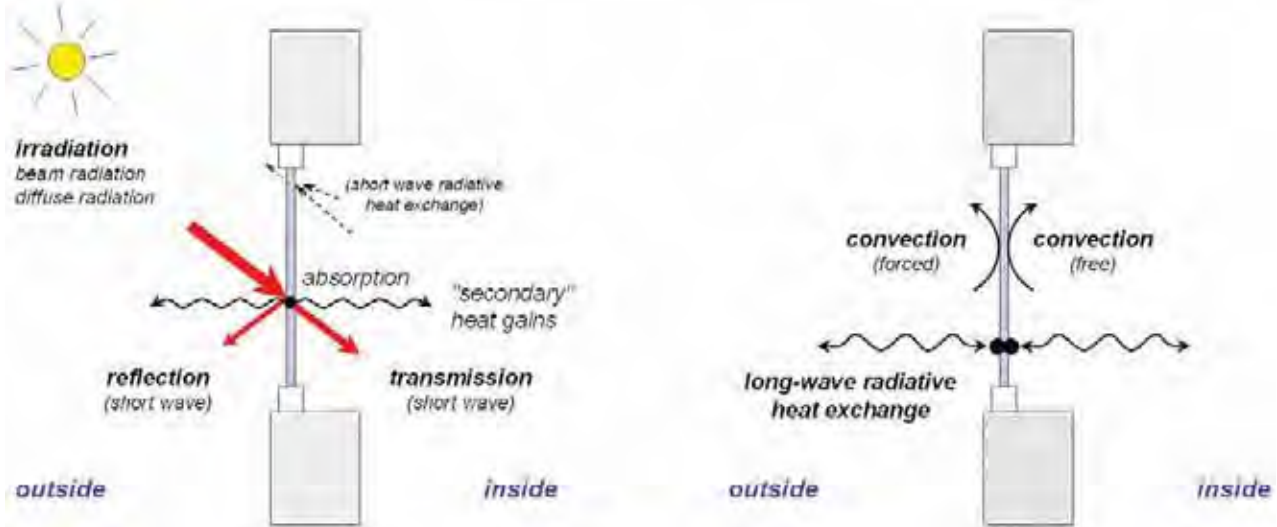


Figure 3.11: Heat transfer mechanisms at a window element. The left hand side shows the heat fluxes with respect to the solar optical properties. For the long-wave radiative heat transfer a window can be assumed as opaque element without thermal mass.

Multi-layered transparent components involve the interdependent properties of solar transmission  $\tau$  with respect to the front and rear direction, absorption  $\alpha$  and reflection  $\rho$ . The properties depend on the angle of solar incidence [21], the wavelength and the polarization of the light. Also the thermal properties of the gas layer between the window panes and the emissivities and conductivities of the panes are important. Absorption  $q_{sw}$  locally increases the temperature of each glazing. Global solar and optical properties of windows [24, 25] can be computed with a detailed window model such as [10] in a recursive manner as explained in Chapter 9. For simplified calculations the properties can be abstracted to form an overall heat transfer coefficient  $U[W/(m^2K)]$  and a solar heat gain coefficient  $g[-]$ . The latter summarizes the transmitted solar energy and the portion of the absorption heat which is transferred to the inside, i.e. the "secondary" heat gains. The instantaneous fenestration energy flow can be accordingly estimated by

$$q = U(\vartheta_{air,amb} - \vartheta_{air,ins}) + g(I_{beam} + I_{diff}) . \quad (3.13)$$

The heat capacity of the window system is usually neglected in simulation. HAUSER [11], however, details a simulation approach where the thermal capacity is considered. The other heat transfer mechanisms are the same as for the walls as described in Section 3.5.1. Windows can be considered as opaque objects for the case of long wave radiative heat transfer, i.e. for wavelengths longer than  $3\mu\text{m}$  [8].

### 3.5.3 Whole zone

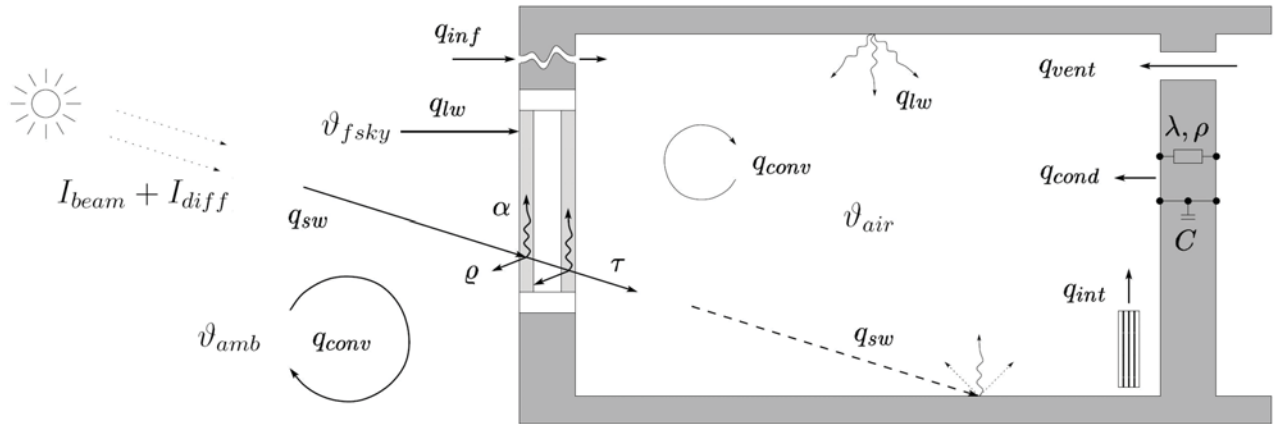


Figure 3.12: Energy flow paths within a building zone.

Figure 3.12 summarizes the energy flow paths and causal effects for a whole zone. In addition to the effects mentioned in Sections 3.5.1 and 3.5.2, internal heat sources  $q_{int}$ , sources and sinks of the heating and cooling system, and the enthalpy exchange with the environment and with adjacent zones in terms of ventilation  $q_{vent}$  and infiltration  $q_{inf}$  must be further taken into account. The enthalpy change due to infiltration or ventilation is given by

$$q_{inf} = \frac{1}{3600} n V \varrho_{air,dry} c_{air,dry} (\vartheta_{air,ins} - \vartheta_{air,amb}) \quad (3.14)$$

where  $n$  [ $1/h$ ] denotes the number of air changes of the zone volume  $V$  [ $m^3$ ] per hour,  $\varrho_{air,dry}$  [ $kg/m^3$ ] is the density of the dry air and  $c_{air,dry}$  [ $J/(kgK)$ ] the heat capacity of dry air at constant pressure. The factor  $1/3600$  is necessary for converting units to [ $W$ ] in this case.

## 3.6 A sample model according to VDI Standard 6020

For the next section, a sample model will be required in order to exemplarily establish a steady-state monthly and annual heat balance. The example will also serve as basis for the further dynamic simulation in the subsequent chapters.

In order to calibrate and validate models for the building performance simulation, a number of benchmarks have been published such as the International Energy Agency Building Energy Simulation Test (BESTEST) [16, 20] and the VDI Standard 6020 [27, 28] which are available for both the building model and the HVAC system. In the following, the structure, geometry

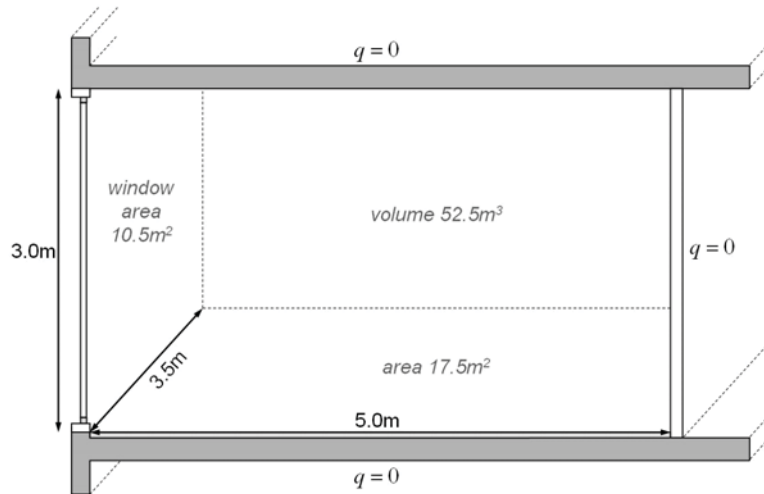


Figure 3.13: Sample model geometry according to the example given in VDI 6020 Part 1 [27].

and properties of the example from VDI 6020 Part 1 will be used.

The sample room is defined as a single rectangular space (office room) with an area of  $17.5m^2$  and a volume of  $52.5m^3$  with the dimensions given in Figure 3.13. In the settings of the standard, the floor and ceiling as well as all internal walls are adiabatically connected to the adjacent zones, i.e. same temperatures are assumed in the neighboring zones. Other simple but realistic connection possibilities in the above sense are discussed in [12], for example. For the moment it is sufficient to mention that the internal structure is of heavy-weight type. The effective overall thermal capacity of the zone is estimated by

$$c_{eff} = 110 \text{ Wh}/(m^2 K)$$

as the main material densities are  $> 1000 \text{ kg/m}^3$  and as the ceiling is not thermally covered. However, the thermal properties of the components are already given in Table 3.2 as they will be required in the following chapters.

Component	layer	$s$ [m]	$\lambda$ [W/(mK)]	$\varrho$ [kg/m³]	$c$ [J/(kgK)]
Ceiling, floor	PVC coating	0.002	0.210	1300	1470
	pavement	0.045	1.400	2200	1050
	rock wool	0.012	0.060	50	840
	concrete	0.150	2.035	2400	1050
Internal walls	cavity block tiles	0.240	0.560	1300	1050
Internal door	wood (beech)	0.040	0.210	700	2520
External wall	concrete	0.240	2.035	2100	920
	insulation	0.062	0.047	75	840
	facade panel	0.025	0.450	1300	1050

Table 3.2: Thermal properties of the massive components.

The window with the area of  $10.5m^2$  is oriented due south, i.e. the surface azimuth angle is  $0^\circ$ . The solar and thermal properties are summarized in Table 3.3. The glazing type consists

of two 6mm clear float panes and an air filled gap of 12mm. Thermal bridges and the frame interactions are neglected in the example.

Glazing type [mm]	<i>U</i> value [W/(m <sup>2</sup> K)]	<i>g</i> value [-]	frame portion [-]	daylight transmission [-]
6/12/6	2.1	0.75	0	0.817

Table 3.3: Thermal and optical window properties.

The convective and combined heat transfer coefficients and the opaque surface absorption coefficients are given in Table 3.4 for the internal and external components. For the steady-state balances, the combined values  $h_{c,r}$  are used which are modified from VDI 6020 according to [4]. Windows are treated in this sense like vertical wall surfaces.

Surface type	$h_c$ [W/(m <sup>2</sup> K)]	$h_{c,r}$ [W/(m <sup>2</sup> K)]	$\alpha$ [-]
external, vertical	20.0	25.0	0.7
internal, horizontal	1.67	6.67	0.7
internal, vertical	2.70	7.69	0.7

Table 3.4: Surface heat transfer and opaque absorption coefficients.

For the summer case a roller blind is available for shading the incident solar radiation. If the blind is closed, the global irradiation is set to 150W/m<sup>2</sup>. The solar heat gains  $g_{tot}$  are calculated with given solar transmission for the blind of 15% for direct and 30% for diffuse radiation by weighting the influence according to the values for the respective beam and diffuse radiation known from the test reference year, i.e.

$$g_{tot} = g(0.15I_{beam} + 0.3I_{diff})/I_{global} \quad .$$

Internal heat gains	by convection	by radiation	operating time
Devices, hardware	200W	-	7am - 5pm, 5 days per week
People	80W	80W	7am - 5pm, 5 days per week
Air-conditioning	heating power <i>not limited</i>	cooling power <i>not limited</i>	operating time 6am - 6pm, 5 days per week

Table 3.5: Internal load profile and air-conditioning operating time.

Set-point temperatures	max	min	set-back temperature
	24°C	22°C	18°C

Table 3.6: Set-point temperatures for air-conditioning system during the office hours.

The internal loads are defined according to the profile given in Table 3.5, lighting is switched off during the whole simulation period. The office working times are five days per week. For the air-conditioning only convective sources and sinks are taken into account. The operating

time is given in Table 3.5 for the respective set-point temperatures of Table 3.6. The heating and cooling power of the system is not limited in this case. Without air-conditioning during setback-times the air change rate is fixed to 0.2 per hour.

### 3.7 Steady-state monthly and annual balances

In the following two subsections heat sources and sinks will be balanced in a steady-state monthly manner for the example given in Section 3.6 for the test reference year TRY5 (Würzburg, Germany; January 1<sup>st</sup> = Wednesday). Depending on the temperature gradient between inside and outside, the approach according to the DIN Standard 18599-2 [7] distinguishes between sources and sinks with respect to transmission, infiltration and ventilation. Parts of the balancing approach are similar to the method defined in Standard EN 832 [6]. In the example, the winter period is defined from October through March, the summer period from April through September.

The values for the solar irradiation  $I_{beam}$  and  $I_{diff}$  are converted for the upright window surface oriented due south and combined to a global irradiation  $I_{global}$  as shown in Tables 3.7 and 3.8 as the TRY data are given for the horizontal case. For transformation algorithms it is referred to Chapter 8. The tables also give the number of working  $d_{wd}$  and weekend days  $d_{we}$  with  $\sum d_{wd} + d_{we} = 365$  for the whole year and the mean monthly ambient temperature  $\vartheta_{amb}$ . The difference between the mean indoor air temperature  $\vartheta_i$  and the ambient temperature is further detailed for the winter case with respect to the operating times of the mechanical ventilation (ON/OFF) and the set-point temperatures given in Table 3.6.

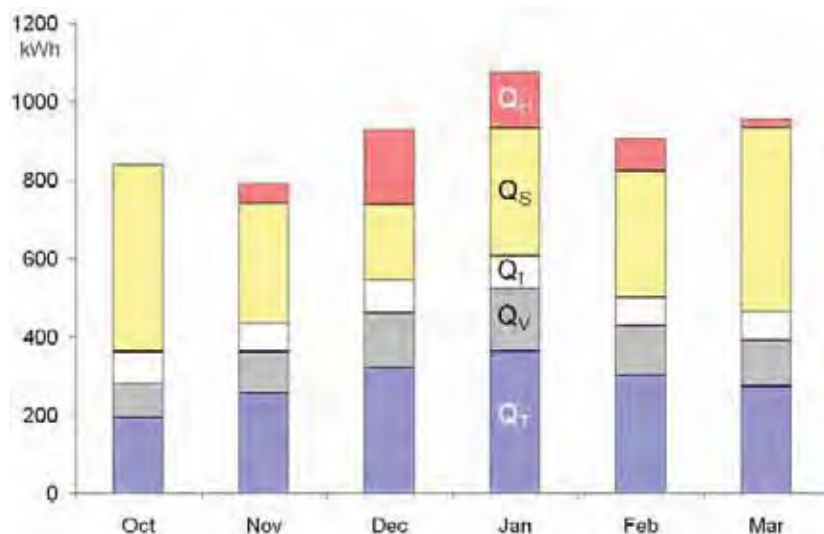


Figure 3.14: Monthly balance of the transmission and ventilation sinks and internal and solar sources during the heating period from October through March. The heating demand is plotted in red color.

### 3.7.1 Winter case

With given window  $U$  value  $U_{window}$  and area  $A_{window}$ , the specific heat transfer by transmission

$$H_T = U_{window} A_{window} \quad [W/K] \quad (3.15)$$

is a constant value. Usually transmission losses due to heat bridges are added to the above by means of the term  $\Psi l$ , where  $\Psi$  is a linear heat bridge coefficient and  $l$  the length scale, respectively [13, 17]. The specific heat transfer by ventilation

$$H_V = \frac{1}{3600} n V \varrho_{air,dry} c_{air,dry} \quad [W/K] \quad (3.16)$$

is obtained with the profile of Table 3.5 and Equation 3.14 for the respective time intervals. For the mechanical ventilation during the office hours the air change rate is assumed with  $n = 1.1$  changes per hour, during set-back time the infiltration rate is  $n = 0.2$ . The transmission losses

$$Q_T = U_{window} A_{window} (\vartheta_i - \vartheta_{amb}) t$$

are calculated according to the temperature difference resulting from the time schedule and respective set-point temperatures of Tables 3.5 and 3.6 and the time interval  $t[h]$ . The same applies for the ventilation losses

$$Q_V = \frac{1}{3600} n V \varrho_{air,dry} c_{air,dry} (\vartheta_i - \vartheta_{amb}) t$$

but separately for the working day and weekend periods with  $Q_{V,wd}$  and  $Q_{V,we}$ . The heat sinks are obtained by

$$Q_{sink} = Q_T + Q_{V,wd} + Q_{V,we}$$

Month		Oct	Nov	Dec	Jan	Feb	Mar	$\Sigma$
$d_{wd}$	$d$	23	20	23	23	20	21	
$d_{we}$	$d$	8	10	8	8	8	10	
$I_{global,mean,90^\circ}$	$W/m^2$	81	54	33	56	61	80	
$\vartheta_{amb,TRY5}$	$^\circ C$	9,1	4,7	1,3	-1,3	0,6	4,0	
$\vartheta_{i,ON} - \vartheta_{amb}$	$K$	12,9	17,3	20,7	23,3	21,4	18,0	
$\vartheta_{i,OFF} - \vartheta_{amb}$	$K$	10,9	15,3	18,7	21,3	19,4	16,0	
$Q_T$	$kWh$	191	254	319	362	298	273	1696
$Q_{V,we}$	$kWh$	7	13	13	14	13	13	74
$Q_{V,wd}$	$kWh$	80	93	129	145	116	102	665
$Q_{sink}$	$kWh$	<b>278</b>	<b>360</b>	<b>460</b>	<b>521</b>	<b>427</b>	<b>388</b>	<b>2434</b>
$\gamma = Q_{source}/Q_{sink}$	-	2,00	1,05	0,60	0,79	0,93	1,40	
$\eta$	-	0,49	0,82	0,97	0,92	0,87	0,67	
$Q_I$	$kWh$	83	72	83	83	72	76	468
$Q_S$	$kWh$	<b>475</b>	<b>306</b>	<b>193</b>	<b>328</b>	<b>323</b>	<b>469</b>	<b>2094</b>
$Q_{source}$	$kWh$	<b>557</b>	<b>378</b>	<b>276</b>	<b>411</b>	<b>395</b>	<b>544</b>	<b>2562</b>
$\eta Q_{source}$	$kWh$	<b>274</b>	<b>309</b>	<b>268</b>	<b>378</b>	<b>343</b>	<b>366</b>	<b>1939</b>
$Q_H$	$kWh$	<b>4</b>	<b>51</b>	<b>192</b>	<b>143</b>	<b>84</b>	<b>22</b>	<b>495</b>
$Q_{h,max}$	$W$	110	361	559	<b>709</b>	596	397	

Table 3.7: Monthly balance for the winter case for obtaining the heating demands.

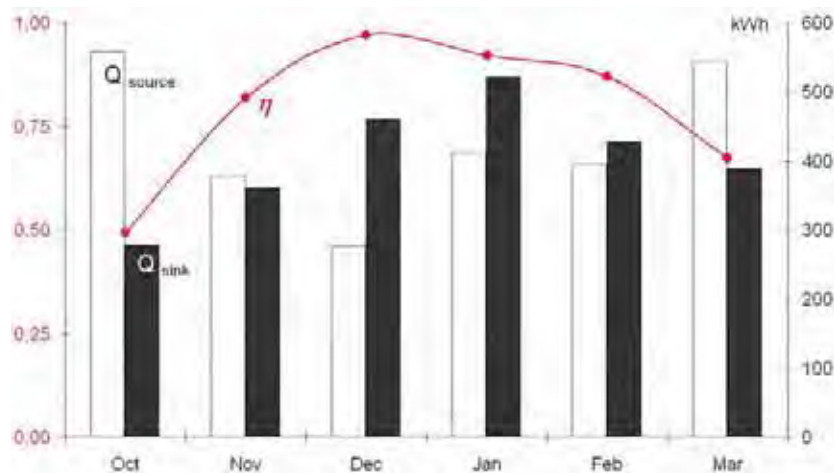


Figure 3.15: Balance of sources and sinks and heat gain utilization factor (red color). During the transition period only half of the heat gains can be used.

and are summarized in Table 3.7. The monthly internal loads are calculated by

$$Q_I = \sum \dot{Q}_{int} t$$

with the profile of Table 3.5. For the monthly balance all heat gains are assumed convective. The solar heat gains are obtained by

$$Q_S = g (1 - f) I_{global,mean,90^\circ} A_{window} t$$

with the frame portion  $f$ . The heat sources are hence

$$Q_{source} = Q_I + Q_S .$$

In order to calculate the monthly heating demand by Equation 3.7, the *utilization factor*  $\eta$  as shown in Figure 3.15 is determined by

$$\eta = \begin{cases} (1 - \gamma^a)/(1 - \gamma^{a+1}) , & \gamma \neq 1 \\ a/(a + 1) , & \gamma = 1 \end{cases} \quad (3.17)$$

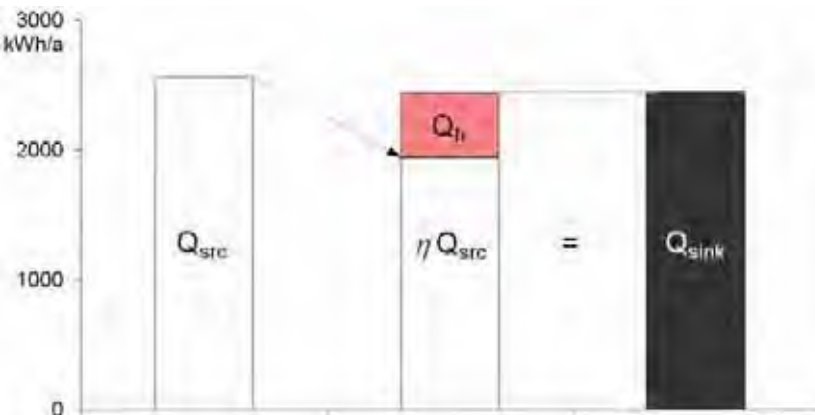


Figure 3.16: Annual balance of all sources and sinks yields the heating demand.

with

$$a = 1 + \tau/\tau_0$$

and  $\tau_0 = 16h$  according to EN 832 [6]. Thereby the *time constant*

$$\tau = \frac{c_{eff} A_{zone}}{\sum H_T + \sum H_V} \quad (3.18)$$

is the ratio between the effective overall thermal capacity of the zone  $C_{eff} = c_{eff}A_{zone}$  and the net specific heat losses, i.e. the discharging potential of the zone. The parameter  $\gamma$  is determined for each month as the *ratio between sources and sinks*

$$\gamma = \frac{Q_{source}}{Q_{sink}} \quad . \quad (3.19)$$

Figure 3.15 indicates that from December through February most of the heat gains can be used whereas in October only 50% are utilizable. The obtained annual heating demand is 495 kWh/a. Figure 3.16 illustrates the procedure in terms of Equation 3.7. The maximum heating power results in 709 W in this case.

### 3.7.2 Summer case

For the summer case the upper range of set-point temperatures of Table 3.6 is used. The total solar heat gains are computed with the value  $g_{tot}$  as described in Section 3.6 in order to account for the shading device. For the mechanical ventilation during the office hours the air change rate is assumed with  $n = 1.5$  changes per hour, during set-back time the infiltration rate is  $n = 0.2$ .

With the same definition for the utilization factor  $\eta$ , cf. Equation 3.17, Equation 3.8 is used for computing the monthly cooling demand. The graph of Figure 3.17 indicates that during

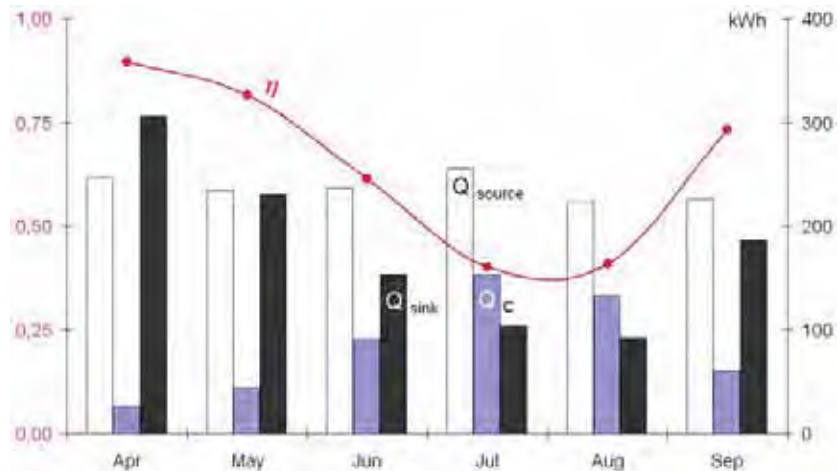


Figure 3.17: Balance of sources and sinks and utilization factor (red color). The obtained monthly cooling demands are painted in blue color.

Month		Apr	May	Jun	Jul	Aug	Sep	$\Sigma$
$d_{wd}$	$d$	22	22	21	23	21	22	
$d_{we}$	$d$	8	9	9	8	10	8	
$I_{global,mean,90^\circ}$	$W/m^2$	137	119	130	135	112	115	
$g_{\text{rel}}$	-	0,16	0,17	0,16	0,16	0,17	0,17	
$\vartheta_{amb,TRY5}$	$^\circ C$	9,5	12,9	15,7	18,0	18,3	14,4	
$\vartheta_i - \vartheta_{amb}$	$K$	12,5	9,1	6,3	4,0	3,7	7,6	
$Q_T$	$kWh$	198	150	100	66	60	120	693
$Q_{V,we}$	$kWh$	8	7	5	3	3	5	31
$Q_{V,wd}$	$kWh$	81	59	39	27	23	49	279
$Q_{sink}$	$kWh$	<b>288</b>	<b>217</b>	<b>144</b>	<b>97</b>	<b>87</b>	<b>175</b>	<b>1007</b>
$\gamma = Q_{source}/Q_{sink}$	-	0,86	1,08	1,64	2,64	2,59	1,29	
$\eta$	-	0,90	0,81	0,59	0,38	0,39	0,72	
$Q_I$	$kWh$	79	79	76	83	76	79	472
$Q_S$	$kWh$	168	155	161	173	148	147	951
$Q_{source}$	$kWh$	<b>247</b>	<b>234</b>	<b>237</b>	<b>256</b>	<b>224</b>	<b>226</b>	<b>1423</b>
$Q_C = (1 - \eta) Q_{source}$	$kWh$	<b>26</b>	<b>45</b>	<b>97</b>	<b>159</b>	<b>138</b>	<b>64</b>	<b>530</b>

Table 3.8: Monthly balance for the summer case for obtaining the cooling demands.

the hot summer time it is more difficult to discharge the heat gains stored by the thermal capacity of the building. The annual cooling demand is estimated to  $530 \text{ kWh/a}$ .

In summary it is noted that the treatment of the ventilation and infiltration terms bears uncertainties. Whereas the transmission losses are well defined and deviations may be due to the insufficient treatment of thermal bridges, for example, the infiltration losses are determined by the air change rate. If a mechanical ventilation system is applied, the inlet air temperature and the mass flow rate must be known. For the calculation of the cooling power and overall performance of the plant system it is referred to [1, 7, 22].

### 3.8 References

- [1] ASHRAE. *Handbook - Fundamentals (SI)*. American Society of Heating, Refrigerating and Air-Conditioning Engineers, 2005.
- [2] D. Baehr and K. Stephan. *Wärme- und Stoffübertragung*. Springer Verlag, 3rd edition, 1998.
- [3] A. Bejan. *Convection heat transfer*. John Wiley & Sons, Inc., 1993.
- [4] DIN 4108:2003. *Normenreihe Wärmeschutz und Energie-Einsparung in Gebäuden*. DIN Deutsches Institut für Normung e.V., Beuth Verlag, 2003.
- [5] DIN 4701:2004. *Normenreihe Energetische Bewertung heiz- und raumluftechnischer Anlagen im Bestand*. DIN Deutsches Institut für Normung e.V., Beuth Verlag, 2004.

- [6] DIN EN 832:2003. *Normenreihe Wärmetechnisches Verhalten von Gebäuden – Berechnung des Heizenergiebedarfes - Wohngebäude*. DIN Deutsches Institut für Normung e.V., Beuth Verlag, 2003.
- [7] DIN V 18599. *Energy efficiency of buildings. Calculation of the net, final and primary energy demand for heating, cooling, ventilation, domestic hot water and lighting*. DIN Deutsches Institut für Normung e.V., Beuth Verlag, 2005.
- [8] J. Duffie and W. Beckman. *Solar Engineering of Thermal Processes*. John Wiley and Sons Inc., New York, 1991.
- [9] E DIN EN ISO 13790:2005. *Energieeffizienz von Gebäuden - Berechnung des Energiebedarfs für Heizung und Kühlung*. DIN Deutsches Institut für Normung e.V., Beuth Verlag, 2005.
- [10] E.U. Finlayson, D.K. Arasteh, C. Huizenga, and M.D. Rubin. *WINDOW 4: Documentation of calculation procedures*. Technical report, Lawrence Berkeley Laboratory, University of California, 1993.
- [11] G. Hauser. *Rechnerische Vorherbestimmungen des Wärmeverhaltens großer Bauten*. PhD thesis, Universität Stuttgart, 1977.
- [12] G. Hauser. Vereinfachte Behandlung des Wärmeverhaltens großer Gebäude durch thermische Systeme. *Betonwerk und Fertigteil-Technik*, 44(5):266–271, 1978.
- [13] G. Hauser and H. Stiegel. *Wärmebrücken Atlas für den Mauerwerksbau*. Bauverlag Wiesbaden, 1990, 1993, 1996.
- [14] G. Hausladen, M. de Saldanha, P. Liedl, and Sager. C. *ClimaDesign, Lösungen für Gebäude, die mit weniger Technik mehr können*. Verlag Callwey, München, 2005.
- [15] E. Hering, R. Martin, and M. Stohrer. *Physik für Ingenieure*. VDI Verlag, 1992.
- [16] R. Judkoff and J. Neymark. *International Energy Agency building energy simulation test (BESTEST) and diagnostic method*. National Renewable Energy Laboratory, U.S. Department of Energy, 1995.
- [17] G.-W. Mainka and H. Paschen. Wärmebrückenkatalog als Arbeitshilfe. *Bauphysik*, 1, 1987.
- [18] METEONORM V 5.0. *Global meteorological database for solar energy and applied climatology*. Meteotest, <http://www.meteotest.ch/products/meteonorm>, 2003.
- [19] M.F. Modest. *Radiative Heat Transfer*. Academic Press, USA, 2nd edition, 2003.
- [20] J. Neymark and R. Judkoff. *International Energy Agency building energy simulation test and diagnostic method for heating, ventilation and air-conditioning equipment models (HVAC BESTEST)*. National Renewable Energy Laboratory, U.S. Department of Energy, 2002.

- [21] W.J. Platzer. Fenster und Verglasungen. In Marko and Braun, P.O. (Fraunhofer ISE), editors, *Thermische Solarenergienutzung an Gebäuden*. Springer Verlag, 1994.
- [22] Recknagel, Sprenger, and Schramek. *Taschenbuch für Heizung, Klima, Technik*. Oldenbourg Verlag, München, Wien, 1997/1998.
- [23] L. Rouvel. *Raumkonditionierung, Wege zum energetisch optimierten Gebäude*. Springer Verlag, Berlin, Heidelberg, 1975.
- [24] M. Rubin. Calculating heat transfer through windows. *U.S. Energy Research*, 6:341–349, 1982.
- [25] M. Rubin. Solar optical properties of windows. *U.S. Energy Research*, 6:123–133, 1982.
- [26] VDI 2067. *Economic efficiency of building installations*. VDI Verein Deutscher Ingenieure, Beuth Verlag, 2000.
- [27] VDI 6020 Part 1. *Requirements for methods of building performance simulation, part 1: buildings*. VDI Verein Deutscher Ingenieure, Beuth Verlag, 2001.
- [28] VDI 6020 Part 2. *Requirements for methods of building performance simulation, part 2: HVAC system*. VDI Verein Deutscher Ingenieure, Beuth Verlag, 2001.

# Chapter 4

## Transition and boundary conditions

This chapter briefly introduces the various external and internal transition and boundary conditions, which are required in building performance simulation. References are given to articles and other text books for further reading, as the topic is very extensive by nature.

The chapter therefore focuses on weather data, the pressure and temperature distribution along the building facade, external and internal heat transfer by forced and free surface convection, the solid earth temperature, internal heat gains and the issue of the user behavior. It closes with a few remarks on the impacts of the climate change and urbanization.

Boundary conditions specific to the respective numerical models used in this book are introduced in the chapters below.

### 4.1 Transition conditions to the external environment

#### 4.1.1 Weather data

The most relevant external boundary conditions are provided by weather data sets. For the model discussed in the scope of this book, at least the following data are required:

- the *direct (beam), diffuse and global irradiation* [ $W/m^2$ ] to a horizontal surface (transformation algorithms to different orientations are discussed in Chapter 8),
- the *ambient dry-bulb temperature* [ $^\circ C$ ] or [ $K$ ],
- the *dew point temperature* [ $^\circ C$ ] or [ $K$ ] or the *relative air humidity* [%], and
- the *wind velocity* [ $m/s$ ] (geometrical or vectorial average) and its *direction*.

In the subsequent chapters, formulae are defined to calculate further quantities, such as the sky coverage, or the incoming long wave radiation. However, some weather files already provide these data.

Well known sources for weather data collections are

- test reference years (TRY) [57, 10],

- data sets created with the METEONORM software [37],
- weather data as per the DIN Standard 4710 [18],
- short reference years (SRY) [12],
- typical meteorological years (TMY2) [41],
- the ASHRAE International Weather for Energy Calculation (IWEC) files [3],
- reference weather data published in the preliminary EN Standard 5060 [44, 39],
- weather data for a period of design days, such as DIN Standard 4701 [19] (winter case) and VDI Standard 2078 [62] (summer case), and
- measurement data of local meteorological services [20, 27].

The weather data sets usually consist of hourly weather data values for a selected reference year. Each row corresponds to one hour, a file thus containing 8760 records. Weather data sets are based on measurements, as well as deterministic and stochastic simulation models to generate weather data synthetically [15]. As indicated by DEGELMAN [15], the intention of simulating weather data is to provide sequences of hourly data if these are not available from measured sources – or to add characteristic periods to the database.

Test reference years (TRY) are defined in terms of local climatological data [57]. Mean values in terms of long time periods correspond to the average seasonal characteristics of the referenced region. In Germany, for example, the data are provided by the Deutscher Wetterdienst (DWD) [20]. Note, that overheating periods in summer are usually not captured by standard TRY data. Special data sets are required, which implement these characteristic side effects [25]. Furthermore, care must be taken, if current data sets account for the continuous process



Figure 4.1: Screenshots of the METEONORM software. The main dialog shows the selection of the location and the underlying weather stations [37].

of the climate change, i.e., if the applied data set is the latest available version. For example, HAUSER ET AL. [27] quantify the differences between a representative test reference year and measured, long-term weather data for a specific climate region in Germany. The study identifies deviations of the operative indoor temperatures for the summer period and the heating demand for the winter period.

The International Weather for Energy Calculation (IWEC) files of the American Society of Heating, Refrigerating and Air-Conditioning Engineers (ASHRAE) are derived from hourly weather data (1982-1999) which are supplemented by solar radiations estimated on an hourly basis from the earth-sun geometry and from other hourly weather elements [3].

METEONORM by Meteotest [37] is a global meteorological database for solar engineering applications and applied climatology at every location at the globe. It is based on databases from all over the world and computational methods, which have been developed in a number of international research programs.

The software contains an hourly value generator which provides stochastic values of the time dependent global horizontal radiation (resolution into beam and diffuse components) and temperature data. The METEONORM output can be customized in terms of the specific format of common building simulation software and other weather data files such as TRY. Figure 4.1

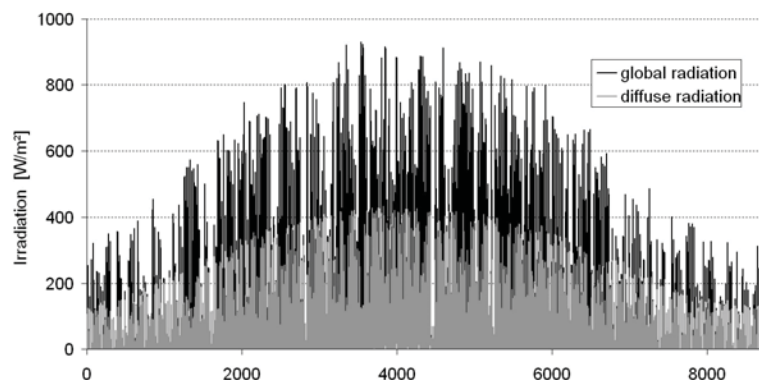


*Figure 4.2: Global and diffuse irradiation [ $W/m^2$ ] to a horizontal surface (Munich).*

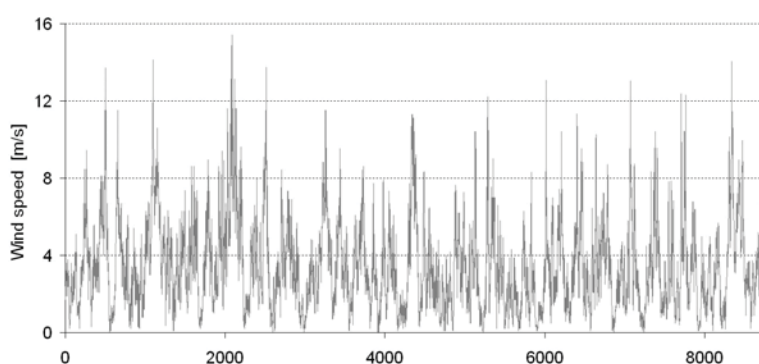


*Figure 4.3: Wind speed [m/s] at 10m height above ground (Munich).*

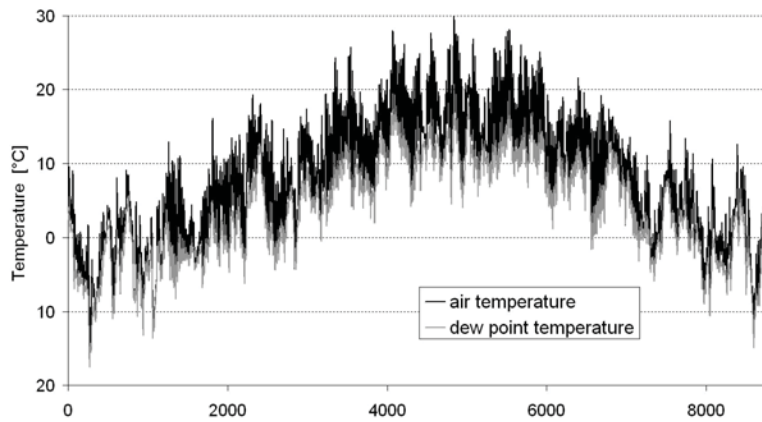


Figure 4.4: Air temperature and dew point temperature [ $^{\circ}\text{C}$ ] (Munich).

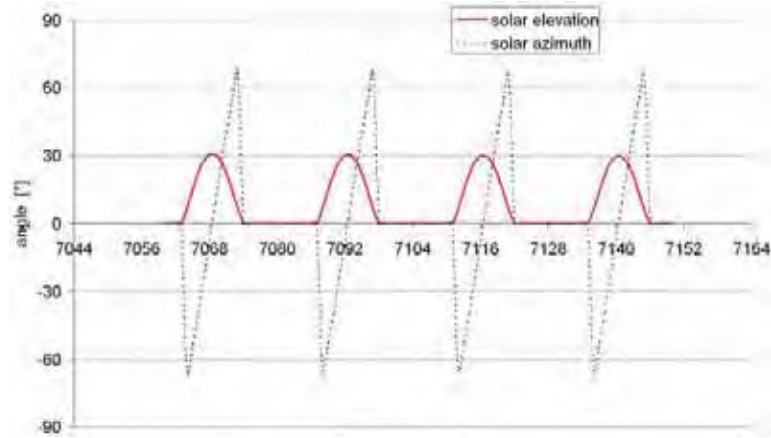


Figure 4.5: Solar elevation and the solar azimuth angles for a few days in October (Munich).

shows a screenshot of the graphical user interface. For details it is referred to the manual [37].

For example, in Figures 4.2 to 4.5 typical boundary conditions are plotted for the location Munich, Germany. The values have been created with the METEONORM software (version 5). In Figure 4.2, the global and diffuse irradiation to a horizontal surface is shown for the whole reference year of 8760 hours. Note, that these values need to be transformed for each time step with respect to the orientation of the respective building surface.

Figure 4.3 gives the local wind speed at 10 m above ground. The distributions of the air temperature and the dew point temperature are plotted in Figure 4.4. In Figure 4.5, finally, the solar elevation and the solar azimuth angles are detailed for a short time period in October of the reference year.

The selection of the weather data clearly impacts the results of a thermal simulation in terms of the energy performance as well as in terms of the overheating risk assessment. For the latter, weather data should be used, which contain critical summer periods, including a series of very hot days. The prediction will fail, if the weather data is only aligned with the average meteorological data of the respective climate region [47, 25, 51, 56]. For example, CRAWLEY

[13] showed, that the predicted annual energy consumption can vary as much as 11 per cent for the range of actual weather data.

### 4.1.2 External pressure and temperature distribution

In order to predict the heat transfer by transmission and by mass transfer due to enthalpy changes by infiltration and ventilation, the external temperature and wind pressure distribution at the building facade must be known. The driving force of the air flow is a pressure difference between inside and outside. Such a pressure difference

- can be imposed by a mechanical ventilation system,
- can result from the wind pressure distribution at the surface of the building envelope,
- or can be induced by air temperature differences between inside and outside (thermal forces).

All three effects influence each other, as indicated in Figure 4.6. Without wind pressure, the thermal forces induce a bi-directional flow profile (right-hand side of Figure 4.6 for the case of natural window ventilation). The base line of the profile is shifted, if external wind driven forces or a mechanical ventilation system influence this effect (left-hand side of Figure 4.6). The effect cannot be neglected for large openings in the building envelope. Further details on window ventilation can be found in the text book of ALLARD [2], the ASHRAE Handbook of Fundamentals [4], or the book of PÜLTZ [48] (in German), for example.

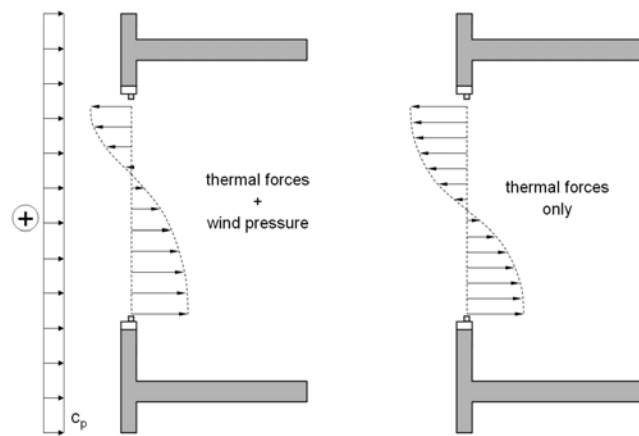
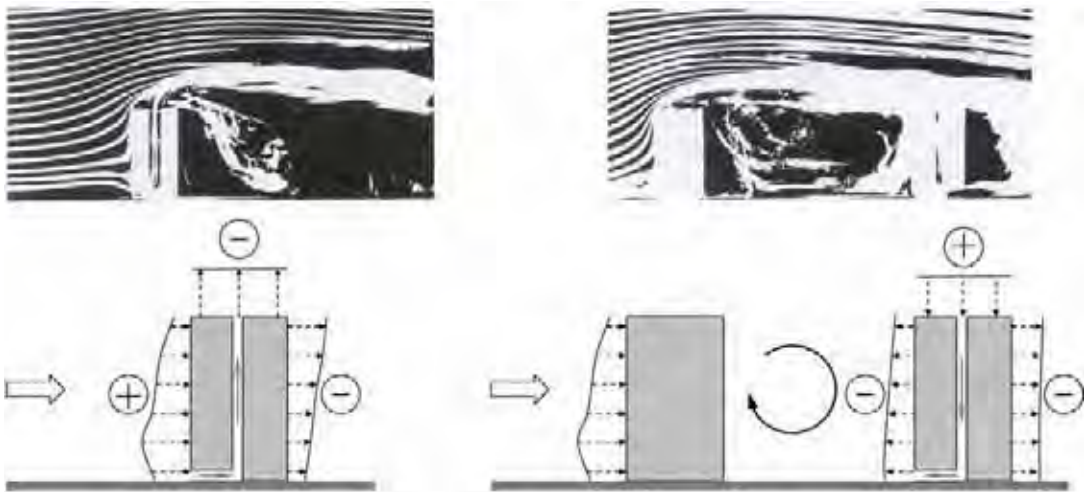


Figure 4.6: Different types of bi-directional air exchange for the case of mechanical ventilation influencing window ventilation (left-hand side) and natural window ventilation (right-hand side) [48].

A weather data set typically provides the dry-bulb temperature and the wind speed, which have been measured at the height of 2 m and 10 m above ground, respectively. Note, that these values have been obtained in regions without the further influence of the urban environment. In fact, the external temperature and pressure distribution are *significantly* influenced by the surrounding structure and environment. This shall be briefly demonstrated in the following.



*Figure 4.7:* Wind tunnel experiment concerning the flow around buildings for two different configurations [45]. In the second case, the pressure distribution changes, as another building has been placed at the windward side of the building in question.

**Static and dynamic wind pressure distribution.** The static and dynamic wind pressure distribution at the external building surface depends on the complex air flow characteristics around the building. The building aerodynamics are characterized by very high Reynolds numbers  $Re = \mathcal{O}(10^6 \dots 10^{11})$  and, thus, an inherent turbulent nature of the flows.

Figure 4.7 shows the example results of a wind tunnel experiment for two different configurations. In the first case on the left-hand-side of the figure, a positive pressure value is obtained at the windward side, and a negative pressure (suction) at the top and leeward surfaces. In the second case, shown on the right-hand-side of the figure, the pressure distribution changes, as another building has been placed at the windward side of the building in question. The reason is, that a large vertex emerges between the two buildings. However, if the direction of the flow changes, the whole situation changes again. The use of wind pressure distribution data along building facades accordingly covers many uncertainties.

In Figure 4.8, the boundary layer profile is shown for the typical configuration of the flow around an obstacle. The stagnation point, the peak value of the dynamic pressure, is found at approximately  $2/3$  of the building height. At the sharp edge, separation of the flow occurs [45, 64]. Along the leeward side, we find a free shear flow with complex re-circulating flows, followed by the wake area.

The atmospheric boundary layer profile and the degree of turbulence are affected by the wind speed and by the surface roughness. The latter depends on the local terrain and the surrounding urban structure. The thickness of the boundary layer  $\delta$  varies from  $300\text{ m}$  (countryside, sea) over  $450\text{ m}$  (flat building structure) up to  $600\text{ m}$  (urban structure) [45]. Near the surface, where viscous forces dominate, a logarithmic profile can be assumed for heights  $z < 0.15\delta$ . In

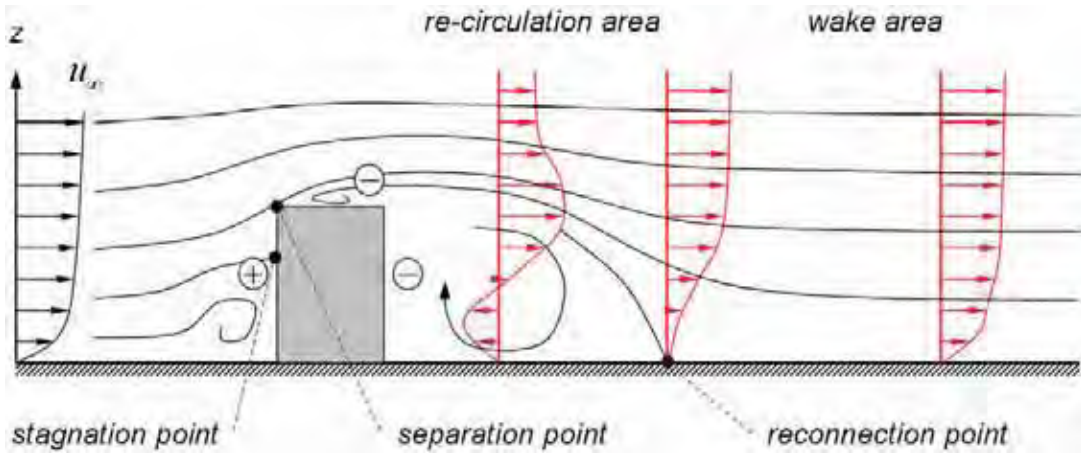


Figure 4.8: Flow around an obstacle with positive and negative pressure distribution at the surface, flow separation, re-circulation area, reconnection point and wake area [45].

the other region, a power law approximation

$$u(z) = u_{ref} \left( \frac{z}{z_{ref}} \right)^\alpha \quad (4.1)$$

can be used for the wind speed, where  $u_{ref}$  is a reference velocity at height  $z_{ref}$ , and  $\alpha$  an empirical coefficient characterizing the surface roughness at given velocity at the reference height [45]. The reference wind speed can be obtained from the hourly values of a weather data file, which are converted in the same manner. For example, with  $u(z) = u_{met}$  at  $z = z_{met}$ , e.g.,  $z_{met} = 10\text{ m}$ , from the weather file,  $u_{ref}$  is obtained according to the location of the meteorological station. If the latter is located in open terrain,  $\alpha = 0.14$  and  $z_{ref} = 270\text{ m}$  [4], and, thus,

$$u(z) = u_{met} \left( \frac{\delta_{met}}{z_{met}} \right)^\alpha \left( \frac{z}{\delta} \right)^\alpha . \quad (4.2)$$

Further coefficients and correlations are detailed in [2, 4], for example.

The total wind pressure  $p(x, y, z)$  is composed of the static pressure  $p_s(z)$  and the dynamic pressure  $p_d(x, y, z)$ , according to the *Bernoulli equation*

$$p(x, y, z) = p_s(z) + p_d(x, y, z) = p_s(z) + \frac{1}{2} c_p(x, y, z) \varrho_\infty u_\infty^2 , \quad (4.3)$$

where  $u_\infty$  is the reference wind speed for  $c_p(x, y, z)$ , and  $\varrho_\infty$  the fluid density.

Figure 4.9 shows the location dependent distribution of  $c_p(x, y, z)$  values, the so-called wind pressure coefficients. The aerodynamic  $c_p(x, y, z)$  coefficients are in fact some kind of shape factors, which are independent of the flow velocity and relate the pressure difference  $\Delta p$  to the local outdoor atmospheric pressure, i.e., the velocity pressure  $\frac{1}{2} \varrho_\infty u_\infty^2$ ,

$$c_p(x, y, z) = \frac{\Delta p}{\frac{1}{2} \varrho_\infty u_\infty^2} . \quad (4.4)$$

For the purpose of simulation, the wind pressure distribution can be predicted using

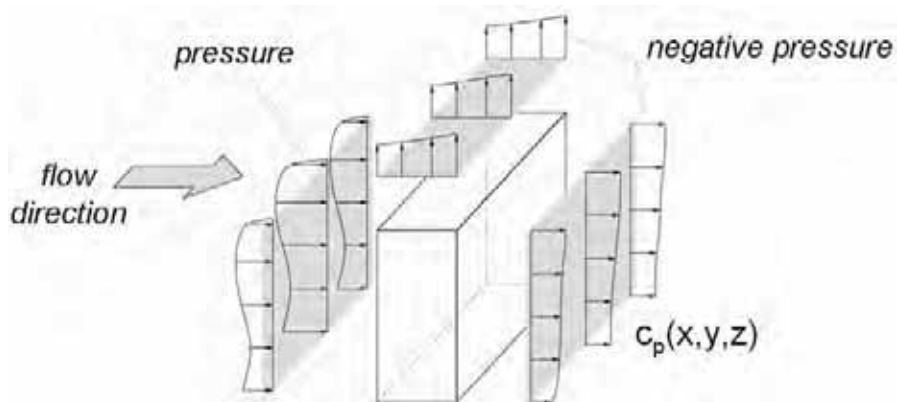


Figure 4.9: Positive and negative pressure distribution at the building surface expressed in terms of  $c_p(x, y, z)$  values [45, 46, 60].

- standards, which provide tabulated wind pressure coefficients for the static load design (not recommended in this scope), such as the DIN Standard 1055-4 [16], for example,
- parametric models, summarized by ALLARD in [2], which are based on empirical findings and which permit a rough estimate only,
- wind tunnel experiments (recommended, expensive), and
- simulation using computational fluid dynamics (CFD).

Wind tunnel experiments provide detailed insight into the air flow characteristics, but are very expensive in terms of model creation and measuring. Besides the model itself, several elements are required to reproduce the flow in terms of the surface roughness and the turbulent flow characteristics. For the surface roughness, a coarse model of the surrounding urban building structure is created. Figure 4.10 shows the typical setup of such an experiment. For details it is referred to [2, 45], for example.

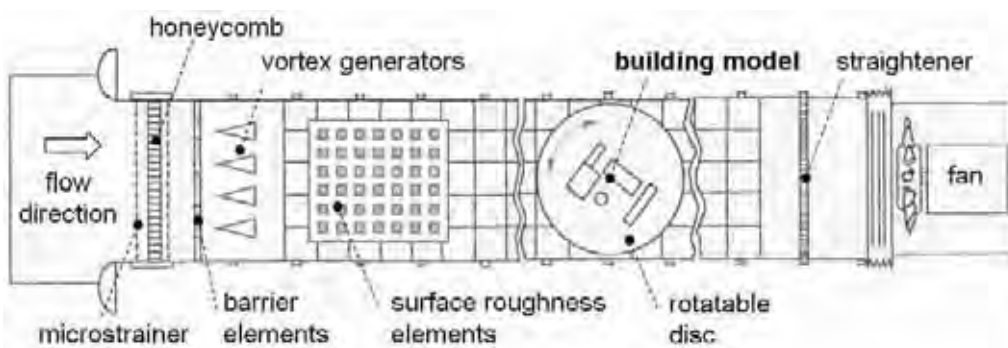


Figure 4.10: Typical setup of a wind tunnel experiment. Modified from [45].

Wind tunnel experiments are further restricted to low Reynolds numbers, which can be seen from the following example:

With the definition of the Reynolds number,  $Re = u_\infty L/\nu$ ,  $L$  being a characteristic length scale such as the height of the wind tunnel, and the kinematic viscosity of the air  $\nu = 1.53 \cdot 10^{-5} \frac{m^2}{s}$ , we can estimate the wind speed, which would be required to realistically capture the dynamics of a turbulent flow at  $Re \approx 10^9$  (which is actually a fairly low Reynolds number in aerodynamics). Assuming  $u_\infty = 30 m/s$ , the characteristic height of the boundary layer  $L = 200 m$ , and the height of our wind tunnel being  $2 m$ , we would require a fan delivering an air speed of  $3000 m/s$  in our experiment!

Therefore, wind tunnel experiments utilize the *dynamic similarity* of the flow characteristics between scales. Relevant dimensionless numbers [8, 24, 55] are

- the Reynolds number, which is the ratio of the inert forces and the viscous forces,
- the Froude number, which is the ratio of the inert forces and the gravitation forces,
- the Prandtl number, which is a fluid property characterizing the thermal boundary layer,
- and the Strouhal number, which describes the time frequency characteristics of a flow, such as oscillations of the structure induced by periodic vortex shedding.

Note, that flows within similar geometrical configuration, same topology but different geometrical scalings show the same streamline picture, if the Reynolds numbers are identical.

Note secondly, that the static and dynamic wind pressure distribution strongly influences the vertical as well as the horizontal air flow through a building. In the horizontal case (such as a large open-plan office with access to opposing facades), crosswise air exchange between windows can lead to fairly high and undesired local air speeds. On the other hand, pressure differences can be utilized for improving a natural ventilation concept. However, such design concepts require a detailed on-site survey of the local aerodynamic situation and contain many uncertainties.

**Thermal effects.** Assuming a polytropic atmosphere, a coarse approximation of the external vertical temperature profile is given by the linear function for the air temperature [43, 55],

$$T(z) = T_{ref} - \frac{1}{100}(z - z_{ref}) , \quad (4.5)$$

with a given reference temperature  $T_{ref}$  at  $z_{ref}$ , i.e. the temperature decreases by  $1^\circ C$  every  $100 m$ .

With known air temperature  $T(z)$ , the static pressure distribution can be empirically expressed by

$$p_s(z) = p_{s,ref} \left( \frac{T(z)}{T_{ref}} \right)^{g/(100 \cdot R_i)} , \quad (4.6)$$

where  $R_i$  is the special gas constant for air [6, 8, 55], and  $g$  the acceleration due to gravity. With the pressure and the temperature, the density  $\varrho$  can be determined by the equation of

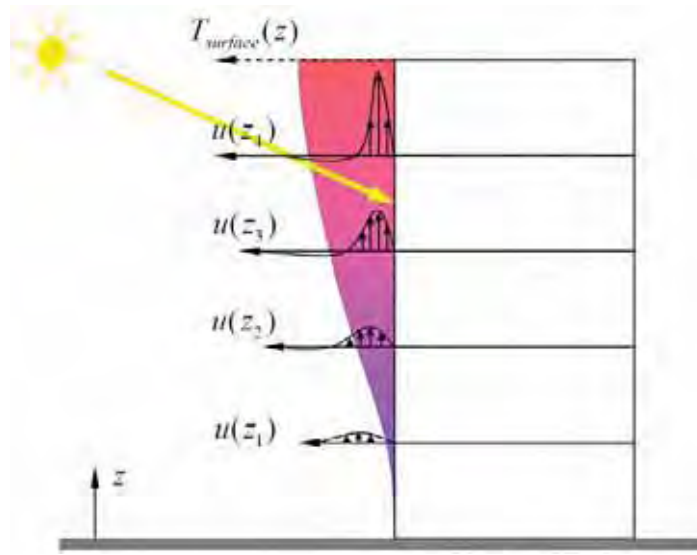


Figure 4.11: Thermal boundary layer at the surface of a building exposed to the sun [48].

state [28],  $\varrho = p/(R_i T)$ .

Note, that at building surfaces, which are exposed to the sun, a thermal boundary layer emerges vertically alongside the building facade. Figure 4.11 shows this effect [48]. In the figure,  $T_{surface}(z)$  indicates the surface temperature, and  $u(z)$  is the local flow velocity profile in  $z$ -direction. As a consequence, natural ventilation may become impossible in the upper storeys of a building, as hot air would be sucked into the building. This effect has to be considered, when designing air intakes within the building envelope (cf. Figure 2.10 in Chapter 2).

### 4.1.3 Heat transfer by forced convection

It is evident from the above section, that the external convective heat transfer is usually dominated by forced convection. A dimensional analysis yields the general expression

$$Nu = c \cdot Re^n \cdot Pr^m , \quad (4.7)$$

with the empirical coefficients  $c$ ,  $n$  and  $m$  obtained from experimental observations and theoretical assumptions [8, 11]. The dimensionless *Nusselt number*  $Nu$  describes the relationship between heat and mass transfer,

$$Nu = \frac{h_c L}{\lambda} , \quad (4.8)$$

i.e., the ratio of the heat transfer by convection to the diffusive heat transfer in the near wall boundary, where  $h_c$  is the convective heat transfer coefficient and  $L$  a characteristic length. The dimensionless *Reynolds number*

$$Re = \frac{u_\infty L}{\nu} , \quad (4.9)$$

is the ratio of the inert forces and the viscous forces, with the velocity  $u_\infty$ , and the kinematic viscosity  $\nu$ . The *Prandtl number*,

$$Pr = \frac{\nu}{\alpha} , \quad (4.10)$$

is a fluid property and describes the ratio of the fluid propagation in terms of momentum and heat transfer, where  $\alpha$  is called the thermal diffusivity.

Various correlations have been proposed in the literature. For example, NUSSELT [42] found an empirical correlation for the external convective heat transfer coefficient [ $W/(m^2K)$ ], which has been modified by FEIST [21],

$$h_c(z) = 1.8 + 4.8 u_0(z) , \quad (4.11)$$

where  $u_0(z)$  is the local wind speed, unit [ $m/s$ ], at height  $z$ .

Another correlation was found by MCADAMS [36, 11],

$$h_c = 5.678 \left[ a + b \left( \frac{1}{0.3048} \frac{294.26}{273.16 + T} u_{\parallel} \right)^n \right] , \quad (4.12)$$

where the coefficients  $a$ ,  $b$  and the exponent  $n$  depend on the wind speed and the surface roughness as depicted in Table 4.1. The formula requires the wind velocity  $u_{\parallel}$  parallel to the respective surface. ITO ET AL. [30] derived an empirical expression for calculating  $u_{\parallel}$  from the free stream velocity. At this point, the reader is referred to the book of CLARKE [11], where these formulae have been summarized.

Surface type	$u < 4.88 m/s$			$4.88 < u < 30.48 m/s$		
	a	b	n	a	b	n
smooth	0.99	0.21	1	0	0.50	0.78
rough	1.09	0.23	1	0	0.53	0.78

Table 4.1: Empirical coefficients of Equation (4.12) of McAdam's model [36].

For wind speeds between 0.5 and 10  $m/s$ , the convective heat transfer  $h_c$  approximately varies between 7 and 43  $W/(m^2K)$ .

#### 4.1.4 Soil temperature

For components with soil contact we distinguish between parts, which are (partially) covered by earth (such as walls), and underground components, such as the base plate, for example. The temperature below ground,  $T_{soil}(t)$ , can be approximated by the seasonal sinusoidal function

$$T_{soil}(t) = 10 + 5 \sin \left( -\frac{453\pi}{552} + \frac{\pi}{4416} \cdot t \right) , \quad (4.13)$$

where  $t$  is the simulation time, unit [ $h$ ]. The formula is a reasonable approximation of a detailed capacitance model. The surface temperature of partially covered components,  $T_{wall}(t)$ ,

can be calculated from the mean value of a 24 h-average of the ambient temperature and a constant earth temperature of 10°C, for example [59].

Figure 4.12 shows both functions. Note, that the function for  $T_{soil}(t)$  is shifted due to the inert behavior in terms of the heat capacity of the earth mass around a building.

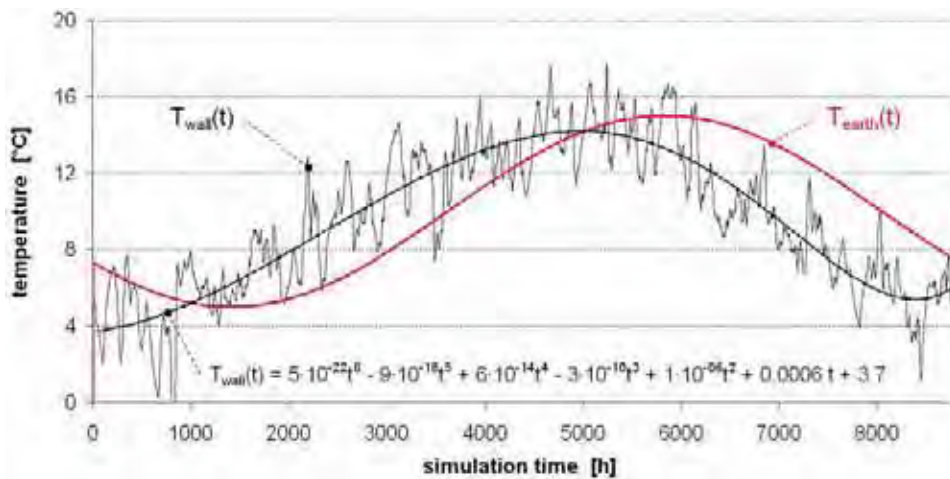


Figure 4.12: Seasonal dependance of the soil and wall temperatures [59].

## 4.2 Transition conditions to the internal environment

### 4.2.1 Room air flow characteristics

Indoor air flows are characterized in terms of free convection, or mixed convection (free and forced convection at the same time). Mixed convection occurs, if a mechanical ventilation

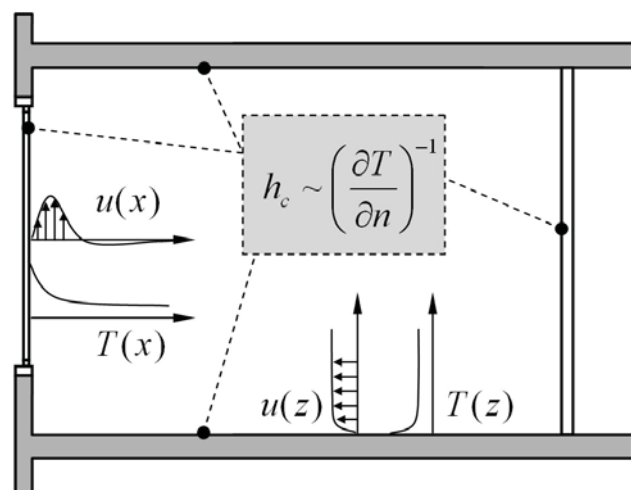


Figure 4.13: Depending on the direction of the heat flux, different boundary layer profiles are observed for the velocity and the temperature distribution near surfaces.

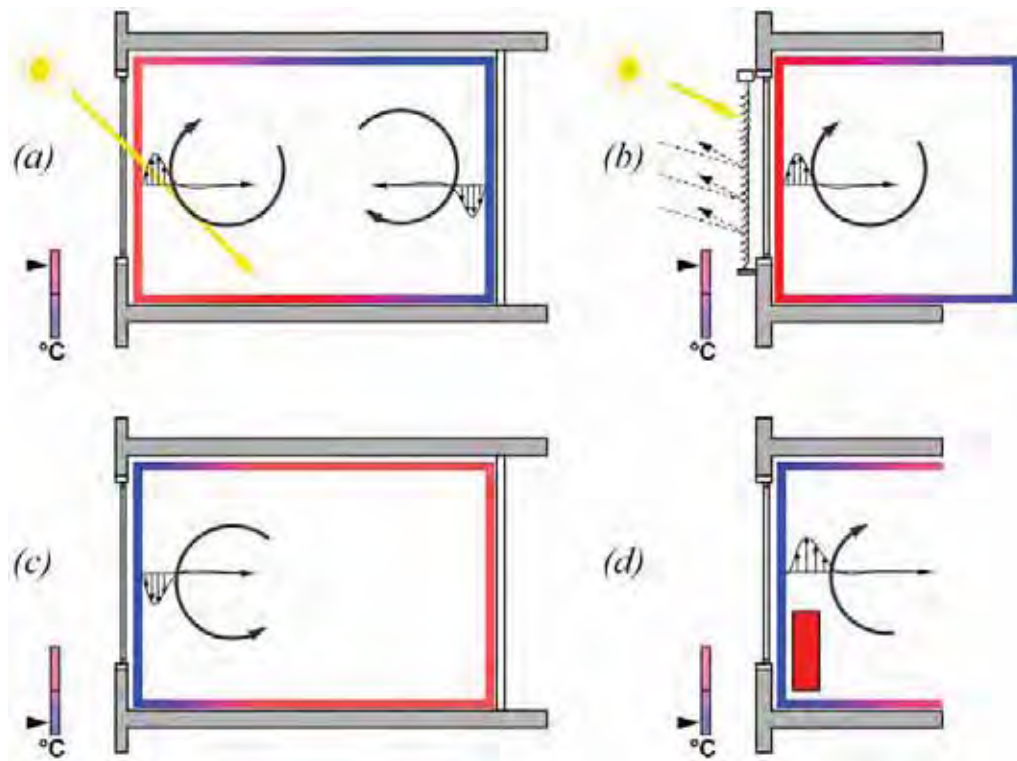


Figure 4.14: Natural convection in buildings depends on the order of magnitude and the spatial distribution of the surface temperatures. The figure shows four configurations: (a) cavity heated from one side and from the bottom due to absorbed solar radiation, (b) cavity heated from the side due to absorption, (c) cold window surface causing downdraught, and (d) reversed flow due to a radiator placed in front of a window.

system acts as a driving force in addition to the buoyancy effects. In building simulation, convective heat transfer is expressed in terms of heat transfer coefficients  $h_c [W/(m^2 K)]$  by linearizing of the heat flux in the boundary layer and by assuming a homogeneous (well-stirred) air temperature distribution. The heat flux  $q_{c,i}$  by convection between the air and an internal surface element  $i$  is then

$$q_{c,i} = h_{c,i} (T_{air} - T_{int,i}) \quad . \quad (4.14)$$

Figure 4.13 shows the different locations, where these heat transfer coefficients are required. As in building simulation the heat transfer is treated in a one-dimensional manner through the fabric, area averaged values are required for each respective surface. It can be seen from Figure 4.14, that the type of convective flow pattern depends on the order of magnitude and the spatial distribution of the surface temperatures.

The relevant dimensionless quantities for free convection type flows are

- the *Grashof number*, which is the ratio of the buoyant forces and the viscous forces,
- and the *Rayleigh number*, which is also known as modified Grashof number.

The Grashof number is defined by

$$Gr = \frac{g\beta(T_{int,i} - T_{air})L^3}{\nu^2}, \quad (4.15)$$

where  $g$  is the acceleration due to gravity,  $L$  is a characteristic length such as the room height, and  $\nu$  is the kinematic viscosity of the air [8, 55]. The Rayleigh number is then given by

$$Ra = Pr \cdot Gr = \frac{g\beta(T_{int,i} - T_{air})L^3}{\alpha\nu} \quad , \quad (4.16)$$

with the thermal diffusivity  $\alpha$ , the thermal expansion coefficient  $\beta$ , and the Prandtl number from Equation (4.10). The Prandtl number of air is 0.71.

The type of convection can be generally classified in terms of the ratio of the Grashof and the Reynolds number:

- If  $Gr/Re^2 \approx 1$ , buoyant forces and viscous forces have the same order of magnitude,
- if  $Gr/Re^2 \gg 1$ , the flow is dominated by free convection, and
- if  $Gr/Re^2 \ll 1$ , then forced convection prevails.

The effects shown in Figure 4.14 can be explained in thermodynamics in terms of a cavity heated from the side (temperature gradient between opposing walls), and a cavity, where either the ceiling or the bottom is heated or cooled, respectively. A free convective flow develops, if inertial forces and density gradients are present, which are not aligned in a parallel manner [6].

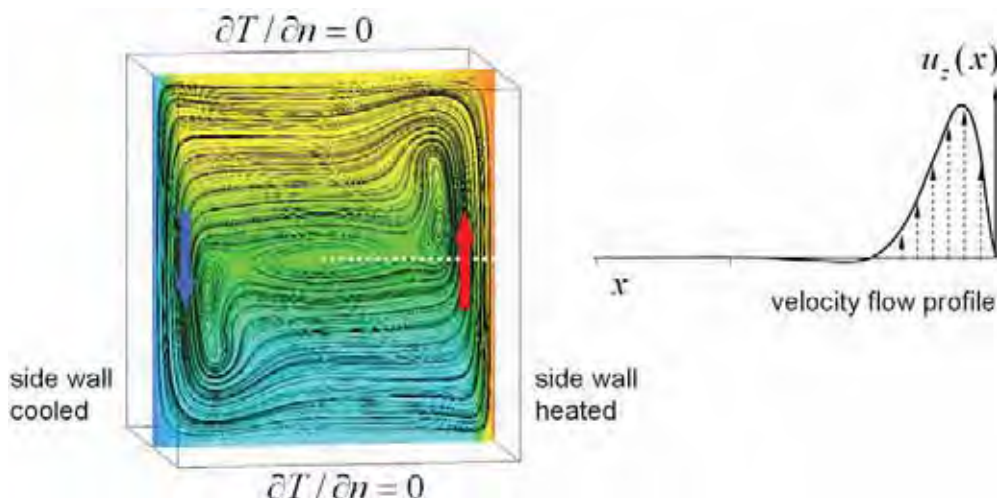


*Figure 4.15:* Natural convection in a square cavity, heated from the side,  $Ra = 10^6$ , the other surfaces are adiabatically connected. On the right-hand-side, the vertical flow profile is shown for the mid cross section, as indicated with the dotted line. The colors indicate the temperature distribution. Adapted from [60].



Figure 4.16: Rayleigh-Bénard convection for  $Ra = 10^8$ . Adapted from [60]. The picture on the left-hand-side shows the streamlines of the velocity field, the figure on the right-hand-side the temperature distribution.

- *Cavity heated (or cooled) from the side.* Figure 4.15 exemplarily shows the parabolic flow profile for the case of  $Ra = 10^6$  (below transition to turbulence), which is typical for buoyant flows [66]. For higher Rayleigh numbers, the boundary layer thickness is further reduced, and other vertices occur symmetrically, until a fully turbulent flow develops.
- *Cavity heated at the top/ceiling.* If the cavity is heated at the ceiling (and/or cooled at the bottom), *thermal stratification* is observed. In practice, this situation is typical for large glazed spaces with sun shading devices installed on top of the courtyard (without figure).
- *Cavity heated at the bottom (and cooled at the ceiling).* After exceeding a critical Rayleigh number (i.e., for  $Ra_{crit} > 1708$ ), we can observe the so-called *Rayleigh-Bénard* convection phenomenon, if the direction of the temperature gradient is opposite to the gravitational forces [8, 61]. Figure 4.16 details this effect for  $Ra = 10^8$ . Note, that in this case heat is exchanged between both sides by thermal plumes (jet streams).

Figure 4.17, finally, shows the temperature and velocity boundary layer profiles (laminar) for forced convective flow over a horizontal plate, which is heated from below [8]. Note, that the profile differs significantly from the one for free convection from Figure 4.15.

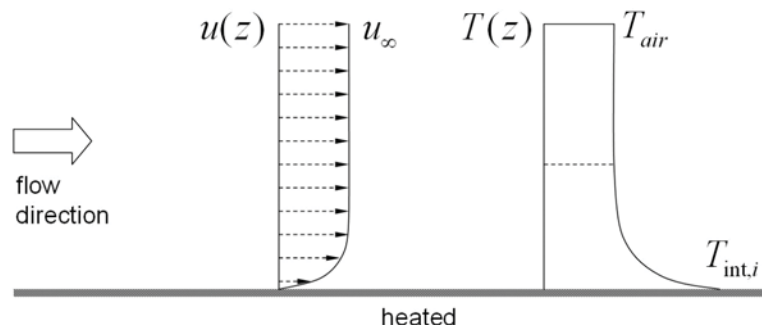


Figure 4.17: Laminar boundary layer profiles for forced flow over a horizontal plate heated from below. Adapted from [8].

Fur further reading on laminar and turbulent boundary layer theory it is referred to the text book of BEJAN [8], and the text book of SCHLICHTING ET AL. [55].

#### 4.2.2 Internal convective heat transfer coefficients

The previous section demonstrated the different flow characteristics for free and forced convection and the related boundary layer profiles. In the literature, several scope-dependent empirical correlations have been proposed, which are summarized in the book of CLARKE [11] and in the thesis of BEAUSOLEIL-MORRISON [7].

Most of the correlations are based on experimental observations. BEJAN [8] recapitulates the various scalings between the dimensionless numbers, which have been found by a number of authors. For a uniformly heated vertical wall, for example,

$$Nu \approx 0.55 Ra^{1/5} \quad \text{for laminar flows } (Ra < 10^{13}), \text{ and} \quad (4.17)$$

$$Nu \approx 0.17 Ra^{1/4} \quad \text{for the turbulent case} \quad (4.18)$$

is recommended by VLIET & LIU [63]. For a horizontal plate with upward facing flow, FUJI & IMURA [23] found

$$Nu \approx 0.13 Ra^{1/3} \quad \text{for } Ra > 5 \cdot 10^8 \quad (4.19)$$

and for a horizontal plate with downward facing flow [11, 23]

$$Nu \approx 0.58 Ra^{1/3} \quad \text{for } 10^6 < Ra < 10^{11} . \quad (4.20)$$

It is accordingly important, to estimate or to predict the local flow pattern reasonably well in simulation, as the empirical correlations are only valid for a narrow range of parameters.

ALAMDARI & HAMMOND [1, 11] provide a general expression for heat transfer by natural convection at vertical and horizontal surfaces, which can be applied in the wide range of  $10^4 < Ra < 10^{12}$ . For vertical surfaces,

$$h_c = \sqrt[6]{\left[ 1.5 \left( \frac{T_{int,i} - T_{air}}{L} \right)^{1/4} \right]^6 + \left[ 1.23 (T_{int,i} - T_{air})^{1/3} \right]^6} , \quad (4.21)$$

where  $L$  is the surface height. For horizontal surfaces with upward heat flow,

$$h_c = \sqrt[6]{\left[ 1.4 \left( \frac{T_{int,i} - T_{air}}{L} \right)^{1/4} \right]^6 + \left[ 1.63 (T_{int,i} - T_{air})^{1/3} \right]^6} , \quad (4.22)$$

where  $L = 4 \cdot A_{surf}/P_{surf}$  is the hydraulic diameter [ $m$ ] of the surface area  $A_{surf}$  and the perimeter  $P_{surf}$ . Expression (4.22) can be further simplified to

$$h_c = 1.63 (T_{int,i} - T_{air})^{1/3} . \quad (4.23)$$

For horizontal plates with downward heat flow, the correlation is

$$h_c = 0.6 \left( \frac{T_{int,i} - T_{air}}{L^2} \right)^{1/5}, \quad (4.24)$$

with  $L$  again being the hydraulic diameter.

Other expressions are given by KHALIFA & MARSHALL [31] in terms of various configurations of rooms heated with equipment, by AWBI & HATTON [5] and by FISHER & PEDERSON [22] concerning jet flows [11]. BEAUSOLEIL-MORRISON [7] further summarized correlations for natural and mixed convection type flows.

### 4.2.3 Internal heat gains and user behavior

In office buildings the dominating heat source are solar heat gains – and internal gains resulting from people and electrical devices such as desktop computer hardware and lighting equipment. Tables in standards summarize the heat generation of such devices, cf. [17] and others. People are convective and radiant heat sources and account for 65..85 W heat production per individual. (Chapter 13 will address this issue in detail.)

In building performance simulation, usually pre-defined load profiles and plant operation schedules are applied. It is thereby important to carefully consider the type of use of a building (residential building, office building, school, hospital, etc.), as the internal heat gains will inherently depend on this.

A new trend is to include user behavior into simulation, in order to improve the prediction accuracy of the respective simulation models. For example, HERKEL ET AL. [29] developed a model based on a large field study to predict the window status of a building in terms of occupancy. The time of the day is thereby used to stochastically model the occupancy, as it is likewise done by REINHART [50]. Similar to the earlier observations by NICOL [40], the authors found a strong correlation between the percentage of open windows, season and the outdoor temperature, which can be described in terms of a logit<sup>1</sup> function. Another stochastic model has been introduced by HALDI ET AL. [26] for blind usage. Based on a flied survey, the authors describe the blind usage in buildings in terms of occupancy, and thermal and visual parameters.

MAHDAVI proposes in [33] his vision of 'sentient' buildings, which possess a dynamic representation of their components, processes and occupants. The information can be used to support facility management operations and (simulation based) systems control. In [34], the implementation of a vision-based object location sensing and occupancy detection system is described, which makes use of image processing methods for identifying tags and movement. Control-oriented occupant behavior in terms of lighting and shading is reported by MAHDAVI ET AL. in [35] and [32]. The authors estimate a theoretical energy reduction potential for lighting in office buildings of up to 70 per cent, if occupancy sensors and dimming devices were installed.

---

<sup>1</sup>inverse of the sigmoid or logistic function

### 4.3 Impacts of the urban environment and the climate change

It has already been mentioned, that weather data are usually acquired in rural areas. Concerning the wind effects, the urban structure influences the surface roughness and the local flow patterns. It is therefore recommended, to investigate the site specific urban microclimate by means of wind tunnel experiments or CFD for a large building in such areas. BLOCKEN ET AL. [9] provide an overview over the status of the application of CFD in this scope.

Likewise the wind distribution and the air temperature distribution are locally different in the urban environment and do not correspond to the weather data. WILLIAMSON ET AL. [65] investigated the error from failure to account for the urban microclimate in building performance simulation for different climate regions. The authors found that the deviations of the air temperature are too large to neglect if the simulation results are used for decision making on building design.

As an example, Figure 4.18 shows the surface temperatures during a summer day for the city of Munich, Germany [58]. Local heat islands can be identified at locations, where green spaces are only scarcely present. Similar observations are made in winter.

In metropolitan areas, the atmospheric pollution is thereby one of the reasons which influences the solar radiation (greenhouse effect). Solar radiation is absorbed and stored by the building structure, which shows an inert behavior releasing the energy [53]. The ground surface temperature is usually a few degrees higher in urban areas than in rural areas [2]. Due to soil sealing, water is draining off and the latent heat losses by evaporation are less than in the countryside. Anthropogenic effects further increase temperature levels. In summary, in metropolitan areas



Figure 4.18: Surface temperatures during a summer day for the city region of Munich, Germany. Courtesy of Umweltreferat der Stadt München [58].

the mean air temperature is higher compared to the countryside, as more short wave radiation is absorbed, the mean wind velocities are lower, and less long wave radiation is emitted [52]. Measurements addressing the intensity of heat island effects are reported by MITCHELL [38]. To some extent, the effects can be generalized in terms of daily and seasonal patterns [2, 54]. HAUSER ET AL. [27] quantify, how differences of meteorological conditions in urban and rural areas affect the summer and winter behavior and the heating demand of buildings.

Predicting the urban microclimate is, however, difficult due to the different spatio-temporal levels and scales. Recently, a number of coupled simulation models have been proposed in the literature, such as the models by ROBINSON ET AL. [53] and RASHEED ET AL. [49]. In [53], for example, an efficient radiosity algorithm is described for calculating the long wave and short wave radiative heat exchange in the urban context.

CRAWLEY [14] published a methodology to create weather data files representing climate change scenarios in the future years and today's heat island impacts. In his study, he investigated prototypical office buildings representing different energy standards in a series of climate regions using typical and extreme weather data. For the net change in the annual energy performance, Crawley found, that for cold climates the energy use is reduced in the order of 10 per cent, for tropical climates he predicts an increase by more than 20 per cent for several months of a year, and for temperate, mid-latitude climates a reduction in heating energy by 25 per cent and up to 15 per cent increase for cooling energy [14].

## 4.4 References

- [1] F. Alamdari and G.P. Hammond. Improved data correlation for buoyancy-driven convection in rooms. SME/J/83/01, Applied Energy Group, Cranfield Institute of Technology, 1983.
- [2] F. Allard, M. Santamouris, S. Alvarez, E. Dascalaki, G. Guerracino, E. Maldonado, S. Sciuto, and L. Vandaele. *Natural ventialtion in buildings*. James and James, 1998.
- [3] ASHRAE. *International Weather for Energy Calculation (IWEC)*. American Society of Heating, Refrigerating and Air-Conditioning Engineers, 2001.
- [4] ASHRAE. *Handbook - Fundamentals (SI)*. American Society of Heating, Refrigerating and Air-Conditioning Engineers, 2005.
- [5] H.B. Awbi and A. Hatton. Natural convection from heated room surfaces. *Energy and Buildings*, 30:233–244, 1999.
- [6] D. Baehr and K. Stephan. *Wärme- und Stoffübertragung*. Springer Verlag, 3rd edition, 1998.
- [7] I. Beausoleil-Morrison. *The adaptive coupling of heat and air flow modelling within dynamic whole building simulation*. PhD thesis, University of Strathclyde, Glasgow, 2000.
- [8] A. Bejan. *Convection heat transfer*. John Wiley & Sons, Inc., 1993.

- [9] B. Blocken, T. Stathopoulos, J. Carmeliet, and J. Hensen. Application of CFD in building performance simulation for the outdoor environment. In *Proc. 11th IBPSA Conf. Building Simulation*, Glasgow, Scotland, 2009.
- [10] CEC. *Test reference years, weather data sets for computer simulations of solar energy systems and energy consumption in buildings*. CEC, DG XII, Brussels: Commission of the European Community, 1985.
- [11] J.A. Clarke. *Energy simulation in building design*. Butterworth-Heinemann, 2nd edition, 2001.
- [12] Commission of the European Communities. Short reference years. Short weather data sets for faster simulations of solar energy systems and energy consumption in buildings.
- [13] D.B. Crawley. Which weather data should you use for energy simulations of commercial buildings? *ASHRAE Trans.*, 104(2):498–515, 1998.
- [14] D.B. Crawley. Estimating the impacts of climate change and urbanization on building performance. *J Building Performance Simulation*, 1(2):91–115, 2008.
- [15] L. Degelman. Simulation and uncertainty – weather predictions. In A. Malkawi and Augenbroe G., editors, *Advanced Building Simulation*. Spon Press, New York, 2004.
- [16] DIN 1055-4. *Action on structures - Part 4: Wind loads*. DIN Deutsches Institut für Normung e.V., Beuth Verlag, 2005.
- [17] DIN 4108:2003. *Normenreihe Wärmeschutz und Energie-Einsparung in Gebäuden*. DIN Deutsches Institut für Normung e.V., Beuth Verlag, 2003.
- [18] DIN 4701:2003. *Statistics on German meteorological data for calculating the energy requirements for heating and air conditioning equipment*. DIN Deutsches Institut für Normung e.V., Beuth Verlag, 2003.
- [19] DIN 4701:2004. *Normenreihe Energetische Bewertung heiz- und raumluftechnischer Anlagen im Bestand*. DIN Deutsches Institut für Normung e.V., Beuth Verlag, 2004.
- [20] Federal Ministry of Transport, Building, and Urban Affairs. Deutscher Wetterdienst (DWD), 2009. <http://www.dwd.de>.
- [21] W. Feist. *Thermische Gebäudesimulation, Kritische Prüfung unterschiedlicher Modellansätze*. C.F. Müller Verlag, Heidelberg, 1994.
- [22] D.E. Fisher and C.O. Pederson. Convective heat transfer in building energy and thermal load calculations. *ASHRAE Trans.*, 103(2):137–148, 1997.
- [23] T. Fuji and H. Imura. Natural convection heat transfer from a plate with arbitrary inclination. *J Heat and Mass Transfer*, 15:755–767, 1970.
- [24] K. Gersten. *Einführung in die Strömungsmechanik*. Vieweg, 6th edition, 1991.

- [25] G. Gültz and S. Hoffmann. Frequency of overheating during the summer – How meaningful are simulation results based on test reference years? *Bauphysik*, 29(2):99–109, 2007.
- [26] F. Haldi and D. Robinson. A comprehensive stochastic model of blind usage: theory and validation. In *Proc. 11th IBPSA Conf. Building Simulation*, Glasgow, Scotland, 2009.
- [27] G. Hauser, C. Kempkes, and S. Schlitzberger. Vergleichende Untersuchungen von Standard-Klimadatensätzen (Testreferenzjahren) mit gemessenen Langzeit-Klimadatensätzen für den Standort Kassel. *Bauphysik*, 28(4):221–232, 2006.
- [28] E. Hering, R. Martin, and M. Stohrer. *Physik für Ingenieure*. VDI Verlag, 1992.
- [29] S. Herkel, U. Knapp, and J. Pfafferott. A preliminary model of user behaviour regarding the manual control of windows in office buildings. In *Building Simulation 2005*, Montreal, Canada, 2005.
- [30] N. Ito, K. Kimura, and J. Oka. A field experiment study on the convective heat transfer coefficient on exterior surface of a building. *ASHRAE Trans.*, 2225:184–191, 1972.
- [31] A.J. Khalifa and R.H. Marshall. Validation of heat transfer coefficients on interior building surfaces using a real-sized indoor test cell. *Int J Heat Mass Transfer*, 33(10):2219–2236, 1990.
- [32] L. Lambeva and A. Mahdavi. User control of indoor-environmental conditions in buildings: an empirical case study. In *Proc. 10th IBPSA Conf. Building Simulation*, Bejing, China, September 3-6 2007.
- [33] A. Mahdavi. Self-organizing models for sentient buildings. In A. Malkawi and Augenbroe G., editors, *Advanced Building Simulation*. Spon Press, New York, 2004.
- [34] A. Mahdavi, O. Icoglu, and S. Camara. Vision-based location sensing and self-updating information models for simulation-based building control strategies. In *Proc. 10th IBPSA Conf. Building Simulation*, Bejing, China, September 3-6 2007.
- [35] A. Mahdavi, A. Mohammadi, E. Kabir, and L. Lambeva. Occupants' operation of lighting and shading systems in office buildings. *J Building Performance Simulation*, 1(1):57–65, 2008.
- [36] W.H. McAdams. *Heat transmission*. McGraw-Hill, New York, 1954.
- [37] METEONORM V 5.0. *Global meteorological database for solar energy and applied climatology*. Meteotest, <http://www.meteotest.ch/products/meteonorm>, 2003.
- [38] J.M. Mitchell. The temperature of cities. *Weatherwise*, 14:224–229, 1961.
- [39] NEN EN ISO 15927:2005. *Hygrothermal Performance of Buildings Calculation And Presentation Of Climatic Data - Part 4: Hourly Data For Assessing The Annual Energy Use For Heating And Cooling*. International Organization For Standardization (ISO), 2005.

- [40] J.F. Nicol. Characterising occupant behaviour in buildings: towards a stochastic model of occupant use of windows, lights, blinds, heaters and fans. In *Proc. 7th IBPSA Conf. Building Simulation*, Rio de Janeiro, Brazil, 2001.
- [41] NREL. *User's manual for TMY2s, NREL/SP-463-7668, and TMY2s, Typical meteorological years derived from the 1961–1990 national solar radiation database*. Golden, Colorado: National Renewable Energy Laboratory, 1995.
- [42] W. Nusselt and W. Jürgens. Die Kühlung einer ebenen Wand durch einen Luftstrom. *Gesundheitsingenieur*, 52, 1922.
- [43] C. Nytsch-Geusen. *Berechnung und Verbesserung der Energieeffizienz von Gebäuden und ihren energietechnischen Anlagen in einer objektorientierten Simulationsumgebung*. PhD thesis, Technische Universität Berlin, VDI-Verlag, 2001.
- [44] Ontwerp NEN 5060:2008. *Hygrothermal performance of buildings – Climatic reference data*. Nederlands Normalisatie-Instituut (NNI), 2008.
- [45] A. Pernpeintner. *Lecture notes on building aerodynamics*. Lehrstuhl für Fluidmechanik, Technische Universität München, 1995.
- [46] A. Pernpeintner and J. Fischer. Der Wind als Faktor in der Bauwerksplanung. In *Proc. Kongress ClimaDesign auf der Messe BAU2003*, München, 2003.
- [47] W. Plokker, J. Evers, C. Struck, A. Wijsman, and J. Hensen. First experiences using climate scenarios for the netherlands in building performance simulation. In *Proc. 11th IBPSA Conf. Building Simulation*, Glasgow, Scotland, 2009.
- [48] G. Pültz. *Bauklimatischer Entwurf für moderne Glasarchitektur, Passive Massnahmen der Energieeinsparung*. Verlag Ernst und Sohn, 2002.
- [49] A. Rasheed and D. Robinson. Multiscale modelling of urban climate. In *Proc. 11th IBPSA Conf. Building Simulation*, Glasgow, Scotland, 2009.
- [50] C. Reinhart. Lightswitch-2002: a model for manual and automated control of electric lighting and blinds. *Solar Energy*, 77:15–28, 2004.
- [51] D. Robinson and F. Haldi. An integrated adaptive model for overheating risk prediction. *J Building Performance Simulation*, 1(1):43–55, 2008.
- [52] D. Robinson, F. Haldi, J. Kämpf, P. Leroux, D. Perez, A. Rasheed, and U. Wilke. CITYSIM: Comprehensive micro-simulation of resource flows for sustainable urban planning. In *Proc. 11th IBPSA Conf. Building Simulation*, Glasgow, Scotland, 2009.
- [53] D. Robinson and A. Stone. Solar radiation modelling in the urban context. *Solar Energy*, 77(3):295–309, 2004.
- [54] K.E. Runnalls and T.R. Oke. Dynamics and controls of the near-surface heat island of vancouver, british columbia. *Physical Geography*, 21(4):283–304, 2000.
- [55] H. Schlichting and K. Gersten. *Boundary layer theory*. Springer, 9th edition, 1996.

- [56] C. Struck, P. de Wilde, J. Evers, J. Hensen, and W. Plokker. On selecting weather data sets to estimate a building design's robustness to climate variations. In *Proc. 11th IBPSA Conf. Building Simulation*, Glasgow, Scotland, 2009.
- [57] TRY. Tape reference manual – test reference year (TRY). Tape deck 9706, Federal Energy Administration (FEA), ASHRAE, National Bureau of Standards (NBS), and the National Oceanic and Atmospheric Administration (NOAA), National Climatic Center, Asheville, NC, 1976.
- [58] Umweltreferat der Stadt München. Umweltatlas München, 2009. <http://www.muenchen.de>.
- [59] C. van Treeck. *Numerische Bestimmung der Transmissionswärmeverluste durch Wärmebrücken in der dynamischen Gebäudesimulation am Beispiel eines hochwärmegedämmten Mehrfamilienhauses*. Diploma thesis, Fraunhofer-Institute for Solar Energy Systems (ISE), Freiburg, 1997.
- [60] C. van Treeck. *Gebäudemodell-basierte Simulation von Raumluftströmungen*. PhD thesis, Technische Universität München, 2004.
- [61] C. van Treeck, E. Rank, M. Krafczyk, J. Tölke, and B. Nachtwey. Extension of a hybrid thermal lbe scheme for Large-Eddy simulations of turbulent convective flows. *Computers and Fluids*, 35:863–871, 2006.
- [62] VDI 2078. *Cooling load calculation of air-conditioned rooms (VDI cooling load regulations)*. VDI Verein Deutscher Ingenieure, Beuth Verlag, 2007.
- [63] G.C. Vliet and C.K. Liu. An experimental study of turbulent natural convection boundary layers. *J Heat Transfer*, 91:517–531, 1969.
- [64] H. Werner and Wengle H. Large eddy simulation of turbulent flow over and around a cube in a plate channel. In Schumann et al., editors, *8th Symp. on Turb. Shear Flows, Schumann et al. (eds.)*. Springer Verlag, Berlin, 1993.
- [65] T.J. Williamson, E. Erell, and V. Soebarto. Assessing the error from failure to account for urban microclimate in computer simulation of building energy performance. In *Proc. 11th IBPSA Conf. Building Simulation*, Glasgow, Scotland, 2009.
- [66] X. Yuan, A. Moser, and P. Suter. Wall functions for numerical simulation of turbulent natural convection along vertical planes. *Int. J. Heat Mass Transfer*, 36(18):4477–4485, 1993.

# Chapter 5

## Geometric modeling

### 5.1 The geometric model: A key element in building simulation

In order to describe heat fluxes or mass transfer rates between spaces by means of energy balances, the geometrical and topological structure of a building must be known in terms of the dimension, alignment and orientation of the respective building components. The object semantics define the physical properties, such as the structural and thermal characteristics. A zone model further requires the adjacencies between spaces and objects.

In the scope of building performance simulation, a geometric model is necessary, for example

- to calculate the incident solar irradiation for each surface element in terms of the local position of the sun in the sky,
- for computing of the amount of the incident short wave radiation in a geometric manner, which is absorbed by each internal surface element of a zone, for example in terms of a raytracing method,
- to derive a facet model for the determination of geometrical shape factors, which are required to calculate the net long wave radiative heat exchange between surfaces,
- to set up the thermal network in terms of a finite volume conservation approach, using solid and fluid elements,
- and to define the relative positions of and the flow paths between the pressure nodes of an artificial air pressure network for calculating the mass flow between spaces.

Surface and volume models are well-suited candidates for describing a building in terms of a computer supported three-dimensional representation of its objects, such as extrusion (sweeping) models or boundary representation schemes (b-rep). A promising trend are constraint-based parametric modeling techniques, especially if combined with so-called building information models (BIM). The following sections will briefly introduce the related thematic background.

## 5.2 Basic geometric representation of objects

For the computer supported geometric representation of three-dimensional objects, we generally distinguish between the terms geometry, topology and semantics.

- The *geometry* describes the (geometric) location of points in space, the spatial progression of curves, and the form and shape of surfaces and volumes.
- The relations between points, curves and surfaces are defined in terms of their *topology*.

Bodies of same topology may thereby have a different geometry. The topology qualitatively describes the relative positioning of geometric entities. Geometric objects may possess attributes which further describe their properties. For example, a curve radius is a geometric attribute.

Objects can be represented in terms of nodes, which are connected by a curve. A *wireframe model*, for example, defines a model only in terms of its edges, and not in terms of its surfaces. A hidden line representation cannot be derived from this representation. It is not clear, which loop of curves represents a surface; surface intersections cannot be detected. This type of representation scheme is accordingly not suited for describing a zone model, as can be seen from Figure 5.1.

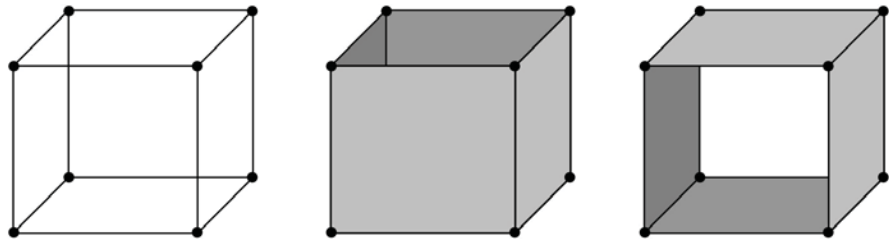


Figure 5.1: A wireframe model and its ambiguities.

*Surface models* are another dimensionally reduced geometrical representation scheme, if further attributes are added. For example, a plate can be approximated by a surface with a surface thickness as geometrical attribute. It is, however, not clear, if a structure described by a closed surface model is a rigid body or a hole within the continuum, if surfaces are not oriented in terms of their surface normal.

In the following, we will consider rigid bodies in terms of a volume model according to the definitions of BUNGARTZ ET AL. [7]. Rigid bodies are translationally and rotationally invariant, and represent three-dimensional structures. They are bounded, regular, and semi-analytic subsets of  $\mathbb{R}^3$ , and exhibit neither isolated points nor isolated or dangling edges or surfaces. For the exact mathematical description in terms of point set theory it is referred to [7], which provides a comprehensive introduction into the topic of computer graphics and the related issues.

For the geometric representation of solid bodies we further distinguish between direct and indirect geometrical representation schemes, which are introduced below.

### 5.2.1 Direct representation schemes

With a *direct* representation scheme, volume bodies are assembled in terms of geometric primitives, rather than describing the body in terms of its bounding surfaces.

Examples are:

- *Constructive Solid Geometry (CSG) models*, which hierarchically combine graphical primitives, such as cubes, cylinders, spheres, etc., in order to form a complex object. The data structure contains the spatial position (translation, rotation) and the scaling of the objects, as well as the concatenation in terms of the Boolean operators intersection, union and difference. Figure 5.2 gives an example. For visualization, the model needs to be transformed into a surface model at runtime.

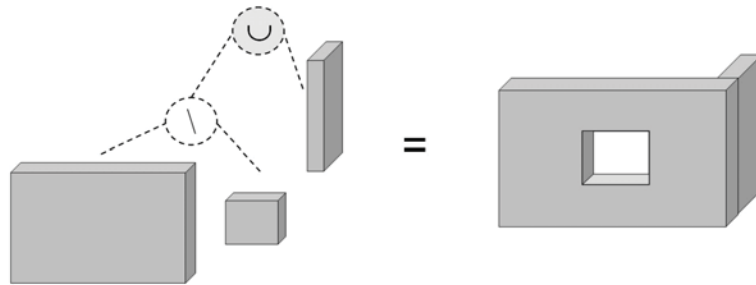


Figure 5.2: Constructive Solid Geometry (CSG) model.

- *Cell enumeration schemes*, where the space is divided into a uniform grid of cells of equal size, for example, by a set of cubic elements [7]. The two-dimensional representation is called a pixel matrix; the three-dimensional model a voxel matrix [33]. Next to the former standard scheme, block-structured cell enumeration schemes are known.
- *Spacetree-based enumeration schemes* (octree in 2D, quadtree in 3D) are hierarchical cell enumeration schemes, which efficiently reduce the memory requirements of the uniform schemes due to their tree-based structure. By enclosing geometrical objects with a

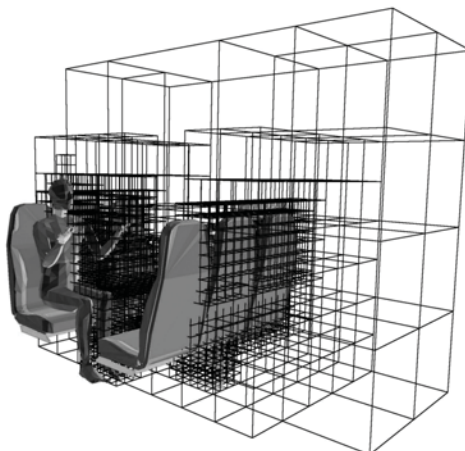


Figure 5.3: Octree representation of a train compartment [32].

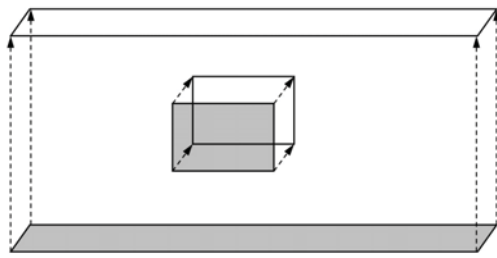


Figure 5.4: Definition of a wall in terms of a surface (ground plan) and a respective height, and of an opening in terms of the aperture and the wall thickness.

cubic bounding box, the algorithm is continued by recursively dividing this cube into eight sub-cubes with half edge-length as long as a cube intersects with the geometry or until a given resolution, i.e. a minimum edge length  $h$ , is reached [24]. An octree of depth  $t$  therefore approximates a domain with the resolution  $h = \mathcal{O}(2^{-t})$ . As shown in Figure 5.3, the technique is well-suited to approximate engineering models with complex geometries.

- *Extrusion or sweeping models* define a solid body in terms of moving a two-dimensional surface element along a displacement curve. The inscribed region gives the volume object. Extrusion models are widely used in the scope of CAD due to their simplicity (cf. Figure 5.4). For example, a wall is described in terms of its ground plan and an associated height. The modeling approach is often referred to as  $2\frac{1}{2}$ D modeling.

### 5.2.2 Indirect representation schemes

*Indirect* geometric representation schemes describe volume objects in terms of their surfaces. The surface of the respective body needs to be *closed*, surfaces must possess an *orientation* in terms of their surface normal, and surfaces are not allowed to intersect one another [21]. The basic geometric primitives are vertices, edges and faces. The graph structure [23] is therefore often referred to as *vef-graph*.

- In a *boundary representation (B-rep) scheme*, vertices (nodes) are connected by edges, edge loops define surfaces, and surfaces are connected to form solid bodies in terms of a closed surface shell. Edges or faces can be curved (e.g., using splines or NURBS), or curves or curved surfaces may be approximated in terms of polygons or facet models with plane triangles or quads. The model integrity and consistency must be maintained by the geometric modeler, i.e., the software. Most CAD software tools are based on B-rep schemes.
- The simplest representation is a *facet model*, where facets (triangles or quads) are defined in terms of their three (or four) vertices, each represented by its  $(x, y, z)$  coordinates. A basic (redundant) data structure may only contain a list of vertices, each row containing three (or four) vectors. Facet models are widely used in computer graphics for rendering and visualization purposes. The modeling accuracy can be increased by successively refining the facet model.

A B-rep scheme provides direct access to its elements. It is well-suited to serve as the basis for the zone model of a building performance simulation software tool. The data structure of a B-rep model is chosen in accordance with the topological structure of the geometric model. For a review of the different relations between the vertices, edges and faces it is referred to [7].

## 5.3 Integration and interoperability

### 5.3.1 Building information modeling (BIM)

Whereas it is the conceptual idea of Computer Aided (Geometric) Design, CA(G)D, to support the traditional draft-oriented design, the (product) model-based approach goes a significant step further. Objects include semantics and are thus more than the accumulation of points, lines and surfaces to form a geometric object [9, 10]. A building product model describes the objects itself, the relationship between these objects and their properties. Using the object-oriented paradigm, a CAD object accordingly 'knows' its properties and how it should interact with other objects.

A Building Information Model (BIM) is the digital footprint of a real building, or its draft. If the model comprises the time development of a building, the approach is called a 4D model. BIMs can describe the whole process from the design, construction, maintenance, up to its disposal, if supported by the specific implementation. For example, by connecting a CAD tool with a construction sequence planning software, a powerful tool is obtained for optimizing the building processes and logistics.

From the 3D model of a BIM, different layouts, plans and views can be derived in a consistent manner. Complex building-specific objects replace the graphical primitives and built-in rules enable the context- and scale-dependent representation of the objects. For example, in a CAD system, objects in a plan appear in a level-of-detail dependent manner, which is affected by the user selection of the scaling. Application programming interfaces of CAD tools enable to exploit these features, if simulation and planning tools are integrated, such as for the facility management, computer-aided manufacturing, computational structural mechanics, or building performance simulation. In fact, the building industry very slowly adapts to using these features in terms of an integrated design.

Examples for commercial BIM software packages are Autodesk Architecture (the former Architectural Desktop), Autodesk REVIT Architecture and REVIT Structure [3], Bentley Architecture [4], Digital Project [13], Graphisoft ArchiCAD [14], Nemetschek Allplan [22] or Tekla Structure [26].

Parametric models further enable the associative modeling of dependencies between objects, the use of (usually pre-defined) geometrical constraints between objects and their evolution history. REVIT [3], ArchiCAD [14] and Tekla Structure [26] support parametric modeling in the scope of AEC<sup>1</sup>, for example.

---

<sup>1</sup>Architecture, Engineering and Construction (AEC)

### 5.3.2 Data exchange and interoperability

The integrated building design comes along with data exchange and the need for interoperability, as a number of different disciplines are involved in the planning process, as shown in Figure 5.5. Each building is thereby a unique construction and each discipline has a different 'view' on the building product. The engineering models accordingly reflect these views in terms of different requirements and needs, which makes the interoperability task a real challenge. The related trades are, for example, the architect, the structural engineer, the building services engineer, the lighting engineer, the facility manager, and the building owner.

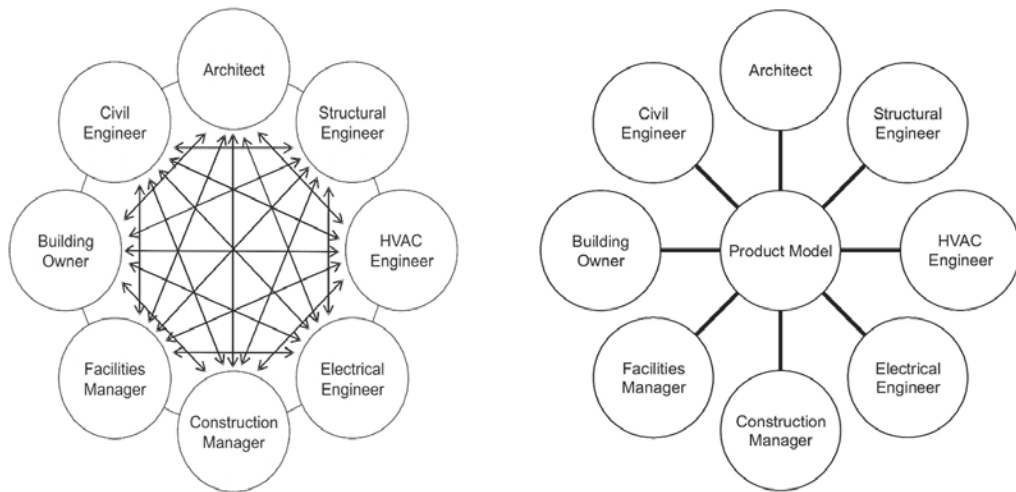


*Figure 5.5:* Data exchange in the AEC domain. Reduction of the interfaces between tools, if a standard product data model is used. Source: BuildingSMART [6].

A promising solution is the Industry Foundation Classes (IFC) Standard [20], which is a STEP-based [1] building product model standard [17, 18, 19] for the data exchange between applications. The IFC are an object-oriented, semantic model of all components, attributes, properties and relationships between objects of a building product. The class scheme provides means to describe a building product with respect to its entire life cycle [16]. The hierarchical class model is structured in terms of different layers and domain specific sub-models, such as for the HVAC, the electrical, the architectural, the FM, and the construction management domain [15].

Several software tools are certified for the IFC by the Industry Alliance for Interoperability (IAI buildingSMART) [6]. Tools for checking data for consistency are available, such as the Solibri Model Checker [25]. However, data exchange in practice is usually based on the proprietary formats of common CAD tools, and not on the IFC.

Another scheme is gbXML, the Green Building XML (extensible markup language) scheme [12]. A number of software tools support gbXML, in order to exchange building information between BIM and design and engineering analysis tools.

### 5.3.3 Integration of building performance simulation

It implies a huge effort in terms of human intervention and data interpretation to derive the zonal model for a building performance analysis from the graphical representation of the geometric objects of a conventional CAD system. Usually, a new physical or numerical model needs to be created from scratch, using the aforementioned model as the starting point within the building performance simulation software. The reason is, that (i) both models are not fully compatible in terms of the geometry and topology, and (ii) that further semantical information may not be available from the CAD system.

A zone model requires the geometric representation of the spaces in terms of the air volumes, the connection between spaces and the associated elements, such as walls, windows, etc., their type, structure and material characteristics. Next to the physical structure of the building, further details are required to perform a thermal simulation, such as concerning the infiltration and ventilation, i.e., the interaction with the HVAC domain, the type of heating and cooling system, the plant operation schedule, the occupancy in terms of the internal loads, etc. Spaces of an architecture model are usually modeled in a different way. For example, a floor slab may connect rooms throughout a whole building storey. A thermal zone would require fragmented pieces of this plate with respect to the space boundary of the respective thermal space. A decomposition algorithm is described by the author in [31], for example.

In the past years, several professional software packages integrated building performance analysis tools into their BIM products. Examples are the Bentley Energy Analysis and Simulation tool [5], the DesignBuilder software [8], which integrates EnergyPlus [28], or Autodesk Ecotect Analysis [2], which is connected with REVIT. A number of building performance simulation tools offer interfaces to BIM, such as VABI [29], which provides a REVIT interface, or the IDA Indoor Climate and Energy Software [11], which has an IFC import functionality, for example. For a full picture, it is referred to the DOE Building Energy Software Tools Directory [27].

## 5.4 A geometric model with minimum semantics using hexahedral elements

This section suggests a basic object-oriented data structure for the mathematical-physical model(s) discussed in this book. The choice of an object-oriented programming language thereby offers several advantages over procedural programming, such as operator overloading, templates, class inheritance, polymorphism and access control to variables. For a basic introduction into the topic of object-oriented modeling and numeric computing, the text book of DAOQI YANG [34] is recommended for further reading. The focus of the book is on the C++ programming language.

As indicated in Figure 5.6, the object model comprises

- the zone model itself (ZModel), which is the core model and aggregates the model geometry and topology in terms of

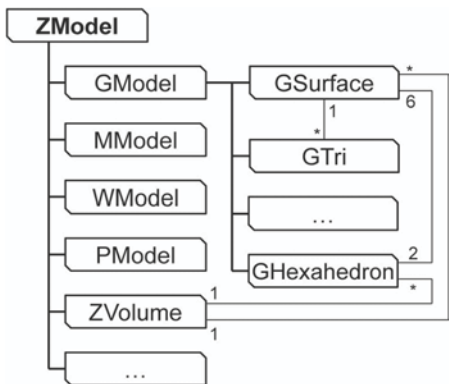


Figure 5.6: Basic UML structure of the zone model [30].

- the geometric model (GModel), which consists of hexahedral elements (GHexahedron), surface elements (GSurface), triangles (GTri), and vertices (GNode),
  - so-called (air) volume elements (ZVolume), which define the interfaces between solid and fluid elements, i.e., the space boundaries of each zone (a very important feature [31]),
  - the different material characteristics (MModel), such as the thermal (and optical) properties of fluid, solid, window elements,
  - a weather data and solar radiation processor (WModel), which provides functions to select, process, interpolate, and store weather data and to compute site specific data, such as for the solar radiation,
  - and a physical model (PModel), which implements further rational and empirical correlations, such as methods to calculate the convective heat transfer coefficients.

In the following, special emphasis is placed on the geometric class model. To keep it simple, we define elements such as walls, plates, slabs, openings, etc. in terms of plane hexahedral elements. Figure 5.7 exemplarily sketches parts of the geometric model from the point of view of a surface element. This is now explained step by step. (The character 'G' denotes that a class belongs to the geometric model.)

- **GElement** is the base element, each geometrical sub-class is derived from it. **GElement** defines the element ID and its type, for example, in terms of an enumeration in C++.
  - The class **GNode** defines a cartesian point using three double precision variables.
  - **GSurface** is a plane surface element, which is defined in terms of four *GNode* objects. The element contains a list of associated triangles. The number of triangles thereby depends on the selected resolution of the radiation model, minimum two. The surface is linked with both of its adjacent hexahedral elements. If the surface contains an opening such as a window, it is linked with the respective *GOpening* surface object. A *GSurface* contains further geometrical attributes, such as its surface normal vector, area, perimeter, slope and azimuth, for example.

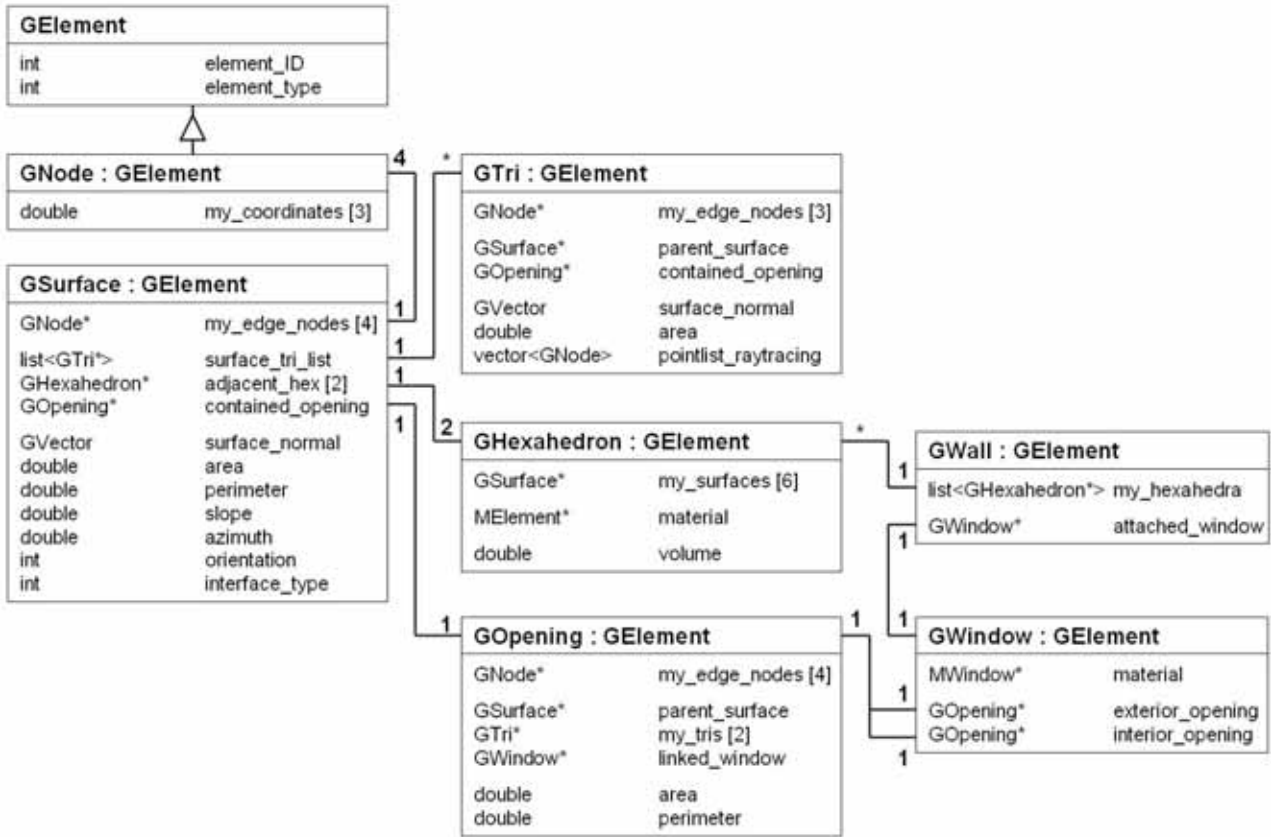


Figure 5.7: Part of the UML structure of the geometric model, which forms a part of the zone model.

- A hexahedral element, **GHexahedron**, consists of six surfaces, and is linked with its material properties, which are modeled in terms of another class, *MElement*. A hexahedral element can describe both a solid or a fluid element.
- Triangular elements, **GTri**, are spanned by three nodes, and have a link to the respective parent surface (and opening, if available). A triangular surface can be further subdivided for raytracing. If so, the respective point list is stored in terms of a static vector.
- Surfaces representing openings are defined by the **GOpening** class, which is similar to the general surface description. A *GOpening* is linked with the associated *GWindow* object, if available. For raytracing, an opening contains two tri objects, which may be further decomposed for raytracing (see above).
- The **GWindow** class accordingly aggregates the respective material characteristics in terms of the thermal and optical glazing properties described by the class *MWindow*. A window is always linked with the two surfaces of the respective openings.
- A solid wall, defined by **GWall**, comprises a list of hexahedral elements and a link to an attached window. Each wall layer is modeled by, at least, one hexahedron. In the settings of this model, each wall can contain a single window only. (The extension of the model is straightforward.)

*GVector* is thereby a class implementing basic vector operations, *<vector>* and *<list>* are basic template classes providing the respective data containers. Figure 5.8 shows the different objects and their interrelations.

Each class contains several functions to access the member variables and to calculate the respective geometrical and physical quantities. For example, the *GSurface* class provides a public function to compute the solar surface incidence angle and the geometric transformation factor to calculate the amount of beam radiation incident to this surface with respect to the current weather data set.

The geometric model, i.e., an instance of the *GModel* class, contains maps (or lists) of all surfaces, hexahedrons, solid wall elements, window elements, tri elements (e.g., for the view factor computation), and floor/ceiling elements of the respective zone. Member functions provide means to add, access (modify), and delete items.

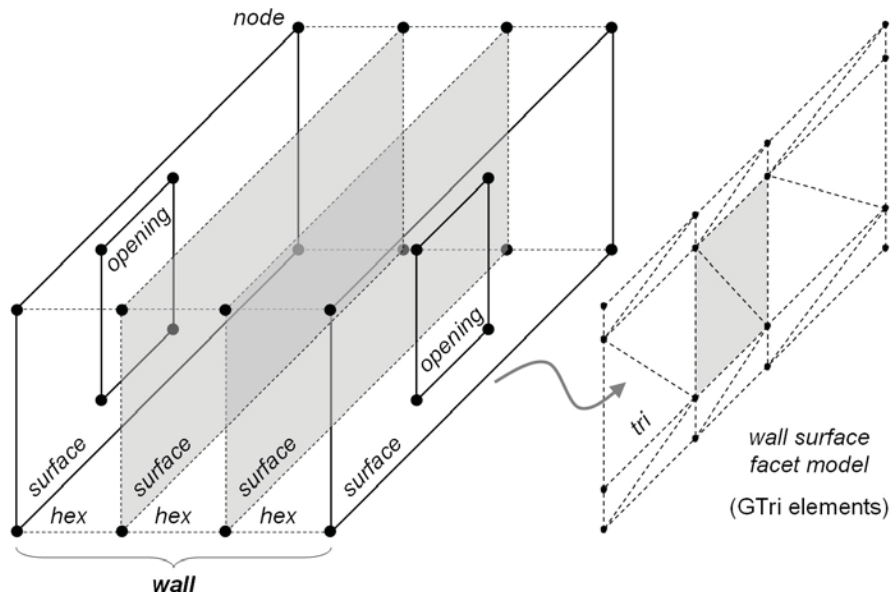


Figure 5.8: A wall comprises a set of hexahedral elements, each consisting of six surfaces with four nodes each, and a list of tris. A window is thereby represented by two surfaces of type *GOpening*, which are decomposed into two tris.

## 5.5 References

- [1] R. Anderl and D. Trippner. *STEP – Standard for the exchange of product model data*. Teubner Verlag, 2000.
- [2] Autodesk, Inc. Autodesk Ecotect Analysis, 2009. <http://www.autodesk.com>.
- [3] Autodesk, Inc. Autodesk REVIT, 2009. <http://www.autodesk.com>.
- [4] Bentley Systems, Inc. Bentley Architecture, 2009. <http://www.bentley.com>.

- [5] Bentley Systems, Inc. Bentley Energy Analysis and Simulation, 2009. <http://www.bentley.com>.
- [6] buildingSMART. Industry Alliance for Interoperability (IAI), 2009. <http://www.buildingsmart.de>.
- [7] H.-J. Bungartz, M. Griebel, and Ch. Zenger. *Introduction to computer graphics*. Charles River Media, Inc., 2nd edition, 2004.
- [8] DesignBuilder Software Ltd. DesignBuilder, 2009. <http://www.designbuilder.co.uk>.
- [9] C.M. Eastman. *Computer Environments Supporting Design and Construction*. CRC Press LLC, 1999.
- [10] C.M. Eastman, P. Teicholz, R. Sacks, and K. Liston. *BIM Handbook: A guide to building information modeling for owners, managers, designers, engineers, and contractors*. John Wiley & Sons, 2008.
- [11] EQUA Simulation AB. IDA Indoor Climate and Energy Software, 2009. <http://www.equa.se>.
- [12] gbXML. Green Building XML scheme, 2009. <http://www.gbxml.org>.
- [13] Gehry Technologies, Inc. Digital Project, 2009. <http://www.gehrytechnologies.com>.
- [14] Graphisoft. ArchiCAD, 2009. <http://www.graphisoft.de>.
- [15] International Allicance for Interoperability (IAI). *IFC Technical guide for release 2x*. <http://iaiweb.lbl.gov>, 2000.
- [16] International Allicance for Interoperability (IAI). *IFC Release 2x Specification (online)*. <http://www.iai-ev.de/spezifikation/Ifc2x>, 2004.
- [17] ISO 10303 (STEP) – Part 1. *Industrial automation systems and integration – Product data representation and exchange – Part 1: Overview and fundamental principles*. International Organization for Standardization, 1994.
- [18] ISO 10303 (STEP) – Part 11. *Industrial automation systems and integration – Product data representation and exchange – Part 11: Description methods: The EXPRESS language reference manual*. International Organization for Standardization, 1994.
- [19] ISO 10303 (STEP) – Part 21. *Industrial automation systems and integration – Product data representation and exchange – Part 21: Implementation methods: Clear text encoding of the exchange structure*. International Organization for Standardization, 2002.
- [20] ISO/PAS 16739. *IAI Industry Foundation Classes 2x Platform Specification*. International Organization for Standardization, 1994.
- [21] M. Mäntylä. *An introduction to solid modeling*. Computer Science Press, 1988.
- [22] Nemetschek Group. Nemetschek Allplan, 2009. <http://www.nemetschek.de>.

- [23] P.J. Pahl and R. Damrath. *Mathematische Grundlagen der Ingenieurinformatik*. Springer Verlag, 2000.
- [24] H. Samet. The quadtree and related hierarchical data structures. *ACM Computing Surveys*, 16(2):187–260, 1984.
- [25] Solibri. Model Checker, 2009. <http://www.solibri.com>.
- [26] Tekla. Tekla Structures Software, 2009. <http://www.tekla.com>.
- [27] US. Department of Energy. Building Energy Software Tools Directory, 2009. [http://http://eere.energy.gov/buildings/tools\\_directory/](http://http://eere.energy.gov/buildings/tools_directory/).
- [28] US Department of Energy (DOE). EnergyPlus Energy Simulation Software, 2009. <http://apps1.eere.energy.gov/buildings/energyplus/>.
- [29] VABI Software BV, 2009. <http://www.vabi.nl>.
- [30] C. van Treeck, J. Frisch, M. Egger, and E. Rank. Model-adaptive analysis of indoor thermal comfort. In *Building Simulation 2009*, Glasgow, Scotland, 2009.
- [31] C. van Treeck and E. Rank. Dimensional reduction of 3d building models using graph theory and its application in building energy simulation. *Engineering with Computers*, 23:109–122, 2006.
- [32] C. van Treeck, P. Wenisch, A. Borrmann, M. Pfaffinger, O. Wenisch, and E. Rank. ComfSim - Interaktive Simulation des thermischen Komforts in Innenräumen auf Höchstleistungsrechnern. *Bauphysik*, 29(1):2–7, 2007. DOI: 10.1002/bapi.200710000.
- [33] P. Wenisch and O. Wenisch. Fast octree-based voxelization of 3D boundary representation objects. Technical report, Lehrstuhl für Bauinformatik, Technische Universität München, 2004.
- [34] Daoqi Yang. *C++ and object-oriented numeric computing for scientists and engineers*. Springer-Verlag New York, Inc., 2001.

# Chapter 6

## Heat conduction in solids

### 6.1 The Fourier heat equation

The first law of thermodynamics states that the energy remains constant in a closed system [1, 3]. It follows for the energy balance of a control volume element, that the internal energy equals the amount of heat which is exchanged via the boundary, as the energy is conserved within the system. For the derivation of the heat equation we consider for the sake of simplicity the transient heat conduction problem in a one-dimensional manner for the small volume element  $\Delta V$  sketched in Figure 6.1. For the uniaxial heat flux in  $x$ -direction, we therefore balance the heat transmission through boundaries at  $x = 0$  and  $x = \Delta x$  with respect to the change of the heat quantity within the volume element. We assume the other surfaces being adiabatically connected.

The change of the heat quantity  $Q$  [ $J$ ] within volume element  $\Delta V$  [ $m^3$ ] over time  $t$  with temperature  $T$  [ $K$ ] is given by

$$\frac{\partial Q}{\partial t} = \varrho \Delta V c_p \frac{\partial T}{\partial t} = m c_p \frac{\partial T}{\partial t} , \quad (6.1)$$

where  $\varrho$  [ $kg/m^3$ ] is the density,  $m$  [ $kg$ ] the mass, and  $c_p$  [ $kg/(m^3 K)$ ] the constant pressure heat

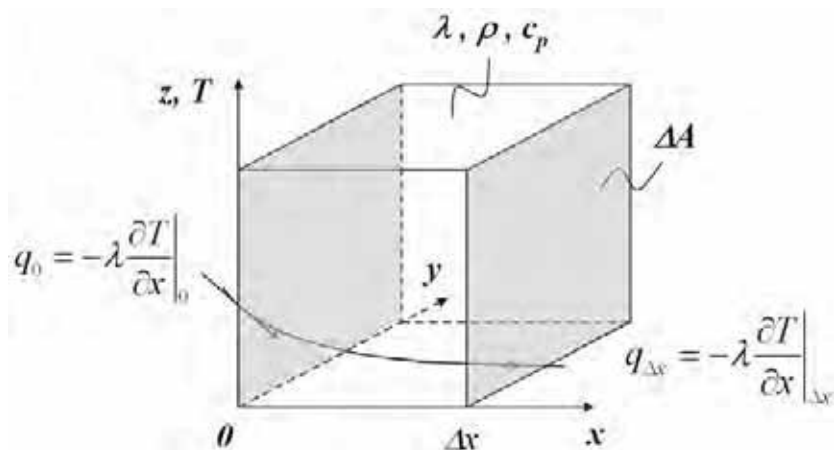


Figure 6.1: Uniaxial heat conduction in  $x$ -direction within volume element  $\Delta V$ .

capacity. The heat flux density  $q$  due to conduction in solids is described in terms of Fourier's equation

$$q = -\lambda \frac{\partial T}{\partial x} = -\lambda \text{grad}(T) , \quad (6.2)$$

where  $\lambda [W/(m K)]$  is the thermal conductivity.

For the energy balance of the volume element  $\Delta V$  for uniaxial heat conduction in  $x$ -direction with internal heat source  $\dot{q}$ , we get

$$(q_0 - q_{\Delta x}) \Delta A = \left( -\lambda \frac{\partial T}{\partial x} \Big|_0 + \lambda \frac{\partial T}{\partial x} \Big|_{\Delta x} \right) \Delta A = \frac{\partial Q}{\partial t} + \Delta V \dot{q} = \varrho \Delta V c_p \frac{\partial T}{\partial t} + \Delta V \dot{q} , \quad (6.3)$$

where  $\Delta A [m^2]$  is the area of the respective bounding surface. If we divide Equation (6.3) by  $\Delta V = \Delta A \cdot \Delta x$ , and if we perform the limiting case  $\Delta x \rightarrow 0$ , we obtain the partial differential equation for uniaxial heat conduction

$$\varrho c_p \frac{\partial T}{\partial t} - \frac{\partial}{\partial x} \left( \lambda \frac{\partial T}{\partial x} \right) = \dot{q} . \quad (6.4)$$

If we further assume, that  $\lambda$  is constant within the element, and after dividing by  $\varrho c_p$ , we can write

$$\frac{\partial T}{\partial t} - \frac{\lambda}{\varrho c_p} \frac{\partial^2 T}{\partial x^2} = \frac{\partial T}{\partial t} - \alpha \frac{\partial^2 T}{\partial x^2} = \frac{\dot{q}}{\varrho c_p} , \quad (6.5)$$

where  $\alpha = \lambda / (\varrho c_p) [m^2/s]$  is called the thermal diffusivity. The extension of the equations to two and three dimensions is straightforward.

## 6.2 Finite difference discretization in space and time

### 6.2.1 Numerical discretization

The partial differential equations (6.4) and (6.5) describe the uniaxial heat conduction within solids in terms of a continuous problem. By *numerical discretization* the continuous problem is solved at a number of finite points or elements. A discrete formulation is therefore an approximation of a partial differential equation or a set of partial differential equations, which is transformed into an algebraic equation system [7].

The **convergence**, **consistency** and **stability** are important properties of a numerical discretization approach. Following the summary of OERTEL [9], we thereby distinguish between

- the exact solution of a partial differential equation (PDE),
- the exact solution of a discrete equation, and
- the numerically approximated solution.

The three solutions are not identical, as the numerical approximation introduces *round-off* and *discretization errors*. Furthermore, the mathematical formulation of a physical problem may introduce a *modeling error*.

The *consistency* of a numerical scheme describes the order of magnitude of the error between the exact solution of the PDE and the exact solution of the discrete equation. The accumulation of truncation errors influences the *stability* of a solution in terms of the deviation of the exact solution of the discrete equation from the numerical approximation.

The *convergence rate* describes the properties of the numerical scheme in terms of how fast the numerical error decreases, if the number of discretization points is increased. Increasing the degrees of freedom comes along with growing computational effort. A method is *consistent*, if the discrete equations become the PDE again, when the finite step size in space and time approaches zero in the limiting case as in the continuous formulation.

The section on-hand introduces the so-called *finite difference method (FDM)*, a method which is based on the principle of Taylor series expansions [8, 11]. Other well-known numerical methods are finite volume methods [6, 9, 10] and finite element methods [2, 5, 12, 13, 14].

### 6.2.2 Forward, backward and central differences

As indicated in Figure 6.2, both derivatives, the time and the spatial derivative,  $\partial T/\partial t$  and  $\partial T/\partial x$ , need to be transformed into *difference* expressions. Equation (6.5) thereby contains a first order derivative for the time and a second order derivative with respect to the space.

Both intervals, time and space, are accordingly decomposed into subintervals. The finite difference method requires a structured mesh with a high degree of regularity [8]. In the settings of this book, we use a uniform grid spacing, i.e., a fixed time step size  $\Delta t$  and a fixed grid spacing  $\Delta x$ , which are determined prior to the computation. The differential equation is only evaluated at these discrete locations, which are, more generally, intersections of rectilinear

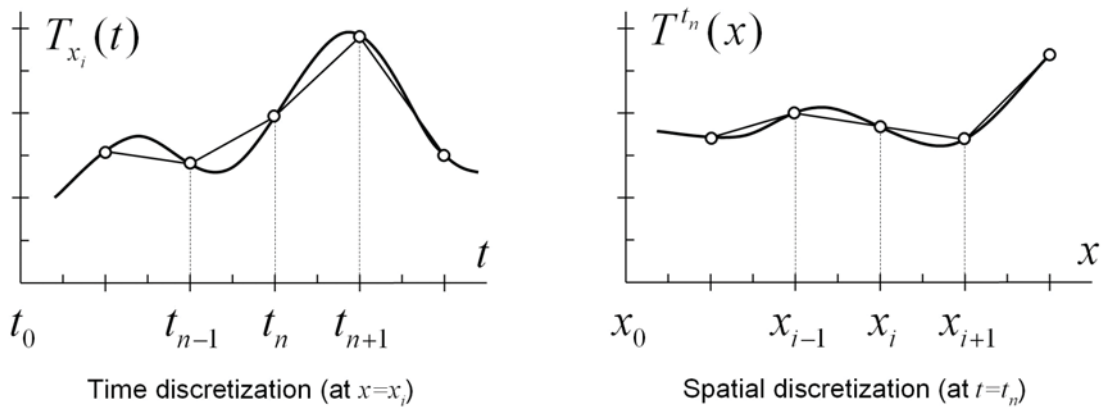


Figure 6.2: Discretization in time of the temperature function  $T(t)$  for a discrete location  $x_i$  and spatial discretization of  $T(x)$  with respect to a discrete time  $t_n$ .

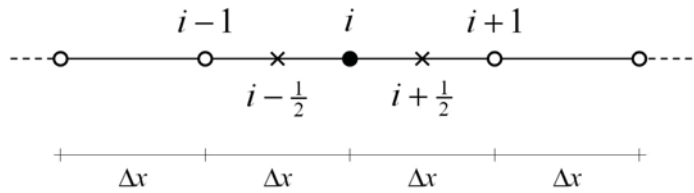


Figure 6.3: One-dimensional grid with uniform spacing  $\Delta x$ .

or curved lines. Modern numerical techniques allow for an adaptive refinement of the model resolution. Therefore, the error is estimated and the mesh or grid is refined only at those locations which violate a given accuracy constraint.

Following the general definition of the derivative [4] of a function  $T(x)$ ,

$$\frac{\partial T}{\partial x} = \lim_{\Delta x \rightarrow 0} \frac{T(x + \Delta x) - T(x)}{\Delta x}, \quad (6.6)$$

we substitute the derivative by the ratio of two differences, such as the *forward difference*

$$\left. \frac{\partial T}{\partial x} \right|_{i+\frac{1}{2}} \approx \frac{T_{i+1} - T_i}{\Delta x}, \quad (6.7)$$

which is in fact a first-order approximation in  $\Delta x$ , as the higher order terms in the respective Taylor series expansion are neglected. The truncation error  $\mathcal{O}(\Delta x)$  accordingly reduces by the first power in  $\Delta x$ . Similarly, the *backward difference* formula is

$$\left. \frac{\partial T}{\partial x} \right|_{i-\frac{1}{2}} \approx \frac{T_i - T_{i-1}}{\Delta x}. \quad (6.8)$$

As indicated in Figure 6.3, the terms are evaluated at  $N$  discrete locations  $x + \Delta x/2$  and  $x - \Delta x/2$ , with  $T_i = T(x)$ ,  $T_{i+1} = T(x + \Delta x)$ ,  $T_{i-1} = T(x - \Delta x)$ , and  $i = 1, \dots, N$ , respectively.

With the *central difference* formula,

$$\left. \frac{\partial T}{\partial x} \right|_i \approx \frac{T_{i+1} - T_{i-1}}{2\Delta x} \quad (6.9)$$

a second order approximation is obtained for the derivative with a truncation error  $\mathcal{O}(\Delta x^2)$ .

To approximate the second order partial derivative  $\partial^2 T / \partial x^2$ , we insert the forward (6.7) and the backward difference (6.8) into the central difference formula (6.9), i.e., we write the central difference with half step size with respect to the first order derivatives at  $x + \Delta x/2$  and  $x - \Delta x/2$ ,

$$\left. \frac{\partial^2 T}{\partial x^2} \right|_i \approx \frac{\left. \frac{\partial T}{\partial x} \right|_{i-\frac{1}{2}} - \left. \frac{\partial T}{\partial x} \right|_{i+\frac{1}{2}}}{\Delta x} \approx \frac{T_{i+1} - 2T_i + T_{i-1}}{(\Delta x)^2}, \quad (6.10)$$

and obtain a scheme of second-order accuracy, as it is explained in the next section in detail.

Usually, the time discretization is written in terms of the first-order forward difference

$$\frac{\partial T}{\partial t} \Big|^{n+\frac{1}{2}} \approx \frac{T^{n+1} - T^n}{\Delta t} . \quad (6.11)$$

Difference formulae for higher order derivatives, and a detailed review on the fundamentals of numerical discretization can be found in the textbook of HIRSCH [8], which is recommended for further reading.

### 6.2.3 Convergence analysis for steady-state conditions

The approximation of the partial differential equation with a finite difference scheme introduces a *discretization or truncation error*. In order to determine the order of magnitude of this error, we perform a Taylor series expansion of the temperature  $T$  around a reference point  $x_p$ , where we assume to know the exact solution  $T(x_p)$ . By inserting this expression into the discrete equation, we will be able to estimate the spatial discretization error.

If we substitute the second order spatial derivative  $\partial^2 T / \partial x^2$  in Equation (6.5) by the central difference expression (6.10) and rewrite the equation for steady state conditions, i.e.,  $\partial T / \partial t = 0$ , we get

$$\frac{1}{(\Delta x)^2} (T_{i-1} - 2T_i + T_{i+1}) = \frac{\dot{q}_i}{\lambda} . \quad (6.12)$$

We insert the (unknown) *exact* solution  $T(x_p)$  at  $x_p$  into the above equation and get

$$\frac{1}{(\Delta x)^2} (T(x_p - \Delta x) - 2T(x_p) + T(x_p + \Delta x)) - \frac{\dot{q}_i}{\lambda} = d_p \neq 0 , \quad (6.13)$$

where  $d_p$  is the spatial discretization error. Inserting the Taylor series expansion of  $T$  with respect to  $(x_p)$ ,

$$T(x_p \pm \Delta x) = T \pm \Delta x \frac{\partial T}{\partial x} + \frac{1}{2} \Delta x^2 \frac{\partial^2 T}{\partial x^2} \pm \frac{1}{6} \Delta x^3 \frac{\partial^3 T}{\partial x^3} + \frac{1}{24} \Delta x^4 \frac{\partial^4 T}{\partial x^4} \pm \dots , \quad (6.14)$$

into the former discrete Equation (6.13), we obtain

$$d_p = \underbrace{\left[ \frac{\partial^2 T(x_p)}{\partial x^2} - \frac{\dot{q}_i}{\lambda} \right]}_{=0 \text{ (exact solution)}} + \frac{\Delta x^2}{12} \left[ \frac{\partial^4 T(x_p)}{\partial x^4} \right] + \dots \quad (6.15)$$

as all other terms are canceled out. It follows, that

$$|d_p| \leq c \Delta x^2 \quad \text{if} \quad c \geq \max \left\{ \left| \frac{1}{12} \left( \frac{\partial^4 T}{\partial x^4} \right) \right| \right\} \quad (6.16)$$

for all  $x$  of the domain. In other words, this means the following. If the exact solution is four times continuously differentiable, and if the fourth derivative is bounded with respect to its absolute value, the discretization error reduces by four times if the mesh size  $\Delta x$  is

bisected. The truncation error is accordingly of the order  $\mathcal{O}(\Delta x^2)$ . The same applies for the approximation error  $e_i = T(x_i) - T_i$ . In the maximum norm, the error is

$$\|e\|_{\max} = \max\{|e_i|, i = 1, \dots, N\} \leq c \Delta x^2 , \quad (6.17)$$

and in the Euclidean norm we obtain

$$\|e\|_2 = \left( \sum_{i=1}^N e_i^2 \right)^{1/2} \leq c \Delta x . \quad (6.18)$$

## 6.3 Forward Euler time integration

### 6.3.1 First order time discretization

Substituting the partial derivatives in Equation (6.5) for the uniaxial heat conduction with constant heat conductivity by the above described finite difference formulae, i.e., by the central difference formula (6.10) for the second order spatial derivative and by the forward difference formula (6.11) for the time, we get

$$\frac{1}{\Delta t} (T_i^{n+1} - T_i^n) - \alpha \frac{1}{(\Delta x)^2} (T_{i-1}^n - 2T_i^n + T_{i+1}^n) = \frac{\dot{q}_i}{\varrho c_p} , \quad (6.19)$$

which is known as *forward Euler* time integration method. Forward means, that the quantities at time row ( $n$ ) are assumed to be known from the previous iteration. If we rewrite Equation (6.19) by grouping the unknown term of the future time row ( $n + 1$ ) at the left-hand-side,

$$T_i^{n+1} = T_i^n + \Delta t \left[ \alpha \frac{1}{(\Delta x)^2} (T_{i-1}^n - 2T_i^n + T_{i+1}^n) + \frac{\dot{q}_i}{\varrho c_p} \right] , \quad (6.20)$$

we get an explicit evolution scheme to compute the future time rows on a successive time step basis. The solution method is therefore also called an *explicit* method.

The solution method requires initial conditions for  $T(x, t)$  at  $t = t_0$  and boundary conditions at  $x = x_0$  and  $x = x_{N+1}$ , respectively. If these conditions are known, values at the next time row can be computed on a per time step basis in a straightforward manner.

The truncation error of the method is of first order in time and of second order in space,  $\mathcal{O}(\Delta t, \Delta x^2)$ .

### 6.3.2 Stability criteria

Explicit methods are prone to oscillations and are constrained by several stability criteria. If we introduce the mesh *Fourier number*

$$Fo := \frac{\alpha \Delta t}{(\Delta x)^2} , \quad (6.21)$$

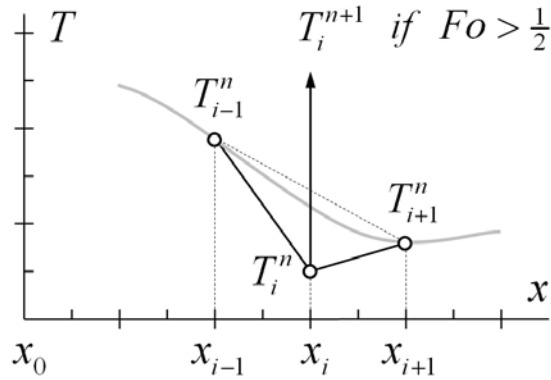


Figure 6.4: Violation of the stability criterion  $Fo < 1/2$  causes overshoot of the solution  $T_i^{n+1}$  for the future time row.

and rewrite Equation (6.19) accordingly,

$$T_i^{n+1} = T_i^n + Fo (T_{i-1}^n - 2T_i^n + T_{i+1}^n) = (1 - 2Fo)T_i^n + 2Fo \frac{T_{i-1}^n + T_{i+1}^n}{2}, \quad (6.22)$$

we find the following behavior:

$$\begin{aligned} \text{If } & \quad Fo = 0 \quad \text{then} \quad T_i^{n+1} = T_i^n, \\ \text{if } & \quad Fo = \frac{1}{2} \quad \text{then} \quad T_i^{n+1} = \frac{1}{2}(T_{i-1}^n + T_{i+1}^n), \quad \text{and} \\ \text{if } & \quad 0 < Fo < \frac{1}{2} \quad \text{then} \quad |T_i^n| \leq |T_i^{n+1}| \leq \frac{1}{2}|T_{i-1}^n + T_{i+1}^n|, \\ \text{but if } & \quad Fo > \frac{1}{2} \quad \text{then} \quad T_i^{n+1} \text{ overshoots}. \end{aligned} \quad (6.23)$$

Figure 6.4 shows this problem graphically. The observation implies, that the Fourier number is accordingly restricted to

$$Fo \leq \frac{1}{2} \quad (6.24)$$

and, thus, the temporal or spatial resolution is constrained by

$$\Delta t \leq \frac{(\Delta x)^2}{2\alpha} \quad \text{or} \quad \Delta x \leq \sqrt{2\alpha \Delta t}. \quad (6.25)$$

Note, that this criterion is only valid for the one-dimensional case. The coefficients change for the two- and three-dimensional cases.

If the stability criterion is violated, due to the overshoot the solution vector oscillates after a few iterations and unfeasible results are obtained beyond physics. Explicit methods are well-suited to capture transient effects but require, at the same time, a large number of time steps to converge.

### 6.3.3 Example: Explicit solution

The following example demonstrates the implementation of the forward Euler solution algorithm. We consider the uniaxial heat conduction in the solid wall brick element sketched in Figure 6.5. The component is discretized using  $N = 8$  internal nodes plus 2 nodes at the internal and external surfaces, respectively, in total 9 layers. With the overall thickness  $d = 0.365 \text{ m}$ , we obtain  $\Delta x = 0.04 \text{ m}$ .

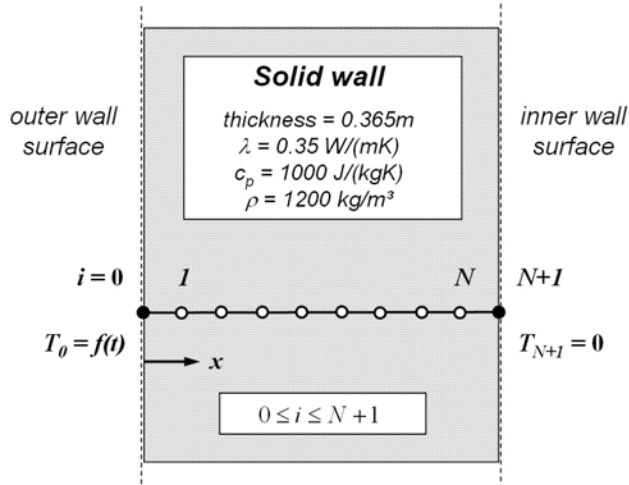


Figure 6.5: Uniaxial discretization of the wall element and physical properties.

The material properties are assumed to be homogeneous, we set the thermal conductivity  $\lambda = 0.35 \text{ W}/(\text{mK})$ , the heat capacity  $c_p = 1000 \text{ J}/(\text{kgK})$ , and the density  $\varrho = 1200 \text{ kg}/\text{m}^3$ . The internal boundary condition shall be fixed at  $T(x = 0.365, t) = T_{N+1}(t) = 0$  and for the external boundary condition  $T(x = 0, t) = T_0(t)$  we assume the sinusoidal function

$$T(x = 0, t) = 1 + \sin\left(\frac{4\pi t}{t_{end}}\right) + \frac{1}{2} \sin\left(\frac{8\pi t}{t_{end}}\right) . \quad (6.26)$$

The function is plotted in Figure 6.6 for the considered two-day simulation period, i.e.,  $t_{end} = 2 \cdot 24 \cdot 60 \cdot 60 = 172800$  seconds.

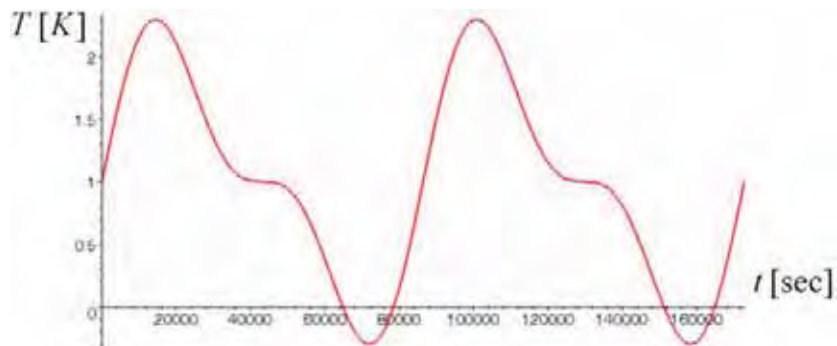


Figure 6.6: Boundary condition  $T(x = 0)$  for the simulation period of two days (172800 seconds).

A well-suited tool for a computer implementation is, for example, a computer algebra simulation package, such as Maple, Mathematica or Matlab. The sequence of operations and the main time loop of the Algorithm (1) is sketched below:

---

**Algorithm A-1** Explicit (forward) Euler solution algorithm.

---

```

1: initialization
2: for all  $i$  from 0 to  $N + 1$  do
3:    $T^{old}[i] = 0$ 
4: end for
5: the time loop
6: for  $t$  from 0 to  $timesteps - 1$  do
7:   set boundary conditions
8:    $T[0] = T_0(t \cdot \Delta t)$ 
9:    $T[N + 1] = 0$ 
10:  compute internal nodes
11:  for  $i$  from 1 to  $N$  do
12:     $T[i] = Fo \cdot (T^{old}[i - 1] - 2 \cdot T^{old}[i] + T^{old}[i + 1])$ 
13:  end for
14:  copy temperature vector
15:  for all  $i$  from 0 to  $N + 1$  do
16:     $T^{old}[i] = T[i]$ 
17:  end for
18: end for

```

---

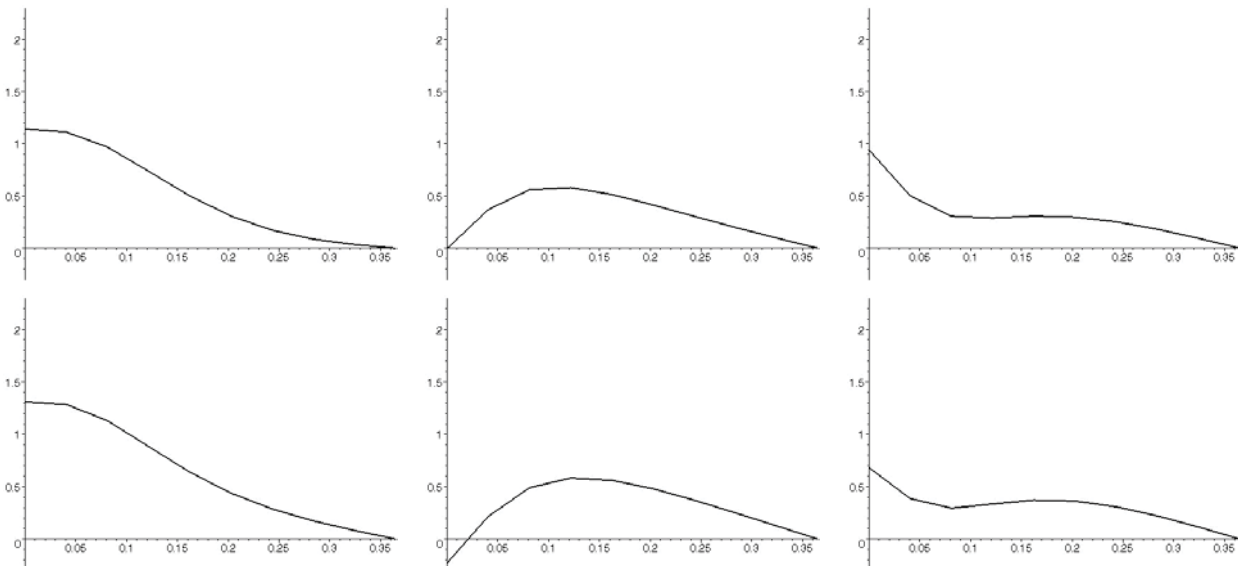


*Figure 6.7:* Simulation sequence using the forward Euler scheme with  $Fo = 0.250 < 1/2$ . The x-axis indicates the spatial position in x direction, the y-axis the temperature values within the element.

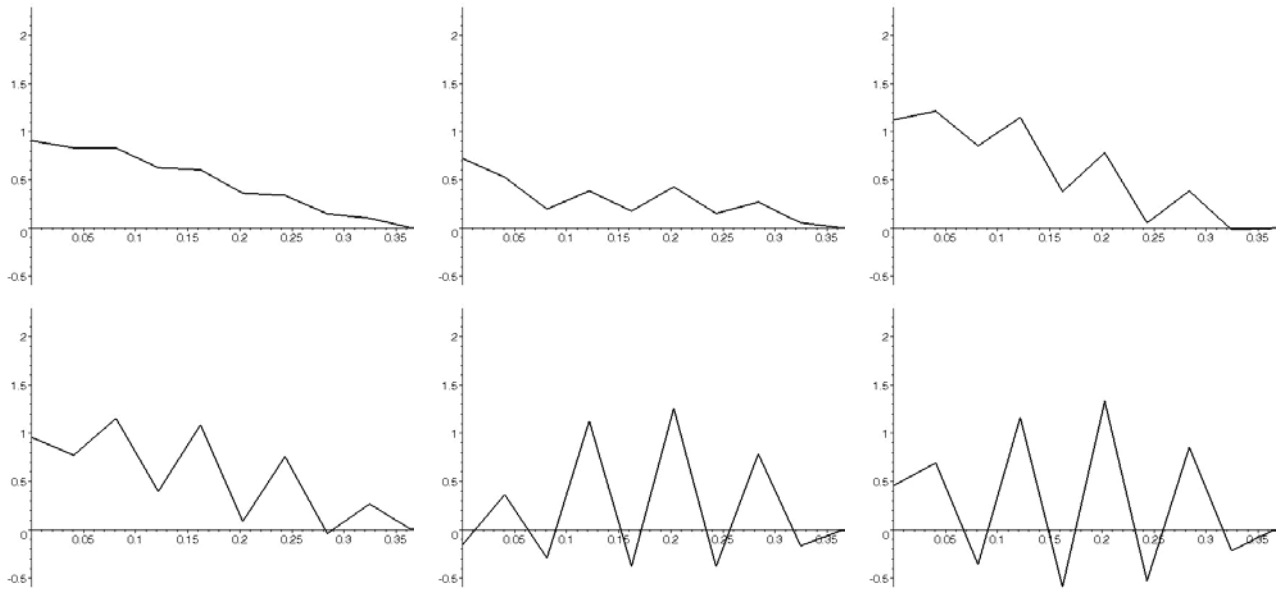


*Figure 6.8:* Simulation sequence using the forward Euler scheme with  $Fo = 0.535 > 1/2$ . The x-axis indicates the spatial position in x direction, the y-axis the temperature values within the element.

The application is demonstrated for the following two cases:

- **Case A.** The time step size is set to  $\Delta t = 1410 \text{ sec} = 23.5 \text{ min}$ , which results in 122 time steps, and in the Fourier number  $Fo = 0.25$ .
- **Case B.** The time step size is set to  $\Delta t = 3017 \text{ sec} = 50.3 \text{ min}$ , which results in 57 time steps, and in the Fourier number  $Fo = 0.535$ .

Figure 6.7 presents some screenshots of the simulation sequence for Case A, and Figure 6.8 for Case B. The solution of the first case is smooth, whereas the solution of the second case oscillates, as the mesh Fourier number exceeds the critical value of  $1/2$ . The amplitude of these oscillations is growing during the computation, and yet after a few iterations, the solution becomes physically irrelevant.

## 6.4 Backward Euler time integration

### 6.4.1 First order time discretization

With the forward Euler scheme (6.19), the solution is calculated in an explicit manner on a per time step basis, as the coefficients are related to the previous (known) time row ( $n$ ). The scheme does therefore not require to solve an equation set.

If we relate the temperature values to the unknown future time row ( $n + 1$ ), we get

$$\frac{1}{\Delta t} (T_i^{n+1} - T_i^n) - \alpha \frac{1}{(\Delta x)^2} (T_{i-1}^{n+1} - 2T_i^{n+1} + T_{i+1}^{n+1}) = \frac{\dot{q}_i}{\rho c_p} \quad (6.27)$$

for the *backward Euler* time integration. Grouping again unknown terms on the left-hand-side, and known terms on the right-hand-side, we obtain

$$-\frac{\alpha}{(\Delta x)^2} T_{i-1}^{n+1} + \left( \frac{1}{\Delta t} + \frac{2\alpha}{(\Delta x)^2} \right) T_i^{n+1} - \frac{\alpha}{(\Delta x)^2} T_{i+1}^{n+1} = \frac{1}{\Delta t} T_i^n + \frac{\dot{q}_i}{\varrho c_p} . \quad (6.28)$$

As the temperature values at time row  $(n+1)$  are unknown and depend on each other, we now have to solve an equation set

$$\mathbf{A} \cdot \mathbf{x}^{(n+1)} = \mathbf{b}^{(n)} \quad (6.29)$$

of  $N$  equations and unknowns for each time step.  $\mathbf{A}$  is the coefficient matrix,

$$\mathbf{x}^{(n+1)} = (T_1^{n+1}, T_2^{n+1}, T_3^{n+1}, \dots, T_N^{n+1})^T$$

is the temperature vector at the future time row  $(n+1)$ , and  $\mathbf{b}$  are the known terms from time row  $(n)$  on the right-hand-side, where  $T^0$  and  $T^{N+1}$  are given boundary conditions.

The *implicit* method is unconditionally stable but comes along with increased computational effort. It principally allows for choosing fairly large time step sizes  $\Delta t$ , which are only constrained by the physical resolution. The accuracy of the backward Euler method is, again, of first order in time and of second order in space,  $\mathcal{O}(\Delta t, \Delta x^2)$ . If nodes are ordered in a successive manner, the coefficient matrix  $\mathbf{A}$  is of band structure type, which can be utilized by the equation solving algorithm.

### 6.4.2 Example: Implicit solution

We consider the example from Section 6.3.3 with the same properties, spatial discretization and boundary conditions. The simulation is repeated with the settings of Case B with  $Fo = 0.535 > 1/2$ , but now with the implicit backward Euler solution procedure shown in Algorithm 2.

Figure 6.9 details parts of the simulation sequence. The solution is smooth and does not show oscillations any more. A drawback of the method is, however, that the equation set is solved for every time step which introduces more computational load compared to the other case.

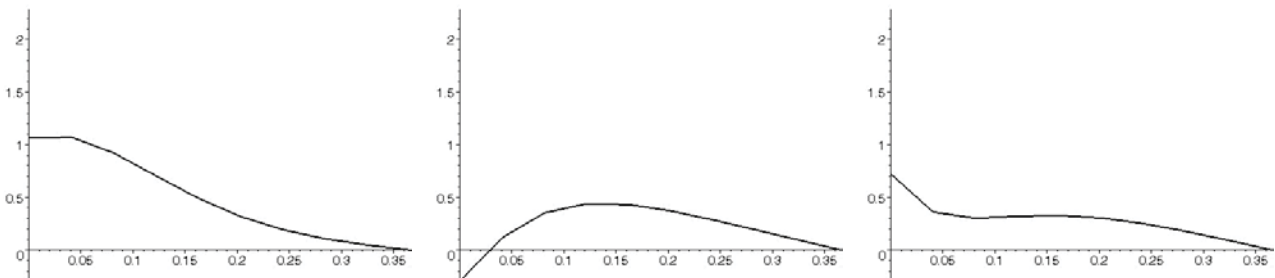


*Figure 6.9:* Simulation sequence using the backward Euler scheme with  $Fo = 0.535 > 1/2$ . The x-axis indicates the spatial position in x direction, the y-axis the temperature values within the element.

---

**Algorithm A-2** Implicit (backward) Euler solution algorithm.

---

```

1: initialization
2: for all  $i$  from 0 to  $N + 1$  do
3:    $T^{old}[i] = 0$ 
4: end for
5: the time loop
6: for  $t$  from 0 to  $timesteps - 1$  do
7:   set boundary conditions
8:    $T[0] = T_0(t \cdot \Delta t)$ 
9:    $T[N + 1] = 0$ 
10:  assemble and solve the equation set (one equation for each internal node)
11:  for  $i$  from 1 to  $N$  do
12:    EQUATION $[i] := T[i] = Fo \cdot (T[i - 1] - 2 \cdot T[i] + T[i + 1]) + T^{old}[i]$ 
13:  end for
14:  solve(EQUATION $[i], T[i]$ ) ,  $i = 1 \dots N$ 
15:  copy temperature vector
16:  for all  $i$  from 0 to  $N + 1$  do
17:     $T^{old}[i] = T[i]$ 
18:  end for
19: end for

```

---

## 6.5 Other time integration methods

The accuracy of both the forward and the backward Euler time integration is of first order in time,  $\mathcal{O}(\Delta t)$ . If both schemes are mixed, a *semi-implicit* method is obtained, which is called *Crank-Nicholson* time integration. The formulation, which averages the spatial derivatives,

$$\frac{1}{\Delta t} (T_i^{n+1} - T_i^n) - \alpha \frac{T_{i-1}^n - 2T_i^n + T_{i+1}^n + T_{i-1}^{n+1} - 2T_i^{n+1} + T_{i+1}^{n+1}}{2(\Delta x)^2} = \frac{\dot{q}_i^n + \dot{q}_i^{n+1}}{2\varrho c_p} , \quad (6.30)$$

is of second order accuracy in time, but still requires fairly small time steps to guarantee stability.

Another schemes is, for example, the *Adams-Basforth approach*, which is an explicit method that makes use of higher order difference terms, comes along with an increased memory use and computational overhead than the Euler approach, but considerably increases the accuracy. Other approaches are *predictor-corrector methods*, or high-order *Runge-Kutta methods*. At this point, the interested reader is referred to [8, 9, 11, 12].

## 6.6 References

- [1] D. Baehr and K. Stephan. *Wärme- und Stoffübertragung*. Springer Verlag, 3rd edition, 1998.

- [2] K.J. Bathe. *Finite element procedures*. Prentice Hall, 1996.
- [3] A. Bejan. *Convection heat transfer*. John Wiley & Sons, Inc., 1993.
- [4] I.N. Bronstein and K.A. Semendjajew. *Taschenbuch der Mathematik*. B.G. Teubner, 25. edition, 1991.
- [5] A. Düster. *High order finite elements for three-dimensional, thin-walled nonlinear continua*. PhD thesis, Lehrstuhl für Bauinformatik, Technische Universität München, 2001.
- [6] J.H. Ferziger and M. Péric. *Computational methods for fluid dynamics*. Springer Verlag, 2nd edition, 1999.
- [7] M. Griebel, T. Neunhoeffer, and T. Dornseifer. *Numerical Simulation in Fluid Dynamics: A Practical Introduction*. Siam Monographs on Mathematical Modeling and Computation, 1997.
- [8] C. Hirsch. *Numerical computation of internal and external flows, Vol. 1, Fundamentals of numerical discretization*. John Wiley & Sons Ltd., 1988.
- [9] H. Oertel and E. Laurien. *Numerische Strömungsmechanik*. Vieweg & Sohn, 2nd edition, 2003.
- [10] S. Patankar. *Numerical heat transfer and fluid flow*. McGraw-Hill, 1980.
- [11] V.S. Ryaben'kii and S.V. Tsynkov. *A theoretical introduction to numerical analysis*. Chapman & Hall/CRC, 2007.
- [12] H.R. Schwarz. *Methode der Finiten Elemente*. B.G. Teubner, 3rd edition, 1991.
- [13] B.A. Szabó and I. Babuska. *Finite element analysis*. John Wiley & Sons, 2001.
- [14] O.C. Zienkiewicz and R.L. Taylor. *The finite element method – Basic formulations and linear problems, vol. 1*. McGraw-Hill Book Company, 5th edition, 2000.

# Chapter 7

## Internal radiation processes

Radiation processes are an important issue in building simulation which introduce mathematical complexity due to the non-linear behavior of radiative transport ( $q \propto T^4$ ) and some intrinsic spatial problems. The analysis of radiative transport significantly differs from the consideration of heat conduction as discussed in the previous chapter. The reasons are that

- radiative properties may be functions of direction as well as of wavelength and that
- the basic variable is the *radiative intensity* and not the temperature [18].

Similar to the principle of energy conservation as applied in the previous chapter, the law of conservation of radiative energy plays an important role for establishing an energy balance for an enclosure such as a building zone. In order to compute the temperatures and the radiative heat exchange between surfaces, the *intensity field* must be known in the first place.

For the surface radiation transport, the radiative properties emissivity  $\varepsilon$ , absorptivity  $\alpha$  and reflectivity  $\rho$  of the surfaces are required, in case of a semitransparent medium further the absorption and scattering coefficients. In this chapter radiative heat transfer will be considered within an enclosure without participating medium as the air at moderate temperatures does not influence radiation significantly. The description follows in some cases the smart book of M. MODEST [18] which is recommended for further reading.

### 7.1 Radiative heat exchange between surfaces

#### 7.1.1 Blackbody emissive power

Assuming that a molecule emits photons at distinct energy levels, MAX PLANCK found the spectral blackbody emissive power (*Planck's law*)

$$E_{b\lambda}(T, \lambda) = \frac{2\pi hc_0^2}{n^2 \lambda^5 (e^{hc_0/n\lambda kT} - 1)} \quad (7.1)$$

which is written here in terms of a constant refractive index  $n$  (for air at room temperature  $n \simeq 1$  over the visible spectrum) with the speed of light in vacuum  $c_0 = 2.998 \cdot 10^8 m/s$ , the Planck's constant  $h = 6.626 \cdot 10^{-34} Js$ , the Boltzmann constant  $k = 1.3806 \cdot 10^{-23} J/K$ , the

wavelength  $\lambda$  and the temperature  $T$  of the medium [2, 18]. Each wave or photon thereby carries the energy  $h\nu$  with the frequency  $\nu = c/\lambda[s^{-1}]$  and  $c = c_0/n$ .

The total emissive power of a blackbody with temperature  $T$  is obtained by integrating  $E_{b\lambda}$  over the spectrum

$$E_b(T) = \int_0^{\infty} E_{b\lambda}(T, \lambda) d\lambda = n^2 \sigma T^4 \quad (7.2)$$

with  $\sigma = 5.670 \cdot 10^8 W/(m^2 K^4)$  known as the *Stefan-Boltzmann constant*. A black opaque surface thereby does not reflect any radiation, i.e. it perfectly absorbs the incident radiative energy. According to *Kirchhoff's law* a black surface emits the same amount of energy. For a black surface this is true at every wavelength and for any direction, i.e. the longwave emissivity equals the longwave absorptivity.

### 7.1.2 Grey, diffuse surfaces

In reality surfaces emit as well as reflect and absorb energy. Kirchhoff's law applies also for usual construction materials under normal temperature conditions, but not for some coatings.

$$\varepsilon = \alpha = 1 - \rho \quad (7.3)$$

As the surface properties vary little across the part of the spectrum which is significant in terms of the respective blackbody emissive power [18], it is reasonable to assume that the radiative properties of building materials are independent of wavelength. Surfaces of this kind are termed *gray*. Real surfaces are rough and reflect radiation in a *diffuse* fashion. The directional dependence of the surface parameters can be neglected in the context of building simulation – except for glazings which are covered in Chapter 9 in detail. In summary, the following simplifications are made in simulation:

- surfaces are assumed to be gray and diffuse (emitting, reflecting and absorbing),
- surfaces have a uniform temperature, and
- the incident energy is uniform over the surface.

The total emissive power [ $W/m^2$ ] of a gray surface with temperature  $T$  is accordingly

$$E(T) = \varepsilon E_b(T) \simeq \varepsilon \sigma T^4 \quad (7.4)$$

for air at room temperature. In the following notation the brackets ( $T$ ) will be dropped. For a detailed review it is referred to the comprehensive book of M. MODEST [18].

Table 7.1 gives the color and surface dependent long-wave emission coefficients  $\varepsilon$  for some typical materials. In the absence of detailed values, a recommended value in simulation for wall and window surfaces is  $\varepsilon = 0.9$ . However, care must be taken if metallic bright surfaces are applied. From the material properties it is immediately clear that the latter is not suited for radiators, i.e. polished stainless steel radiators would have a bad performance in terms of radiative heat transfer.

Coating	$\varepsilon$
aluminium surface (polished)	0.03...0.06
aluminium surfaces (dull, rough polish)	0.18...0.30
glass	0.88...0.937
mineral materials	0.80...0.95
brick	0.85...0.95
bitumen felt/roofing sheets	0.91

Table 7.1: Color and surface dependent emission coefficients  $\varepsilon$ .

### 7.1.3 Surface energy balance

The surface energy balance for a grey, diffuse surface is depicted in Figure 7.1. The heat flux  $q(\mathbf{x})$  supplied to the surface at location  $\mathbf{x}$ , e.g. by heat conduction, equals the energy emitted by that surface  $H$  minus the absorbed energy. The latter absorbed energy is composed of the irradiation  $H$  minus the reflected portion ( $\rho H$ ).

With the the *radiosity*  $J(\mathbf{x})$ , i.e. the total heat flux leaving the surface,

$$J(\mathbf{x}) = \varepsilon(\mathbf{x})E_b(\mathbf{x}) + \rho(\mathbf{x})H(\mathbf{x}) \quad (7.5)$$

the supplied heat flux is

$$\begin{aligned} q(\mathbf{x}) &= J(\mathbf{x}) - H(\mathbf{x}) = [\varepsilon(\mathbf{x})E_b(\mathbf{x}) + \rho(\mathbf{x})H(\mathbf{x})] - H(\mathbf{x}) \\ &= \varepsilon(\mathbf{x})E_b(\mathbf{x}) - \alpha(\mathbf{x})H(\mathbf{x}) . \end{aligned} \quad (7.6)$$

As shown in Figure 7.2 the surface in question thereby exchanges radiative energy with all other surfaces of the enclosure, no matter how far removed. In other words, in order to compute the net radiative heat exchange between two surfaces, *all* surfaces must be considered *simultaneously*.

The amount of exchanged energy depends on the surface areas, the separation distance ( $\propto s^{-2}$ ), the respective orientation, the temperature of each surface ( $\propto T^4$ ) and the surface emissivities. The determining geometric properties are expressed in terms of *view factors*.

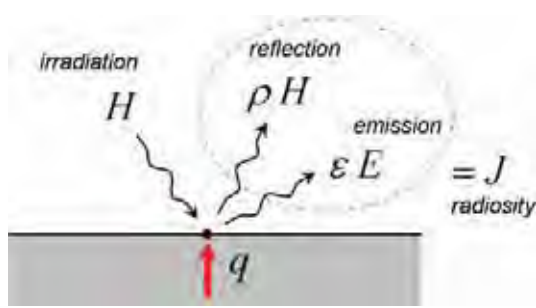
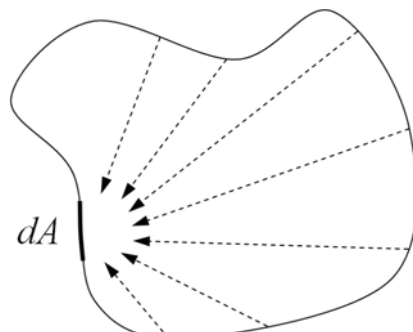


Figure 7.1: Surface energy balance [18].

Figure 7.2: Irradiation to differential element  $dA$ .

### 7.1.4 View factor definition

View factors (or shape or form factors) are basic geometric functions which describe the ratio of the diffuse energy leaving a surface element  $dA$  of the enclosure toward and intercepted by a surface element  $dA'$  to the total diffuse energy leaving the surface element  $dA$ . View factors are functions of the surface areas, the separation distance and the orientation; surfaces are assumed as ideal, gray, diffuse reflectors [18]. In order to determine the view factor  $dF_{dA-dA'}$  for the two infinitesimal surface elements  $dA$  and  $dA'$ , some points need further explanation.

A surface element  $dA$  radiates into infinitely many directions, every ray penetrating through a hemisphere as shown in Figure 7.3. The unit hemisphere is defined in terms of spherical coordinates, the zenith angle  $0 \leq \theta \leq \pi/2$ , the azimuth angle  $0 \leq \gamma \leq 2\pi$ , and the unit radius.

For the hemisphere, the *unit solid angle*

$$d\Omega = \sin \theta \, d\theta \, d\gamma \quad (7.7)$$

denotes the infinitesimal area  $dA''$  of the projection of the surface element  $dA'$  first onto a plane normal to the direction vector  $\mathbf{s}' = \mathbf{x} - \mathbf{x}'$ , i.e.  $\cos \theta' \, dA'$ , and secondly onto the unit hemisphere. It intuitively describes "how a surface is seen" from a specified location. The integral over the hemisphere

$$\int_0^{2\pi} \int_0^{\pi/2} \sin \theta \, d\theta \, d\gamma = 2\pi \quad (7.8)$$

accordingly equals the total surface area of the unit hemisphere. For a surface element  $dA'$  in distance  $s = \|\mathbf{s}\|$  from  $dA$ , with  $\mathbf{s} = \mathbf{x}' - \mathbf{x}$ , the solid angle becomes

$$d\Omega = \int_{A'} \frac{1}{s^2} \cos \theta' \, dA' \quad , \quad (7.9)$$

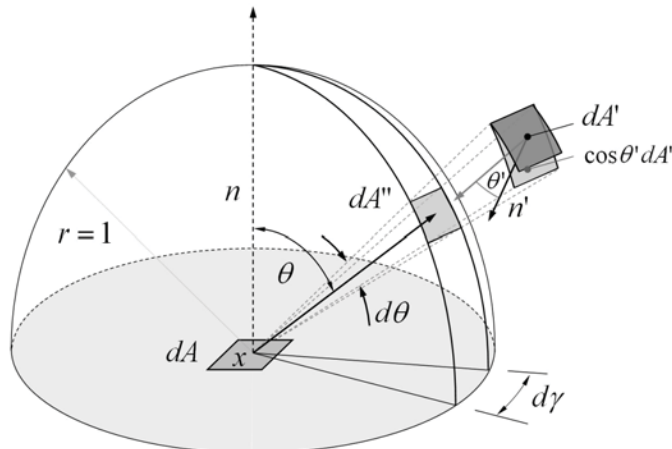


Figure 7.3: Projection to unit hemisphere and definition of the (unit) solid angle [18].

the projection of  $dA'$  onto the plane normal to  $\mathbf{s}'$  divided by the distance squared.

The *radiative intensity*  $I(\mathbf{x}, \theta, \gamma)$  is defined as the radiative energy flow per unit solid angle  $d\Omega$  and unit area normal to the respective rays. The total energy  $E(\mathbf{x})$  emitted from a surface  $dA$  (not  $dA'$  for the moment) is obtained by integrating the radiative intensity over all possible directions

$$E(\mathbf{x}) dA = \int_0^{2\pi} \int_0^{\pi/2} I(\mathbf{x}, \theta, \gamma) \underbrace{dA \cos \theta}_{\substack{\text{projection of } dA \\ \text{towards observer}}} \underbrace{\sin \theta d\theta d\gamma}_{d\Omega} . \quad (7.10)$$

For the case of diffuse radiation the radiative intensity is independent from the direction and, hence,

$$E(\mathbf{x}) = \pi I(\mathbf{x}) . \quad (7.11)$$

The radiative heat transfer rate from  $dA$  to  $dA'$  is now found by

$$I(\mathbf{x}) \underbrace{dA \cos \theta}_{\substack{\text{leaving } dA \\ \text{towards } dA'}} \underbrace{d\Omega_{dA'}}_{\substack{\text{intercepted} \\ \text{by } dA'}} = I(\mathbf{x}) \cos \theta \cos \theta' dA dA' / s^2 . \quad (7.12)$$

Following the definition of the surface energy balance given in Figure 7.1, the total radiative energy leaving surface  $dA$  equals the radiosity  $J(\mathbf{x})$ , and with (7.11)

$$J(\mathbf{x}) dA = \pi I(\mathbf{x}) dA . \quad (7.13)$$

With (7.12) and (7.13), for the view factor  $dF_{dA-dA'}$  between the two *infinitesimal* surface elements  $dA$  and  $dA'$  one finally obtains

$$dF_{dA-dA'} = \frac{I(\mathbf{x}) \cos \theta \cos \theta' dA dA' / s^2}{\pi I(\mathbf{x}) dA} = \frac{\cos \theta \cos \theta'}{\pi s^2} dA' , \quad (7.14)$$

where the zenith angle  $\theta$  becomes the angle between the surface normal  $\mathbf{n}$  and the vector  $\mathbf{s} = \mathbf{x}' - \mathbf{x}$  between both infinitesimal surfaces and vice versa for  $\theta'$ .

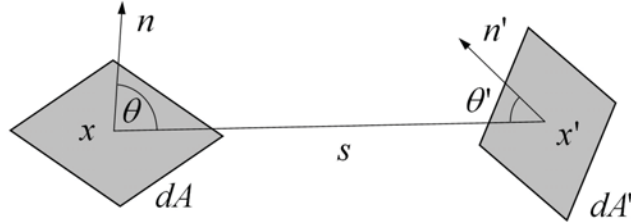


Figure 7.4: View factor definition: geometrical dependencies.

For the sake of numerical efficiency it makes sense to express  $\cos$  in terms of the scalar product of the two normalized vectors  $\mathbf{n}$  and  $\mathbf{s}$ , and

$$dF_{dA-dA'} = \frac{(\mathbf{n} \cdot \mathbf{s}) (\mathbf{n}' \cdot \mathbf{s}')}{\pi s^2} dA' . \quad (7.15)$$

Note that generally  $dF_{dA-dA'} \neq dF_{dA'-dA}$  but from (7.15) it follows the *law of reciprocity*

$$dA \cdot dF_{dA-dA'} = dA' \cdot dF_{dA'-dA} . \quad (7.16)$$

### 7.1.5 Net radiation method

Following the principle of conservation of radiative energy the radiative heat transfer rates between surfaces are computed by balancing the *net outgoing radiation* in terms of their radiosity.

Assuming a closed system, the irradiation  $H(\mathbf{x})$  to a surface  $dA$  at location  $\mathbf{x}$  is obtained by considering the contribution  $J$  from a differential surface  $dA'$  at location  $\mathbf{x}'$  which is intercepted by  $dA$ , i.e.  $J(\mathbf{x}') dA' \cdot dF_{dA'-dA}$ , as shown in Figure 7.5. Subsequent integration over the whole enclosure gives

$$H(\mathbf{x}) dA = \int_A J(\mathbf{x}') dA' dF_{dA'-dA} , \quad (7.17)$$

which can be simplified using the reciprocity relation  $dA \cdot dF_{dA-dA'} = dA' \cdot dF_{dA'-dA}$  to

$$H(\mathbf{x}) = \int_A J(\mathbf{x}') dF_{dA-dA'} . \quad (7.18)$$

By solving (7.6) for  $J(\mathbf{x})$  and inserting (7.18), an *integral equation* for the radiosity

$$J(\mathbf{x}) = \varepsilon(\mathbf{x}) E_b(\mathbf{x}) + \rho(\mathbf{x}) \int_A J(\mathbf{x}') dF_{dA-dA'} \quad (7.19)$$

is found. The discrete version of (7.19) is often referred to as *radiosity equation* which is applied for rendering techniques in practice [3]. Therefore the surface temperatures or, in terms of computer graphics, the rate at which light is emitted from the surfaces must be known.

In the context of building simulation the radiosity can be eliminated from the equations and expressed in terms of surface temperature and heat flux. This is now done in two steps. Therefore  $H(\mathbf{x})$  is first eliminated from Equation (7.6)

$$q - \alpha q = (\varepsilon E_b - \alpha H) - \alpha(J - H) = \varepsilon E_b - \alpha J$$

and by recalling that  $\alpha = \varepsilon$  for grey surfaces, cf. (7.3), one obtains after some algebra

$$J(\mathbf{x}) = E_b(\mathbf{x}) - \left( \frac{1}{\varepsilon(\mathbf{x})} - 1 \right) q(\mathbf{x}) . \quad (7.20)$$

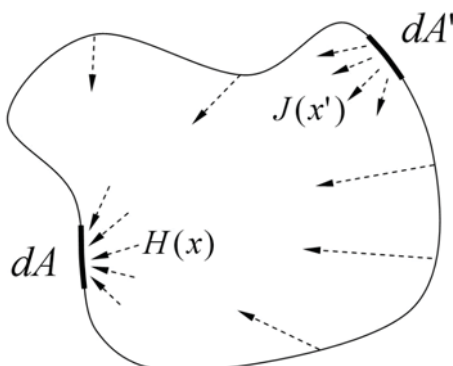


Figure 7.5: Radiative exchange between multiple surfaces.

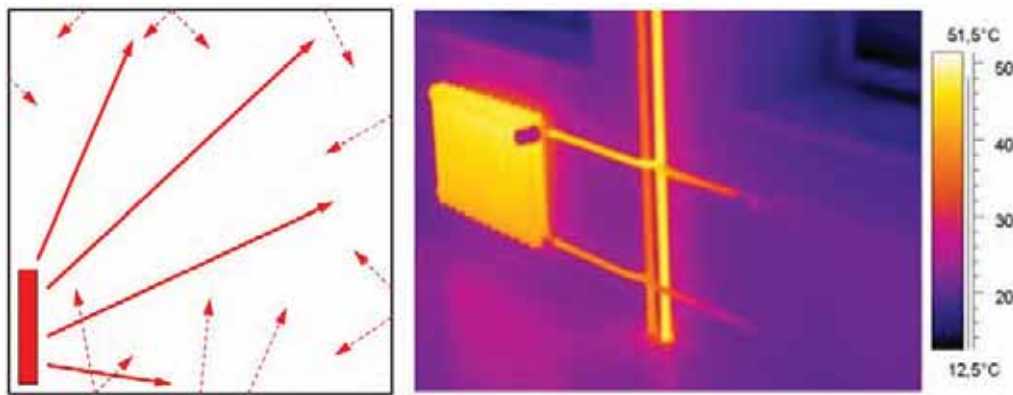


Figure 7.6: Example of longwave radiative transfer between a radiator and the surrounding surfaces. After multiple reflections, emitted radiation is totally re-absorbed and again re-distributed. The right-hand picture has been captured by a thermographic camera.

Secondly, the term (7.18) for the irradiation  $H(\mathbf{x})$  is inserted into the surface energy balance equation (7.6) which is solved for  $q(\mathbf{x})$ ,

$$q(\mathbf{x}) = \varepsilon(\mathbf{x})E_b(\mathbf{x}) - \alpha(\mathbf{x}) \int_A J(\mathbf{x}') dF_{dA-dA'} . \quad (7.21)$$

Substituting (7.20) into this (7.21), an *integral equation* balancing the net outgoing radiation is obtained which relates (unknown) heat fluxes with (known) temperatures. Gathering unknown quantities on the left and known quantities on the right side one gets

$$\underbrace{\frac{q(\mathbf{x})}{\varepsilon(\mathbf{x})} - \int_A \left( \frac{1}{\varepsilon(\mathbf{x}')} - 1 \right) q(\mathbf{x}') dF_{dA-dA'}}_{{\text{unknown heat fluxes } q}} = \underbrace{E_b(\mathbf{x}) - \int_A E_b(\mathbf{x}') dF_{dA-dA'}}_{{\text{known temperatures } \propto T^4}} . \quad (7.22)$$

Note that in this equation (i)  $E_b(\mathbf{x})$  is expressed in terms of the blackbody radiation and (ii) that the dependent variable  $q(\mathbf{x})$  is inside an integral.

### 7.1.6 View factors for finite surfaces

Before discussing the numerical approximation of the integral equation in the next section, the view factor definition from Section 7.1.4 is expanded to the case of finite subsurfaces.

**Exchange between one infinitesimal and one finite area.** Considering Equation 7.12, the view factor between the infinitesimal surface element  $dA_i$  and a finite surface  $A_j$  is

$$dF_{dA_i-A_j} = \int_{A_j} \frac{\cos \theta_i \cos \theta_j}{\pi s^2} dA_j , \quad (7.23)$$

and between  $A_j$  and  $dA_i$ , assuming  $I(\mathbf{x}) = I_j = \text{const}$  over the finite surface,

$$dF_{A_j-dA_i} = \frac{1}{A_j} \int_{A_j} \frac{\cos \theta_i \cos \theta_j}{\pi s^2} dA_j dA_i . \quad (7.24)$$

**Exchange between two finite areas.** For the case of two finite surfaces  $A_i$  and  $A_j$  and again assuming that the intensity leaving  $A_i$  remains constant over the surface one obtains

$$F_{i,j} = F_{A_i-A_j} = \frac{1}{A_i} \int_{A_i} \int_{A_j} \frac{\cos \theta_i \cos \theta_j}{\pi s^2} dA_j dA_i , \quad (7.25)$$

together with the reciprocity (for constant intensities)

$$A_i \cdot F_{A_i-A_j} = A_j \cdot F_{A_j-A_i} . \quad (7.26)$$

## 7.2 Numerical solution techniques

### 7.2.1 Analytical, numerical and sampling methods

Most numerical algorithms are well known from the calculation of photo-realistic images such as *raytracing* techniques [10] which are well capable of reproducing highlight effects on bright surfaces and specular reflection or the *radiosity methods* [1, 11] similar to the net radiation method (see Section 7.1.5) for representing view point independent diffuse light sources [3].

Radiative heat transfer problems are usually governed by integral equations rather than partial differential equations. In the absence of a participating medium, the energy travels from a point of absorption in terms of discrete packets along a straight path until a point of absorption. It is therefore possible to solve a radiation problem by tracing the path (or the history) of a statistically meaningful sample of photons. This statistical sampling technique is called a *Monte Carlo method* [14]. The key question is thereby how to choose a statistically meaningful sample of photons in terms of the selected points of emission, direction and wavelength [18].

Monte Carlo methods are computationally expensive but are in complex geometries advantageous over conventional numerical solution techniques and are well suited for considering multiple bands. A simplification used in commercial codes is for example the *discrete transfer method*. It makes use of a fixed sampling (instead of random) where the hemisphere is discretized into a finite number of rays [4]. For the *raytracing* itself, several acceleration techniques have been suggested in the literature, such as hierarchical space tree based methods for tracking the rays and solving the visibility check (ray casting) [9].

However, for computing the internal radiative heat exchange in the context of building performance simulation it is convenient to use the net radiation method [13]. As it is based on the principle of energy conservation, the method already accounts for multiple reflections, i.e. it is well suited to model the *diffuse* part of the short and long wave radiation. For tracking the direct beam radiation, a simple raytracing algorithm will be introduced in Section 8.6.2.

For the determination of view factors it is generally distinguished between analytical and numerical methods. *Analytical solutions* are available in the literature for a few special cases with basic geometry and for plane surfaces with polygonal shape via view factor algebra [15, 18]. Another method is the *crossed strings method* suggested by HOTTEL [12], for example. Analytical solutions, such as the one known for two parallel finite surfaces, are useful as benchmark solution for code validation.

The *numerical approaches* generally distinguish between methods in terms of a *double area or double line integration* and methods which consider the exchange between an infinitesimal and a finite surface, usually referred to as *single line or single area integration*:

- For the evaluation of the *area integrals*, it is integrated over both finite surfaces according to Equation (7.25). For the numerical integration, the surface can be divided into a number of small finite subsurfaces in terms of an  $h$ -refinement, or the *Gaussian quadrature* can be used to approximate the integral expression, for example.
- In the case of a *line integral*, one or two of the area integrals of Equation (7.25) are converted into line integrals using Stokes' theorem. If both integrals are substituted, one obtains

$$F_{i,j} = \frac{1}{2\pi A_i} \oint_{C_i} \oint_{C_j} \ln(s) d\mathbf{v}_i d\mathbf{v}_j , \quad (7.27)$$

where  $C_i$  and  $C_j$  are the contours of finite surfaces  $A_i$  and  $A_j$  as shown in Figure 7.7. The distance  $s$  is evaluated between the two differential vectors  $\mathbf{v}_i$  and  $\mathbf{v}_j$ , which are each located on the contours of the surfaces  $A_i$  and  $A_j$ , respectively.

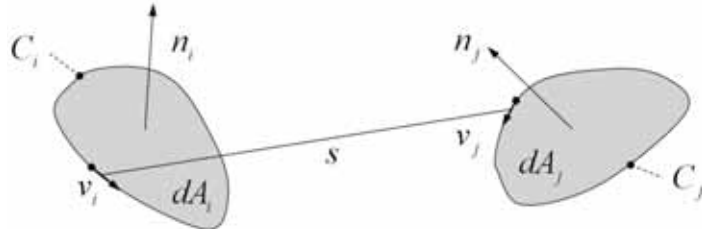


Figure 7.7: Geometrical dependencies in case of the line integration [27].

For the *exchange between an infinitesimal and a finite surface*, several sampling methods are proposed in the literature to speed up the view factor determination. For example, the *hemicube method* suggested by COHEN & GREENBERG [5] makes use of the observation of the *unit sphere method* published by NUSSELT [19], i.e. that the exact solution of the (inner) integral over  $A_j$  of (7.25) equals the surface area of  $A_j$  which is first projected onto a unit sphere around  $i$  and secondly orthogonally projected onto the plane surface of the base circle of that hemisphere. The *hemicube* substitutes the hemisphere with a cube whose surface is decomposed into a set of (finite) patches. For each patch, view factors are computed in advance. The surface  $A_j$  can then be projected onto that cube and the view factor is determined by subsequent summation of the corresponding values from the patches intersecting with the projected surface. The technique is well known from algorithms in computer graphics as summarized by BUNGARTZ et al. in [3], for example.

### 7.2.2 Numerical determination of view factors

In order to save computing time, a "cheap" initial test is to evaluate if both surfaces  $i$  and  $j$  see each other in terms of the orientation of the surface normals as shown in Figure 7.4. This is true, if

$$\mathbf{n}_i \cdot \mathbf{s}_{i,j} > 0 \quad \text{and} \quad \mathbf{n}_j \cdot \mathbf{s}_{j,i} > 0 \quad . \quad (7.28)$$

**Double area integration (midpoint rule).** In the case of the double area integration, the surfaces  $i$  and  $j$  are each divided into a set of  $m$  and  $n$  finite subsurfaces [27]. Using the expression (7.15) for the cosine, the integral Equation (7.25) becomes

$$F_{i,j} \approx \frac{-1}{\pi A_i} \sum_k^m \sum_l^n \frac{(\mathbf{s}_{k,l} \cdot \mathbf{n}_k)(\mathbf{s}_{l,k} \cdot \mathbf{n}_l)}{s} \Delta A_k \Delta A_l \quad . \quad (7.29)$$

One possibility is the application of the *midpoint rule* for integration and a successive refinement of the model in terms of increasing the number of the  $m \cdot n$  subsurfaces. The vectors  $\mathbf{s}_{k,l}$ ,  $\mathbf{s}_{l,k}$ ,  $\mathbf{n}_k$  and  $\mathbf{n}_l$  are then evaluated at the center of each subsurface  $k$  and  $l$ .

**Double area integration (Gaussian quadrature).** Another possibility instead of the former  $h$ -refinement is to perform the numerical integration via the *Gaussian quadrature*. The method is better in terms of computational speed and accuracy, especially if facets are far away from each other. If surfaces are too close, the method may be disadvantageous [27]. In a one-dimensional form the quadrature reads

$$\int_{-1}^1 (\cdot) d\xi \approx \sum_i^n (\cdot) |_{\xi_i} w_{\xi_i} \quad , \quad (7.30)$$

where  $\xi_i$  denotes the quadrature points at which the integrand  $(\cdot)$  is evaluated and  $w_{\xi_i}$  are the corresponding weights [24]. With  $n$  quadrature points a polynomial of degree  $2n - 1$  can be exactly integrated. The abscissas and weight factors of the Gaussian quadrature are listed in Table 7.10 and can be derived using the Gauss-Legendre polynomials as described by SZABÓ & BABUSKA in [24].

As shown by DÜSTER et al. [7], with the help of the mapping function (see Figure 7.8)

$$\mathbf{q} = \mathbf{Q}(u, v) = \sum_i^4 N_i(u, v) \mathbf{x}_i \quad , \quad (7.31)$$

and the bi-linear shape functions (see Figure 7.9)

$$\begin{aligned} N_1(u, v) &= \frac{1}{4}(1-u)(1-v) ; & N_2(u, v) &= \frac{1}{4}(1+u)(1-v) ; \\ N_3(u, v) &= \frac{1}{4}(1+u)(1+v) ; & N_4(u, v) &= \frac{1}{4}(1-u)(1+v) , \end{aligned} \quad (7.32)$$

the numerical integration of the respective surface areas  $A_k$  and  $A_l$  is possible with a two-dimensional Gaussian quadrature which is defined on a standard quadrilateral.

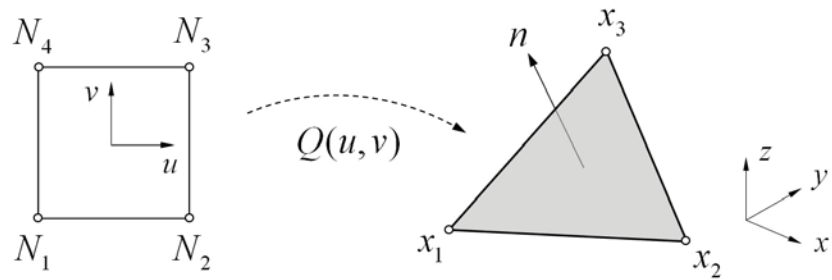


Figure 7.8: Mapping from standard quadrilateral element (local coordinates) to facet (global coordinates) [7].

Figure 7.8 shows the mapping of the standard quadrilateral element ( $[-1, -1] \times [1, 1]$ ) with the local coordinates  $(u, v)$  to the global coordinates  $\mathbf{x}_i = (x_i, y_i, z_i)^T$  of the three nodes ( $i = 1, 2, 3$ ) of the triangle. Note that the quadrilateral domain is thereby transformed by the mapping function  $\mathbf{Q}(u, v)$  to fit the facet by simply choosing  $\mathbf{x}_4 = \mathbf{x}_3$ . Of course instead of a triangle, also a quadrilateral element can be used without the need for "degenerating" the element.

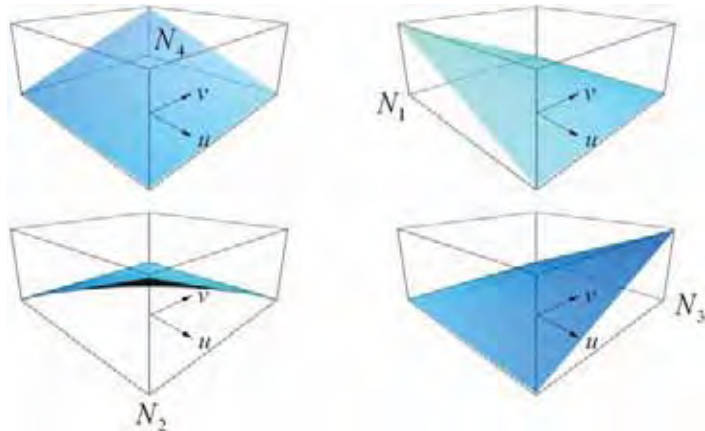


Figure 7.9: The bi-linear shape functions  $N_1(u, v)$ ,  $N_2(u, v)$ ,  $N_3(u, v)$  and  $N_4(u, v)$  (7.32) [6].

With the described mapping, the areas of the subsurfaces  $A_k$  and  $A_l$  are each *exactly* obtained by

$$A = \int_u \int_v \left| \frac{\partial \mathbf{q}(u, v)}{\partial u} \times \frac{\partial \mathbf{q}(u, v)}{\partial v} \right| du dv , \quad (7.33)$$

where the vector product  $\frac{\partial \mathbf{q}}{\partial u} \times \frac{\partial \mathbf{q}}{\partial v}$  corresponds to the respective normal vector at  $(u, v)$ . Using  $a$  and  $b$  Gaussian points in  $u$  and  $v$  direction, the *numerical* integration of each surface area accordingly reads

$$A = \sum_{\alpha}^a \sum_{\beta}^b \left| \frac{\partial \mathbf{q}(u_{\alpha}, v_{\beta})}{\partial u} \times \frac{\partial \mathbf{q}(u_{\alpha}, v_{\beta})}{\partial v} \right| w_{\alpha} w_{\beta} \quad (7.34)$$

with the weight  $w_i$  of each  $i$ th Gaussian point at the local coordinates  $u_i$  and  $v_i$ , respectively.

Number of points	Gaussian ordinates	weights
1	0.50	1.00000
4	0.21 0.79	0.50000 0.50000
9	0.11 0.50 0.89	0.27778 0.44444 0.27778
16	0.07 0.33 0.67 0.93	0.17393 0.32607 0.32607 0.17393
25	0.05 0.23 0.50 0.77 0.95	0.11846 0.23931 0.28444 0.23931 0.11846
36	0.03 0.17 0.38 0.62 0.83 0.97	0.08566 0.18038 0.23396 0.23396 0.18038 0.08566

Figure 7.10: Gaussian points: Ordinates and weights [24].

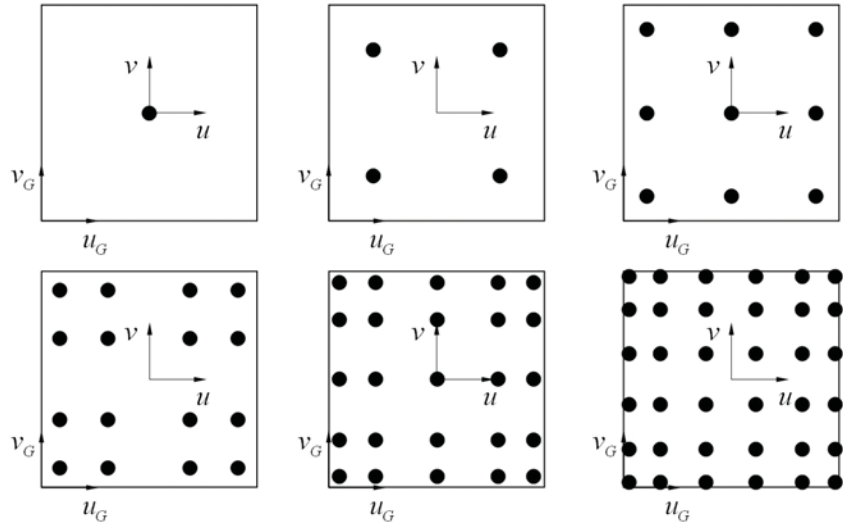


Figure 7.11: Standard quadrilateral with 1, 4, 9, 16, 25 and 36 Gaussian points. Ordinates are defined in terms of the local coordinate system  $(u_g, v_g)$ .

For the implementation this means – in other words – the following. Within the outer loop  $\alpha = 1 \dots a$  and the inner loop  $\beta = 1 \dots b$  over all Gaussian points, for each direction the coordinates  $u_\alpha$  and  $v_\beta$  and the corresponding weights  $w_\alpha$  and  $w_\beta$  are read from the table as shown in Figure 7.11. The derivatives of the mapping function (7.31) are evaluated at  $(u_\alpha, v_\beta)$ , where the mapping transforms the latter local coordinates into global coordinates taking the global nodes of the triangle/quadrilateral as input. Finally, the norm of the vector product is computed, multiplied with the weights and summed up.

In the scope of the view factor  $F_{i,j}$  computation, in Equation (7.29) both surface integrals for  $A_i$  and  $A_j$  of the integral Equation (7.25) are computed by the expression (7.34). The surfaces  $A_i$  and  $A_j$  are approximated by  $a \cdot b$  and  $c \cdot d$  Gaussian points, respectively. With the abbreviations  $\mathbf{q}_{\alpha,\beta} = \mathbf{q}(u_\alpha, v_\beta)$  and  $\mathbf{q}_{\gamma,\delta} = \mathbf{q}(u_\gamma, v_\delta)$ , the final expression is

$$F_{i,j} \approx \frac{-1}{\pi A_i} \sum_{\alpha}^a \sum_{\beta}^b \sum_{\gamma}^c \sum_{\delta}^d \frac{(\mathbf{s}_{\alpha,\beta \rightarrow \gamma,\delta} \cdot \mathbf{n}_{\alpha,\beta})(\mathbf{s}_{\gamma,\delta \rightarrow \alpha,\beta} \cdot \mathbf{n}_{\gamma,\delta})}{(\mathbf{s}_{\alpha,\beta \rightarrow \gamma,\delta} \cdot \mathbf{s}_{\alpha,\beta \rightarrow \gamma,\delta})^2} \cdot \\ \left| \frac{\partial \mathbf{q}_{\alpha,\beta}}{\partial u} \times \frac{\partial \mathbf{q}_{\alpha,\beta}}{\partial v} \right| w_\alpha w_\beta \left| \frac{\partial \mathbf{q}_{\gamma,\delta}}{\partial u} \times \frac{\partial \mathbf{q}_{\gamma,\delta}}{\partial v} \right| w_\gamma w_\delta \quad . \quad (7.35)$$

As indicated in Figure 7.12, the vectors  $\mathbf{s}$  and  $\mathbf{n}$  are evaluated at the global coordinates which are obtained by inserting the local coordinates of the respective Gaussian points into the mapping function (7.31). It should be noted, that likewise the Gaussian quadrature can be formulated for a triangle element. However, this method is not recommended as some of the weights become negative which impacts the convergence of the method.

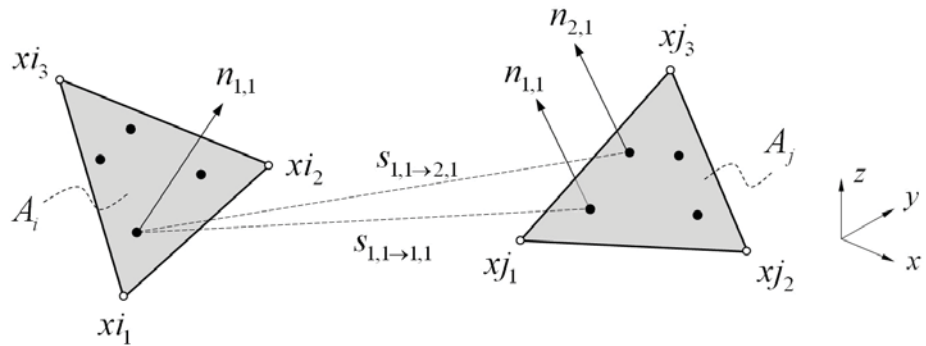


Figure 7.12: Evaluation of Equation (7.35) for each Gaussian point. Note that the quadrilateral is “degenerated” to a triangle by choosing  $\mathbf{x}_4 = \mathbf{x}_3$ .

**Double line integration.** As summarized by WALTON [27], Equation (7.27) can be numerically evaluated by the expression (7.36) via *line integration*, if the boundary contours  $C_i$  and  $C_j$  are approximated by polygons with  $np_i$  and  $np_j$  edges, each further subdivided into  $nv_i$  and  $nv_j$  short vectors  $\mathbf{v}_\alpha$  and  $\mathbf{v}_\beta$ .

$$F_{i,j} \approx \frac{1}{4\pi A_i} \sum_p^{np_i} \sum_q^{np_j} \cos(\psi_{p,q}) \sum_\alpha^{nv_i} \sum_\beta^{nv_j} \ln(\mathbf{s}_{\alpha,\beta} \cdot \mathbf{s}_{\alpha,\beta}) \Delta \mathbf{v}_\alpha \Delta \mathbf{v}_\beta \quad (7.36)$$

In Equation (7.36),  $\psi_{p,q}$  is the angle between the two polygon edges  $\mathbf{e}_p$  and  $\mathbf{e}_q$ , which is constant between these edges and which can be evaluated by  $\cos(\psi_{p,q}) = (\mathbf{e}_p \cdot \mathbf{e}_q) / (|\mathbf{e}_p| \cdot |\mathbf{e}_q|)$ . The logarithm is transformed such that now only a scalar is to be evaluated.

Likewise this equation can be computed via the Gaussian quadrature, which reduces here to the one-dimensional form without the need for transformation. In this case the terms  $\Delta \mathbf{v}_\alpha$  and  $\Delta \mathbf{v}_\beta$  are multiplied with the corresponding weights and the vector  $\mathbf{r}_{\alpha,\beta}$  is calculated at the position of the Gaussian point. The latter can be easily computed via some vector operations. With the Gaussian quadrature, the integration becomes much more accurate than without [24, 27].

**Other integration schemes.** WALTON summarizes other numerical integration methods for the view factor computation in [27]. For example, the *single area integration* addresses the exchange between an infinitesimal area and the boundary contour in terms of a polygon. In the *single line integration* [17] one of the contour integrals is treated in an analytical way [27]. Furthermore, analytical expressions exist for the case of polygon-based double line integrals.

### 7.2.3 Accuracy and computational effort

The calculation of view factors is very expensive in terms of the computational effort as the calculation time increases exponentially with the number of facets. However, if the geometry remains unchanged during simulation (which is the usual case in building performance simulation), the view factors can be determined in a preprocessing step prior to the main simulation time loop, i.e. only once.

Each facet is in radiant contact with each other. Having  $n$  facets, the number of view factors is in the order  $\mathcal{O}(n^2)$ . With the assumption of plane facets and using the reciprocity relation (7.26) the order reduces to  $\mathcal{O}(\frac{n(n-1)}{2})$ . The problem gets worse,  $\mathcal{O}(n^3)$ , if surface obstruction tests needs to be further accounted for [18, 27].

If, for example, the double area integration method (7.29) is applied, each of the latter surfaces is decomposed into another set of subsurfaces. This effect becomes clear from Equation (7.29) and especially from (7.35). Hence, the complexity increases from  $\mathcal{O}(n^2)$  to  $\mathcal{O}(n^4)$ .

Integration scheme	order
double area integration	$\mathcal{O}(n^4)$
double line integration	$\mathcal{O}(8n^2)$
single area integration	$\mathcal{O}(4n^2)$
single line integration	$\mathcal{O}(8n)$

Table 7.2: Order of the different numerical integration schemes in terms of the computing time with respect to the number of facets  $n$  [27].

WALTON [27] investigated the order of the above mentioned algorithms which is summarized in Table 7.2. Walton also showed another important fact. If facets are relatively close, a large set of subsurfaces or integration points is necessary. On the other hand is the analytical approach advantageous if surfaces are not obstructed by other objects in between. Walton therefore suggests an *adaptive integration algorithm* which takes into account the distances between surfaces and computes view factors via successive refinement. The iterative refinement is terminated as soon as the difference between two steps is less than a tolerance value.

In order to further clarify this problem, this section quantifies the trade-off between accuracy and computational effort for the case of the view factor computation for two parallel finite surfaces of size  $a \times a$  and distance  $a$  with a developed code [8]. On the right hand side of Figure 7.13 the geometrical configuration for the two finite planes is shown. In this case, the analytical, i.e. exact, solution [2, 18] for the view factor can be obtained via view factor algebra ( $F_{1,2} = 0.19982489569838738304159925119307\dots$ ).

In Figure 7.13, the convergence is detailed for

- the  $h$ -refinement using the first order midpoint method,
- the double area Gaussian integration using degenerated triangle elements with 4, 64, 256 and 1024 Gaussian points each as well as quadrilateral elements with 2 and 8 Gaussian points, and
- the double line integration using the Gaussian quadrature.

Both surface areas were successively refined for each integration method by a subsequent subdivision into sub-facets. The figure indicates that the midpoint rule shows algebraic convergence whereas the line and the area integration converge exponentially. The contour integration is superior over the area integration in this case. For example, using 72 quadrilateral elements

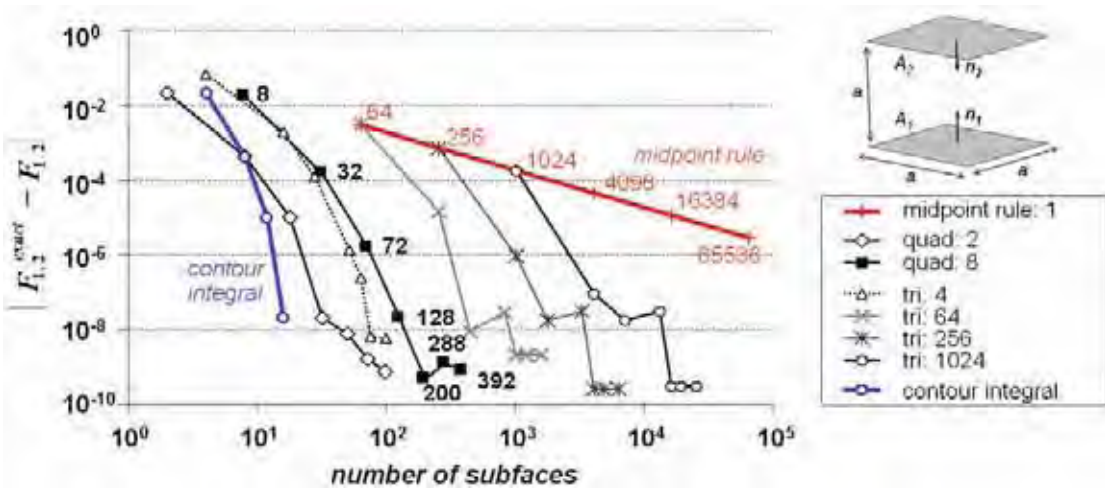


Figure 7.13: Convergence study of numerical integration methods (midpoint rule, Gaussian quadrature contour integration). The deviation between the computed view factor from the analytical value is plotted against the number of facets [8, 25].

with 8 integration points each (i.e. 576 points in total) yields a better accuracy than 65,536 elements with the midpoint rule.

Figure 7.14 compares some of these methods with respect to the required computational effort. The first order scheme comes along with extensive computing times – up to several hours for more than 10,000 facets. With the other schemes, the computing time can be reduced by several orders of magnitude for the same accuracy.

In summary, in building simulation the reasonable choice of a well-suited integration method in terms of both accuracy and computational effort is crucial. A good solution is suggested by WALTON with an adaptive integration algorithm [27].

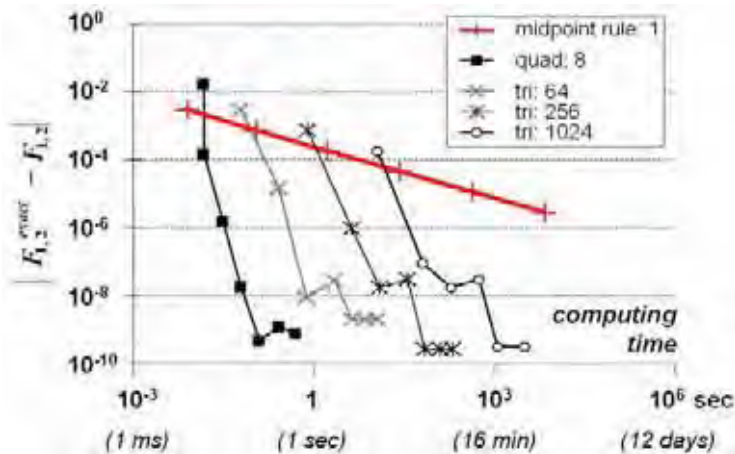


Figure 7.14: Comparison of the computational effort of the different integration schemes from Figure 7.13. The deviation between the computed view factor from the analytical value is plotted against the computing time [8, 25].

### 7.2.4 Numerical approximation of the integral equation

For the numerical solution, and thus an approximation of the integral Equation (7.22), the enclosure is discretized into a set of  $n$  facets. The radiosity and the heat flux are assumed constant over each discrete (not necessarily finite) surface. Using the relation

$$\sum_{j=1}^n F_{i,j} = 1 \quad (7.37)$$

one obtains a set of  $n$  algebraic equations which describe the radiative interchange between the surfaces of the enclosure with  $i = 1, \dots, n$  by

$$\frac{q_i}{\varepsilon_i} - \sum_{j=1}^n \left( \frac{1}{\varepsilon_j} - 1 \right) q_j F_{i,j} = \sum_{j=1}^n (E_{b,i} - E_{b,j}) F_{i,j} . \quad (7.38)$$

In matrix notation

$$\mathbf{A} \mathbf{q} = \mathbf{b} \quad (7.39)$$

with unknowns  $\mathbf{q} = [q_1, q_2, \dots, q_i, \dots, q_n]^T$  and load vector

$$\mathbf{b} = \begin{bmatrix} F_{1,2}(E_{b1} - E_{b2}) + F_{1,3}(E_{b1} - E_{b3}) + F_{1,4}(E_{b1} - E_{b4}) + \dots + F_{1,n}(E_{b1} - E_{bn}) \\ F_{2,1}(E_{b2} - E_{b1}) + F_{2,3}(E_{b2} - E_{b3}) + F_{2,4}(E_{b2} - E_{b4}) + \dots + F_{2,n}(E_{b2} - E_{bn}) \\ F_{3,1}(E_{b3} - E_{b1}) + F_{3,2}(E_{b3} - E_{b2}) + F_{3,4}(E_{b3} - E_{b4}) + \dots + F_{3,n}(E_{b3} - E_{bn}) \\ \dots \\ F_{n,1}(E_{bn} - E_{b1}) + F_{n,2}(E_{bn} - E_{b2}) + F_{n,3}(E_{bn} - E_{b3}) + \dots + F_{n,n-1}(E_{bn} - E_{bn-1}) \end{bmatrix}$$

with  $E_{bi} = \sigma T_i^4$ , the generally non-symmetric coefficient matrix is obtained by

$$\mathbf{A} = \begin{bmatrix} \frac{1}{\varepsilon_1} - \left( \frac{1}{\varepsilon_1} - 1 \right) F_{1,1} & -\left( \frac{1}{\varepsilon_2} - 1 \right) F_{1,2} & -\left( \frac{1}{\varepsilon_3} - 1 \right) F_{1,3} & \dots & -\left( \frac{1}{\varepsilon_n} - 1 \right) F_{1,n} \\ -\left( \frac{1}{\varepsilon_1} - 1 \right) F_{2,1} & \frac{1}{\varepsilon_2} - \left( \frac{1}{\varepsilon_2} - 1 \right) F_{2,2} & -\left( \frac{1}{\varepsilon_3} - 1 \right) F_{2,3} & \dots & -\left( \frac{1}{\varepsilon_n} - 1 \right) F_{2,n} \\ -\left( \frac{1}{\varepsilon_1} - 1 \right) F_{3,1} & -\left( \frac{1}{\varepsilon_2} - 1 \right) F_{3,2} & \frac{1}{\varepsilon_3} - \left( \frac{1}{\varepsilon_3} - 1 \right) F_{3,3} & \dots & -\left( \frac{1}{\varepsilon_n} - 1 \right) F_{3,n} \\ -\left( \frac{1}{\varepsilon_1} - 1 \right) F_{4,1} & -\left( \frac{1}{\varepsilon_2} - 1 \right) F_{4,2} & -\left( \frac{1}{\varepsilon_3} - 1 \right) F_{4,3} & \dots & -\left( \frac{1}{\varepsilon_n} - 1 \right) F_{4,n} \\ \dots & & & \dots & \\ -\left( \frac{1}{\varepsilon_1} - 1 \right) F_{n,1} & -\left( \frac{1}{\varepsilon_2} - 1 \right) F_{n,2} & -\left( \frac{1}{\varepsilon_3} - 1 \right) F_{n,3} & \dots & \frac{1}{\varepsilon_n} - \left( \frac{1}{\varepsilon_n} - 1 \right) F_{n,n} \end{bmatrix}$$

which can be further reduced for the special case if  $F_{i,i} = 0$  assuming flat or convex surfaces of the geometric model (see Chapter 5).

### 7.2.5 Solving the equation set by LU decomposition

The linear equation set (7.39) of  $n$  equations with the coefficient matrix  $\mathbf{A}$  and load vector  $\mathbf{b}$  needs to be solved with respect to the unknowns  $\mathbf{q}$ . For the solution, a direct solver can be applied, such as the Gaussian elimination scheme, the Cholesky algorithm, or the LU-factorization, or an iterative solver which is based on a Krylov subspace method [16]. As the matrix  $\mathbf{A}$  is non-symmetric and positive definite, an appropriate choice is the Generalized Minimal Residual (GMRES) method [22], for example. For a review of the issue of equation

solving it is referred to standard textbooks such as [16, 20, 21, 23] and others. In this section, the *LU-decomposition method* [20, 21] is briefly sketched for solving (7.39).

The matrix  $\mathbf{A}$  is written as the product

$$\mathbf{A} = \mathbf{L} \cdot \mathbf{U} \quad (7.40)$$

of two matrices, the lower triangular  $\mathbf{L}$  with elements on the diagonal and below, and the upper triangular  $\mathbf{U}$  with elements on the diagonal and above, i.e.

$$\begin{bmatrix} \alpha_{0,0} & 0 & 0 & 0 \\ \alpha_{1,0} & \alpha_{1,1} & 0 & 0 \\ \alpha_{2,0} & \alpha_{2,1} & \alpha_{2,2} & 0 \\ \alpha_{3,0} & \alpha_{3,1} & \alpha_{3,2} & \alpha_{3,3} \end{bmatrix} \cdot \begin{bmatrix} \beta_{0,0} & \beta_{0,1} & \beta_{0,2} & \beta_{0,3} \\ 0 & \beta_{1,1} & \beta_{1,2} & \beta_{1,3} \\ 0 & 0 & \beta_{2,2} & \beta_{2,3} \\ 0 & 0 & 0 & \beta_{3,3} \end{bmatrix} = \begin{bmatrix} a_{0,0} & a_{0,1} & a_{0,2} & a_{0,3} \\ a_{1,0} & a_{1,1} & a_{1,2} & a_{1,3} \\ a_{2,0} & a_{2,1} & a_{2,2} & a_{2,3} \\ a_{3,0} & a_{3,1} & a_{3,2} & a_{3,3} \end{bmatrix} \quad (7.41)$$

for the case of a  $4 \times 4$  matrix. With the decomposition (7.40) of  $\mathbf{A}$ , the equation set  $\mathbf{A} \cdot \mathbf{q} = \mathbf{b}$  can be solved in two successive steps, first for  $\mathbf{y}$  by

$$\mathbf{L} \cdot \mathbf{y} = \mathbf{b} \quad (7.42)$$

and then for  $\mathbf{q}$  by

$$\mathbf{U} \cdot \mathbf{q} = \mathbf{y} \quad (7.43)$$

as

$$\underbrace{(\mathbf{L} \cdot \mathbf{U})}_{\mathbf{A}} \cdot \mathbf{q} = \mathbf{L} \cdot \underbrace{(\mathbf{U} \cdot \mathbf{q})}_{\mathbf{y}} = \mathbf{b} . \quad (7.44)$$

The idea of the method is that once the decomposition is done a triangular set of equations can be solved without much effort. In this case, Equation (7.42) is solved by the *forward substitution*

$$y_0 = \frac{b_0}{\alpha_{0,0}} \quad \text{and} \quad y_i = \frac{1}{\alpha_{i,i}} \left[ b_i - \sum_{j=0}^{i-1} \alpha_{i,j} y_j \right] \quad \text{for } i = 1, 2, \dots, n-1 \quad (7.45)$$

and Equation (7.43) by the *backward substitution*

$$x_{n-1} = \frac{y_{n-1}}{\beta_{n-1,n-1}} \quad \text{and} \quad x_i = \frac{1}{\beta_{i,i}} \left[ y_i - \sum_{j=i+1}^{n-1} \beta_{i,j} x_j \right] \quad \text{for } i = n-2, \dots, 0 . \quad (7.46)$$

The cost of either solution is of the order  $\mathcal{O}(n^2)$  operations.

Note, that for the net radiation method, the LU-decomposition needs to be computed *only once* as matrix  $\mathbf{A}$  remains unchanged during the computation. Only the right hand side of (7.39), i.e. the load vector, changes cyclically. The cost for obtaining the decomposition is of the order  $\mathcal{O}(n^3)$  arithmetic operations. The algorithm for performing the LU-decomposition can be obtained from a textbook such as *Numerical Recipes in C++* [20], for example, which contains further improvements in terms of computational efficiency such as pivoting.

### 7.2.6 Example: View factors for the VDI 6020 sample room

The following example details the view factor computation for the geometry of the VDI 6020 [26] sample room shown in Figure 7.15 which was defined in Section 3.6. The facet model consists in this case of 16 triangles. The view factors are computed with the integration techniques from Section 7.2.2 and by further applying the adaptive integration scheme of WALTON [27].

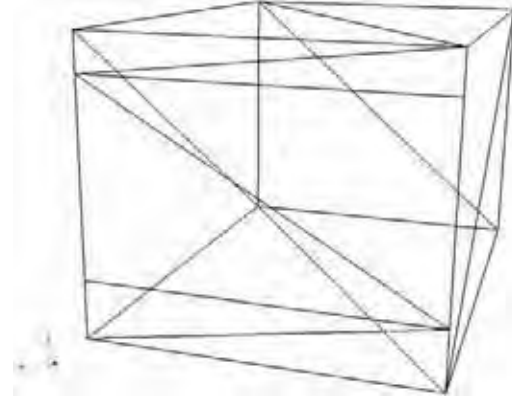


Figure 7.15: Facet model of the VDI 6020 sample room [26] using 16 triangles.

**Preprocessing phase.** The non-symmetrical view factor matrix  $\mathbf{F}$

$$\begin{bmatrix} 0.000 & 0.000 & 0.049 & 0.092 & 0.044 & 0.032 & 0.216 & 0.063 & 0.005 & 0.005 & 0.042 & 0.045 & 0.038 & 0.077 & 0.112 & 0.181 \\ 0.000 & 0.000 & 0.216 & 0.063 & 0.137 & 0.075 & 0.049 & 0.092 & 0.005 & 0.004 & 0.004 & 0.006 & 0.033 & 0.024 & 0.181 & 0.112 \\ 0.057 & 0.252 & 0.000 & 0.000 & 0.067 & 0.144 & 0.104 & 0.117 & 0.003 & 0.003 & 0.010 & 0.013 & 0.021 & 0.030 & 0.119 & 0.061 \\ 0.107 & 0.073 & 0.000 & 0.000 & 0.033 & 0.046 & 0.117 & 0.104 & 0.019 & 0.008 & 0.010 & 0.019 & 0.112 & 0.043 & 0.206 & 0.103 \\ 0.073 & 0.229 & 0.096 & 0.047 & 0.000 & 0.000 & 0.065 & 0.206 & 0.006 & 0.006 & 0.011 & 0.010 & 0.033 & 0.038 & 0.097 & 0.082 \\ 0.054 & 0.125 & 0.206 & 0.065 & 0.000 & 0.000 & 0.047 & 0.096 & 0.008 & 0.007 & 0.009 & 0.010 & 0.039 & 0.034 & 0.257 & 0.045 \\ 0.252 & 0.057 & 0.104 & 0.117 & 0.046 & 0.033 & 0.000 & 0.000 & 0.006 & 0.012 & 0.030 & 0.012 & 0.040 & 0.111 & 0.061 & 0.119 \\ 0.073 & 0.107 & 0.117 & 0.104 & 0.144 & 0.067 & 0.000 & 0.000 & 0.006 & 0.009 & 0.004 & 0.005 & 0.031 & 0.023 & 0.103 & 0.206 \\ 0.061 & 0.063 & 0.029 & 0.200 & 0.044 & 0.057 & 0.065 & 0.068 & 0.000 & 0.000 & 0.000 & 0.000 & 0.000 & 0.000 & 0.059 & 0.353 \\ 0.065 & 0.052 & 0.036 & 0.085 & 0.047 & 0.052 & 0.125 & 0.092 & 0.000 & 0.000 & 0.000 & 0.000 & 0.000 & 0.000 & 0.009 & 0.437 \\ 0.348 & 0.033 & 0.068 & 0.072 & 0.057 & 0.045 & 0.213 & 0.031 & 0.000 & 0.000 & 0.000 & 0.000 & 0.000 & 0.000 & 0.056 & 0.076 \\ 0.376 & 0.052 & 0.090 & 0.138 & 0.052 & 0.048 & 0.087 & 0.037 & 0.000 & 0.000 & 0.000 & 0.000 & 0.000 & 0.000 & 0.063 & 0.058 \\ 0.096 & 0.082 & 0.044 & 0.239 & 0.050 & 0.058 & 0.086 & 0.066 & 0.000 & 0.000 & 0.000 & 0.000 & 0.000 & 0.000 & 0.084 & 0.194 \\ 0.192 & 0.059 & 0.064 & 0.093 & 0.058 & 0.051 & 0.238 & 0.050 & 0.000 & 0.000 & 0.000 & 0.000 & 0.000 & 0.000 & 0.058 & 0.138 \\ 0.112 & 0.181 & 0.102 & 0.176 & 0.058 & 0.154 & 0.052 & 0.088 & 0.005 & 0.001 & 0.007 & 0.008 & 0.033 & 0.023 & 0.000 & 0.000 \\ 0.181 & 0.112 & 0.052 & 0.088 & 0.049 & 0.027 & 0.102 & 0.176 & 0.028 & 0.035 & 0.009 & 0.007 & 0.077 & 0.055 & 0.000 & 0.000 \end{bmatrix}$$

is computed during preprocessing, i.e. only once per simulation. As requested by Equation (7.37), the sum over each line gives  $\approx 1$ .

The net radiation method (see Sections 7.1.5 and 7.2.4) requires assembling the coefficient matrix  $\mathbf{A}$  from Equation (7.39), which results from the set of 16 algebraic equations (7.38) in this case and takes the surface emissivities and view factors as input. The LU-decomposition of  $\mathbf{A}$  yields

$$\begin{bmatrix} 1.111 & 0.000 & -0.005 & -0.010 & -0.005 & \dots & \dots & \dots & -0.005 & -0.004 & -0.009 & -0.012 & -0.020 \\ 0.000 & 1.111 & -0.024 & -0.007 & -0.015 & & & & -0.001 & -0.004 & -0.003 & -0.020 & -0.012 \\ -0.006 & -0.025 & 1.110 & 0.000 & -0.008 & & & & -0.001 & -0.002 & -0.003 & -0.014 & -0.007 \\ -0.011 & -0.007 & 0.000 & 1.111 & -0.004 & & & & -0.002 & -0.012 & -0.005 & -0.023 & -0.012 \\ -0.007 & -0.023 & -0.010 & -0.005 & 1.111 & & & & -0.001 & -0.004 & -0.004 & -0.012 & -0.010 \\ -0.005 & -0.012 & -0.021 & -0.007 & 0.000 & \dots & & & -0.001 & -0.004 & -0.004 & -0.029 & -0.005 \\ -0.025 & -0.006 & -0.011 & -0.012 & -0.005 & \dots & & & -0.002 & -0.005 & -0.013 & -0.008 & -0.014 \\ -0.007 & -0.011 & -0.012 & -0.011 & -0.015 & & \dots & & -0.001 & -0.004 & -0.003 & -0.013 & -0.024 \\ -0.006 & -0.006 & -0.003 & -0.020 & -0.005 & & \dots & & 0.000 & 0.000 & 0.000 & -0.008 & -0.040 \\ -0.007 & -0.005 & -0.004 & -0.009 & -0.005 & & \dots & & 0.000 & 0.000 & 0.000 & -0.002 & -0.049 \\ -0.035 & -0.003 & -0.007 & -0.008 & -0.006 & & \dots & & 0.000 & 0.000 & -0.001 & -0.007 & -0.010 \\ -0.038 & -0.005 & -0.009 & -0.014 & -0.006 & & & & 1.111 & 0.000 & -0.001 & -0.008 & -0.008 \\ -0.010 & -0.008 & -0.005 & -0.024 & -0.005 & & & & 0.000 & 1.111 & 0.000 & -0.011 & -0.023 \\ -0.019 & -0.006 & -0.007 & -0.010 & -0.006 & & & & 0.000 & 0.000 & 1.110 & -0.008 & -0.017 \\ -0.011 & -0.018 & -0.011 & -0.018 & -0.006 & & & & -0.001 & -0.004 & -0.003 & 1.109 & -0.001 \\ -0.018 & -0.011 & -0.006 & -0.009 & -0.005 & \dots & \dots & \dots & -0.001 & -0.008 & -0.006 & -0.001 & 1.109 \end{bmatrix}$$

The matrices  $\mathbf{F}$  and the LU-decomposed matrix  $\mathbf{A}$  are saved for the subsequent computations.

**Simulation phase.** The computational effort for solving the equation set is comparatively small as the LU-decomposition is performed only once during preprocessing. However, if the internal radiation solving is decoupled from the thermal network – as it is in this book – the surface temperatures (and heat fluxes) need to be determined iteratively.

Therefore, *for each simulation time step*, the following sequence is iterated together with the thermal network as described in Chapter 10 until convergence:

- The load vector  $\mathbf{b}$  from Equation (7.39) is assembled with respect to the respective surface temperatures  $T_i$  in order to get  $E_{bi}$ . The view factors  $F_{i,j}$  are known from the preprocessing.
- With the LU-decomposed matrix  $\mathbf{A}$  and the vector  $\mathbf{b}$ , the equation set is solved for the unknowns  $\mathbf{q}$ .

## 7.3 References

- [1] I. Ashdown. *Radiosity: A programmer's perspective*. John Wiley & Sons, New York, 1994.
- [2] D. Baehr and K. Stephan. *Wärme- und Stoffübertragung*. Springer Verlag, 3rd edition, 1998.
- [3] H.-J. Bungartz, M. Griebel, and Ch. Zenger. *Introduction to computer graphics*. Charles River Media, Inc., 2nd edition, 2004.
- [4] CFX-5, Computational Fluid Dynamics Software, ANSYS, Inc., 2004. <http://www.ansys.com>.
- [5] M.F. Cohen and D.P. Greenberg. The Hemi-Cube: A radiosity solution for complex environments. *Computer Graphics (Proc. ACM SIGGRAPH '85)*, 19(3):31–40, 1985.
- [6] A. Düster. *High order finite elements for three-dimensional, thin-walled nonlinear continua*. PhD thesis, Lehrstuhl für Bauinformatik, Technische Universität München, 2001.
- [7] A. Düster, J. Parvizian, Z. Yang, and E. Rank. The finite cell method for three-dimensional problems of solid mechanics. *Comput. Methods Appl. Mech. Engrg.*, 197:3768–3782, 2008.
- [8] M. Egger, M. Pfaffinger, C. van Treeck, and E. Rank. Berechnung der Wärmestrahlungsausbreitung für die thermische Komfortanalyse in Innenräumen. In R. Koenigsdorff and C. van Treeck, editors, *BauSIM2006, Erste deutsch-österreichische IBPSA Konferenz, 9.-11. Oktober*, TU München, ISBN-13: 978-3-00-019823-6, 2006.
- [9] R. Endl. *Octree Strahlgeneratoren*. Würfel-Verlag, 1994.
- [10] A.S. Glassner. *An introduction to ray tracing*. Academic Press, London, 1989.

- [11] C.M. Goral, K.E. Torrance, D.P. Greenberg, and B. Battaile. Modeling the interaction of light between diffuse surfaces. *Computer Graphics (Proc. ACM SIGGRAPH '84)*, 18(3):213–222, 1984.
- [12] H.C. Hottel. Radiant heat transmission. In W.H. McAdams, editor, *Heat Transmission*, chapter 4. McGraw-Hill, New York, 3rd edition, 1954.
- [13] H.C. Hottel and A.F. Sarofim. *Radiative Transfer*. McGraw-Hill, New York, 1967.
- [14] J.R. Howell and M. Perlmutter. Monte Carlo solution of thermal transfer through radiant media between gray walls. *ASME Journal of Heat Transfer*, 86(1):116–122, 1964.
- [15] A. Kollmar and W. Liese. *Die Strahlungsheizung*. R. Oldenbourg, München, 1957.
- [16] A. Meister. *Numerik linearer Gleichungssysteme*. Vieweg, 2nd edition, 2005.
- [17] G.P. Mitalas and D.G. Stephenson. FORTRAN IV programs to calculate radiant interchange factors. BDR-25, National Research Council of Canada, Division of Building Research, Ottawa, Canada, 1966.
- [18] M.F. Modest. *Radiative Heat Transfer*. Academic Press, USA, 2nd edition, 2003.
- [19] W. Nusselt. Graphische Bestimmung des Winkelverhältnisses bei der Wärmestrahlung. *VDIZ*, 72:673, 1928.
- [20] W.H. Press, S.A. Teukolsky, W.T. Vetterling, and B.P. Flannery. *Numerical recipes in C++*. Cambridge University Press, 2nd (C++) edition, 2002.
- [21] V.S. Ryaben'kii and S.V. Tsynkov. *A theoretical introduction to numerical analysis*. Chapman & Hall/CRC, 2007.
- [22] Y. Saad and M.H. Schultz. A generalized minimal residual algorithm for solving nonsymmetric linear systems. *SIAM J. Sci. Stat. Comput.*, 7:856–869, 1986.
- [23] H.R. Schwarz. *Numerische Mathematik*. B.G. Teubner, 4th edition, 1997.
- [24] B.A. Szabó and I. Babuska. *Finite element analysis*. John Wiley & Sons, 2001.
- [25] C. van Treeck, J. Frisch, M. Egger, and E. Rank. Model-adaptive analysis of indoor thermal comfort. In *Building Simulation 2009*, Glasgow, Scotland, 2009.
- [26] VDI 6020 Part 1. *Requirements for methods of building performance simulation, part 1: buildings*. VDI Verein Deutscher Ingenieure, Beuth Verlag, 2001.
- [27] G.N. Walton. Calculation of obstructed view factors by adaptive integration. NISTIR 6925, National Institute of Standards and Technology (NIST), 2002.

# Chapter 8

## Solar radiation processes

### 8.1 Required quantities and definitions

For the dynamic simulation detailed knowledge about the solar irradiation is required in order to calculate the absorption of solar radiation at opaque surfaces, the transmission, absorption and reflection of multi-cover glazing systems as well as the internal distribution of the transmitted portion. The specific optical properties of windows is covered by the next chapter.

It is distinguished between *beam radiation*  $I_{beam}$ , the received solar radiation without having been scattered by the atmosphere, and the *diffuse radiation*  $I_{diff}$  which is received after its direction has been changed by atmospheric scattering [5], cf. Figure 8.1. The *global radiation* in terms of the intensity normal to the rays is the sum of both components

$$I_{global} = I_{beam} + I_{diff} \quad (8.1)$$

given per unit area in  $[W/m^2]$ . (Note, that the term global radiation is sometimes also defined in terms of the sum of direct and diffuse radiation incident to a horizontal receiver [27].) It is further distinguished between the *irradiance*, the rate at which radiant energy is incident on a surface, and the *irradiation*, the incident energy on a surface obtained by integration of the irradiance over time (SI unit for the time is [s]). The *radiosity* is the rate at which radiant energy leaves the surface [5].

The incidence angle of the beam radiation depends on the location of the building, the slope and orientation of the surface in question and the respective time of the year. Figure 8.2 indicates the seasonal dependence of the sun path and elevation (the plan view of the diagram is called sun chart). Values for the directed, diffuse and global irradiance as obtained from local



Figure 8.1: Beam and diffuse radiation,  $I_{beam}$  and  $I_{diff}$ .

weather data (see section 4.1.1) are usually given for a horizontal surface and must accordingly be converted. The algorithms will be described in the next sections.

In addition to the diffuse radiation due to atmospheric scattering, also solar radiation reflected from the ambient environment and the urban environment contributes to the energy balance of a building.

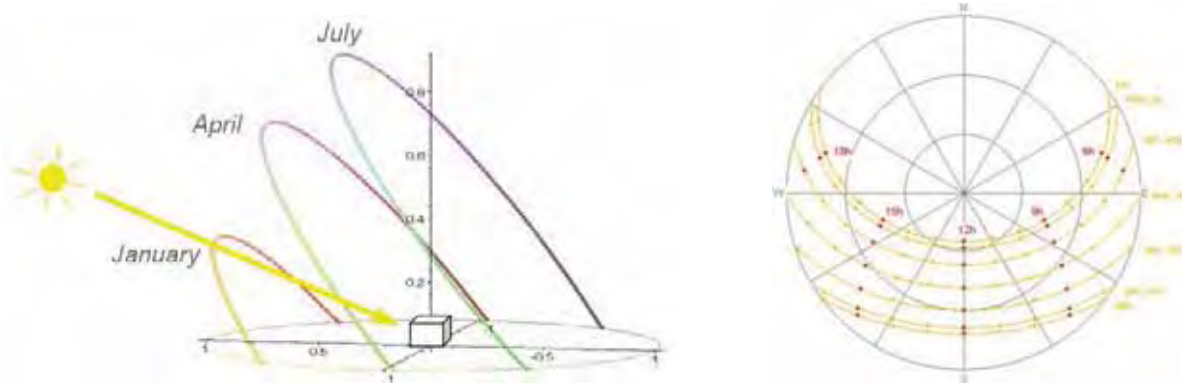


Figure 8.2: Seasonal dependence of the position of the sun, shown as sun chart in 3D and 2D, respectively. The right hand picture is taken from the software SunPath.

## 8.2 The solar spectrum

For solar radiation processes, the wavelength of interest ranges from  $0.3\ldots3\mu m$ . The blackbody surface temperature of the sun is close to  $6000^{\circ}C$  (for exact values refer to [5]). The *solar constant* ( $1367\text{ W/m}^2$ ) indicates "the energy from the sun, per unit time, received on a unit area of surface perpendicular to the direction of propagation of radiation, at mean earth-sun distance, outside of the atmosphere" [5].

The geometry of the sun–earth configuration is given in Figure 8.3. Due to the variation of

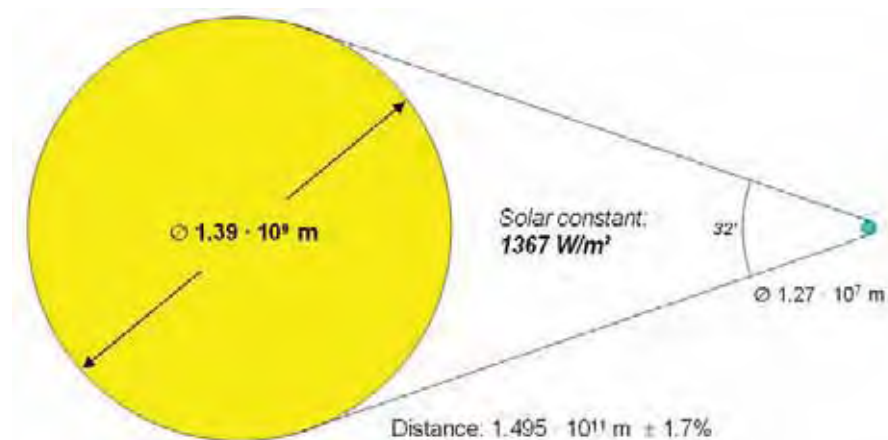


Figure 8.3: Geometry of sun–earth relationship, adapted from [5].

the earth–sun distance of  $\pm 1.7\%$ , the extraterrestrial radiation flux varies by  $\pm 3\%$  as shown in Figure 8.4. According to [5] other sources of variations can be neglected for engineering related purposes.

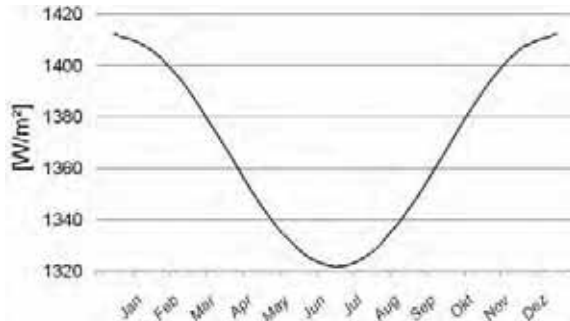


Figure 8.4: Variation of the extraterrestrial radiation flux [5].

The relevance of short and long wave radiation in simulation is immediately clear from Figure 8.5. The figure shows the radiation emitted from a Planck emitter at  $6000^{\circ}\text{C}$ , see axis on the left hand side, and the emitted radiation for the case of operative room temperature at  $20^{\circ}\text{C}$ . As indicated above, the solar spectrum ranges from  $\lambda = 0.3\dots 3\mu\text{m}$  whereas the infrared range begins at approximately  $\lambda > 2\mu\text{m}$ . The visible range which is important for daylighting is  $0.38\dots 0.78\mu\text{m}$ . The amount of emitted energy varies by one order of magnitude. From the shifted curves it can be seen that windows can be treated as opaque for the long wave radiation.

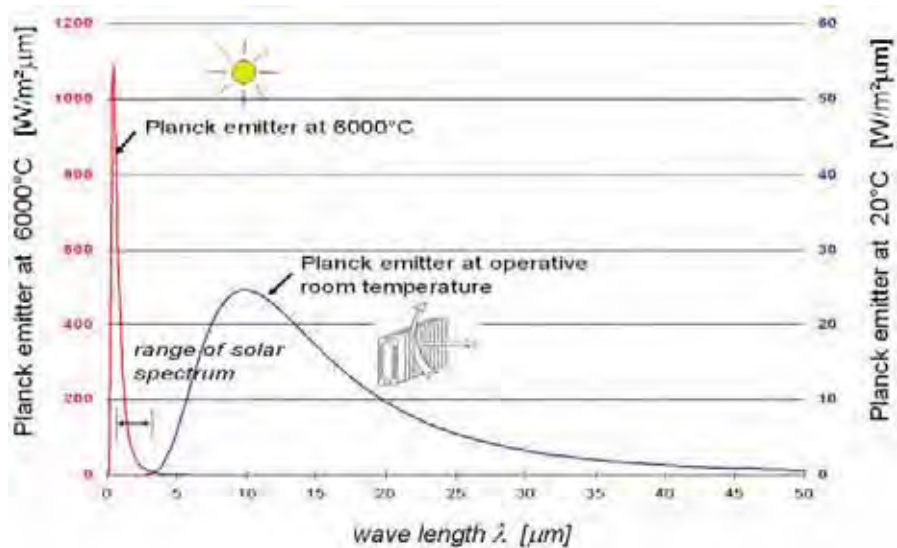


Figure 8.5: Emitted radiation of different Planck emitters (cave: different scaling).

Figure 8.6 shows the solar spectrum according to ISO 9050 which considers scattering and absorption of the radiation within the atmosphere. Scattering is caused by the interaction with air molecules, water vapor and other particles (Rayleigh theory). The absorption in the atmosphere is due to ozone (ultraviolet range), water vapor and carbon dioxide (infrared range).

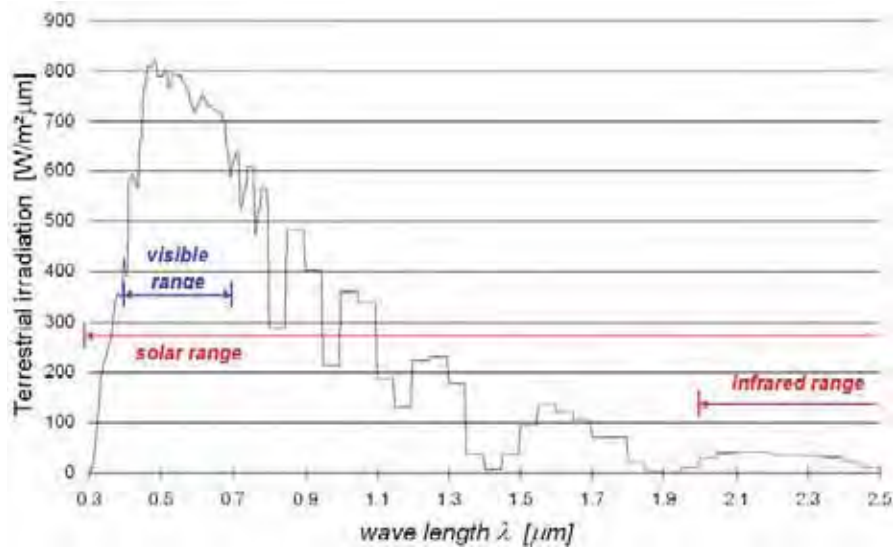


Figure 8.6: Atmospheric solar spectrum according to ISO 9050. The local minima are due to scattering and atmospheric absorption.

## 8.3 Position of the sun in the sky

### 8.3.1 Local position and orientation of the building model

In order to transform irradiation values known for the horizontal case to an arbitrarily tilted surface, the position of the sun in the sky must be determined. In terms of the local position of the building, the following variables are required according to Figures 8.7 and 8.8:

- the *site latitude*  $\phi$  which is the angular location north or south of the equator, north positive, with  $-90^\circ \leq \phi \leq 90^\circ$ ,
- the *longitude*  $L_{local}$  of the location, measured west positive, starting from base meridian  $L_{std}$ , with  $0^\circ \leq L \leq 360^\circ$ ,

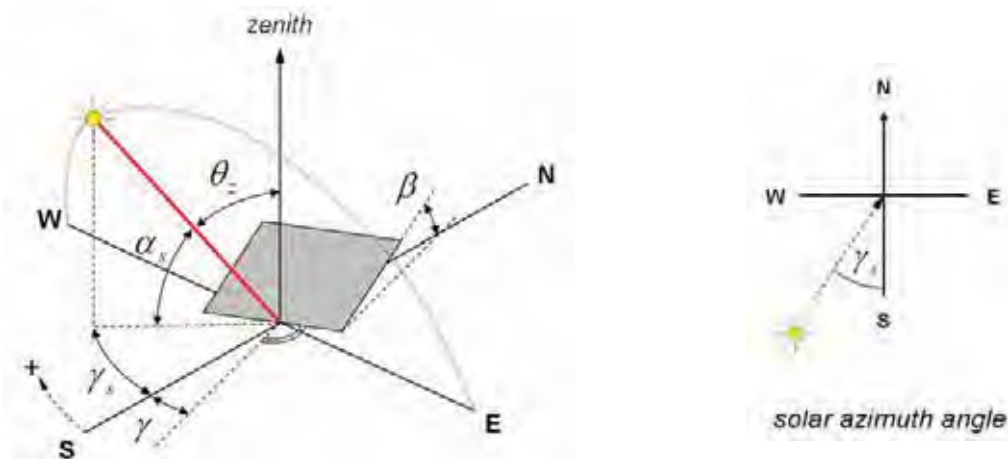


Figure 8.7: Definition of angular dependencies according to [5].

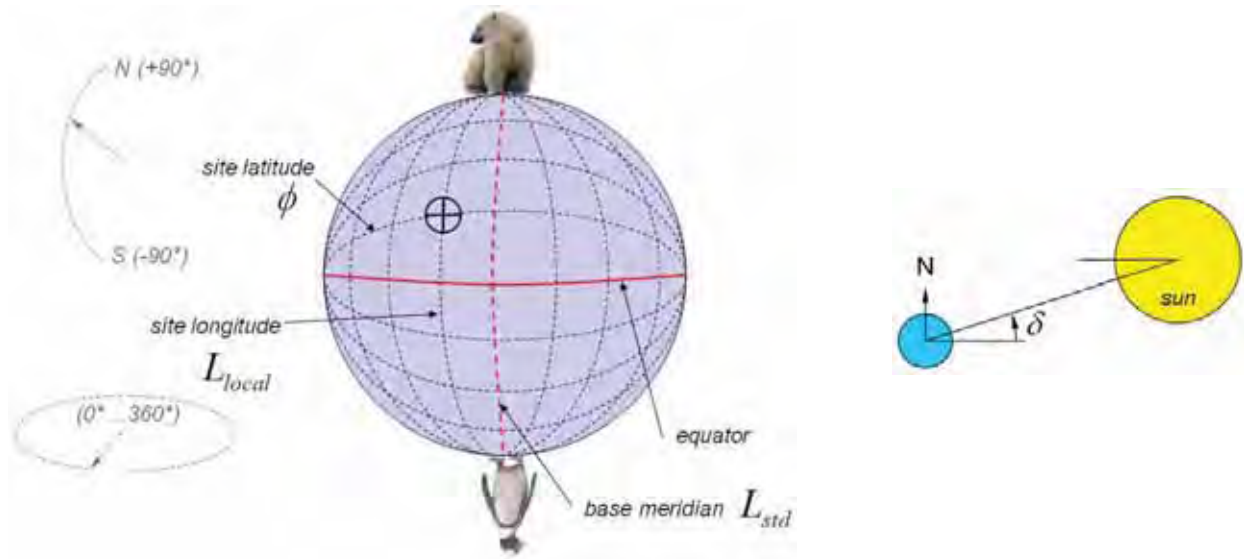


Figure 8.8: Local position of the building with respect to the site latitude  $\phi$ , longitude  $L_{local}$  and base meridian  $L_{std}$ . The right hand side shows the meaning of the declination angle  $\delta$ .

- the *surface slope*  $\beta$ , the angle between the plane of the surface in question and the horizontal,  $0^\circ \leq \beta \leq 180^\circ$ , where  $\beta = 90^\circ$  means an upright surface, and
- the *surface azimuth angle*  $\gamma$ , i.e. the deviation of the projection of the surface normal onto a horizontal plane from the local meridian, zero due south, west positive,  $-180^\circ \leq \gamma \leq 180^\circ$ .

In the following subsections (angles in formulae in radians), formulae are given for calculating

- the *solar zenith angle*  $\theta_z$  or its complement, the *solar elevation angle*  $\alpha_s$ ,
- the *solar azimuth angle*  $\gamma_s$ , and
- the *surface incidence angle*  $\varphi$  according to Figure 8.9.

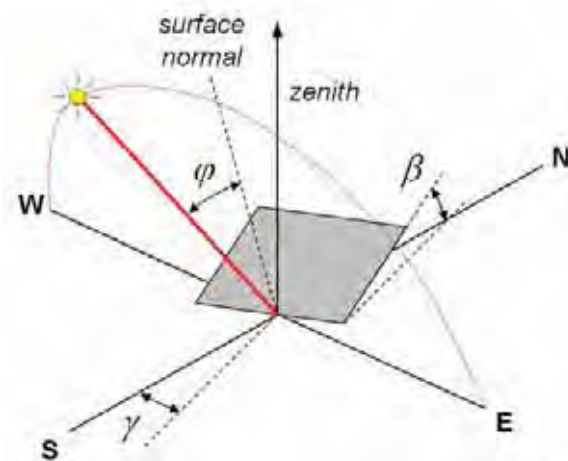


Figure 8.9: Definition of the surface incidence angle  $\varphi$ .

### 8.3.2 Solar time and hour angle

In order to express the angular dependencies with transcendent functions, the simulation (standard) time  $t$  [h] is converted to the *solar time*. The latter serves as input to calculate the so-called *hour angle*. The solar time  $t_{sol}$  is the time based on the apparent angular motion of the sun across the sky, with solar noon the time the sun crosses the meridian of the observer. The solar time accordingly differs from the local clock time.

$$t_{sol} = t - \frac{4}{60} (L_{std} - L_{local}) + \frac{Z(t)}{60} \quad [h] \quad (8.2)$$

Two corrections are necessary with respect to the standard time  $t$ :

- The difference in the longitude between the observer's meridian  $L_{local}$  and the base meridian for the local standard time  $L_{std}$  (Greenwich =  $1^\circ$ , for example). It takes the sun 4 minutes to transverse  $1^\circ$  of longitude (longitudes in degrees west according to Figure 8.8).
- The perturbations in the earth's rate of rotation are expressed by the equation of time  $Z(t)$  as plotted in Figure 8.10 with

$$Z(t) = -7.66 \sin\left(\frac{x\pi}{180}\right) - 9.87 \sin\left[\left(2x + 24.99 + 3.83 \sin\left(\frac{x\pi}{180}\right)\right) \frac{\pi}{180}\right] \quad (8.3)$$

$$\text{and } x = 0.9856 \cdot \text{day}(t) - 2.72 \quad [\text{rad}] .$$

The simulation time  $t$  is usually given in hours with  $0 \leq t \leq 8760$  (or seconds). The day of the year is obtained by

$$\text{day}(t) = \text{round}(t/24 + 0.49) \quad \text{with} \quad 1 \leq \text{day}(t) \leq 365 \quad (8.4)$$

and for the hour of the day one gets

$$\text{hour}(t) = t + 24(1 - \text{day}(t)) \quad \text{with} \quad 1 \leq \text{hour}(t) \leq 24 \quad . \quad (8.5)$$

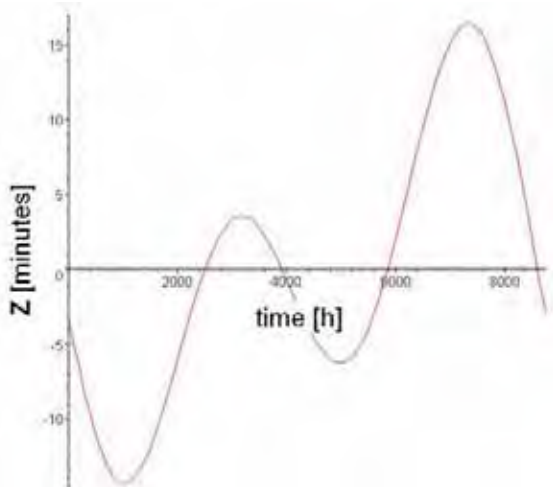
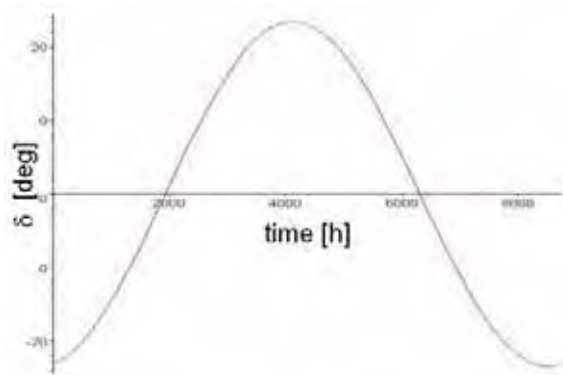


Figure 8.10: Equation of time  $Z(t)$ .



The *hour angle*  $\omega$  is defined as the angular displacement of the sun east or west of the local meridian due to the rotation of the earth on its axis at  $15^\circ$  per hour, morning negative, afternoon positive [5], where  $t$  is given in [h].

$$\omega = 15 (t_{sol} - 12) \frac{\pi}{180} \quad (8.6)$$

### 8.3.3 Solar declination

The *solar declination angle*  $\delta$  is the angular position of the sun at solar noon, i.e. when sun is at the local meridian with respect to the plane of the equator, north positive, compare to Figure 8.8 [5].

$$\delta = \frac{23.45 \pi}{180} \sin \left[ (280.1 + 0.9863 \cdot day(t)) \frac{\pi}{180} \right] , \quad -23.45^\circ \leq \delta \leq 23.45^\circ \quad (8.7)$$

The function is plotted in Figure 8.11.

### 8.3.4 Solar zenith and elevation angle

As defined in Figure 8.7 the *solar zenith angle*  $\theta_z$  is the angle between the vertical and the line to the sun which equals the incidence angle for a horizontal surface if  $\beta = 0^\circ$ . It is implicitly given by

$$\cos \theta_z = \sin \phi \sin \delta + \cos \phi \cos \delta \cos \omega , \quad 0^\circ \leq \theta_z \leq 90^\circ . \quad (8.8)$$

The *solar elevation angle*  $\alpha_s$  is the angle between the horizontal and the line to the sun and is thus defined as the complement of the zenith angle by

$$\alpha_s = 90^\circ - \theta_z , \quad 0^\circ \leq \alpha_s \leq 90^\circ . \quad (8.9)$$

### 8.3.5 Surface incidence angle

The *surface incidence angle*  $\varphi$  is the deviation of the line to the sun from the normal of the surface under consideration according to Figure 8.9.

$$\begin{aligned} \cos \varphi = & \sin \delta \sin \phi \cos \beta \\ & - \sin \delta \cos \phi \sin \beta \cos \gamma \\ & + \cos \delta \cos \phi \cos \beta \cos \omega \\ & + \cos \delta \sin \phi \sin \beta \cos \gamma \cos \omega \\ & + \cos \delta \sin \beta \sin \gamma \sin \omega , \quad -90^\circ \leq \theta_z \leq 90^\circ . \end{aligned} \quad (8.10)$$

An incidence angle of  $\varphi = 0^\circ$  means a direct normal direction. The formula can be further simplified for the upright or the horizontal case as some of the expressions become zero in these cases.

### 8.3.6 Solar azimuth angle

Last but not least, the *solar azimuth angle*  $\gamma_s$  is the displacement from south, west positive, of the beam projected on the horizontal plane and is implicitly given by [18]

$$\cos \gamma_s = \frac{\sin \phi \cos \theta_z - \sin \delta}{\cos \phi \sin \theta_z} , \quad -180^\circ \leq \gamma_s \leq 180^\circ , \quad (8.11)$$

or, in a similar manner, by the relationship

$$\sin \gamma_s = \frac{\sin \omega \cos \delta}{\cos \alpha_s} , \quad \cos \gamma_s = \frac{\cos \omega \cos \delta \sin \phi - \sin \delta \cos \phi}{\cos \alpha_s} . \quad (8.12)$$

### 8.3.7 Sun trajectory expressed with spherical coordinates

With the above defined functions, the sun chart shown in Figure 8.2 can be drawn using spherical coordinates [1], for example. For a radius  $r$  the trajectory on the ground plane  $z = 0$  is obtained by the parametric definition

$$\begin{aligned} x(t) &= -r \sin \theta_z \sin \gamma_s \\ y(t) &= -r \sin \theta_z \cos \gamma_s \\ z(t) &= r \cos \theta_z \end{aligned} \quad (8.13)$$

where values for the curve parameter  $t$  are taken for characteristic daytimes each.

## 8.4 Solar irradiation to arbitrarily tilted surface

### 8.4.1 Transformation of beam radiation

The horizontal beam radiation  $I_{beam}$  as interpolated from the weather data for the current time step can be transformed with respect to the tilted surfaces by a geometric factor  $R$ .

$$I_{beam,\varphi} = R \cdot I_{beam} \quad (8.14)$$

The factor expresses the ratio of beam radiation on a tilted to that on a horizontal surface [5] and can be determined by

$$R = \frac{\cos \varphi}{\cos \theta_z} , \quad R \leq 5 , \quad (8.15)$$

with  $\theta_z$  and  $\varphi$  obtained from equations (8.8) and (8.10)<sup>1</sup>.

### 8.4.2 Transformation of diffuse radiation

The total radiation to a sloped surface can be approximated by the isotropic diffuse sky model by LIU and JORDAN [15]. It is calculated as the sum of the beam radiation  $I_{beam,\varphi}$ , the isotropic diffuse and the solar radiation which is reflected from the ground and environment

---

<sup>1</sup>In (8.15) the parameter range of  $\cos \theta_z$  must be restricted as the denominator can become zero.

[5]. The latter two terms are both diffuse and quasi independent of the direction.

In the model, the view factor for a tilted surface with respect to the sky is  $(1 + \cos \beta)/2$  and the view factor to the ground is given by  $(1 - \cos \beta)/2$ . The influence of the surrounding environment is approximated by the lump-sum diffuse reflectance  $\rho_{ground}$  (usually estimated by 20%).

The total radiation for a tilted surface with surface slope angle  $\beta$  is then given by

$$I_{global,\varphi} = R \cdot I_{beam} + I_{diff,\varphi} \quad (8.16)$$

with

$$I_{diff,\varphi} = \frac{(1 + \cos \beta)}{2} I_{diff} + \rho_{ground} \frac{(1 - \cos \beta)}{2} I_{global} . \quad (8.17)$$

In simulation practice, the sum of beam radiation  $I_{beam,\varphi}$  and the diffuse sky radiation  $\frac{1}{2}(1 + \cos \beta) I_{diff}$  should be restricted with respect to the solar constant (and atmospheric absorption). For the general definition of view factors it is referred to Chapter 7.

With special emphasis on the urban context, ROBINSON et al. [22] developed a fast radiosity solver for solar radiation modeling and compared their approach with results obtained with the simulation tool RADIANCE [14]. The algorithms are available in the simulation code SUNtool [21].

### 8.4.3 Absorption at opaque surfaces

In order to compute the absorption of short wave radiation at opaque surfaces, the color and surface dependent absorption properties are required. In building simulation it is sufficient to express the specific heat flux density for a tilted surface  $q_{sw,\varphi}$  according to Equation (3.9) by

$$q_{sw,\varphi} = \alpha_{sw} (I_{beam,\varphi} + I_{diff,\varphi}) \quad (8.18)$$

where  $\alpha_{sw}$  is obtained from standards or from the literature. For typical coatings, values are given in Table 8.1. For a general discussion of short wave radiation absorption at opaque surface it is referred to the book of MODEST [17].

Coating	$\alpha_{sw}$
white coating	0.3
bright finery	0.4
clinker	0.6
bituminised board	0.95

Table 8.1: Color and surface dependent absorption coefficients.

#### 8.4.4 Example

The following example details the application of the above defined formulae for the location of the climatic region of the test reference year TRY5 (Würzburg, Germany) which was already used in Section 3.7 for the monthly energy balance method. In this case, the site longitude is  $L = -9.9$  and the latitude  $\phi = 49.8$ . The results are shown for a winter and a summer day each.

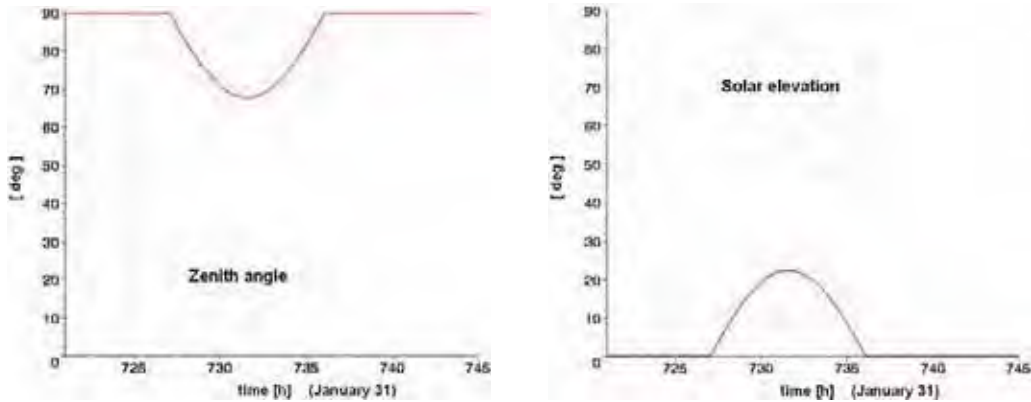


Figure 8.12: Zenith and elevation angle for January 31 ( $L = -9.9, \phi = 49.8$ ).

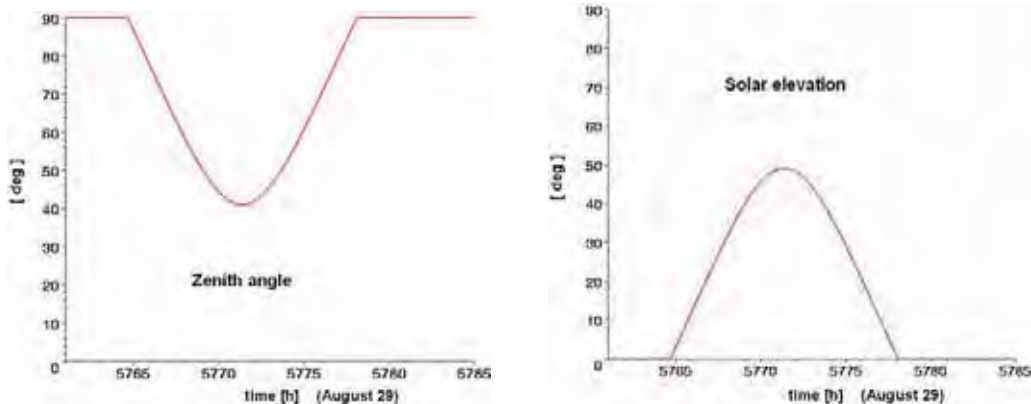


Figure 8.13: Zenith and elevation angle for August 29 ( $L = -9.9, \phi = 49.8$ ).

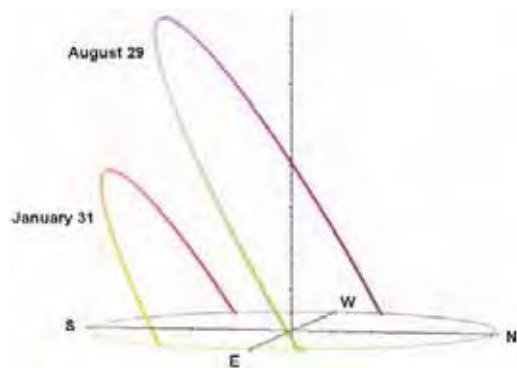


Figure 8.14: Sun chart for January 31 and August 29 (location:  $L = -9.9, \phi = 49.8$ ).

Figure 8.12 shows the course of the solar zenith  $\theta_z$  and its complement, the elevation angle  $\alpha_s$ , for January 31 ( $t = 721\ldots745$ ) and Figure 8.13 for August 29 ( $t = 5761\ldots5785$ ). By further considering the solar azimuth angle, the sun trajectory can be drawn for these days which is shown in Figure 8.14.

As indicated in Sections 8.4.1 and 8.4.2, the irradiation data for the beam and diffuse radiation, which are specified for a horizontal surface in a weather data file, must be transformed according to the orientation and slope of each surface in question. Figure 8.15 depicts the differences between beam and diffuse radiation for a horizontal surface (slope  $\beta = 0^\circ$ ) and an upright surface (slope  $\beta = 90^\circ$ ) oriented due west (azimuth  $\gamma = +90^\circ$ ), respectively, for January and August. In Figure 8.16, the corresponding surface incidence angles  $\varphi$  can be seen.

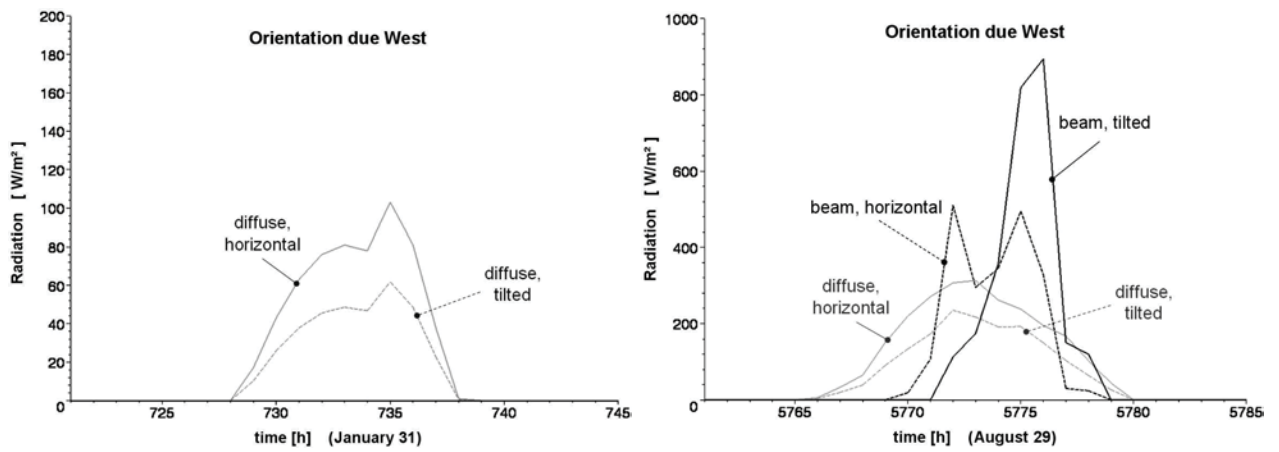


Figure 8.15: Comparison between diffuse and beam radiation incident to horizontal surface and to upright surface oriented due west ( $1m^2$ ) for January 31 and August 29 of TRY5.

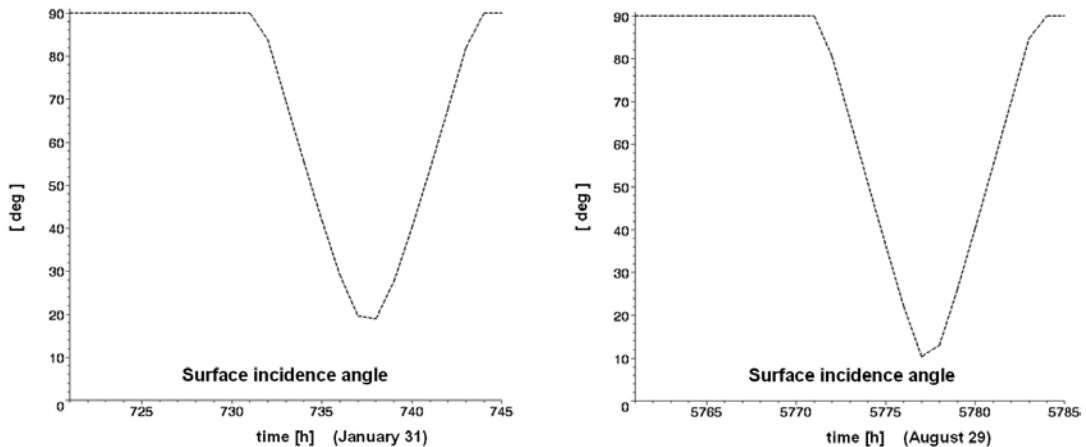


Figure 8.16: Surface incidence angles  $\varphi$  for an upright surface oriented due west for January 31 and August 29. If  $\varphi > 90^\circ$ , the surface cannot be seen by the sun;  $\varphi = 0^\circ$  means perpendicular to the surface which is obviously never the case.

The next figures further address the differences in the orientation. In Figure 8.17 the amount

of beam and diffuse radiation incident to an upright surface (slope  $\beta = 90^\circ$ ) oriented due east, south, west and north is shown for the January time frame. Figure 8.18 indicates the same but for August. It is noted that the axes are differently scaled.

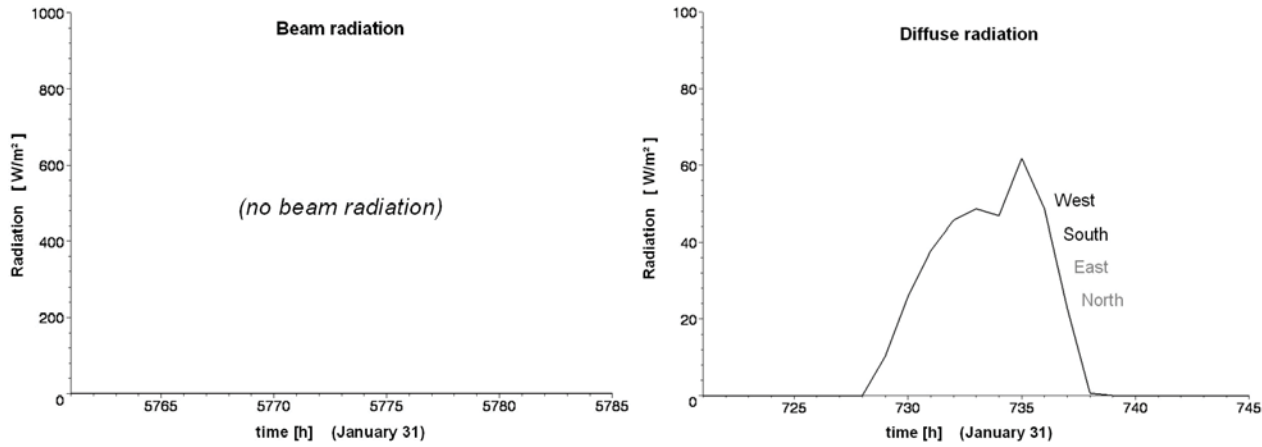


Figure 8.17: Incident beam and diffuse radiation for January 31 ( $t = 721\ldots745$ ) of TRY5 to upright surface ( $1m^2$ ) oriented due east, south, west and north.

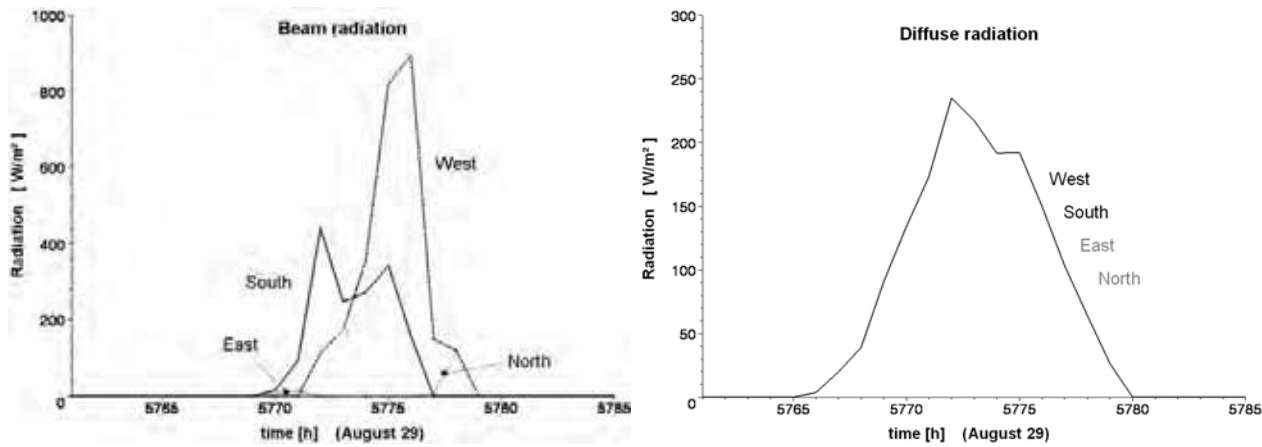


Figure 8.18: Incident beam and diffuse radiation for August 29 ( $t = 5761\ldots5785$ ) of TRY5 to upright surface ( $1m^2$ ) oriented due east, south, west and north.

## 8.5 Shading analysis

A part of the incident diffuse short wave radiation depends on the reflection from the ground and the environment as indicated in Section 8.4.2. The values are accordingly influenced by the surrounding objects and differ between the country side and an urban environment. Likewise the beam radiation is affected by the surrounding environment. Depending on the respective position of the sun, the sun may not be visible from a wall or window surface of the building in question, i.e. the beam may be obstructed by other buildings or objects.

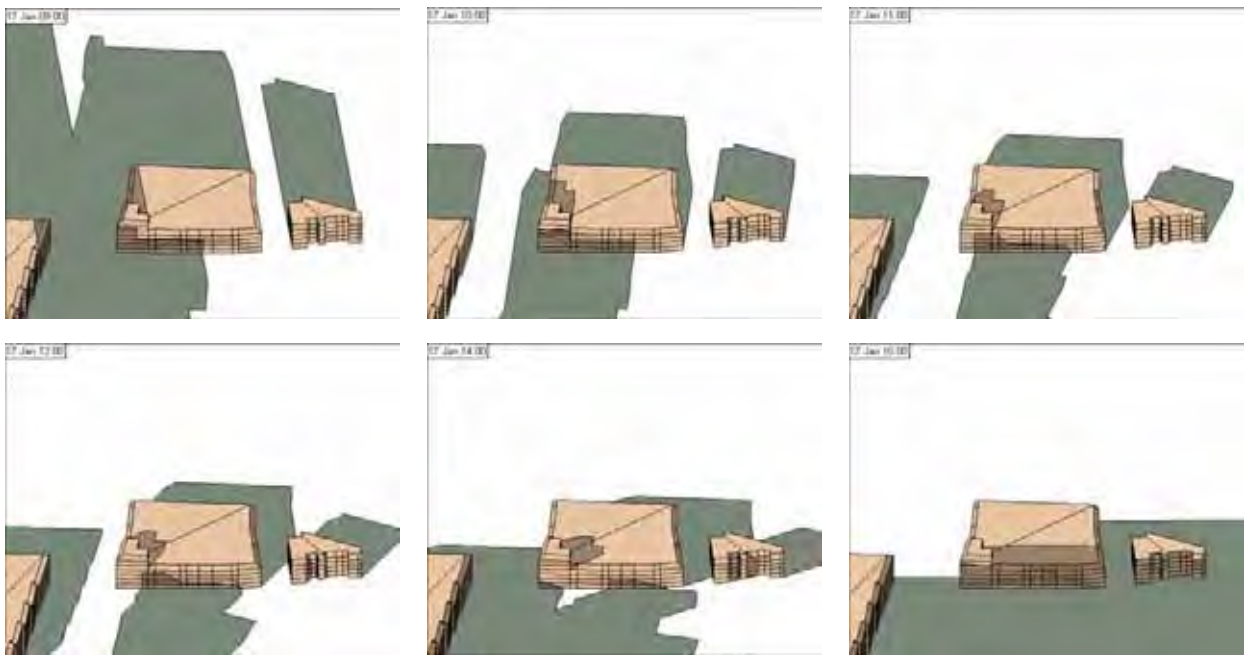


Figure 8.19: Shading analysis for January 17 at 9:00, 10:00, 11:00, 12:00, 14:00 and 16:00 [20]. Picture courtesy of MÜLLER-BBM, Germany.

In building simulation, this effect can be a priorily quantified by the *geometrical shading coefficient (GSC)*, which expresses the ratio of an arbitrarily oriented surface being obstructed. The GSC can be computed in advance for every building surface and each time step for a given location, provided that a geometric model of the building and the relevant surrounding objects is available. The GSC data file can be used as input for a dynamic thermal simulation. Figure 8.19 gives an example of a shading analysis for a building ensemble with an inhouse developed tool by the company MUELLERBBM [20]. The algorithm is based on a triangulated surface mesh and computes the change over time of the shade of the surrounding buildings with respect to a building facade in question.

Most building simulation tools include simplified obstruction algorithms [5, 26] for standard configurations such as wing walls, overhangs or skyline profiles. Other tools such as TAS [24] make use of a geometric model and allow for a detailed shading analysis. Tools capable of calculating shading information are summarized in the *Building Energy Software Tools Directory* [25] of the US. Department of Energy. For example, the GSC coefficients can be computed with the tool SOMBRERO [19].

## 8.6 Internal distribution of shortwave radiation

### 8.6.1 Simplified methods

The most simple configuration is a non-geometric model for calculating the zonal distribution of the incident shortwave irradiance according to Figure 8.20. Thereby the net irradiance  $\dot{Q}_{sw}$ , i.e. the sum of beam and diffuse radiation entering the zone, is equally distributed to

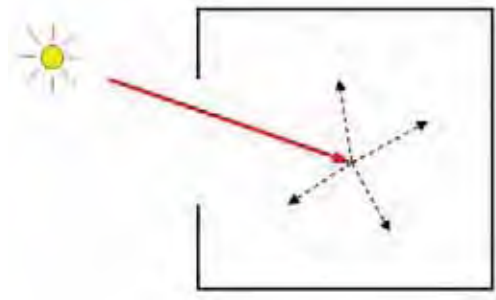


Figure 8.20: Equal or weighted distribution of the irradiance to the surfaces of a zone.

all  $n$  surfaces of the zone in question, for example, using area weighted factors in terms of the absorption and by further neglecting multiple reflections. A similar method is discussed in [8] for example. The heat flux density  $q_{sw,i}$  for surface  $i$  is then obtained by

$$q_{sw,i} = \frac{\alpha_{sw,i}}{\sum_{j=1}^n \alpha_{sw,j} A_j} \dot{Q}_{sw} . \quad (8.19)$$

Some simulation kernels such as [13] make use of a so-called two-star network method for calculating the convective heat transfer to the air node and the radiative heat exchange between the surfaces with an additional artificial temperature node in a parallel manner [23]. According to FEIST [7], this type of model is affordable in terms of the accuracy if compared to single-star methods and helps to reduce the computational effort.

However, in the opinion of the author these approaches are not recommended as the convective air flow pattern inside rooms is strongly influenced by the resultant surface temperatures. If the irradiation is smoothed over multiple surfaces, local effects cannot be resolved. For example, the predominant irradiance to the floor of a zone causes a local increase of the surface temperature and, in turn, a buoyant flow which would not occur if the irradiance is equally distributed over all the surfaces of the respective zone. Chapter 4 further details the subject of air flow patterns.

### 8.6.2 A raytracing algorithm for tracking beam radiation

In simulation it is accordingly more convenient to track the *beam* radiation which enters a zone through a glazing system. It is therefore necessary to treat the distribution of short wave radiation inside rooms in a *geometrical* manner. The *diffuse* part of the radiation is independent of the direction and can be handled in a different way. A well suited method for addressing the latter is the *radiosity method* which was introduced in Chapter 7. As the radiosity method is based on the principle of energy conservation, it already accounts for multiple reflections between surfaces for the diffuse part.

This section will address a very simple *raytracing* algorithm for tracking the beam radiation  $I_{beam}$  which enters and, as the case may be, goes through a zone volume. For the moment it is assumed that the amount  $\tau(\varphi) \cdot I_{beam}$  passes a transparent medium, where  $\tau(\varphi)$  is the transmissivity of the respective window system with respect to the absorption and reflection

losses of the glazing. It depends on the surface incidence angle  $\varphi$  according to Figure 8.9. Chapter 9 below will address the specification of the solar optical properties of windows in detail in terms of the angular and specular dependencies.

**The basic algorithm.** A core advantage of using a geometric model is that radiation can be tracked through multiple zones and air volume elements, if necessary. In order to reduce the computational complexity, the algorithm can account for this effect by the following simplification.

- In a first cycle, for each zone the impact of the directly incident (beam) radiation is calculated separately, after passing through the glazing system(s). This gives the received amount of beam radiation for each surface. For opaque surfaces, a part is absorbed and another part is redistributed (reflected) in a diffuse way ( $\rightarrow$  proceed with radiosity method).
- In a subsequent step, the beam radiation collected for transparent surfaces again passes the respective medium and the former step is repeated. This step is iterated according to the number of zones which are in visible contact. However, in practice a single step is sufficient, for example, if the incident radiation is tracked through a double skin facade or an inner courtyard.

For each time step, the inner algorithm is as follows:

---

**Algorithm A-3** Computation of the direct and diffuse solar radiation distribution.

---

```

1: for all (zones) do
2:   for all (internal triangular surfaces) do
3:     if (window surface) then
4:       if (first run) then
5:         calculate  $I_{\text{beam}}$  and  $I_{\text{diff}}$  for each external surface
6:       else
7:         collect  $I_{\text{beam}}$  and  $I_{\text{diff}}$  at internal transparent surfaces
8:       end if
9:       transmit radiation through medium (separately for beam and diffuse)
10:      distribute  $I_{\text{beam}}$  by raytracing
11:      increment counter of received beam radiation
12:    end if
13:    distribute  $I_{\text{diff}}$  by radiosity
14:    transfer values from facets to surface elements
15:  end for
16: end for

```

---

**Direction of the beam radiation.** The time dependent direction of the beam radiation is specified in terms of the solar azimuth angle  $\gamma_s$  and the zenith angle  $\theta_z$  (cf. Figure 8.7) with the spherical coordinates  $(\gamma_s(t), \theta_z(t), r)$ . With the parametric formulation from Equation (8.13), the normalized direction is obtained by

$$\mathbf{x}_0(t) = \frac{\mathbf{x}(t)}{\|\mathbf{x}(t)\|} \quad \text{with} \quad \mathbf{x}(t) = (x(t), y(t), z(t))^T \quad . \quad (8.20)$$

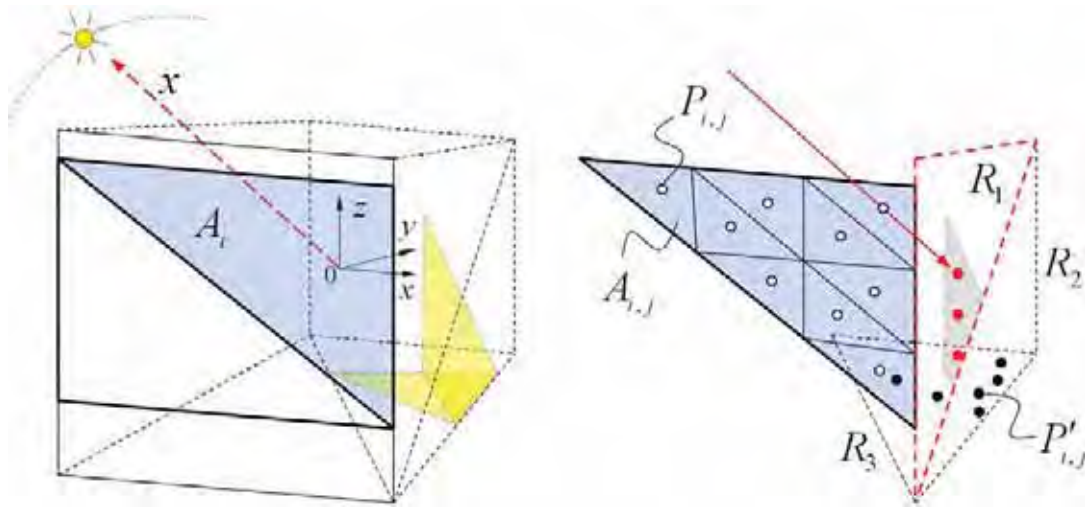


*Figure 8.21:* Left: Subdivision of each window surface into triangular elements  $A_i$  and definition of the vector  $\mathbf{x}$  pointing from the local origin to the sun.  
Right: Decomposition of the triangle into  $n$  congruent sub-triangles  $A_{i,j}$  and determination of center points  $P_{i,j}$ . The beam radiation is tracked for each point  $P_{i,j}$  until intersecting with another surface element  $R_k$  at  $P'_{i,j}$ .

In order to save computing time, it is initially to be checked in terms of the window orientation(s), if the beam radiation enters the zone or not.

**Surface decomposition.** For the wireframe model of the inner air volume shell, each transparent (window) surface is described in terms of two triangles (see Chapter 5). Each triangular element  $A_i$  is decomposed into a set of  $n$  congruent sub-triangles  $A_{i,j}$  ( $j = 1 \dots n$ ), with the points  $P_{i,j}$  at the center of gravity of each facet as shown in Figure 8.21. (Subdivision of a triangle into  $m$  elements per side gives  $n^2$  facets.) The local coordinates of  $P_{i,j}$  are determined once during the preprocessing.

**Tracking the beam radiation.** Having passed the transparent element  $A_i$ , each ray accordingly carries the energy

$$I'_{i,j}(\varphi) = \frac{1}{n} \tau(\varphi) I_{beam} A_i \quad [W] \quad . \quad (8.21)$$

With known direction  $\mathbf{x}_0(t)$  at time  $t$ , the beam radiation is tracked for each point  $P_{i,j}$  until intersecting at  $P'_{i,j}$  with another receiving surface element  $R_k$  of the respective zone. For the latter intersection test an efficient algorithm is required as the test needs to be performed for each ray and window subsurface and time step.

*Note that the geometrical treatment of the short wave radiation takes a significant part of the overall computing time.*

In a first step, it is tested if the ray with direction  $\mathbf{x}_0(t)$  would hit the surface element  $R_k$  from

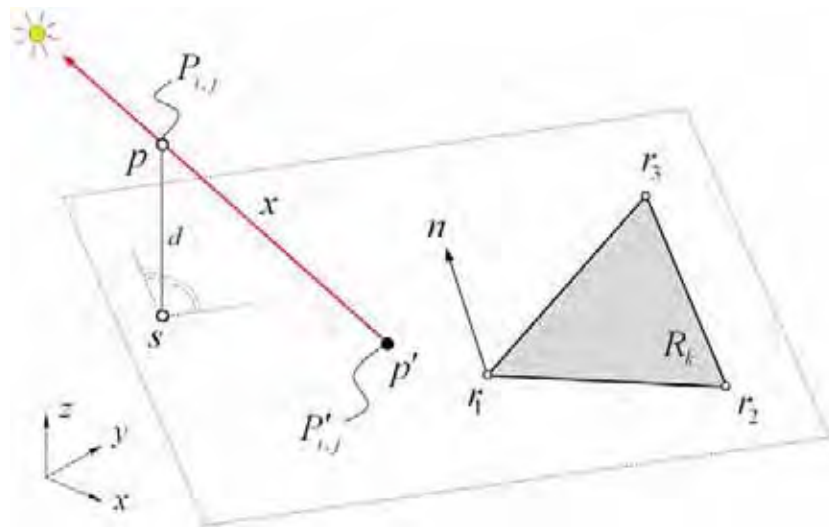


Figure 8.22: Determination of the intersection point  $\mathbf{p}' = P'_{i,j}$  of the line  $\mathbf{p} + \xi \mathbf{x}_0(t)$  (in red) and the plane defined by  $\mathbf{n}_0 \cdot (\mathbf{v} - \mathbf{r}_1) = 0$  (dotted line).

the inward facing side. This is evaluated by

$$\mathbf{n} \cdot \mathbf{x}_0(t) \begin{cases} > 0 & \rightarrow \text{wrong side (stop)} \\ = 0 & \rightarrow \text{beam and surface are parallel (stop)} \\ \leq 0 & \rightarrow \text{correct side (proceed)} \end{cases}, \quad (8.22)$$

where  $\mathbf{n}$  is the surface normal of  $R_k$ .

Secondly, for each triangular surface element  $R_k$  of the zone (without light sources  $A_i$ ), the intersection point  $P'_{i,j}$  between the straight line given by  $\mathbf{p} = P_{i,j}$  and direction  $\mathbf{x}_0(t)$ ,

$$\mathbf{v} = \mathbf{p} + \xi \mathbf{x}_0(t) , \quad (8.23)$$

and the plane of the triangle  $(r_1, r_2, r_3)$

$$\mathbf{n}_0 \cdot (\mathbf{v} - \mathbf{r}_1) = 0 \quad (8.24)$$

is determined. The configuration is detailed in Figure 8.22;  $\mathbf{n}_0$  is the normalized surface normal. Inserting (8.23) into (8.24) gives after some algebra the distance

$$\xi = \frac{(\mathbf{n}_0 \cdot \mathbf{r}_1) - (\mathbf{n}_0 \cdot \mathbf{p})}{(\mathbf{n}_0 \cdot \mathbf{x}_0(t))} \quad (8.25)$$

from point  $P_{i,j}$  to the intersection point  $\mathbf{p}' = P'_{i,j}$  which is obtained by

$$\mathbf{p}' = \mathbf{p} + \xi \mathbf{x} . \quad (8.26)$$

Note that  $P'_{i,j}$  is not necessarily within the triangle  $(r_1, r_2, r_3)$ . This fact is accounted for with a simple area test which evaluates if  $P'_{i,j}$  is inside the triangle  $R_k$  or not. Therefore, the surface

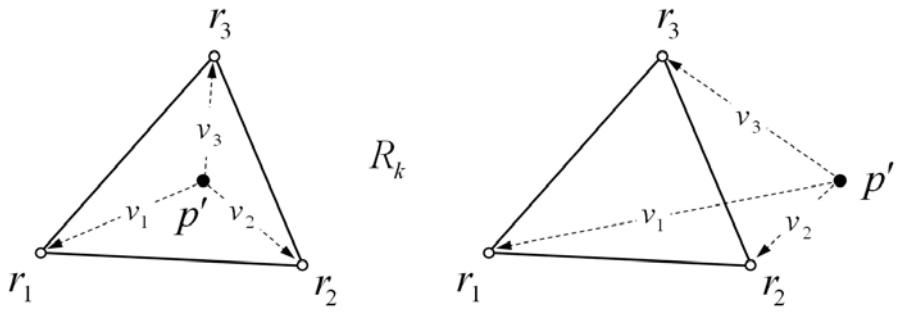


Figure 8.23: Test (2D) if point  $\mathbf{p}'$  is inside the triangle  $(r_1, r_2, r_3)$  or not by comparing the sum of the areas of the three sub-elements with the area of the original element.

areas of the three triangles spanned by the vectors

$$\begin{aligned}\mathbf{v}_1 &= \mathbf{r}_1 - \mathbf{p}' , \\ \mathbf{v}_2 &= \mathbf{r}_2 - \mathbf{p}' \quad \text{and} \\ \mathbf{v}_3 &= \mathbf{r}_3 - \mathbf{p}'\end{aligned}$$

as shown in Figure 8.23 are compared with the surface area of  $R_k$ . If

$$\frac{1}{2} (\|\mathbf{v}_1 \times \mathbf{v}_2\| + \|\mathbf{v}_2 \times \mathbf{v}_3\| + \|\mathbf{v}_3 \times \mathbf{v}_1\|) > R_k , \quad (8.27)$$

then point  $P'_{i,j}$  is outside the triangle  $R_k$ . In this case, the ray does not contribute to the energy balance of the element  $R_k$  and the algorithm is continued until the ray hits a surface. If the ray intersects, the portion  $I'_{i,j}(\varphi)$  is added to the amount of incident beam radiation for this specific element.

As the distance between  $P_{i,j}$  and  $P'_{i,j}$  is known, the question of visibility and obstruction can be further accounted for in terms of a *z-buffer algorithm* known from computer graphics [2, 3].

The application of the algorithm is demonstrated in Figure 8.24 which shows the results of a sequence of successive calculations for the geometry of the VDI 6020 [28] sample room

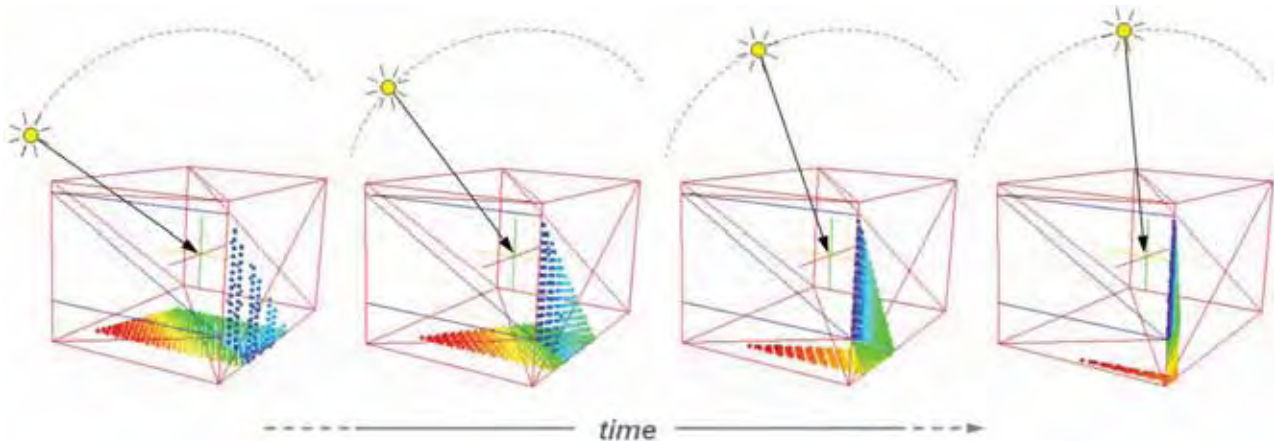


Figure 8.24: Prediction of the incident short wave radiation for different time steps in *iZone*.

defined in Section 3.6. For each window surface and time step, the total amount of the transmitted beam radiation through the window surface is divided into a number of rays which are tracked until reaching another internal surface. For each internal surface, the intersections are counted giving the total amount of the incident beam radiation to each surface. The choice of the number of rays per facet is thereby a tradeoff between the required accuracy and the computational costs.

### 8.6.3 Daylight analysis

Besides the energetic point of view, the location and building geometry also determines the lighting conditions. The daylight quality is influenced by the room partitioning, spatial depth and height as well as the alignment of the facade elements and the urban environment. In simulation, a simplified daylighting analysis according to DIN 5034 [4] is often sufficient in order to estimate the illuminance and daylight quotient and in order to design appropriate shading devices. For a detailed daylight analysis, the software tools *Adeline* [6] or *Radiance* [14] can be used for obtaining photorealistic results.

The lighting demands of office buildings can be covered by daylight up to 80% if appropriate blinds for shading and light reflection are installed together with control devices [11]. In the design, the daylight properties are also determined by the thermal behavior of the building – which sometimes yields opposed optimization strategies in terms of heat protection. For the latter, external shading devices are the best solution. Overhead light elements and lamellae are appropriate measures for re-directing incident (and also diffuse) daylight. An important design parameter is thereby the sky portion that is visible from the point of view of the working place, i.e. the desk.

For example, Figure 8.25 indicates the relation between the room depth and the daylight coefficient. In Figure 8.26, the daylight analysis in an office building is shown [10, 9]. The illuminance describes luminous flux incident on a surface  $e$  per unit area. The typical range

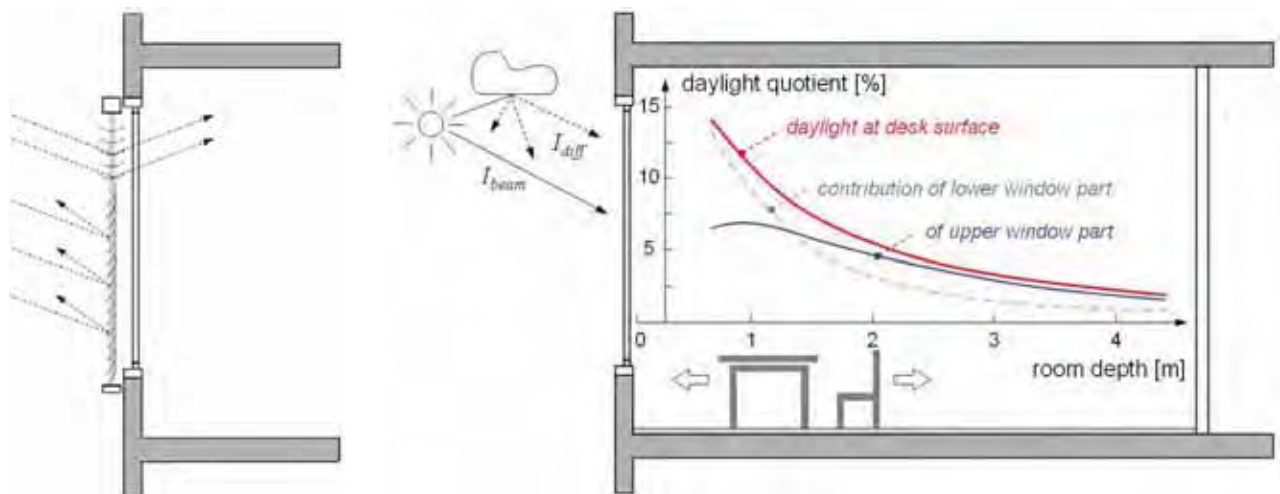


Figure 8.25: Left hand side: External shading blind with different lamellae types for light reflection. Right hand side: Relation between room depth and daylight coefficient ([11], modified).

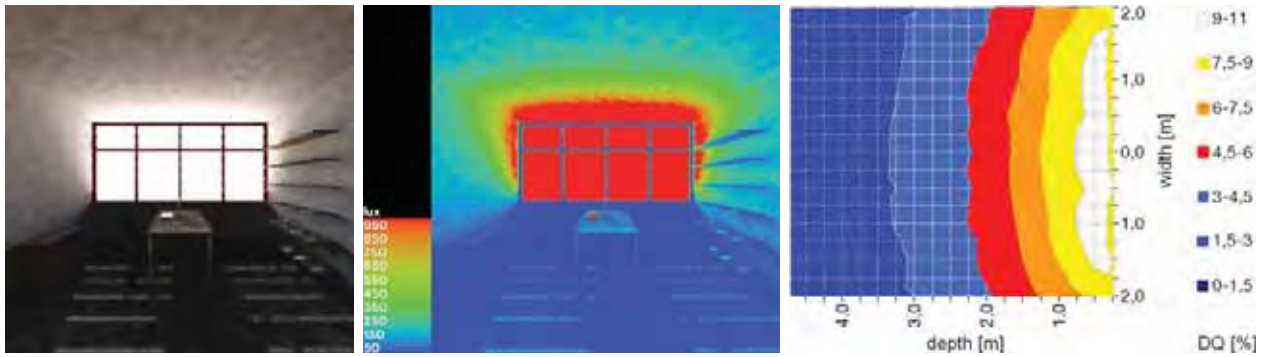


Figure 8.26: Daylight analysis in an office building. Illuminance (*lux*) and daylight quotient with respect to the distance from the window, respectively. Adapted from [10, 9].

is  $100 \cdot 10^3$  *lux* for a bright sunny day over  $10 \cdot 10^3$  *lux* for a cloudy day up to the required 100...1000 *lux* for a typical office room.

In a daylight analysis the influence of the environment and the surrounding buildings must be further taken into account. As already indicated in Section 8.5, prior to a thermal analysis a geometrical shading coefficient (GSC) can be determined, which serves as an input parameter for the building performance simulation. The analysis can be performed with a faceted surface model of the building and its surroundings using a simplified raytracing technique. A model of the surroundings can be obtained from the database of a geographic information system (GIS).

## 8.7 External radiative heat exchange

In order to account for the external radiative heat exchange building surfaces are assumed small compared to the sky firmament. With known external surface emissivities  $\varepsilon_{lw,i}$ , the Stefan-Boltzmann constant  $\sigma$  and the temperature  $T_i$  of the component  $i$  in question the heat flux between the large sky enclosure and the small convex surface is

$$q_{lw,i} = \varepsilon_{lw,i} \sigma (T_{sky}^4 - T_i^4) \quad . \quad (8.28)$$

The *equivalent blackbody sky temperature*  $T_{sky}$  considers that the atmosphere is not at a uniform temperature and that it radiates in the wavelength band from 8 to  $14\mu m$  only [5].

MARTIN and BERDAHL [16], for example, relate the sky temperature to the ambient temperature  $T_{amb}$  [ $K$ ], the dew point temperature  $\vartheta_{dew}$  [ $^{\circ}C$ ] and the sky coverage  $b_{sky}$  by

$$T_{sky} = T_{amb} (\varepsilon_{sky} + (1 - \varepsilon_{sky}) b_{sky})^{1/4} \quad (8.29)$$

with the longwave sky emissivity

$$\varepsilon_{sky} = 0.711 + 0.0056 \vartheta_{dew} + 0.000073 \vartheta_{dew}^2 + 0.013 \cos \left( 15 \frac{\pi t}{180} \right) \quad (8.30)$$

and time  $t$  in hours from midnight. For estimating the sky coverage, KASTEN and CZEPLAK [12] suggest

$$b_{sky} = \begin{cases} \left( 1.4286 \frac{I_{beam}}{I_{global}} - 0.3 \right)^{1/2}, & I_{beam} > 0 \\ 0, & I_{beam} = 0 \end{cases} \quad (8.31)$$

with the radiation values  $I_{beam}$  and  $I_{global}$  for the horizontal case. Further details are summarized in [5]. In simulation, the external radiative heat exchange may be linearized by calculating a radiative heat transfer coefficient with respect to the sky radiation

$$h_{lw,i} = \varepsilon_{lw,i} \sigma (T_{sky}^2 + T_i^2) (T_{sky} + T_i) \quad (8.32)$$

and thus

$$q_{lw,ext,i} = h_{lw,i} \sigma (T_{sky} - T_i) . \quad (8.33)$$

## 8.8 References

- [1] I.N. Bronstein and K.A. Semendjajew. *Taschenbuch der Mathematik*. B.G. Teubner, 25. edition, 1991.
- [2] H.-J. Bungartz, M. Griebel, and Ch. Zenger. *Introduction to computer graphics*. Charles River Media, Inc., 2nd edition, 2004.
- [3] E. Catmull. A hidden-surface algorithm with anti-aliasing. *Computer Graphics (Proc. ACM SIGGRAPH '78)*, 12(3):6–11, 1978.
- [4] DIN 5034:2007. *Daylight in interiors*. DIN Deutsches Institut für Normung e.V., Beuth Verlag, 2007.
- [5] J. Duffie and W. Beckman. *Solar Engineering of Thermal Processes*. John Wiley and Sons Inc., New York, 1991.
- [6] H. Erhorn, J. de Boer, and M. Dirksmöller. ADELIN – An integrated approach to lighting simulation. In *Proc. 5th IBPSA Conf. Building Simulation*, Prague, Czech Republic, September 8-10 1997.
- [7] W. Feist. *Passivhäuser in Mitteleuropa*. PhD thesis, Universität Kassel, 1993.
- [8] G. Hauser. *Rechnerische Vorherbestimmungen des Wärmeverhaltens großer Bauten*. PhD thesis, Universität Stuttgart, 1977.
- [9] G. Hausladen, M. de Saldanha, and P. Liedl. *ClimaSkin, Konzepte für Gebäudehüllen, die mit weniger Energie mehr leisten*. Verlag Callwey, München, 2006.
- [10] G. Hausladen, M. de Saldanha, P. Liedl, and Sager. C. *ClimaDesign, Lösungen für Gebäude, die mit weniger Technik mehr können*. Verlag Callwey, München, 2005.

- [11] D. Hennings and J. Knissel. *Energieeffiziente Bürogebäude*, volume II. BINE Informationsdienst, Fachinformationszentrum Karlsruhe, Germany, 2000.
- [12] F. Kasten and G. Czeplak. Solar and terrestrial radiation dependent on the amount and type of cloud. *Solar Energy*, 24:177–189, 1980.
- [13] S.A. Klein et al. *TRNSYS, A transient system simulation program, reference manual 14.2*. Solar Energy Laboratory, University of Wisconsin-Madison, 1994.
- [14] Lawrence Berkeley National Laboratory, 2008. <http://radsite.lbl.gov>.
- [15] B.Y. Liu and R.C. Jordan. The long-term average performance of flat-plate solar energy collectors. *Solar Energy*, 7:53, 1963.
- [16] M. Martin and P. Berdahl. Characteristics of infrared sky radiation in the United States. *Solar Energy*, 3(4):321–336, 1984.
- [17] M.F. Modest. *Radiative Heat Transfer*. Academic Press, USA, 2nd edition, 2003.
- [18] National Oceanic and Atmospheric Administration (NOAA), US Dep. of Commerce. Solar position calculations. <http://www.srrb.noaa.gov/>.
- [19] A. Niewienda and F.D. Heidt. SOMBRERO, a PC-tool to calculate shadows on arbitrarily oriented surfaces. *Solar Energy*, 58(4–6):253–263, 1996.
- [20] G. Pültz. private communications, 2009. MüllerBBM, Planegg, Germany.
- [21] D. Robinson, N. Campbell, W. Gaiser, K. Kabel, A. Le-Mouel, N. Morel, J. Page, S. Stankovic, and A. Stone. SUNtool - A new modelling paradigm for simulating and optimising urban sustainability. *Solar Energy*, 81(9):1198–1211, 2007.
- [22] D. Robinson and A. Stone. Solar radiation modelling in the urban context. *Solar Energy*, 77(3):295–309, 2004.
- [23] J.E. Seem. *Modeling of heat transfer in buildings*. PhD thesis, Solar Energy Laboratory, University of Wisconsin Madison, 1987.
- [24] TAS – Thermal Analysis Software. Vertrieb durch IFES GmbH, 50226 Frechen, Deutschland.
- [25] US. Department of Energy. Building Energy Software Tools Directory, 2009. [http://http://eere.energy.gov/buildings/tools\\_directory/](http://http://eere.energy.gov/buildings/tools_directory/).
- [26] D.M. Utzinger and S.A. Klein. A method of estimating monthly average solar radiation on shaded receivers. *Solar Energy*, 23:369–378, 1979.
- [27] VDI 3789 Blatt 2. *Environmental meteorology - Interactions between atmosphere and surfaces – Calculation of short-wave and long-wave radiation*. VDI Verein Deutscher Ingenieure, Beuth Verlag, 1994.
- [28] VDI 6020 Part 1. *Requirements for methods of building performance simulation, part 1: buildings*. VDI Verein Deutscher Ingenieure, Beuth Verlag, 2001.

# Chapter 9

## Optical and thermal properties of windows

### 9.1 Heat transfer through multi-layered glazings

The preceding Chapters 7 and 8 explained the terms short and long wave radiation, the difference between diffuse and beam radiation, and how to calculate the position of the sun with respect to the time of the year and the position of a respective building surface. It was shown, how to compute the amount of the incident diffuse and direct solar radiation to an arbitrarily oriented surface and the long wave radiative heat exchange between the sky and a small (building) surface.

In this chapter, we consider a *window model* in order to determine the transmission of the solar radiation through a window with respect to the losses by reflection and absorption. As it was previously explained in Section 3.5.2, the transmitted solar energy plus the portion of the heat absorbed within the glazing, which is transferred to the inside, can be summarized to the solar heat gain coefficient  $g [-]$  (which still is a function of the solar incidence angle).

For the long wave radiation, windows are usually treated as opaque objects. The long wave radiative heat transfer therefore depends on the physical properties of the surfaces in terms of the surface emissivities, and the heat transmission through the fenestration product. However, in the scope of this book, we will neglect the thermal capacity of the windows, and temperature values are calculated via surface heat balances at the internal and external window surfaces only, as it will be explained in Chapter 10 in detail. We therefore compute the transmission heat gains or losses by means of an overall U-value, i.e., the total heat transfer coefficient [ $W/(m^2K)$ ] of the glazing system. A model which takes into account the thermal capacity of windows is discussed in [9], for example. It is also referred to [8, 21, 20, 1].

#### 9.1.1 Structure of a glazing system

A window system consists of several materials and thermal domains which interact with each other. The glazing system is usually composed of two or three parallel glass panes, the gap between filled with air or a rare gas such as argon or krypton. The panes may be coated with

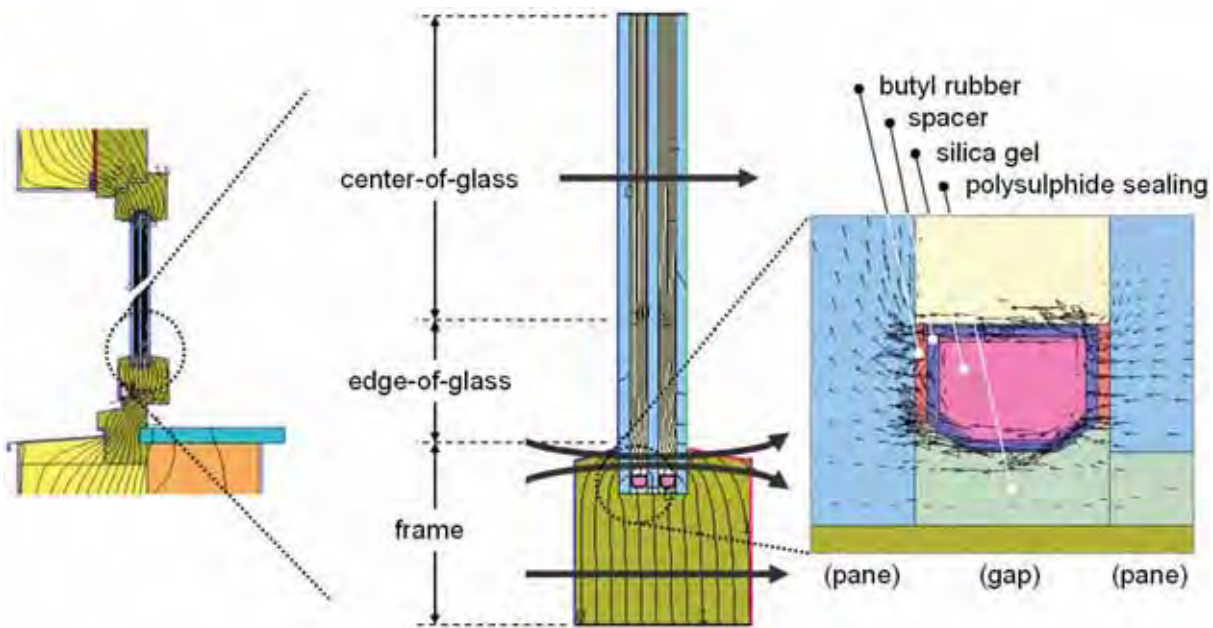


*Figure 9.1:* The tree different window domains and their interaction. The figure shows isotherms through a glazing system computed by the software THERM [23]. On the right-hand-side, the heat flux vectors through the metal spacer are illustrated. Adapted from [25].

a ultra thin metal film in order to further improve the solar optical and thermal properties (sun protective glazing vs. high performance glazing).

The window panes are agglutinated in a gas-tight manner by means of the so-called window spacer and a sealing such as polysulphide. The spacer is in fact a thin metal profile, filled with silica gel, which is thermally separated from the glazing by a butyl rubber band, for example. Together with the frame itself, the spacer contributes to the thermal losses as a significant thermal bridge [18, 25].

### 9.1.2 The different domains and their interaction

As shown in Figure 9.1, we can therefore distinguish between [8]

- the center-of-glass domain, i.e. the area where the isotherms are parallel and not influenced by the thermal effects of the surrounding domains,
- the edge-of-glass domain, which is influenced by the interaction with the frame and spacer, and
- the window frame (frame area), which is again connected with the building envelope.

In the glazing area, as depicted in Figure 9.2, solar and long wave radiation are treated separately. The solar optical properties transmission  $\tau$ , reflection  $\rho$  and absorption  $\rho$  describe the amount of the short wave radiation, which is accordingly transmitted, reflected or absorbed within *each* glazing element. The absorbed energy causes the glazing temperature to raise,

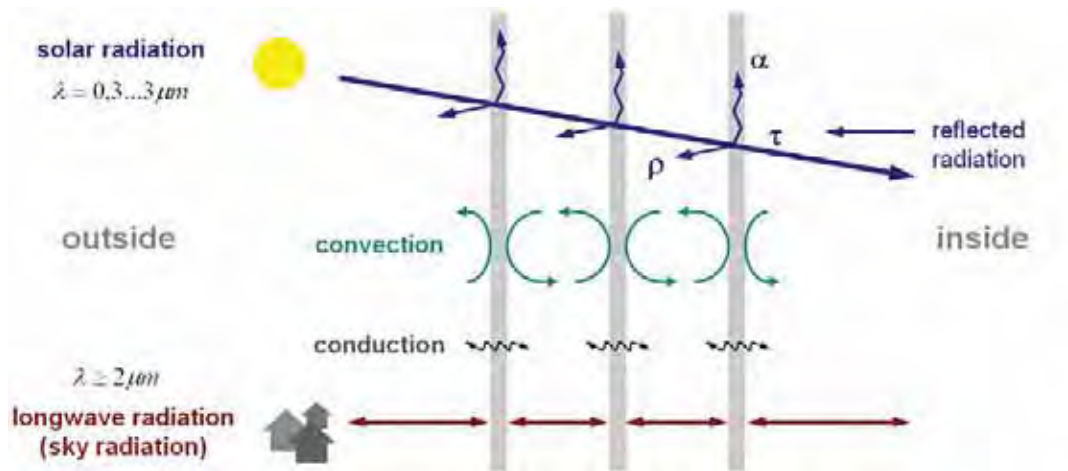


Figure 9.2: Separate treatment of the different heat transfer mechanisms within a glazing system.

and the energy is transported partially to the inside and to the outside. The computation of the overall solar optical properties involves multiple reflections between the surfaces between media, where spectral properties require special treatment. The latter spectral effects may, however, be neglected only for the case of uncoated glazings.

The other heat transfer mechanisms are well described in terms of the overall thermal resistance, the U-value. Similar to a solid wall, energy is transferred at the surfaces via convection and via long wave radiative heat exchange with the surrounding surfaces. Inside the panes, heat is transported by heat conduction only, as windows are opaque for long wave radiation. In the gaps between the panes, heat is exchanged via convection, conduction, and long wave radiation, this time between parallel surfaces each. The distance between the panes as well as the gas filling can be optimized in terms of minimizing (and nearly suppressing) convection and conduction [16, 18].

### 9.1.3 The total window heat transfer coefficient

According to the EN ISO Standard 10077-2:2003 [7] and the ISO Standard 15099:2003 [14], the overall heat transfer coefficient of a window system comprises

- the heat transfer coefficient of the glazing,  $U_g$ ,
- the heat transfer coefficient of the frame,  $U_f$ , and
- a linear heat transfer coefficient  $\Psi_g$  in order to account for the additional heat losses with respect to the thermal bridges spacer and frame/window.

Calculation procedures for obtaining  $\Psi_g$  are given in the EN ISO Standard 10077-2:2003 [7] and, more generally, in the ISO Standard 10211:2007 [13]. Usually, a 2D finite element-based calculation procedure can be applied in order to compute the respective heat transfer coefficients. Examples are software packages THERM [23] by the Lawrence Berkeley National Laboratory, or BISCO [22] and TRISCO [24] by Physibel. Early applications of the respective

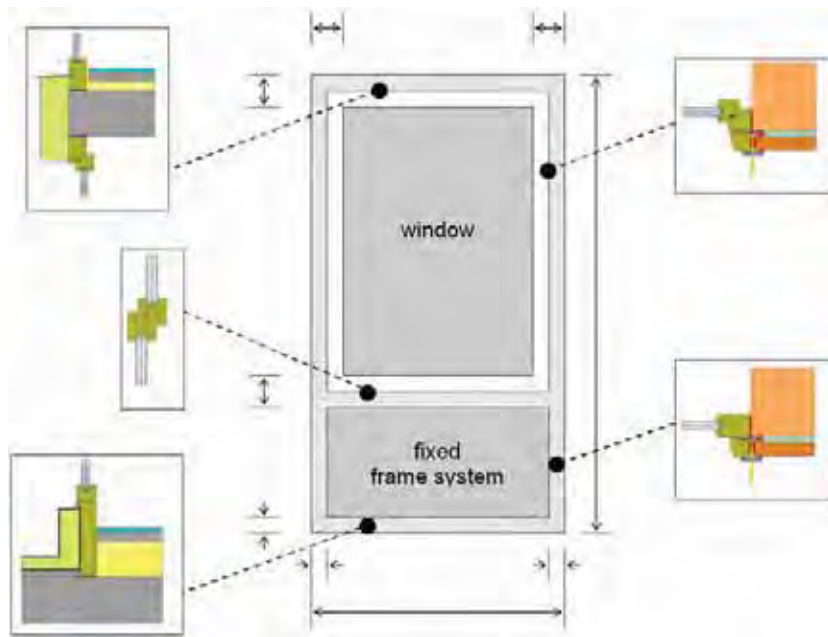


Figure 9.3: Connection of the window system with the building. Adapted from [25].

calculation methods are, for example, reported in [27].

The overall window heat transfer coefficient, the total thermal transmittance,

$$U_t = \frac{\sum A_g U_g + \sum A_f U_f + \sum l_g \Psi_g}{\sum A_g + \sum A_f} \quad (9.1)$$

is obtained by totaling the area averaged sum of the individual transmittances [14]. EN Standard 673:2003 [5] introduces a simplified method to calculate the U-value of the glazing system,  $U_g$ , for steady-state situations. In usual situations, the method can be applied with reasonable accuracy. In the EN Standard 674:1999 [6], a method is defined for measuring the glazing U-value. ISO Standard 15099:2003 [14] describes a more detailed method to compute the temperature dependent U-value of a glazing system by means of energy balances at the surface of each window pane. With the latter method, the temperature profile is obtained as by-product. The paper of RUBIN [20] describes the theoretical background.

Note, that the coefficient  $\Psi$  does not, however, capture the thermal bridge between frame and building. In the literature, correlations are available for such connections in tabular form [10, 11]. Likewise, this effect can be investigated with the mentioned FEM packages and should be considered in simulation. Figure 9.3 indicates that this (tedious) process requires detailed knowledge, how the fenestration is connected to the building envelope. The procedure has been demonstrated by the author in [25].

Alternatively, and instead of calculating the linear  $\Psi$  coefficient, other formulations make use of an edge-of-glass U-value. Details are given in ISO Standard 15099:2003 [14]. For example, the correlation between the center- and edge-of-glass U-value can be described in terms of a polynomial correlation. The model of the WINDOW software [8] makes use of such a formu-

lation.

For further reading, the reader is referred to the cited standards and to the publications [16, 18, 20, 26].

### 9.1.4 Daylight transmittance versus solar heat gains

Next to the solar heat gain coefficient  $g$  [–], the daylight transmittance  $\tau_L$  [–] is an important optical property in simulation. Note, that both quantities are not equal. For special configurations such as coated or laminated glazings, these properties are calculated on the basis of spectral data. This shall be demonstrated in Figure 9.4. For example, by considering the visible range of the solar spectrum (380...780 nm), for a glazing system we may obtain the daylight transmittance  $\tau_L = 68\%$  and reflectivity  $\rho_L = 10\%$ . For the same glazing system, the solar heat gain coefficient  $g = 34\% + 3\% = 37\%$ , if the overall transmittance  $\tau = 34\%$  and the secondary heat gains are  $q_{int} = 3\%$ .

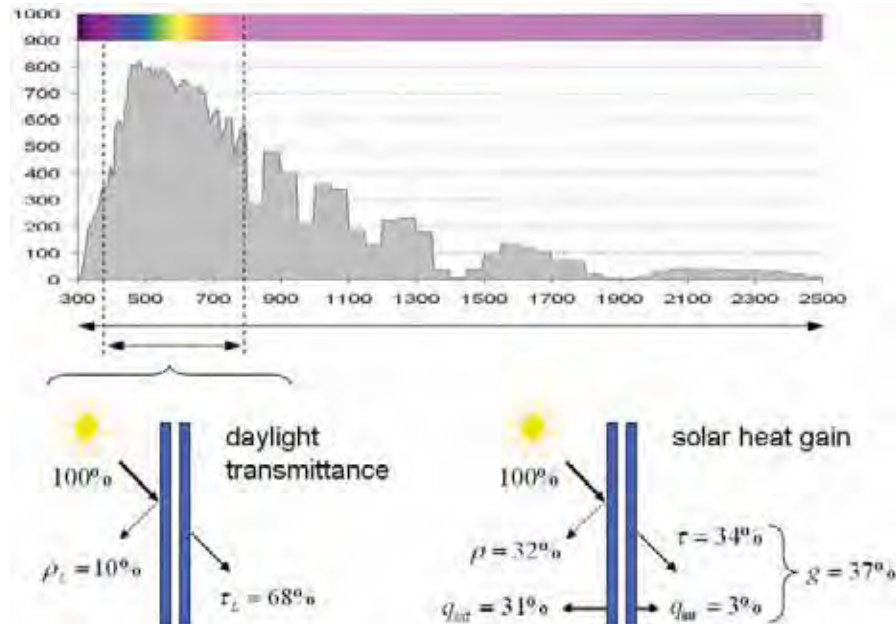


Figure 9.4: Daylight transmittance  $\tau_L$  versus the solar heat gain coefficient  $g$ . The diagramm shows the solar spectrum of ISO Standard 9050.

The *selectivity*

$$s = \frac{\tau_L}{g} \quad (9.2)$$

is thereby the ratio of the daylight transmittance and the solar heat gain coefficient. In moderate climate zones it is desirable to minimize the solar heat gains and to maximize the daylight transmittance at the same time, in other words, to obtain a high level of selectivity.

Another important optical property is the shading system reduction factor  $F_c$ . If a shading system such as a roller blind is active, the total solar heat gain coefficient is obtained by

$g_{tot} = g_{\perp} \cdot F_c$ , where  $g_{\perp}$  is the solar heat gain coefficient without shading and for an incidence angle  $\varphi = 0$ . A calculation scheme is provided by the EN Standard 13363-2:2005 [3], for example.

## 9.2 Solar optical properties: A simplified model

The transmittance  $\tau$ , reflectivity  $\rho$  and absorption  $\alpha$  of the solar radiation in glazings are generally functions of

- the direction of the incoming diffuse and beam radiation,  $I_{\text{diff}}$  and  $I_{\text{beam}}$  [ $W/m^2$ ],
- the polarization of the light ( $\parallel$  and  $\perp$  components),
- and its wavelength  $\lambda$  [ $nm$ ],
- the thickness  $h$  [ $m$ ] of the respective window pane,
- the refractive index  $n$  [-], and
- the extinction coefficient  $K$  [ $m^{-1}$ ] of the material.

Typical refractive indices are  $n = 1.0$  (air) and  $n = 1.526$  (glass); the extinction coefficient varies from  $K = 4 m^{-1}$  (white glass) to  $K = 32 m^{-1}$  (greenish glass), for example. Both the refractive index and the extinction coefficient of the cover material are functions of the wavelength. For glazings without coating this effect may be neglected. However, glazings *with* coating show very significant variations of the optical properties with wavelength. In this case, the spectral dependencies must be considered. Subsection 9.4.2 below will address this issue in detail.

In the following, we consider the optical properties of uncoated glazings first. A simplified calculation scheme is presented for calculating the transmittance-absorptance product of a glazing system.

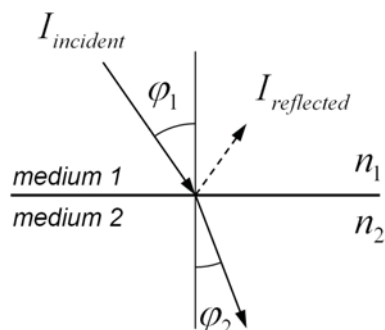


Figure 9.5: Relationship between refractive angles at the interface between media (Snell's law).

### 9.2.1 Transmittance by reflection losses considered

The relationship of the refractive angles  $\varphi_1$  and  $\varphi_2$  at the interface between two media with refractive indices  $n_1$  and  $n_2$  is given by *Snell's law* [2, 15]

$$\frac{n_1}{n_2} = \frac{\sin \varphi_2}{\sin \varphi_1} \quad (9.3)$$

as shown in Figure 9.5. The incidence angle  $\varphi_1$  (air) depends on the position of the sun in the sky, i.e., it is a time and location dependent function, which varies from time step to time step (cf. Section 8.3).

According to the model of *Fresnel*, the reflection  $r$  of the unpolarized radiation on passing from medium 1 to medium 2,

$$r = \frac{I_{\text{reflected}}}{I_{\text{incident}}} = \frac{1}{2} (r_{\parallel} + r_{\perp}) , \quad (9.4)$$

is obtained as the average between the parallel  $r_{\parallel}$  and the perpendicular  $r_{\perp}$  components,

$$r_{\parallel} = \frac{\tan^2(\varphi_2 - \varphi_1)}{\tan^2(\varphi_2 + \varphi_1)} \quad \text{and} \quad r_{\perp} = \frac{\sin^2(\varphi_2 - \varphi_1)}{\sin^2(\varphi_2 + \varphi_1)} . \quad (9.5)$$

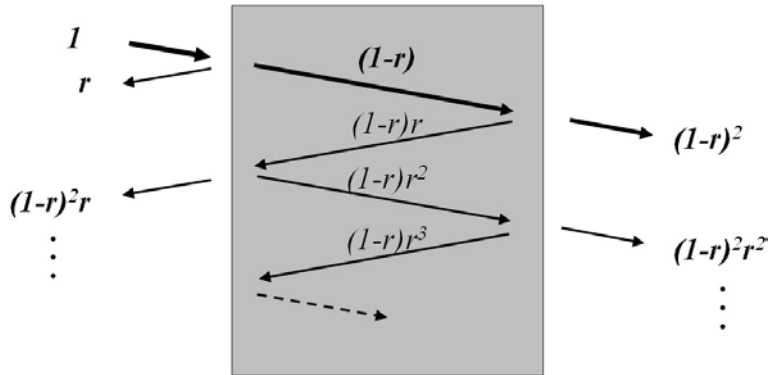


Figure 9.6: Multiple reflections inside a medium.

When passing a medium, two interfaces per cover contribute to the reflection losses. The reflected radiation inside the medium is again re-reflected by the other interface and vice versa, as shown in Figure 9.6. The magnitude of the "ray" decreases thereby continuously. After some algebra, the successive accumulation of all  $n$  transmitted parts  $\{(1-r)^2, (1-r)^2r^2, \dots\}$ , with  $n = 0, \dots, \infty$ , yields

$$\tau_{\perp} = (1 - r_{\perp})^2 \sum_{n=0}^{\infty} r_{\perp}^{2n} = \frac{(1 - r_{\perp})^2}{1 - r_{\perp}^2} = \frac{1 - r_{\perp}}{1 + r_{\perp}} \quad (9.6)$$

which is written here in terms of the perpendicular part. For the parallel part, which is treated separately, the same formula is obtained. The transmittance of the initially unpolarized radiation is obtained as the average of both components,

$$\tau_r(\varphi) = \frac{1}{2} \left( \frac{1 - r_{\perp}}{1 + r_{\perp}} + \frac{1 - r_{\parallel}}{1 + r_{\parallel}} \right) . \quad (9.7)$$

The term  $\tau_r$  accordingly denotes the transmittance through a single medium with the *reflection losses considered*.

DUFFIE & BECKMAN [2] provide a simplified formula for a system with  $N$  covers, each cover consisting of the same material,

$$\tau_{r,N}(\varphi) = \frac{1}{2} \left( \frac{1 - r_\perp}{1 + (2N - 1)r_\perp} + \frac{1 - r_\parallel}{1 + (2N - 1)r_\parallel} \right) . \quad (9.8)$$

### 9.2.2 Transmittance by absorption losses considered

The transmission with respect to the absorption of radiation in a partially transparent medium can be formulated by *Bouguer's law*

$$\tau_\alpha(\varphi) = \frac{I_{\text{transmitted}}}{I_{\text{incident}}} = e^{-\frac{K \cdot h}{\cos \varphi}} , \quad (9.9)$$

where  $\varphi$  is the respective incidence angle. For a system with  $N$  covers, the simplified formula [2, 15] reads

$$\tau_{\alpha,N}(\varphi) = \frac{I_{\text{transmitted}}}{I_{\text{incident}}} = e^{-\frac{K \cdot N \cdot h}{\cos \varphi}} . \quad (9.10)$$

### 9.2.3 Transmittance-absorptance product

The total transmittance due to both reflection and absorption losses considered can be approximated by

$$\tau(\varphi) = \tau_r(\varphi) \cdot \tau_\alpha(\varphi) , \quad (9.11)$$

where  $\varphi$  is the solar incidence angle. A reasonable approximation in simulation for calculating the total transmittance of the diffuse radiation is the choice

$$\tau_{\text{diff}} = \tau(60^\circ) , \quad (9.12)$$

instead of explicitly integrating over the hemisphere.

However, the transmittance with respect to the reflection and absorption losses can be computed in a detailed manner, if the same raytracing techniques are applied as before. Following Figure 9.7 and the procedure from Subsection 9.2.1, the successive accumulation of the transmitted parts of the perpendicular part of the radiation through a single cover material (same formula for the parallel part) gives

$$\tau_{\perp\alpha} = (1 - r_\perp)^2 \tau_\alpha \left( 1 + \sum_{n=1}^{\infty} r_\perp^{2n} \tau_\alpha^{2n} \right) = \frac{(1 - r_\perp)^2 \tau_\alpha}{1 - r_\perp^2 \tau_\alpha^2} , \quad (9.13)$$

with  $\tau_\alpha(\varphi)$  from Equation (9.9). Similarly, the terms of the reflected radiation can be accumulated, and we obtain

$$\rho_{\perp\alpha} = r_\perp + \frac{(1 - r_\perp)^2 \tau_\alpha^2 r_\perp}{1 - (r_\perp \tau_\alpha)^2} = r_\perp (1 + \tau_\alpha \tau_\perp) \quad (9.14)$$

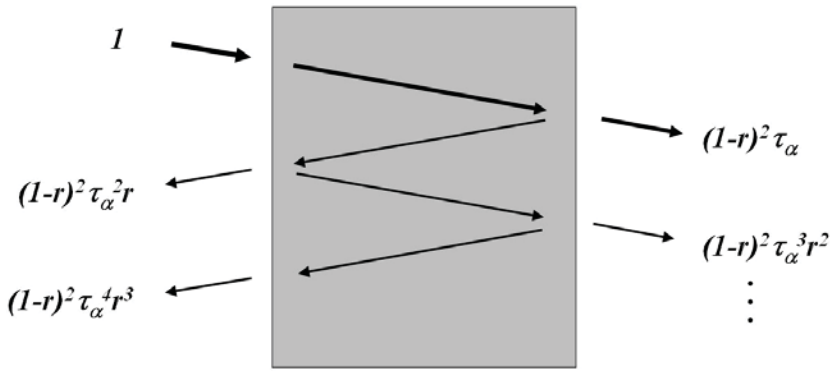


Figure 9.7: Multiple reflections inside an absorbing medium.

for the perpendicular part of the reflectivity (same formula for the parallel part).

The values for the unpolarized radiation are obtained by averaging both parts, i.e.,

$$\tau_{r\alpha}(\varphi) = \frac{1}{2} (\tau_{\perp\alpha} + \tau_{\parallel\alpha}) \quad \text{and} \quad \rho_{r\alpha}(\varphi) = \frac{1}{2} (\rho_{\perp\alpha} + \rho_{\parallel\alpha}) . \quad (9.15)$$

The relation between the transmittance, reflectance and absorption follows from the principle of energy conservation [15]

$$\tau(\varphi) + \rho(\varphi) + \alpha(\varphi) = 1 . \quad (9.16)$$

#### 9.2.4 Secondary heat gains due to solar absorption (half-stack)

With Equation (9.10), the transmission of the direct and diffuse solar radiation by absorption losses, which are considered within the *half stack* of  $N$  window panes, can be approximated by

$$\tau_{\alpha,\text{half}}(\varphi) = e^{-\frac{1}{2} \frac{K \cdot N \cdot h}{\cos \varphi}} \quad \text{and} \quad \tau_{\alpha,\text{diff,half}}(\varphi) = e^{-\frac{1}{2} \frac{K \cdot N \cdot h}{\cos 60^\circ}} . \quad (9.17)$$

The amount of the absorbed solar radiation within the *outwards facing* half stack of the glazing system can be predicted by the approximation

$$q_{sw,\varphi,\text{win,out}} \approx (1 - \tau_{\alpha,\text{half}}) I_{\text{beam}} + (1 - \tau_{\alpha,\text{diff,half}}) I_{\text{diff}} + (\tau_{\alpha,\text{diff,half}} - \tau_{\alpha,\text{diff},N}) I_{\text{diff,rfl,int}} . \quad (9.18)$$

The term  $I_{\text{diff,rfl,int}}$  denotes the diffuse short wave radiation, which has been reflected from the internal walls of the respective zone and therefore contributes to the outward facing heat flux through the window. It can be calculated with the radiosity method as indicated in Algorithm 3 of Section 8.6.2. (The amplitude of the latter heat flux is orders of magnitude below the primary heat gains.)

The absorbed radiation within the *inwards facing* half stack is accordingly obtained by

$$q_{sw,\varphi,\text{win,int}} \approx (\tau_{\alpha,\text{half}} - \tau_{\alpha,N}) I_{\text{beam}} + (\tau_{\alpha,\text{diff,half}} - \tau_{\alpha,\text{diff},N}) I_{\text{diff}} + (1 - \tau_{\alpha,\text{diff,half}}) I_{\text{diff,rfl,int}} . \quad (9.19)$$

With the above formulae, the total transmitted solar radiation through a window system can be computed. For a window system with aperture area  $A$ , frame portion  $f_{\text{frame}}$ , the total solar heat flux is

$$\dot{Q} = (1 - f_{\text{frame}}) A [\tau(\varphi) I_{\text{beam}}(\varphi) + \tau(60^\circ) I_{\text{diff}}] + q_{sw,\varphi,win,int}, \quad (9.20)$$

where  $q_{sw,\varphi,win,int}$  is the absorbed solar radiation within the inwards facing part of the respective glazing system.

Note, that the accuracy of the approximation of the term  $q_{sw,\varphi,win,int}$  decreases, if the glazing system comprises more than two panes. EN Standard 410 [4] defines an accurate method, provided that spectral data are available.

### 9.3 Example

In the following example, we consider first an uncoated single glass pane with thickness  $d = 4 \text{ mm} = 0.004 \text{ m}$ . Secondly, the optical properties are calculated for a standard double glazing using two ( $N = 2$ ) of the aforementioned panes. The refractive indices are  $n = 1.0$  for air and  $n = 1.526$  for glass, the extinction coefficient of the glazing is  $K = 4.0$ , and the overall U-value of the glazing is assumed to be  $U_g = 1.4 \text{ W}/(\text{m}^2 \text{K})$ , including the internal and external combined heat transfer.

Figure 9.8 shows the transmittance and absorptance of the single glazing as a function of the incidence angle  $\varphi$ . The transmittance for direct sun transmission (i.e.,  $\varphi = 0$ ) is 90.2%. In Figure 9.9, the optical properties  $\tau(\varphi)$ ,  $\rho(\varphi)$  and  $\alpha(\varphi)$  are plotted for a single glazing (left-hand-side of Fig. 9.9). The right-hand-side of the figure shows the overall properties of the double glazing, computed with the formulae defined in Sections 9.2.2 and 9.2.3. The transmittance-

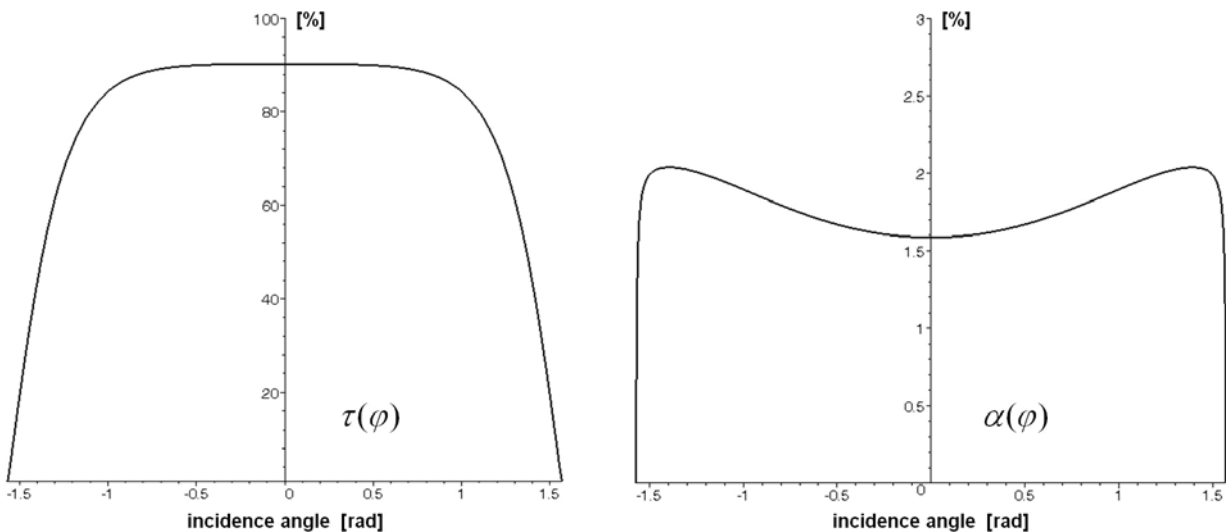


Figure 9.8: Transmittance and absorption of an uncoated single glass pane as a function of the incidence angle  $\varphi$  in the range  $-\pi/2 \dots \pi/2$ .

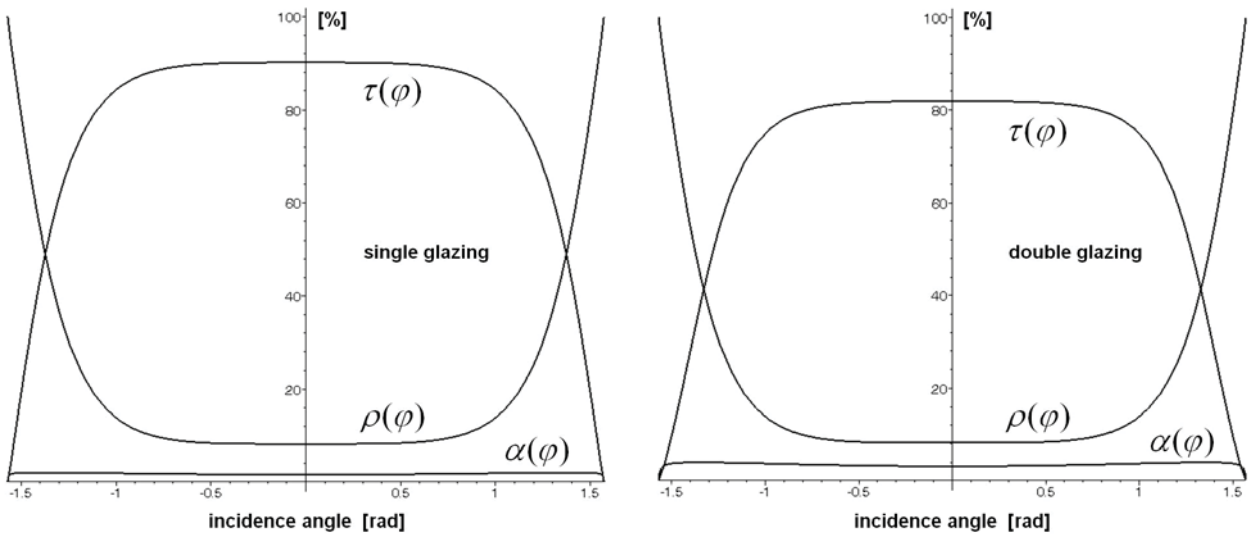


Figure 9.9: Optical properties  $\tau, \rho, \alpha$  of a single glazing as a function of the incidence angle  $\varphi$ , plotted in the range  $-\pi/2 \dots \pi/2$  (left-hand-side). The right-hand-side shows the properties of a double glazing, computed with the above mentioned formulae.

absorptance product is calculated by Equation (9.13) in both cases.

Note, that  $\tau + \rho + \alpha \equiv 1$  by definition.

Figure 9.10 quantifies the error function

$$e(\varphi) = |\tau_r(\varphi) \cdot \tau_\alpha(\varphi) - \tau_{r,\alpha}(\varphi)| \quad (9.21)$$

between the simplified treatment of the transmittance-absorptance product  $\tau_r(\varphi) \cdot \tau_\alpha(\varphi)$  of Equation (9.11) and the detailed formula (9.13). It is evident from the figure, that the error

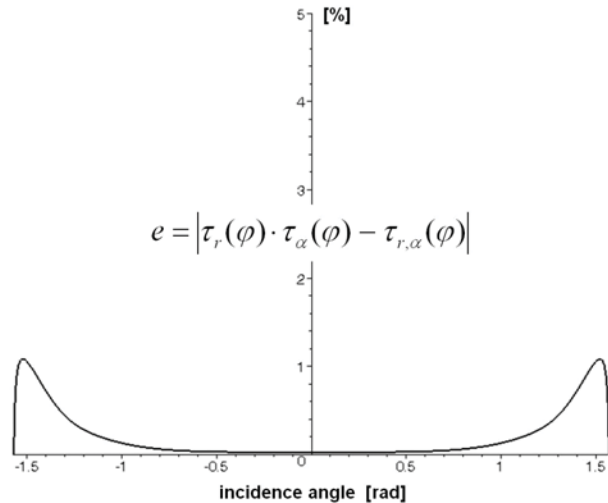


Figure 9.10: Deviation between the simplification of the transmittance-absorptance product  $\tau_r(\varphi) \cdot \tau_\alpha(\varphi)$  of Equation (9.11) and the detailed formula (9.13).

is small, as the maximum energy is transmitted between  $-\pi/3 \dots \pi/3$ , where the error is close to zero.

The application of the simplified window model shall be demonstrated for two time periods of TRY5, a few days of January, and, secondly, a short period in October. Figures 9.11 and 9.12 summarize the obtained results. The figures show the primary and secondary solar heat gains in relation to the solar irradiation for the case of an upright surface which is oriented to the south side.

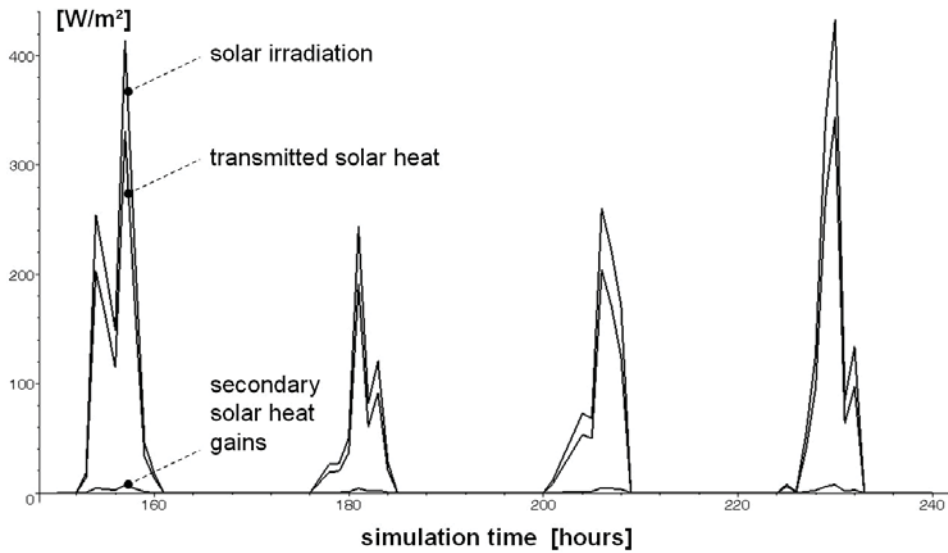


Figure 9.11: Primary and secondary solar heat gains calculated with the simplified window model for four days in January of TRY5 (simulation hour 150...240).

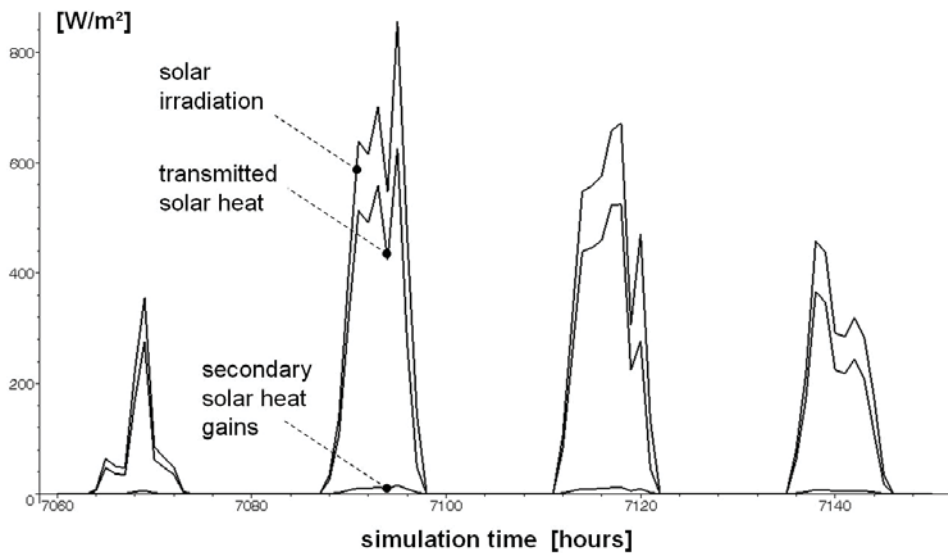


Figure 9.12: Primary and secondary solar heat gains calculated with the simplified window model for four days in October of TRY5 (simulation hour 7060...7150).

## 9.4 Overall optical properties of multi-layered glazings

### 9.4.1 Recursive calculation of the overall optical properties

The overall optical properties of a multiple-layered glazing system can be calculated, having obtained the solar optical properties  $\tau(\lambda)$ ,  $\rho(\lambda)$  and  $\alpha(\lambda)$  of a single (coated or uncoated) window pane, either via computation or by measurements. Note, that these quantities still are functions of the wavelength  $\lambda$ .

With the recursive application of the above mentioned raytracing method (cf. Sections 9.2.1 and 9.2.3) we can find the *total* transmissivity and reflectivity of a glazing system consisting of  $N$  layers [21]. The formulae are similar to equations (9.13) and (9.14), but this time for the reflection and absorption it is distinguished between the direction of the rays on passing the medium. The superscript "f" (front) denotes, that a quantity (i.e.,  $\rho(\lambda)$  or  $\alpha(\lambda)$ ) is evaluated from the outside to the inside, "b" (back) means the backward direction, i.e., from the inside to the outside.

In Figure 9.13, equal numbers in the subscript indicate the properties of the respective layer. For example,  $\tau_{1,1}(\lambda)$  is the transmissivity of layer 1. Step by step, the overall properties are recursively calculated by the following procedure:

For a system of two layers (counting in ascending order from the outside to the inside), the spectral transmissivity is given by

$$\tau_{1,2}(\lambda) = \frac{\tau_{1,1}(\lambda) \tau_{2,2}(\lambda)}{1 - \rho_{1,1}^b(\lambda) \rho_{2,2}^f(\lambda)}, \quad (9.22)$$

and the spectral reflectivity is

$$\rho_{1,2}(\lambda) = \rho_{1,1}(\lambda) + \frac{\tau_{1,1}^2(\lambda) \rho_{2,2}(\lambda)}{1 - \rho_{1,1}^b(\lambda) \rho_{2,2}^f(\lambda)}. \quad (9.23)$$

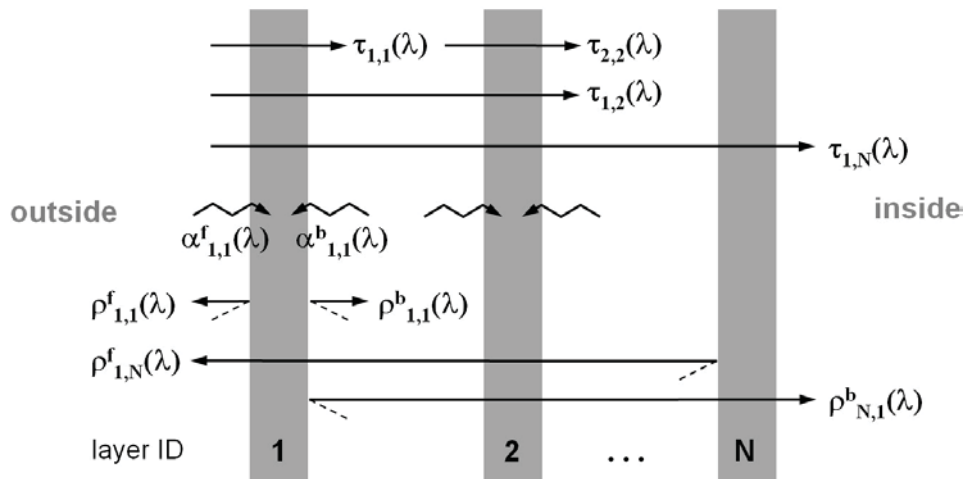


Figure 9.13: Calculation of the global optical properties for a set of  $N$  panes [21].

In order to obtain the transmissivity and reflectivity for a set of three layers, two neighboring layers are evaluated first and are considered as a composite object in the subsequent step.

With these formulae, the optical properties of a window system with an arbitrary number of layers, which may themselves be composites, can be computed, if the properties of the single panes are described in terms of their overall optical properties ( $\tau, \rho, \alpha$ ) rather than the pane thickness, refractive index, extinction coefficient, etc. EN Standard 410 [4] summarizes these formulae for the common cases of a double and triple glazing system. EN Standard 13363-2 [3] contains additional information concerning shading devices. For the general calculation procedure it is referred to the article of RUBIN [21].

#### 9.4.2 Selective transmittance through coated glazings

During the past decades, windows (and frames) have been subject to several improvements of the thermal and optical properties. It has already been mentioned, that the heat transfer by convection and conduction between the panes can be significantly reduced in terms of choosing an appropriate distance between panes and by using a rare gas filling. Isolating the gap by vacuum is a new technique in order to further improve the thermal characteristics and to reduce the thickness at the same time.

Likewise, the optical properties can be improved by coating the panes with an ultra thin metal film in terms of a selectively transmitting and reflecting material. According to where this coating is placed, either a sun protective glazing or a high performance insulation glazing can be realized. For example, for a *sun protective* (sun stop) glazing it is desirable to achieve a high level of daylight transmission (i.e., within the range  $380\text{ nm} < \lambda < 780\text{ nm}$ ) and a high reflection for the infrared part of the spectrum from the outside. A *low-e glazing*, in turn, shall reflect the infrared radiation from the inside (insulation) and show a high level of daylight transmission from the outside. Figure 9.14 shows the relative positioning of these respective coatings. The thickness of the selective coatings is in the order of the wavelength of the solar radiation [17, 18].

The related physical effects are known as *interference at thin transparent layers* in optics.

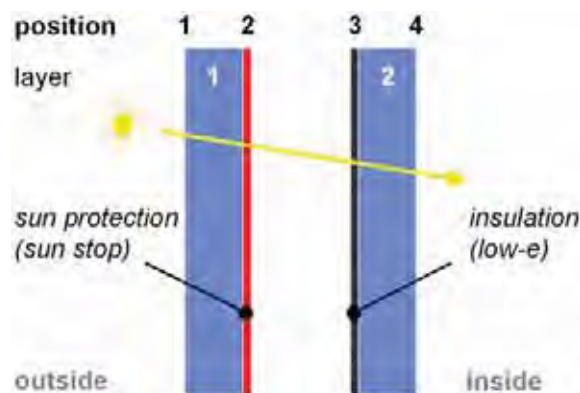


Figure 9.14: Relative positioning of coatings.

The thickness  $d$  and the refractive index  $n$  of the cover material are selected such, that the radiation of a well-defined wavelength  $\lambda$  is annihilated by extinction (or amplified) in terms of the optical retardation of the rays which have been reflected at both interfaces of the cover layer. Figure 9.15 clarifies the geometrical settings.

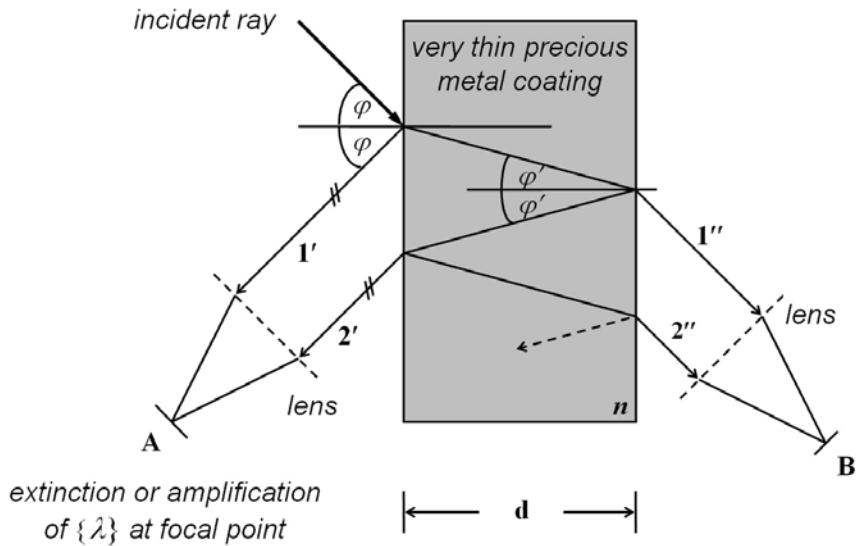


Figure 9.15: Interferences at the coating of a glazing with plane-parallel surfaces. Adapted from [25].

The optical path difference  $\Delta$  of rays  $1'$  and  $2'$ ,

$$\Delta = 2d\sqrt{n^2 - \sin^2 \varphi} - \frac{\lambda}{2}, \quad (9.24)$$

is calculated from the geometrical configuration and with the law of refraction (cf. Section 9.2.1). Note, that in the above formula, the optical retardation is further reduced by the term  $\lambda/2$ , as the reflection of ray  $1'$  at the interface of the dense cover material implies an additional phase change by  $\pi$ . The second ray  $2'$  is not subject to this additional phase change [12].

It follows from the principle of energy conservation, that the radiant power of the transmitted part of the non-reflected radiation in point  $B$  holds the overall energy part. The waves are accordingly amplified at the focal point  $A$  for  $\Delta = m\lambda$  (with the multiplier  $m = 1, 2, 3, \dots$ ) ("light in  $A$ "), and are damped for  $\Delta = (2m+1)\lambda/2$  ("darkness in  $A$ "). Hence, for the range of a specific wavelength  $\lambda$ , the reflectance can be reduced and the transmittance increased, and vice versa, depending on the thickness and position of the cover material, as the interference in  $B$  is complementary to the one observed in  $A$  [12, 15].

Note, that conditional of manufacturing the cover is never perfectly parallel. It is accordingly difficult, to calculate the optical properties with an algebraic model [21]. In practice, the optical properties of glazings are measured for a predefined set of wavelengths and are provided in terms of a spectral database.

In order to account for the spectral dependence of the optical properties  $\tau(\lambda)$ ,  $\rho(\lambda)$  and  $\alpha(\lambda)$ , a detailed window model calculates *spectral mean values* by numerical integration over the respective part of the spectrum in question.

- For the daylight transmittance, we consider the range  $380\text{ nm} < \lambda < 780\text{ nm}$ ,
- for the energy transmittance the range  $300\text{ nm} < \lambda < 2500\text{ nm}$ .
- Glazings can be considered as opaque for the infrared part of the spectrum,  $\lambda > 2500\text{ nm}$ .  
For detailed models it is referred to the text book of MODEST [15], for example.

Note, that this procedure is repeated for each angle of incidence  $\varphi$ . However, in practice, the spectral mean values are pre-computed for a set of incidence angles, say, in steps of  $10^\circ$ , and provided in a table. These values can be linearly interpolated in simulation, in order to speed-up the computation.

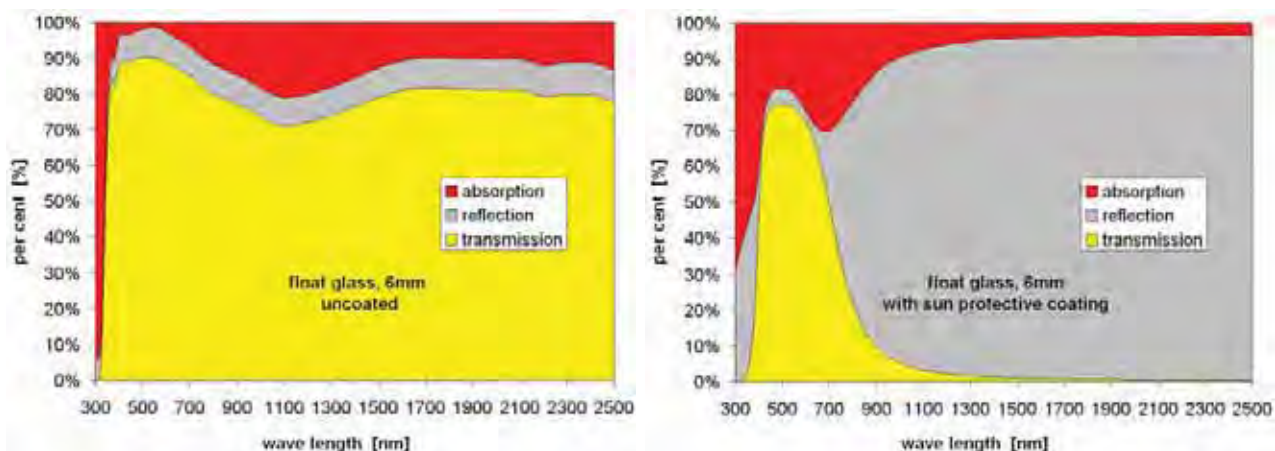


Figure 9.16: Stack plot of the optical properties  $\tau$ ,  $\rho$  and  $\alpha$  of Figure 9.17 for the same float glass panes as a function of wavelength  $\lambda$ . Redrawn from [19] with substituted data.

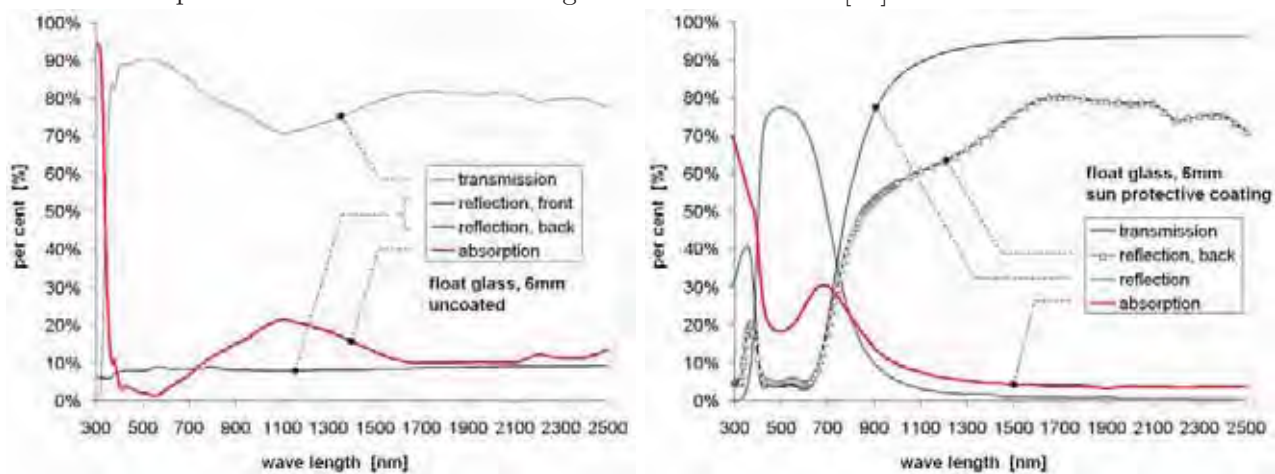


Figure 9.17: Optical properties  $\tau$ ,  $\rho_f$ ,  $\rho_b$  and  $\alpha$  of two single 6mm float glass panes as a function of wavelength  $\lambda$ . In the first case, the glazing is uncoated, in the second case, the pane contains a sun protective coating at position 2.

The spectral mean values of the solar energy transmittance are calculated from the monochromatic values by

$$\bar{\tau}(\varphi) = \frac{\int_{\lambda} S_{\lambda} \tau(\lambda) d\lambda}{\int_{\lambda} S_{\lambda} d\lambda} \approx \frac{\sum_{300 nm}^{2500 nm} S_{\lambda} \tau(\lambda) \Delta\lambda}{\sum_{300 nm}^{2500 nm} S_{\lambda} \Delta\lambda} , \quad (9.25)$$

where  $S_{\lambda}$  is the relative spectral distribution of the solar radiation [4] and  $\Delta\lambda$  is the respective wavelength interval. For the reflectance, we obtain

$$\bar{\rho}(\varphi) = \frac{\int_{\lambda} S_{\lambda} \rho(\lambda) d\lambda}{\int_{\lambda} S_{\lambda} d\lambda} \approx \frac{\sum_{300 nm}^{2500 nm} S_{\lambda} \rho(\lambda) \Delta\lambda}{\sum_{300 nm}^{2500 nm} S_{\lambda} \Delta\lambda} . \quad (9.26)$$

For the daylight transmittance and reflectance, the solar radiation is further multiplied with a spectral brightness sensitivity. It is referred to the EN Standard 410 [4] for details.

Figures 9.16 and 9.17 indicate the spectral optical properties for the case of an uncoated 6mm float glazing and a coated float glazing. It is evident from the figures, that the properties of the uncoated glazing are relatively constant over the spectrum, whereas the spectral properties vary significantly for the coated glazing. The transmissivity of the sun protective pane shows a peak within the visible range. In the remaining part of the spectrum, the reflectivity dominates.

The example clarifies, that the spectral dependencies of coated glazings cannot be neglected in simulation. Furthermore, these dependencies need special consideration, if multiple selective glazings are combined with each other, as it is the case for a double glazing facade system – a typical configuration in the modern glass architecture [19].

## 9.5 Professional software packages

Several software packages have been developed to compute the solar optical and thermal properties of glazings including spectral properties. The two most widespread known programs are

- the American WINDOW [8] software package which has been developed at the Lawrence Berkeley Laboratory of the University of California, and
- the Advanced Window Information System (WIS) [1], which is an European development by TNO Building and Construction Research (The Netherlands). WIS is freely available and is based on an MS Access database of customized and vendor-specific window data of the Window Energy Data Network (WinDat).

Most of the building performance simulation software packages, that make use of a detailed window model, are able to import window properties which are pre-calculated by one of these tools. WIS can be used to calculate the optical and thermal properties according to the ISO Standard 15099:2003 [14] and the EN Standard 673:2003 [5].

Next to WINDOW and WIS, a set of vendor-specific software packages are available. MUNEER ET AL. [16] provide in their book a spreadsheet-based computational model using MS Excel.

For further work on this topic, it is recommended to the interested reader to download and install the WIS system and to perform a set of simulations for typical sun protective and high-performance glazing systems, in order to become familiar with the solar optical, thermal and physical properties.

## 9.6 References

- [1] TNO Building and Construction Research (TNO Bouw). *Advanced Window Information System (WIS), Version 3.0.1, Window Energy Data Network (WinDat)*. Sustainable Energy and Buildings (DEG), The Netherlands, 2006.
- [2] J. Duffie and W. Beckman. *Solar Engineering of Thermal Processes*. John Wiley and Sons Inc., New York, 1991.
- [3] EN 13363-2. *Solar protection devices combined with glazing – Calculation of total solar energy transmittance and light transmittance – Part 2: Detailed calculation method*. CEN – European Committee for Standardization, 2005.
- [4] EN 410. *Glass in building – Determination of luminous and solar characteristics of glazing*. DIN Deutsches Institut für Normung e.V., Beuth Verlag, 1998.
- [5] EN 673. *Glass in building – Determination of the thermal transmittance (U value) – Calculation method*. DIN Deutsches Institut für Normung e.V., Beuth Verlag, 2003.
- [6] EN 674. *Glass in building – Determination of the thermal transmittance (U value) – Guarded hot plate method*. DIN Deutsches Institut für Normung e.V., Beuth Verlag, 1999.
- [7] EN ISO 10077-2. *Thermal performance of windows, doors and shutters – Calculation of thermal transmittance – Part 2: Numerical method for frames*. DIN Deutsches Institut für Normung e.V., Beuth Verlag, 2003.
- [8] E.U. Finlayson, D.K. Arasteh, C. Huizenga, and M.D. Rubin. *WINDOW 4: Documentation of calculation procedures*. Technical report, Lawrence Berkeley Laboratory, University of California, 1993.
- [9] G. Hauser. *Rechnerische Vorherbestimmungen des Wärmeverhaltens großer Bauten*. PhD thesis, Universität Stuttgart, 1977.
- [10] G. Hauser and H. Stiegel. *Wärmebrücken Atlas für den Mauerwerksbau*. Bauverlag Wiesbaden, 1990,1993,1996.
- [11] G. Hauser and H. Stiegel. *Wärmebrücken Atlas für den Holzbau*. Bauverlag Wiesbaden, 1992.
- [12] E. Hering, R. Martin, and M. Stohrer. *Physik für Ingenieure*. VDI Verlag, 1992.

- [13] ISO 10211 – Part 1 and 2. *Thermal bridges in building construction – Heat flows and surface temperatures – Detailed calculations*. DIN Deutsches Institut für Normung e.V., Beuth Verlag, 2007.
- [14] ISO 15099, Ausgabe November 2003. *Thermal performance of windows, doors and shading devices - Detailed calculations*. DIN Deutsches Institut für Normung e.V., Beuth Verlag, 2003.
- [15] M.F. Modest. *Radiative Heat Transfer*. Academic Press, USA, 2nd edition, 2003.
- [16] T. Muneer, N. Abodahab, G. Weir, J. Kubie, and D. Kinghorn. *Windows in buildings: Thermal, acoustic visual and solar performance*. Architectural Press, 2000.
- [17] W.J. Platzer. *Solare Transmission und Wärmetransportmechanismen bei transparenten Wärmedämmmaterialien*. PhD thesis, Albert-Ludwigs-Universität Freiburg, 1988.
- [18] W.J. Platzer. Fenster und Verglasungen. In Marko and Braun, P.O. (Fraunhofer ISE), editors, *Thermische Solarenergienutzung an Gebäuden*. Springer Verlag, 1994.
- [19] G. Pültz. *Bauklimatischer Entwurf für moderne Glasarchitektur, Passive Massnahmen der Energieeinsparung*. Verlag Ernst und Sohn, 2002.
- [20] M. Rubin. Calculating heat transfer through windows. *U.S. Energy Research*, 6:341–349, 1982.
- [21] M. Rubin. Solar optical properties of windows. *U.S. Energy Research*, 6:123–133, 1982.
- [22] BISCO Software, 2009. Physibel), <http://www.physibel.be/v0n2bi.htm>.
- [23] THERM Software, 2009. Lawrence Berkeley National Laboratory (LBNL), <http://windows.lbl.gov/software/therm/therm.html>.
- [24] TRISCO Software, 2009. Physibel), <http://www.physibel.be/v0n2tr.htm>.
- [25] C. van Treeck. *Numerische Bestimmung der Transmissionswärmeverluste durch Wärmebrücken in der dynamischen Gebäudesimulation am Beispiel eines hochwärmegedämmten Mehrfamilienhauses*. Diploma thesis, Fraunhofer-Institute for Solar Energy Systems (ISE), Freiburg, 1997.
- [26] A. Wagner, S. Herkel, and W. Kohne. *Energieeffiziente Fenster und Verglasungen*. BINE Informationsdienst, Solarpraxis AG, Karlsruhe, 3rd edition, 2007.
- [27] U. Wolfseher. PhD thesis, Universität Essen, 1978.

# Chapter 10

## The zone model

### 10.1 Zone-based modeling

It is the conceptual idea of building performance simulation to capture the thermodynamic behavior of a complete building over a whole year ( $1a = 365d = 8760h$ ), i.e., the dynamics of heat fluxes and temperatures in response to ambient conditions and system control. Usually, a fairly coarse discretization is used in space, e.g., heat transfer through walls is treated in a one-dimensional manner as described in Chapter 6, and a fine discretization in time with a resolution from hours to seconds or less.

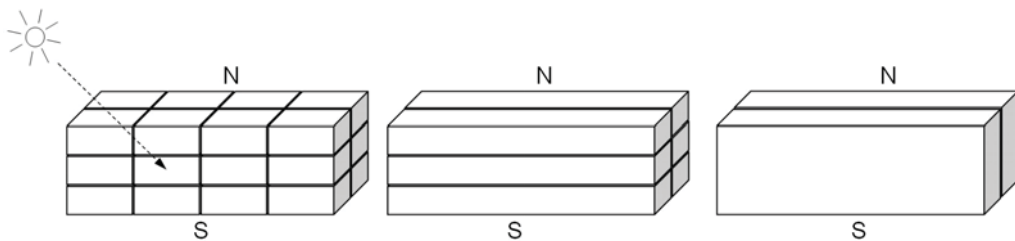


Figure 10.1: From room-based to zone-based modeling.

In order to further reduce the model complexity, spaces or rooms with similar orientation and same using conditions can be grouped together in order to form *zones*. It is accordingly not meaningful to combine spaces which are oriented to the north and to the south (or west). Spaces of a zone should be adjacent but do not necessarily have to be connected by air. Figure 10.1 explains the difference between room-based and zone-based modeling.

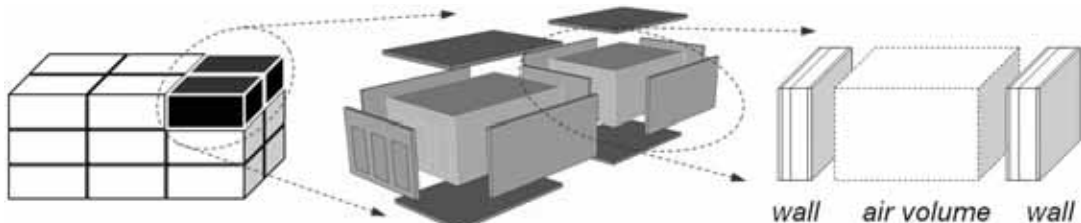


Figure 10.2: Adjacencies and interdependencies between building components and air volumes.

Figure 10.2 shows the link between air volumes and building components, such as multi-layered wall objects. Describing components in a one-dimensional way leads to the use of internal dimensions. Multi-dimensional effects, such as the additional heat transfer by transmission through thermal bridges (geometrical and structural thermal bridges) can be modeled with linear heat transfer coefficients. At this point, the reader is referred to the literature [4] and the standards [2, 5, 6].

## 10.2 Assembling the energy matrix equation

### 10.2.1 Energy conservation

As suggested by CLARKE [1], thermal multizone models are usually formulated on the basis of an (anisotropic) finite volume method (FVM). A set of conservation equations for energy, mass and momentum is integrated at successive time-steps in response to ambient climate, occupant and control system influences.

It was shown in the previous chapters, that the heat transfer involves the interaction between various domains which are in thermodynamic contact with each other (Chapter 3). The energy balances are affected by

- short and long wave radiation processes (Chapters 8 and 7),
- transient heat conduction through the structure (Chapter 6),
- surface convection (see Chapter 4), and
- enthalpy changes, e.g., due to interzonal air exchange (to be explained in Chapter 11).

Depending on the formulation, i.e., if it is separately accounted for radiation or not, the discretization generally leads to a set of linear (or nonlinear) equations with *temperatures as unknowns*, to be solved at each successive time-step.

Note, that the thermal model does not solve for the air exchange (mass conservation) in terms of the mass flow between zones and environment. These mass flow rates are calculated with a so-called artificial nodal network with *pressure values as unknowns*. The resulting nonlinear equation set is solved separately and is coupled with the thermal network. Both sets have to be solved iteratively in a partitioned way.

In its general integral form, the energy conservation equation can be expressed by

$$\varrho c \int_V \frac{\partial T}{\partial t} dV = k \int_S \frac{\partial T}{\partial n} dS + q , \quad (10.1)$$

i.e., the change of the energy in a volume  $V$  over time  $t$  equals the amount of energy which is exchanged through the boundaries  $S$  plus internal sources or sinks  $q$ . Thereby,  $\varrho$  is the mass density,  $c$  is the specific heat capacity,  $n$  is the surface normal at the respective boundary, and  $k$  a thermal conductivity.

Surface heat transfer is usually treated in a linearized manner in building performance simulation. Therefore, equivalent thermal conductivities  $k$  can be established for the convective, advective and, as the case may be, for the radiative heat transfer. (In this book, radiation is treated separately.)

It is accordingly convenient to describe the heat transfer within components by conduction as well as the heat transfer within or between fluid elements by means of the conservation equation (10.2), provided that the mass flow rate between fluid elements is known. The discretization method is similar to the analogy of an electrical network. The building model is degenerated to an RC-network of thermal resistances and capacitances assuming isotropic material characteristics and a well-stirred zone air temperature distribution. Note, that internal capacities, such as furniture etc., may become relevant and must be treated additionally.

For a control volume  $i$  around point  $P_i$ , with  $m = 2, 4$ , or  $6$  surfaces that are in thermodynamic contact with another element  $j$  (neglecting the heat transfer to other surfaces or assuming other surfaces being adiabatically connected, i.e.,  $\partial T / \partial n = 0$  for  $m \neq 2, 4, 6$ ), the discrete approximation of Equation (10.2) reads

$$\varrho_i c_i V_i \frac{T_i(t + \Delta t) - T_i(t)}{\Delta t} \approx \sum_{j=1}^m K_{i,j} [T_j(t + \Delta t) - T_i(t + \Delta t)] + q_i(t + \Delta t) , \quad (10.2)$$

where  $K_{i,j}$  is an equivalent resistance and  $V_i$  is the volume of the element. For the sake of stability, Equation (10.2) is written implicitly here using a backward Euler scheme, i.e., temperature values are related to the (unknown) future time row  $(t + \Delta t)$ .

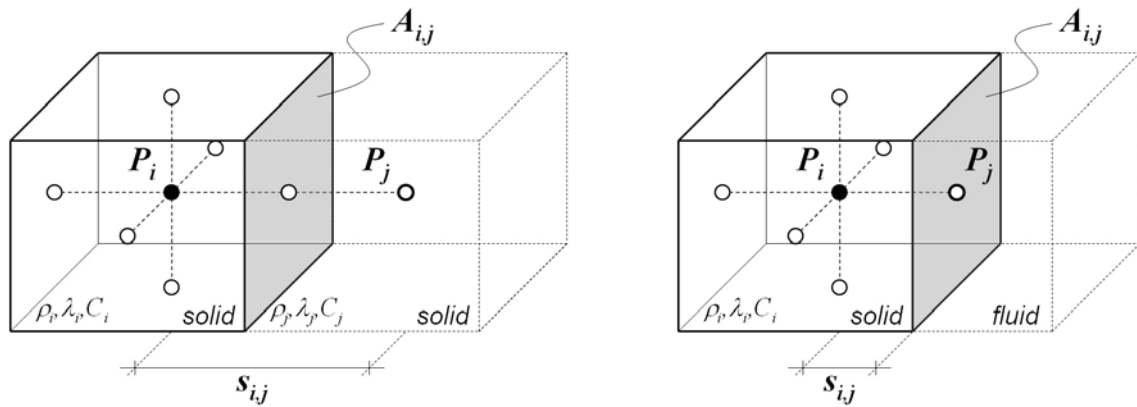
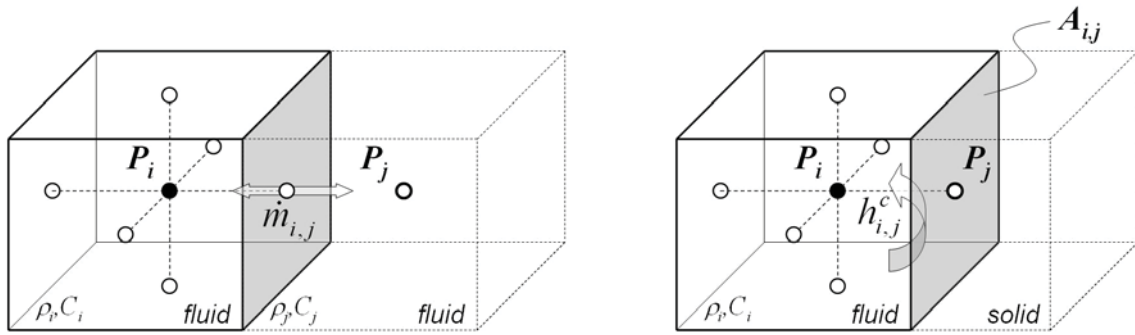
With the hexahedral elements introduced in Chapter 5, points  $P_i$  are placed

- within structural elements, e.g., at the center of each wall layer,
- within each fluid element, e.g., at the center of a zone air volume, and
- at the interfacing surfaces between fluid and structure.

In order to derive a zone model from CAD, a geometric or building information model (BIM) should therefore provide both a volume model of the structure as well as a surface model of the air volume bodies itself. The reader is referred to [14] for an appropriate BIM decomposition algorithm.

For the resistance  $K_{i,j}$  it is accordingly distinguished between the following cases:

- If both control points  $P_i$  and  $P_j$  are within a solid component, or if control point  $P_j$  is located at the bounding surface between solid and fluid, solely heat conduction is present. In this case,  $K_{i,j} = A_{i,j} \lambda_{i,j} / s_{i,j}$ , where  $A_{i,j}$  is the area of the interfacing surface,  $\lambda_{i,j}$  the (combined) heat conductivity and  $s_{i,j}$  the distance between  $P_i$  and  $P_j$ . Figure 10.3 details this situation.
- If  $P_i$  is within a fluid element,  $K_{i,j} = \dot{m}_{i,j} \bar{\varrho}_{i,j} \bar{c}_{i,j}$  for the advection between two fluid elements  $i$  and  $j$ , or  $K_{i,j} = h_{i,j}^c A_{i,j}$  for the convective heat flux from a surface with  $P_j$  to

Figure 10.3: Heat balances within solid elements  $P_i$ .Figure 10.4: Heat balances within fluid elements  $P_i$ .

element  $i$ , with the convective heat transfer coefficient  $h_{i,j}^c$ . Quantities with superscript  $\bar{\cdot}$  are evaluated at regions where the flow originates. This case is shown in Figure 10.4.

At all interfaces between solid and fluid, a *steady-state heat balance* is established (no thermal capacity present). Source terms are added at those surfaces for the incident short wave radiation  $q_{sw,i}$  and the net internal radiative heat exchange  $q_{lw,i}$  between this surface and all other surfaces of the respective zone (see Chapters 7 and 8 for a detailed description, how to compute these terms). Figures 10.3 and 10.4 clarify the domains and their interaction.

Note first, that the treatment of the internal (long wave) radiation requires to simultaneously consider the heat exchange between *all* participating surfaces of each zone. If the long wave radiation is not calculated separately (as it is explained in this book), the equation set of the thermal model itself remains sparse but becomes non-linear.

Note secondly, a drawback of the described discretization method is, however, that multizone modeling starts already by definition with a discrete model. The originally continuous physical problem, described by partial differential and integro-differential equations, is transformed into a set of difference expressions and several heat transfer mechanisms are linearized. Of course, a model still can be locally refined, e.g., by increasing the number of cells or grid points in the wall discretization which improves the accuracy. In multi-physics, the different thermodynamic domains are usually treated separately by a partitioned solution approach.

### 10.2.2 Heat conduction within solid components

In building performance simulation, the time-dependent heat conduction through solid wall components is usually treated in a one-dimensional manner. Within the scope of this book, a wall consists of a set of  $n$  layers, where each layer is further decomposed into  $m$  sub-layers, giving  $N = m \cdot n$  control volume elements. Figure 10.5 details the discretization for the case of three control volumes  $i$  with different material properties density  $\varrho_i$ , heat conductivity  $\lambda_i$  and capacity  $c_i$  each.

For each control volume  $i$ , with  $i = 1 \dots N$ , a total heat capacity

$$C_i = \varrho_i c_i s_i \quad (10.3)$$

can be calculated, where  $s_i$  is the thickness of the respective layer. In order to account for different layer material characteristics, equivalent resistances  $\Lambda_i$  are computed between each center point of a control volume or surface balance location, respectively:

$$\Lambda_i = \begin{cases} 2 \lambda_i / s_i & \text{for } i = 1 \\ 2 / \left( \frac{s_i}{\lambda_i} + \frac{s_{i-1}}{\lambda_{i-1}} \right) & \text{for } 2 \leq i \leq N \\ 2 \lambda_N / s_N & \text{for } i = N + 1 \end{cases} \quad (10.4)$$

The numbering hereby starts by definition at the inner surface. In Figure 10.5,  $T_{int}$  is the temperature at the internal wall surface, and  $T_{ext}$  the temperature at the external wall surface, respectively.

Using a central finite difference stencil in space and a first order backward Euler scheme for the time discretization, which have been both introduced in Chapter 6, we obtain a discrete

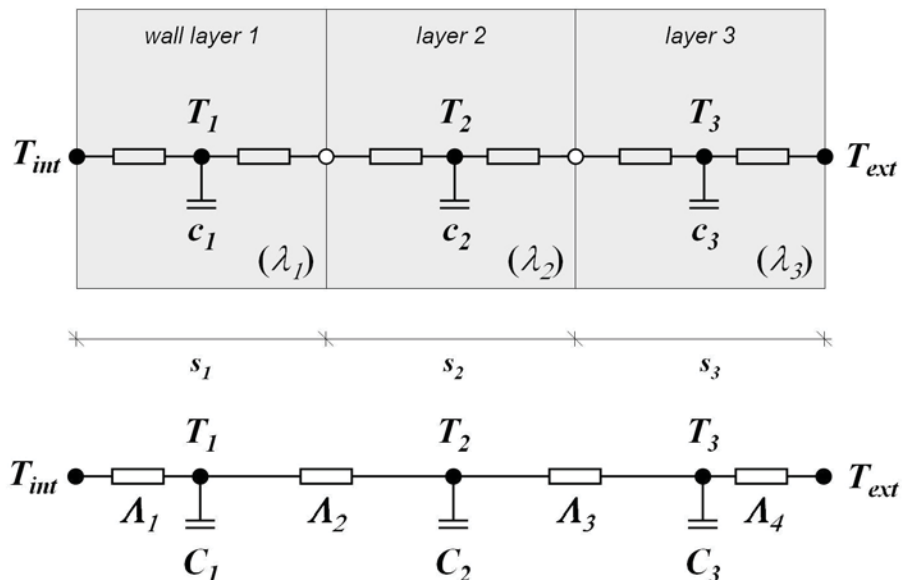


Figure 10.5: Model of a multi-layered wall component.

heat balance equation

$$\frac{1}{\Delta t} C_i \left( T_i^{(t+\Delta t)} - T_i^{(t)} \right) = \Lambda_i T_{i-1}^{(t+\Delta t)} - (\Lambda_i + \Lambda_{i+1}) T_i^{(t+\Delta t)} + \Lambda_{i+1} T_{i+1}^{(t+\Delta t)} \quad (10.5)$$

for each solid control volume element  $i$ , with  $i = 1 \dots N$ . At the boundaries, i.e., the surfaces of the respective walls, we get

$$T_0 = T_{int} \quad \text{and} \quad T_{N+1} = T_{ext}$$

as (unknown) boundary conditions.

### 10.2.3 Room air energy balance equation

The energy balance equation (10.6) for the dry room air of a control volume element  $i$  is written in terms of the change of the internal energy on the left-hand-side, and, on the right-hand-side, in terms of the convective heat fluxes to or from this volume  $\dot{Q}_{conv,int,i}$ , the infiltration  $\Delta \dot{H}_{inf,ext,i}$ , the enthalpy change due to inter-zonal air flows (or air exchange between fluid elements)  $\Delta \dot{H}_{zone,i}$ , and the plant output  $\Delta \dot{H}_{plant,i}$ , respectively. Thereby,  $\varrho_{air,i}$  is the density of the dry air,  $V_{air,i}$  is the volume of the respective fluid element,  $c_{air}$  the heat capacity of the dry air, and  $T_{air,i}$  the homogeneous air temperature. The unit of the terms is Watt [W].

$$\frac{1}{\Delta t} \varrho_{air,i} V_{air,i} c_{air} \left( T_{air,i}^{(t)} - T_{air,i}^{(t+\Delta t)} \right) = \dot{Q}_{conv,int,i} + \Delta \dot{H}_{inf,ext,i} + \Delta \dot{H}_{zone,i} + \Delta \dot{H}_{plant,i} \quad (10.6)$$

The convective heat fluxes to or from this element are obtained by collecting the convective heat fluxes of all  $n$  surfaces, which are bounding element  $i$ .

$$\dot{Q}_{conv,int,i} = \sum_{j=1}^n h_j^c A_j \left( T_{int,j}^{(t+\Delta t)} - T_{air,i}^{(t+\Delta t)} \right) \quad (10.7)$$

$T_{int,j}$  is the temperature and  $A_j$  the area of surface  $j$ . The values are evaluated at the future time row  $(t + \Delta t)$ . The convective heat transfer coefficients  $h_j^c$  depend on the type of the boundary layer at the respective location and are therefore chosen in a scope-dependent manner. Details have already been summarized in Section 4.2.2.

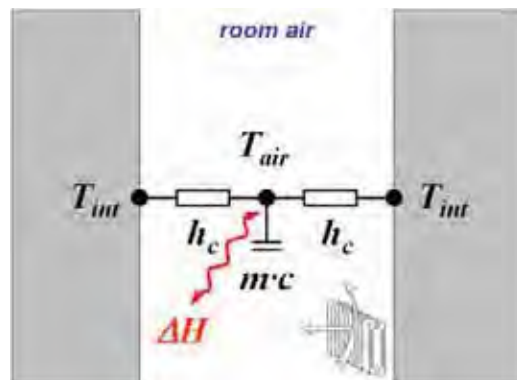


Figure 10.6: Idealized room air energy balance.

The enthalpy change due to infiltration can be approximated in terms of a fixed air change rate  $n$ , if it is not determined explicitly.

$$\Delta \dot{H}_{inf,ext,i} = \frac{1}{3600} n_i \varrho_{air,amb} V_{air,i} c_{air} \left( T_{amb}^{(t+\Delta t)} - T_{air,i}^{(t+\Delta t)} \right) \quad (10.8)$$

Likewise, the mass flow rate  $\dot{m}_{i,r}$  (unit [ $m^3/s$ ]) between zones or, more generally, between  $s$  adjacent fluid elements  $i$  and  $r$ , can be computed with the artificial air pressure nodal network method (cf. Chapter 11). Values  $\varrho_{air}$  and  $c_{air}$  are evaluated at the location, where the flow originates.

$$\Delta \dot{H}_{zone,i} = \sum_{r=1}^s \dot{m}_{i,r} \varrho_{air,i,r} c_{air} \left( T_{air,r}^{(t+\Delta t)} - T_{air,i}^{(t+\Delta t)} \right) \quad (10.9)$$

In the absence of an HVAC control device, the plant can be assumed to respond in a steady-state manner. The plant output can be modeled in an idealized way by calculating the amount of cooling or heating energy, which is supplied by convection in order to maintain element  $i$  at a fixed setpoint temperature  $T_{set,i}$ .  $T_{set,i}$  is chosen according to a plant operation schedule.

$$\begin{aligned} \Delta \dot{H}_{plant,i} &= \frac{1}{3600} n_i \varrho_{air,amb} V_{air,i} c_{air} \left( T_{set,i}^{(t+\Delta t)} - T_{amb}^{(t+\Delta t)} \right) \\ &+ \sum_{j=1}^n h_j^c A_j \left( T_{set,i}^{(t+\Delta t)} - T_{int,j}^{(t+\Delta t)} \right) \end{aligned} \quad (10.10)$$

For a review on modeling control systems, for example, using a PID (proportional plus integrative plus derivative) controller, the reader is referred to the text book of UNDERWOOD [13], or the technical guide of RECKNAGEL ET AL. [9], for example.

#### 10.2.4 Surface heat balance equations

Solid and fluid elements are coupled by formulating steady-state heat balances at each interface between the respective control volumes with the surface temperatures  $T_{int}$  and  $T_{ext}$  as unknowns. Wall and window components accordingly contribute with two surfaces. Heat transmission through windows is treated in a solely steady-state manner, i.e., the heat capacity

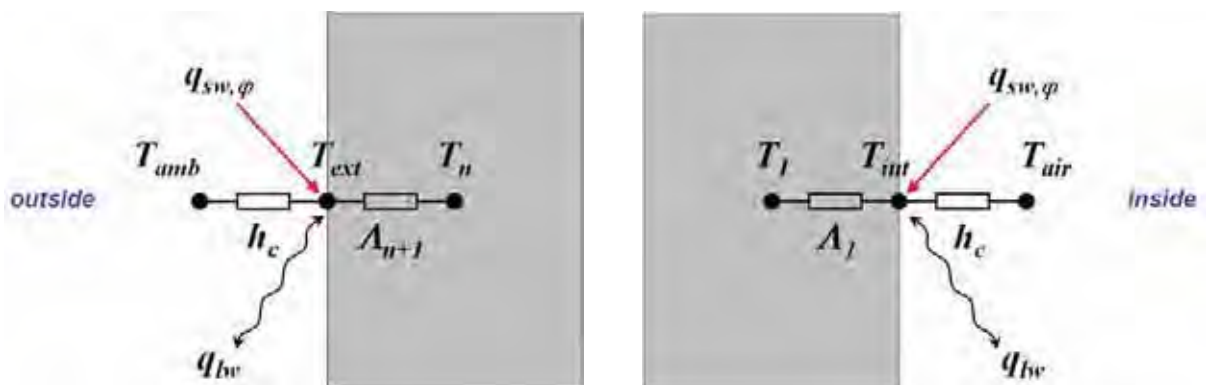


Figure 10.7: Heat balances at external wall surfaces (left) and internal surfaces (right).

of the glass is neglected. Figure 10.7 shows the different terms of the surface energy balances for both cases of an external and an internal surface.

For external wall and window surfaces, the long wave radiative heat exchange between surface and environment,  $q_{lw,ext,i}$ , is given by Equation (8.28) with  $T_{sky}$  the equivalent sky temperature. In the linearized form, cf. Equation (8.33),  $h_{lw,i}$  is the radiative heat transfer coefficient and  $\sigma$  the Stefan-Boltzmann constant.

The absorbed solar radiation,  $q_{sw,\varphi,i}$ , is calculated from Equation (8.18) with the time and site specific values of the beam and diffuse radiation and surface incidence angle  $\varphi$ . The external convective heat transfer, denoted by the coefficient  $h_{amb}^c$ , depends on the wind-driven forced convection. For the empirical formulae it is referred to Section 4.1.3.

**External wall surfaces.** For an external wall surface  $i$  with unknown surface temperature  $T_{ext,i}$ , we get the balance equation

$$\begin{aligned} h_{lw,i}^{(t)} \left( T_{sky}^{(t+\Delta t)} - T_{ext,i}^{(t+\Delta t)} \right) + q_{sw,\varphi,i}^{(t+\Delta t)} \\ + h_{amb}^c \left( T_{amb}^{(t+\Delta t)} - T_{ext,i}^{(t+\Delta t)} \right) + \Lambda_{N+1} \left( T_N^{(t+\Delta t)} - T_{ext,i}^{(t+\Delta t)} \right) = 0 , \end{aligned} \quad (10.11)$$

where  $\Lambda_{N+1}$  is the thermal resistance of the outer-most layer according to Equation (10.4). Due to the linearization,  $h_{lw,i}$  is evaluated at the past (known) time row ( $t$ ). For surfaces with earth contact, the balance equation reduces to

$$\Lambda_{N+1} \left( T_N^{(t+\Delta t)} - T_{earth}^{(t+\Delta t)} \right) = 0 , \quad (10.12)$$

with the earth temperature  $T_{earth}$  (cf. Section 4.1.4).

**External window surfaces.** For external window surfaces with unknown surface temperatures  $T_{ext,i}$  and  $T_{int,i}$ , the balance equation is

$$\begin{aligned} h_{lw,i}^{(t)} \left( T_{sky}^{(t+\Delta t)} - T_{ext,i}^{(t+\Delta t)} \right) + q_{sw,\varphi,win,out}^{(t+\Delta t)} \\ + h_{amb}^c \left( T_{amb}^{(t+\Delta t)} - T_{ext,i}^{(t+\Delta t)} \right) + \Lambda_{win} \left( T_{int,i}^{(t+\Delta t)} - T_{ext,i}^{(t+\Delta t)} \right) = 0 , \end{aligned} \quad (10.13)$$

where  $q_{sw,\varphi,win,out}$  is the absorbed solar radiation within the outwards facing part of the glazing system (cf. Chapter 9), and  $\Lambda_{win}$  is thermal resistance of the overall window system (without internal and external radiative and convective heat transfer  $h^{c,r}$ ), i.e.,

$$\Lambda_{win} = 1 / \left( \frac{1}{U_t} - \frac{1}{h_{amb}^{c,r}} - \frac{1}{h_{int}^{c,r}} \right) . \quad (10.14)$$

**Internal wall surfaces.** In a similar manner, the energy balances are drawn for the internal wall surfaces. With unknown surface temperature  $T_{int,i}$ , we get

$$q_{lw,int,i}^{(t+\Delta t)} + q_{sw,int,i}^{(t+\Delta t)} + h_{int}^c \left( T_{air}^{(t+\Delta t)} - T_{int,i}^{(t+\Delta t)} \right) + \Lambda_1 \left( T_1^{(t+\Delta t)} - T_{int,i}^{(t+\Delta t)} \right) = 0 . \quad (10.15)$$

The source term  $q_{lw,int,i}$  can be computed with the radiosity method of Section 7.2.4 by solving the equation set (7.38), taking the surface temperatures of the past (known) time row as input. The term denotes the net long wave radiative heat exchange between surface  $i$  and *all* other surfaces of the respective zone. Similarly, the amount of the solar radiation  $q_{sw,int,i}$ , which is distributed to surface  $i$ , is obtained by applying the raytracing method shown in Section 8.6.2. Formulae for  $h_{int}^c$  addressing the internal convective heat transfer by free convection are detailed in Section 4.2.2.  $\Lambda_1$  is the thermal resistance of the inner-most wall layer, cf. Equation (10.4).

**Internal window surfaces.** The energy balance equation for an internal window surfaces with unknown surface temperatures  $T_{int,i}$  and  $T_{ext,i}$  is given by

$$q_{lw,int,i}^{(t+\Delta t)} + q_{sw,\varphi,win,int}^{(t+\Delta t)} + h_{int}^c \left( T_{air}^{(t+\Delta t)} - T_{int,i}^{(t+\Delta t)} \right) + \Lambda_{win} \left( T_{ext,i}^{(t+\Delta t)} - T_{int,i}^{(t+\Delta t)} \right) = 0 . \quad (10.16)$$

Thereby,  $q_{sw,\varphi,win,int}$  is the absorbed solar radiation within the inwards facing part of the glazing system (cf. Chapter 9).  $\Lambda_{win}$  is again the thermal resistance of the overall window system.

## 10.3 Structure of the energy matrix equation

### 10.3.1 The energy matrix equation

Applying the above described discretization scheme yields a linear equation set

$$\mathbf{A} \cdot \mathbf{x}^{(t+\Delta t)} = \mathbf{b}^{(t)} \quad (10.17)$$

with coefficient matrix  $\mathbf{A}$ , unknown temperature vector

$$\mathbf{x}^{(t+\Delta t)} = \left( T_1^{(t+\Delta t)}, T_2^{(t+\Delta t)}, T_3^{(t+\Delta t)}, \dots \right)^T$$

at the future time row  $(t + \Delta t)$ , and with the known terms  $\mathbf{b}$  on the right-hand-side.

One equation is obtained for each solid and fluid control volume, and one for each interface between a solid and a fluid element. The difference formulae of the balance equations are evaluated at the center of gravity of each control volume and interface surface, respectively. In summary, for each zone the equation set contains

- one equation for each fluid element (room air energy balance),
- $n \cdot m$  equations for each wall (transient heat conduction in solids), which is composed of  $n$  layers, each being discretized into  $m$  control volumes (sub-layers), and
- two additional equations for each wall and each window, originating from the steady-state surface energy balances.

For example, Figure 10.8 shows the coefficient matrix  $\mathbf{A}$  which is obtained for a typical single zone model. The sample model consists of a single hexahedral fluid element (one equation for

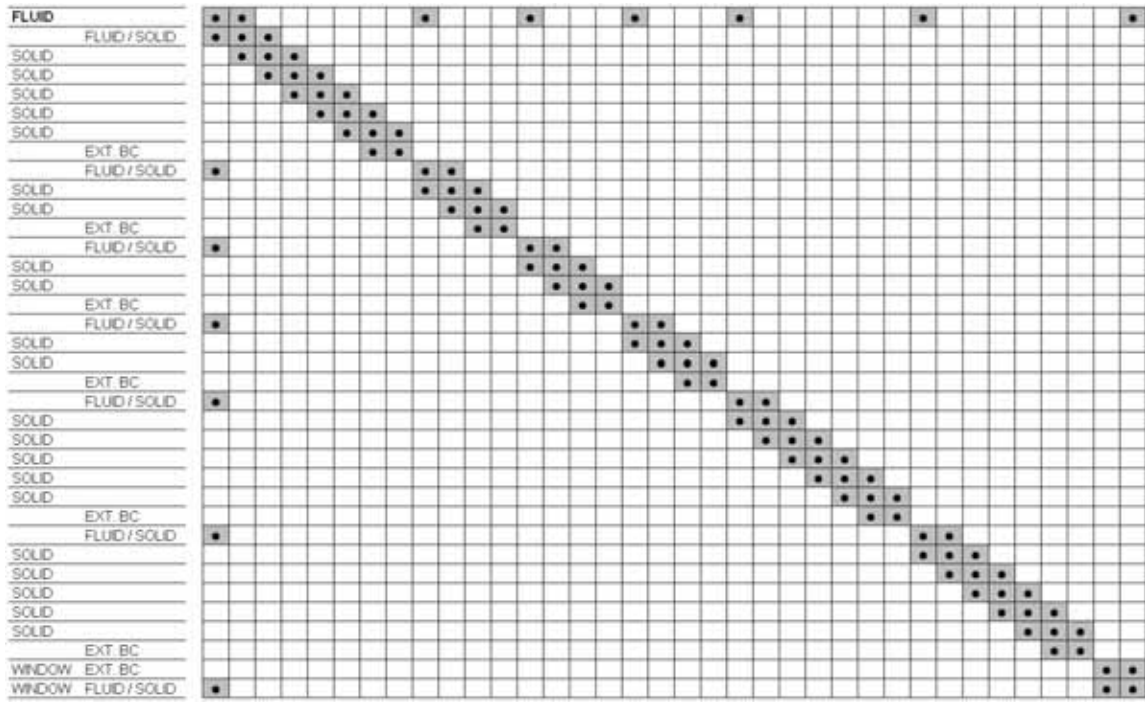


Figure 10.8: Example: Matrix structure of a single zone model. The legend on the left-hand-side indicates the type and reference location of the balance equation.

the fluid control volume), which is connected to six wall components (six equations for the surface balances). Three of the wall elements are thereby decomposed into six sub-elements, the other three are composed of three layers (accordingly 27 control volumes and equations for the solid elements). Only a single wall contains an opening with window element (another two equations for the surface balances). In total, the assembled equation set comprises  $1 + 6 + 3 \cdot 6 + 3 \cdot 3 + 2 = 36$  equations and unknowns.

### 10.3.2 Solving the energy matrix equation

The coefficient matrix  $\mathbf{A}$  of the linear equation set (10.17) is positive definite and *non-symmetric*. Using the shown discretization scheme, it shows a characteristic band structure but comprises sparsely populated columns and rows which originate from the convective coupling between solid and fluid control volume elements as indicated in Figure 10.8.

If the system is not too large, a direct solver can be used to solve the equation set (10.17) for the unknown temperature values. An appropriate method is, for example, the LU-factorization, which has been introduced in Section 7.2.5, or the Gauss-Jordan algorithm with pivotization [8]. As the coefficient matrix is non-symmetric, for example, a Generalized Minimal Residual (GMRES) method [11] can be applied, if an iterative solver is preferred. For a review on equation solving techniques, the interested reader is referred to [7, 8, 10, 12] and the references therein.

CLARKE [1] discusses matrix partitioning techniques with special emphasis on the dynamics

of the different subsystems that contribute to the coefficient matrix in building performance simulation, including plant components. Sub-matrices are obtained with the method, which can be inverted with a direct solver with respect to their inherent frequency characteristics. For a review on solution techniques for stiff differential equations which are characterized by different time scales it is referred to [3], for example.

With known solution vector, i.e., temperature values, at time  $(t + \Delta t)$ , heat fluxes can be computed and integrated over the last time interval  $\Delta t$  in a straightforward manner. Results are usually exported to a data file which can be processed by a common spreadsheet tool.

## 10.4 The overall solution algorithm

In summary, we obtain the following overall solution algorithm for the thermal network. It is referred to Section 8.6.2 for the algorithm (3) to compute the direct and diffuse solar radiation distribution using a raytracing and a radiosity method. For the sake of simplicity, the algorithm is written here without an adaptive choice of time step size.

---

### **Algorithm A-4** Overall solution algorithm for the thermal network.

---

- 1: **for all** time steps of one year **do**
  - 2:   store values of preceding time step
  - 3:   get and interpolate current weather data
  - 4:   reset assembly
  - 5:   compute external and internal direct and diffuse solar energy distribution
  - 6:   compute internal long wave radiative heat exchange
  - 7:   compute surface convective heat transfer coefficients
  - 8:   evaluate sky temperature and compute external radiation
  - 9:   assemble coefficient matrix
  - 10:   solve
  - 11:   compute and integrate heat gains
  - 12:   output to file
  - 13: **end for**
- 

## 10.5 Time discretization convergence analysis

Section 6.2 already discussed the accuracy of the spatial finite difference discretization. In this section, a convergence study is carried out in order to check the model consistency in terms of the time discretization of the overall numerical algorithm which was discussed before. Chapter 12 below will further address the issue of the dynamic answers of the system and will compare the solutions obtained with the developed model "iZone" with the benchmark published in the VDI Standard 6020 [15].

In the following analysis, the geometry and material parameter of the model are defined according to the specifications of Section 3.6 which equals the definition of *Example 13* of the VDI Standard 6020 [15]. The components are of heavy weight type (type "S"). All results are

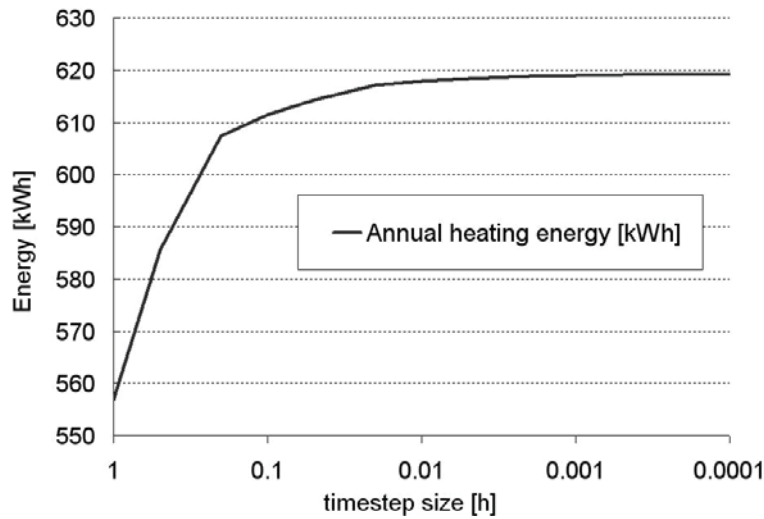


Figure 10.9: Annual heating energy against time resolution (logarithmic scaling).

given for a whole year simulation using the weather data of the test reference year TRY5 as input.

The time discretization makes use of an implicit first order (backward Euler) scheme for solving the equation set of the zone model for each time step via LU decomposition. Section 10.4 indicated the sequence of the overall solution algorithm. The major computing time during each time step is thereby required (i) for assembling the coefficient matrix and (ii) for tracking the direct beam radiation in detail. For small sized problems, the other parts of the computation contribute less. CLARKE [1] discusses in his book several optimization techniques concerning this scope.

Figure 10.9 shows the convergence of the required annual heating energy with respect to the choice of the time step size. It is apparent that a time step interval of one hour is a very coarse approximation for predicting the annual heating demand if a first order method is applied. Re-

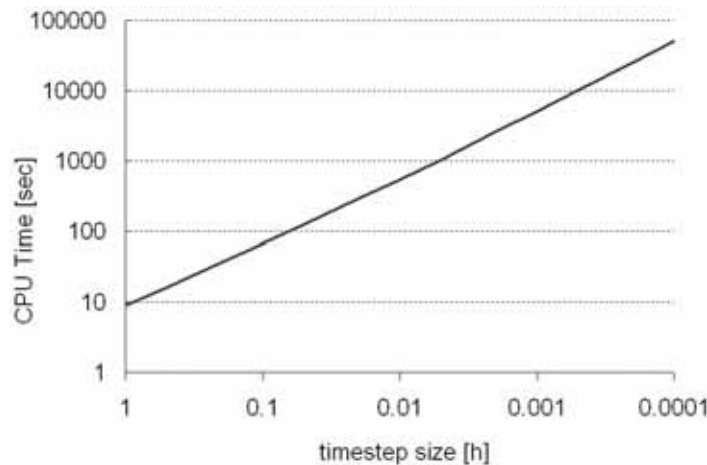


Figure 10.10: CPU time according to time step size (annual simulation, double logarithmic scaling).

ducing the time step size to a 6-minute interval ( $0.1h$ ) yields a high gain of accuracy while the overall computation time only slightly increases. Time steps smaller than 36 seconds ( $0.01h$ ) do not significantly contribute to the accuracy but raise the overall computational effort.

The computational effort in terms of CPU time is plotted in Figure 10.10 in double logarithmic scaling. It can be seen from the figure that

$$\text{CPU time} = \mathcal{O}(1 / \Delta t) ,$$

i.e. refining the time discretization by a factor of 10 also increases the computing time by a factor of 10. The choice of the timestep size is therefore a tradeoff between computational effort and accuracy<sup>1</sup>.

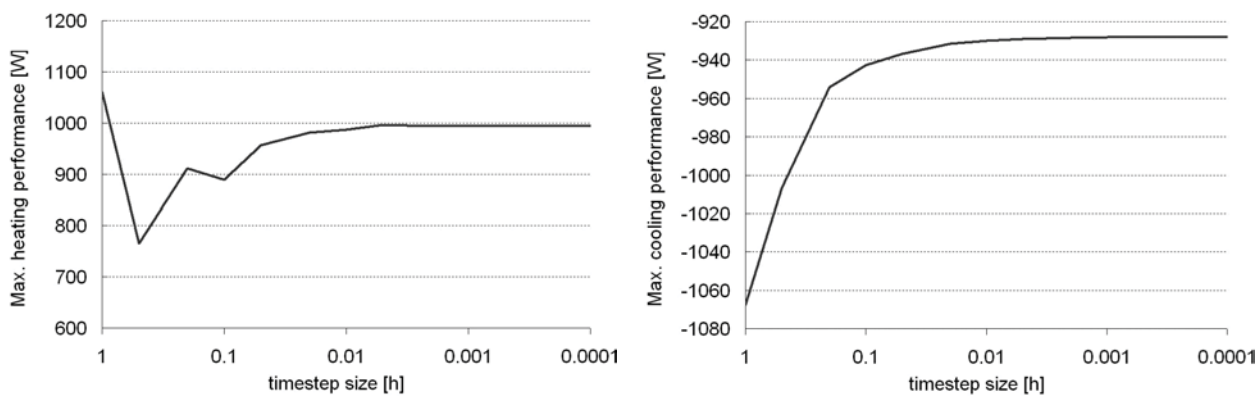


Figure 10.11: Maximum heating and cooling performance and time resolution (logarithmic scaling).

Figure 10.11 indicates the convergence of the maximum required heating and cooling performances with respect to the time resolution. Again, a time step resolution of 36 seconds ( $0.01h$ ) yields acceptable results for a whole year simulation at the expense of approximately 12 minutes overall computing time.

The last example of Figure 10.12 compares the annual sum of the internal heat gains to the time resolution. The figure indicates the minimum timestep size which would be required in order to resolve the plant operation time schedule (on/off), if no interpolation scheme is used to capture this effect otherwise.

## 10.6 References

- [1] J.A. Clarke. *Energy simulation in building design*. Butterworth-Heinemann, 2nd edition, 2001.
- [2] EN ISO 10077-2. *Thermal performance of windows, doors and shutters – Calculation of thermal transmittance – Part 2: Numerical method for frames*. DIN Deutsches Institut für Normung e.V., Beuth Verlag, 2003.

<sup>1</sup>In this case, an Intel Core2 Duo P9500 architecture was used with 2.53 GHz clock frequency.

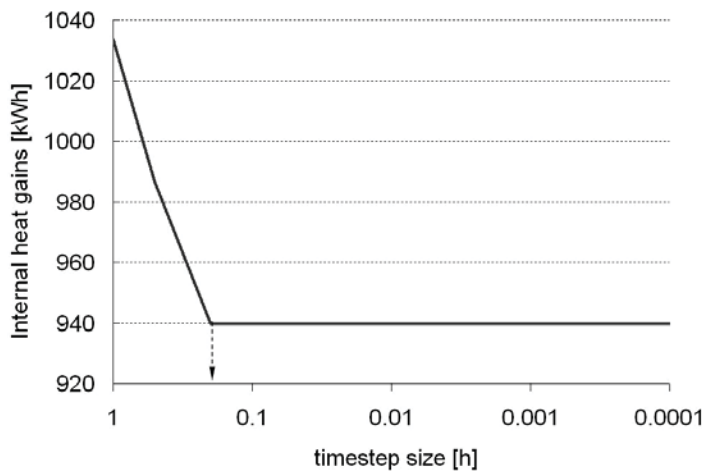


Figure 10.12: Internal heat gains in terms of timestep size.

- [3] M. Günther, M. Hoschek, and P. Rentrop. Differential algebraic equations in electric circuit simulation. Technical Report 1964, Technische Universität Darmstadt, Fachbereich Mathematik, 1998.
- [4] G. Hauser, H. Schulze, and U. Wolfseher. Wärmebrücken im Holzbau. *Bauphysik*, 5(1):17–21, 1983.
- [5] ISO 10211 – Part 1 and 2. *Thermal bridges in building construction – Heat flows and surface temperatures – Detailed calculations*. DIN Deutsches Institut für Normung e.V., Beuth Verlag, 2007.
- [6] ISO 15099, Ausgabe November 2003. *Thermal performance of windows, doors and shading devices - Detailed calculations*. DIN Deutsches Institut für Normung e.V., Beuth Verlag, 2003.
- [7] A. Meister. *Numerik linearer Gleichungssysteme*. Vieweg, 2nd edition, 2005.
- [8] W.H. Press, S.A. Teukolsky, W.T. Vetterling, and B.P. Flannery. *Numerical recipes in C++*. Cambridge University Press, 2nd (C++) edition, 2002.
- [9] Recknagel, Sprenger, and Schramek. *Taschenbuch für Heizung, Klima und Technik*. Oldenburg Verlag, München, 73 edition, 2007.
- [10] V.S. Ryaben'kii and S.V. Tsynkov. *A theoretical introduction to numerical analysis*. Chapman & Hall/CRC, 2007.
- [11] Y. Saad and M.H. Schultz. A generalized minimal residual algorithm for solving nonsymmetric linear systems. *SIAM J. Sci. Stat. Comput.*, 7:856–869, 1986.
- [12] H.R. Schwarz. *Numerische Mathematik*. B.G. Teubner, 4th edition, 1997.
- [13] C. Underwood and F. W. H. Yik. *Modelling methods for energy in buildings*. Blackwell Publishing, Oxford, 2004.

- [14] C. van Treeck and E. Rank. Dimensional reduction of 3d building models using graph theory and its application in building energy simulation. *Engineering with Computers*, 23:109–122, 2006.
- [15] VDI 6020 Part 1. *Requirements for methods of building performance simulation, part 1: buildings*. VDI Verein Deutscher Ingenieure, Beuth Verlag, 2001.

# Chapter 11

## Modeling air flows in buildings

### 11.1 The nodal network method

#### 11.1.1 Artificial air pressure nodal network

The infiltration and ventilation rate for the air exchange between zones and between zone and environment can be either estimated in terms of a fixed air change rate per hour, as it is formulated in Section 10.2.3, or it can be explicitly computed by means of steady-state air mass flow balances using an artificial air pressure nodal network.

As indicated in Figure 11.1, a fluid control volume is approximated by a single air pressure node which is located at the center of gravity of the respective element. It is linked with other control volumes, if a flow path between these volumes exists.

The air temperature at the air nodes is determined by the thermal multizone model. The model assumes a well stirred and uniform air temperature distribution within each control volume  $i$ . For large spaces, the air volume is therefore decomposed into a set of smaller, preferably vertically stacked, fluid control volumes.

With the artificial air pressure nodal network, the vertical temperature stratification of a large enclosure can be reasonably well described if recirculation is not present. Bidirectional air change patterns are captured by the model but require knowledge about the flow characteristics. In this case, it is recommended to use a computational fluid dynamics (CFD) model instead (see Section 11.4).

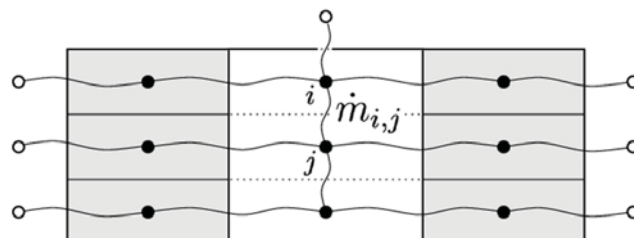


Figure 11.1: Artificial air pressure nodal network of a building with inner courtyard.

Boundary conditions (cf. Chapter 4) of the pressure network is the static and dynamic air pressure distribution alongside the building facade and the pressure or flow induced by a mechanical ventilation system. The pressure distribution at the facade is influenced by the building aerodynamics and further thermal effects. For further reading, the reader is referred to [1, 7, 27], and the article of HENSEN in [21].

### 11.1.2 The Bernoulli equation

For steady-state conditions and incompressible fluids, the pressure drop  $\Delta p_{i,j}$  between two nodes  $i$  and  $j$  can be described by the *Bernoulli equation* [10, 28] in a one-dimensional manner. Likewise, spaces in building simulation are connected by a flow path, and can be represented by a single node with total pressure  $P_i$  each, further assuming a uniform air temperature distribution  $T_{air,i}$  within each space.

The Bernoulli equation is derived from the law of conservation of the total energy, that is, the sum total of the energies in a fluid flow remains constant along a streamline. The total energy comprises the kinetic energy terms  $\varrho u^2/2$ , the static pressure energy  $p$ , and the potential energy terms  $\varrho(T_{air}) g z$ , with the temperature-dependent density  $\varrho(T_{air})$ , the flow velocity  $u$ , the acceleration due to gravity  $g$ , and a respective reference datum  $z$ . With  $\Delta p_{1,2}$ , the dissipation due to friction and dynamic losses,

$$\frac{\rho}{2} u_1^2 + p_1 + \rho g z_1 - \Delta p_{1,2} = \frac{\rho}{2} u_2^2 + p_2 + \rho g z_2 . \quad (11.1)$$

Terms in (11.1) can be grouped to find the stack effect  $\varrho(T_{air}) g (z_1 - z_2)$  and the total pressure  $P = p + \varrho u^2/2$ . If nodes represent spaces, the dynamic pressure is zero (note that this is not the case for nodes within pipes or ducts), and Equation (11.1) can be reduced to

$$\Delta p_{i,j} = P_i - P_j + \varrho(T_{air}) g (z_i - z_j) \quad (11.2)$$

to describe the pressure difference between two nodes  $i$  and  $j$  due to dissipation with openings located at heights  $z_I$  and  $z_J$ , respectively [10]. The flow direction is from  $i$  to  $j$ , if  $\Delta p_{i,j} > 0$ . The temperature dependent mass density can be obtained from the ideal gas law

$$\varrho(T_{air}) = \frac{\varrho_0 T_0}{T_{air}} , \quad (11.3)$$

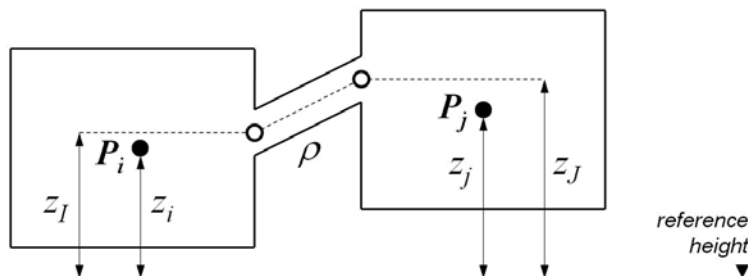


Figure 11.2: Nodal positions and reference datum of a connected system (example).

with known density  $\varrho_0$  at reference level  $T_0$ , taking the temperature  $T_{air}$  of the fluid streaming through the connection component, i.e.,

$$T_{air} = \begin{cases} T_{air,i} & \text{if } P_i > P_j \\ T_{air,j} & \text{if } P_i < P_j \end{cases}. \quad (11.4)$$

### 11.1.3 Mass conservation

By means of the Bernoulli equation, an expression is found for the mass flow rate  $\dot{m}_{i,j}$  with respect to the pressure drop  $\Delta p_{i,j}$  between the two spaces:

$$\dot{m}_{i,j} = sign(\Delta p_{i,j}) C_d \varrho A \sqrt{\frac{2 |\Delta p_{i,j}|}{\varrho}} \quad (11.5)$$

A positive *sign* function means, that the flow is originating at region  $i$ . The coefficient  $C_d$  denotes the flow resistance between both spaces. For large spaces with discharge area  $A$ , such as an open window,  $C_d = 0.7$ ; other values are detailed in [1, 32], for example.

In building performance simulation, the air flows are generally characterised by the power law

$$\dot{m}_{i,j} = sign(\Delta p_{i,j}) \rho k_d |\Delta p_{i,j}|^x \quad (11.6)$$

with flow coefficient  $k_d$  and flow exponent  $x$  [12, 21, 23].

- For the case of a fully developed turbulent flow between spaces, Equation (11.6) becomes (11.5), i.e., if  $x = 0.5$  and  $k_d = C_d A (2/\varrho)^{0.5}$ .
- For laminar flows through small cracks, the mass flow rate is determined by the dynamic fluid viscosity  $\mu$  setting  $x$  to unity. In this case,  $k_d = \pi d^4 / (128 \mu L)$ , with crack diameter  $d$  and length  $L$  [23].

Note, that the air change between spaces in reality is of bi-directional nature, as already indicated in Figure 2.13 in Chapter 2. ALLARD ET AL. [1] discuss an appropriate integration scheme for both flow directions by assuming a flow profile and by estimating the location of the neutral line. In this case, in the thermal multizone model, both enthalpy flows must be considered.

**Mass conservation.** From the continuity equation for incompressible fluids,

$$div \vec{u} = 0 , \quad (11.7)$$

it follows for each control volume, that the net mass flow from and to the respective control volume equals zero. Applying the principle of mass conservation to each node  $i$ , we obtain a non-linear equation set with the unknown nodal air pressure values.

## 11.2 Iterative solution by a Newton-Raphson method

The resulting equation set is non-linear due to the power law formulation in Equation (11.6). It can be iteratively solved with the *Newton-Raphson method*, which is distinguished by fast convergence within a few iteration steps [12, 14].

Following the description in [29], we obtain the equation set

$$\mathbf{R}(\mathbf{p}) = 0 \quad (11.8)$$

with the unknown nodal total pressure values  $\mathbf{p} = [P_i]$ , and the residuals

$$\mathbf{R}(\mathbf{p}) = [R_i(P_i)] \quad \text{with} \quad R_i(P_i) = \sum_{j=1}^{n_i} \dot{m}_{i,j} = \sum_{j=1}^{n_i} \rho k_{d_{i,j}} \text{sign}(\Delta p_{i,j}) |P_i - P_j|^{x_{i,j}} \quad (11.9)$$

in terms of the  $n_i$  mass flows from or to node  $i$  with  $j = 1, \dots, n_i$ . The values  $\mathbf{p}_k$  are known from the previous iteration  $k$ . For each successive step, with the correction terms  $\mathbf{c}$ , a new approximation

$$\mathbf{p}_{k+1} = \mathbf{p}_k + \omega \mathbf{c} \quad (11.10)$$

is computed towards the (unknown) exact solution, until the residuals satisfy a defined epsilon threshold. With the unity relaxation coefficient  $\omega = 1.0$ , the approach is called a Newton-Raphson method.

The correction terms  $\mathbf{c}$  are approximated by means of a Taylor series expansion, taking the constant and linear terms

$$\mathbf{R}(\mathbf{p}_{k+1}) \approx \mathbf{R}(\mathbf{p}_k) + D \mathbf{R}(\mathbf{p}_k)[\mathbf{c}] = 0 \quad . \quad (11.11)$$

Evaluating the directional derivative by the chain rule [5] within the environment  $\epsilon = 0$ , we get

$$D \mathbf{R}(\mathbf{p}_k)[\mathbf{c}] = \frac{d}{d\epsilon} \Big|_{\epsilon=0} \mathbf{R}(\mathbf{p}_k + \epsilon \mathbf{c}) = \mathbf{J}(\mathbf{p}_k) \mathbf{c} \quad . \quad (11.12)$$

The *Jacobian matrix*  $\mathbf{J}(\mathbf{p}_k)$  thereby denotes the nodal pressure correction in terms of the branch flow partial derivatives, where

$$\mathbf{J}(\mathbf{p}_k) = [J_{i,j}(\mathbf{p}_k)] \quad \text{with} \quad J_{i,j}(\mathbf{p}_k) = \left. \frac{\partial R_i}{\partial p_j} \right|_{\mathbf{p}_k} \quad . \quad (11.13)$$

Substituting the derivative in Equation (11.11) by the expression (11.12), we obtain a *linear* equation set with non-symmetric and sparse coefficient matrix and with unknown correction vector  $\mathbf{c}$ ,

$$\mathbf{c} = -\mathbf{J}(\mathbf{p}_k)^{-1} \mathbf{R}(\mathbf{p}_k) \quad , \quad (11.14)$$

which can be solved by a direct method within each iteration.

The diagonal elements of the Jacobian,

$$J_{i,i} = \sum_j^{n_i} \left( \frac{\partial \dot{m}_{i,j}}{\partial p_i} \right)_i , \quad (11.15)$$

correspond with the correction of the residuals in terms of the pressure change at node  $i$ . The off-diagonal values denote changes due to pressure differences between nodes  $i$  and  $j$ ,

$$J_{i,j} = \sum_j^{n_i} \left( -\frac{\partial \dot{m}_{i,j}}{\partial p_j} \right)_i \quad \text{if } i \neq j . \quad (11.16)$$

WALTON ET AL. [14, 31] suggest a relaxation method for extrapolating the (oscillating) corrections to an assumed solution and, thus, to further accelerate convergence. Correction values  $c_i^{(k)}$  at iteration ( $k$ ) are then multiplied by the individual relaxation factors

$$\omega_i = \frac{1}{1 - (c_i^{(k)} / c_i^{(k-1)})} . \quad (11.17)$$

## 11.3 Coupling with the thermal zone model

HENSEN [12, 13] summarizes the partitioned solution approaches for coupling a thermal multizone model (energy conservation) with an artificial nodal air pressure network (mass conservation). If the airflow in buildings is buoyancy driven, both the heat and the airflows are strongly coupled, which is the usual case in the scope of energy efficient building design [1, 21]. In this case, the thermal model must be considered at the same time with the infiltration and ventilation model. Only for flows, which are primarily pressure-driven, such as a constant flow imposed by the HVAC system, a separate treatment is possible (but not recommended).

We distinguish between the following approaches:

- *Direct coupling.* A direct coupling is obtained, if the equations for the air and heat flow are combined into a single expression to form a global system, also referred to as full integration [17]. This approach is not recommended in terms of the above described advantages of a partitioned solution approach. See also the discussion in [21].
- *Sequential coupling.* Figure 11.3 indicates the sequential coupling of both methods [17], which is also known as 'ping-pong' method [12]. Results of the thermal network (temperatures) are communicated with the pressure network. With the updated nodal pressure

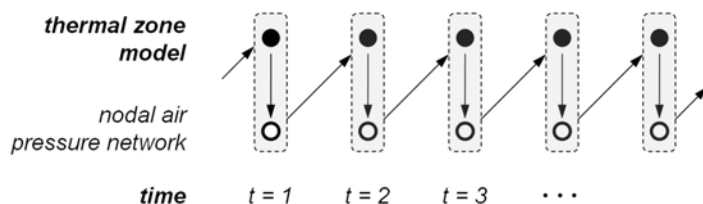


Figure 11.3: Explicit coupling between both solvers ('ping-pong') [1, 12, 29].

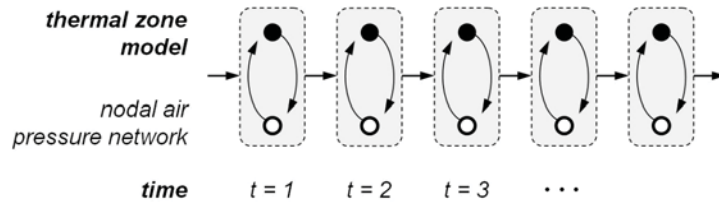


Figure 11.4: Iterative coupling between both solvers ('onion') [1, 12, 29].

values, the computed mass flow rates are sent back to the thermal network, and so on. As the coupling is based on an explicit time step basis, fairly small time steps are necessary in order to reach convergence and to avoid severe oscillations in simulation [13].

- *Iterative coupling.* The best option is shown in Figure 11.4, where both procedures are repeated iteratively for the same time step, until the residuals are below a certain threshold. The method, thus, allows for larger overall time steps, provided that the iteration reaches convergence. The iterative coupling comes along with increased computational effort.

For case studies with the above described methods, the reader is referred to the article of HENSEN in [21].

## 11.4 Outlook: Computational fluid dynamics (CFD)

With computational fluid dynamics (CFD), the Navier-Stokes equations and the energy equation are solved numerically, which offers a detailed insight into the room air flow behavior. For setting up a CFD simulation, a geometric model is required in order to create a surface and volume mesh. The latter process is very time consuming in terms of engineering work and therefore restricts the application of CFD in practice.

Most commercial CFD codes make use of a finite volume discretization method (FVM) [9]. Other numerical techniques in this context are finite difference (FDM), or finite element methods (FEM) [24]. Recently, lattice Boltzmann methods (LBM) are maturing as an alternative tool for solving fluid flow problems governed by the Navier-Stokes equations [4, 8, 18, 19, 25, 30]. For an introduction into the basics of CFD, the reader is referred to the book of GRIEBEL ET AL. [11], or the REHVA guidebook series, e.g., [22]. Background information concerning the numerical methods can be found in [15, 16, 24].

The turbulent convective nature of the air flows requires the application of appropriate turbulence models. With a turbulence model, at least parts of the turbulent energy spectrum are modeled, instead of explicitly resolving all dynamic scales in space and time. Generally, we distinguish between models which are based on the Reynolds averaged Navier-Stokes (RANS) equations [28], and models in the scope of the large eddy simulation (LES), which make use of a volume-averaged formulation of the Navier-Stokes equations [6, 26]. Likewise, mixed formulations exist. The hierarchy of turbulence models can be separated into eddy viscosity

approaches and Reynolds stress models. In both cases, algebraic turbulence models or formulations, which are based on one or more transport equations, are known. For example, the well known  $k\epsilon$ -model is a RANS-based two equation model [20]. A good overview is given, for example, by OERTEL ET AL. in [24].

In the scope of indoor air flow simulation, i.e., for air temperatures at room temperature level and for small temperature variations, it is usually convenient to couple the momentum equations and the energy equation in terms of the Boussinesq approximation [3, 28]. As the temperature dependence of the fluid properties density, viscosity, specific heat capacity and heat conductivity is small, a linear correlation between temperature and density is assumed. The density variation is accordingly modeled in terms of a body force term.

Initial and boundary conditions are required such as in- and outflow conditions (velocity or pressure values) or temperatures or heat fluxes at surfaces bounding the flow domain. Realistic boundary conditions can be obtained by a preceding simulation or coupling with a thermal multizone model as shown by BEAUSOLEIL-MORRISON [2] or by the author in [29].

For modeling the region close to walls with a wall function approach, it is important to bear in mind, that the boundary layer profile (cf. [28]) depends on the flow characteristics and the orientation of a respective surface. For example, the boundary layer profile of forced convection along a horizontally orientated floor surface can be described in terms of a viscous sublayer and a logarithmic profile within the turbulent near-wall region. The thin boundary layer of a vertically oriented wall surface with free convection type flow, in turn, has the shape of a parabolic function [33]. Applying either wall function model to the other problem would fail to produce proper results.

## 11.5 References

- [1] F. Allard, M. Santamouris, S. Alvarez, E. Dascalaki, G. Guerracino, E. Maldonado, S. Sciuto, and L. Vandaele. *Natural ventilation in buildings*. James and James, 1998.
- [2] I. Beausoleil-Morrison. *The adaptive coupling of heat and air flow modelling within dynamic whole building simulation*. PhD thesis, University of Strathclyde, Glasgow, 2000.
- [3] A. Bejan. *Convection heat transfer*. John Wiley & Sons, Inc., 1993.
- [4] P. Bhatnagar, E.P. Gross, and M.K. Krook. A model for collision processes in gases. *Physical Review*, 94(3):511–525, 1954.
- [5] J. Bonet and R.D. Wood. *Nonlinear continuum mechanics for finite element analysis*. Cambridge University Press, 1997.
- [6] M. Breuer. *Direkte numerische Simulation und Large-Eddy Simulation turbulenter Strömungen auf Hochleistungsrechnern*. Professorial dissertation, Lehrstuhl für Strömungsmechanik, Friedrich-Alexander-Universität Erlangen-Nürnberg, 2001.

- [7] J.A. Clarke. *Energy simulation in building design*. Butterworth-Heinemann, 2nd edition, 2001.
- [8] D. d'Humières, I. Ginzburg, M. Krafczyk, P. Lallemand, and L.-S. Luo. Multiple-relaxation-time lattice Boltzmann models in three dimensions. *Phil. Trans. R. Soc. Lond. A*, 360:437–451, 2002.
- [9] J.H. Ferziger and M. Péridier. *Computational methods for fluid dynamics*. Springer Verlag, 2nd edition, 1999.
- [10] K. Gersten. *Einführung in die Strömungsmechanik*. Vieweg, 6th edition, 1991.
- [11] M. Griebel, T. Neunhoeffer, and T. Dornseifer. *Numerical Simulation in Fluid Dynamics: A Practical Introduction*. Siam Monographs on Mathematical Modeling and Computation, 1997.
- [12] J.L.M Hensen. *On the thermal interaction of building structure and heating and ventilating system*. PhD thesis, University of Strathclyde, Glasgow, 1991.
- [13] J.L.M. Hensen. A comparison of coupled and de-coupled solutions for temperature and air flow in a building. *ASHRAE Trans.*, 105(2):962–969, 1999.
- [14] M. Herrlin and F. Allard. Solution methods for the air balance in multizone buildings. *Energy and Buildings*, 18:159–170, 1992.
- [15] C. Hirsch. *Numerical computation of internal and external flows, Vol. 2, Computational methods for inviscid and viscous flows*. John Wiley & Sons Ltd., 1984.
- [16] C. Hirsch. *Numerical computation of internal and external flows, Vol. 1, Fundamentals of numerical discretization*. John Wiley & Sons Ltd., 1988.
- [17] J. Kendrick. An overview of combined modelling of heat transport and air movement. Technical note AIVC 30, Air Infiltration and Ventilation Centre, Coventry, UK, 1993.
- [18] P. Lallemand and L.-S. Luo. Theory of the lattice Boltzmann method: Dispersion, dissipation, isotropy, Galilean invariance, and stability. *Physical Review E*, 61(6):6546–6562, 1999.
- [19] P. Lallemand and L.-S. Luo. Theory of the lattice Boltzmann method: Acoustic and thermal properties in two and three dimensions. *Physical Review E*, 68(036706), 2003.
- [20] B.E. Launder and D.B. Spalding. The numerical computation of turbulent flows. *Computer Methods in Applied Mechanics and Engineering*, 3:269–289, 1974.
- [21] A. Malkawi and Augenbroe G. (eds.). *Advanced Building Simulation*. Spon Press, New York, 2004.
- [22] P.V. Nielsen, F. Allard, H.B. Awbi, L. Davidson, and A. Schälin. *Computational fluid dynamics in ventilation design*. REHVA Guidebook No. 10. rehva – Federation of European Heating and Air-conditioning Associations, 2007.

- [23] C. Nytsch-Geusen. *Berechnung und Verbesserung der Energieeffizienz von Gebäuden und ihren energietechnischen Anlagen in einer objektorientierten Simulationsumgebung*. PhD thesis, Technische Universität Berlin, VDI-Verlag, 2001.
- [24] H. Oertel and E. Laurien. *Numerische Strömungsmechanik*. Vieweg & Sohn, 2nd edition, 2003.
- [25] Y.H. Qian, D. d'Humières, and P. Lallemand. Lattice BGK models for Navier-Stokes equations. *Europhys. Lett.*, 17(6):479–484, 1992.
- [26] P. Sagaut. *Large Eddy simulation for incompressible flows*. Springer Verlag, 2nd edition, 2001.
- [27] A. Schälin, A. Moser, J. van der Maas, and D. Aiulfi. Application of air flow models as design tools for atria. In *Roomvent*, Yokohama, Japan, 1996.
- [28] H. Schlichting and K. Gersten. *Boundary layer theory*. Springer, 9th edition, 1996.
- [29] C. van Treeck. *Gebäudemodell-basierte Simulation von Raumluftströmungen*. PhD thesis, Technische Universität München, 2004.
- [30] C. van Treeck, E. Rank, M. Krafczyk, J. Tölke, and B. Nachtwey. Extension of a hybrid thermal lbe scheme for Large-Eddy simulations of turbulent convective flows. *Computers and Fluids*, 35:863–871, 2006.
- [31] G.N. Walton. A computer program for building air flow network modeling. 89-4072, National Institute of Standards and Technology (NIST), 1988.
- [32] T.R. Weber. Checking of simulation models in a ventilation test room. In *18th annual AIVC conference*, Athens, 1997.
- [33] X. Yuan, A. Moser, and P. Suter. Wall functions for numerical simulation of turbulent natural convection along vertical planes. *Int. J. Heat Mass Transfer*, 36(18):4477–4485, 1993.

# Chapter 12

## Validation and benchmarking

Chapter 6 already introduced the terms convergence, consistency and stability in the scope of numerical discretization. In Chapter 7, a numerical solution was verified against an analytical solution. However, analytical solutions exist for special cases only, and next to the mentioned round-off and discretization errors, a simulation model must be tested against other data in order to detect modeling errors and to assess the uncertainties of the model. Suitable candidates for validation are thus data of analytical and empirical models, or data which are obtained by an inter-model comparison.

### 12.1 Benchmark tests in the literature

A number of benchmark tests have been proposed in the literature in order to validate building performance simulation tools with special focus on thermal multizone models. Most of these tests isolate typical effects of the multi-physics approach such as considering a building of light or heavy weight type, or by solely investigating the effects of solar radiation, for example. In the literature also comparisons with measurements are available. A good source of information are the projects conducted under guidance of the *International Energy Agency (IEA)*, for example regarding the ventilation of large (glazed) spaces [3, 6, 11].

Examples for benchmark tests addressing thermal multizone models are

- the BESTEST energy simulation test by the International Energy Agency (IEA) [7, 8],
- the ASHRAE Standard 140 [1] which is based on the above BESTEST,
- the German VDI Standard 6020 addressing the building model (part 1) and the HVAC system (part 2) [12, 13],
- the EN Standard 15255 [4] regarding general criteria and validation procedures with respect to the sensible room cooling load calculation, and
- the EN Standard 15265 [5] concerning the calculation of energy demands for space heating and cooling using dynamic methods.

In the main part of this chapter, the VDI Standard 6020 [12] will be applied in order to investigate the dynamic behavior of the type of model discussed in this book.

## 12.2 The BESTEST energy simulation test and diagnostic method

The BESTEST has been developed by the International Energy Agency (IEA) and reported by JUDKOFF & NEYMARK [7] as energy simulation test and diagnostic method for the building system. Later this was expanded with a benchmark for heating, ventilating, and air-conditioning equipment models (HVAC BESTEST) [8]. BESTEST was developed for use with envelope models in the IEA Task 12 [7] and was extended to the HVAC BESTEST which emerged from the activities in the IEA Task 22 on "Building Energy Analysis Tools". The projects investigated the accuracy of building energy analysis tools and the respective engineering models in terms of an analytical verification and comparative diagnostic procedure for evaluating the energy performance of buildings. The HVAC test focusses on the performance of unitary space cooling equipment.

In BESTEST [7], a number of simulation programs were tested (BLAST, CLIM2000, DEROB, DOE2, ESP, SERIES, S3PAS, TAS and TRNSYS) against a series of benchmarks. The documentation contains tables and graphs for comparing the programs with respect to annual loads, annual maximum and minimum temperatures, peak loads, and some hourly data. For a simple geometric model, the dynamic effects regarding thermal mass, solar gains, shading devices, infiltration, sunspaces and others are compared.

ASHRAE Standard 140 is based on BESTEST related work and "specifies test procedures for evaluating the technical capabilities and ranges of applicability of computer programs that calculate the thermal performance of buildings and their HVAC systems" [1].

## 12.3 VDI Standard 6020 benchmark application

In this section, the numerical zone model *iZone* developed in Chapter 10 of this book is compared with some of the benchmark solutions of the VDI Standard 6020-1 [12] considering the individual heat transfer domains, i.e. heat conduction (Chapter 6), long wave radiative heat transfer (Chapter 7), and solar radiation using the detailed window model (Chapters 8 and 9).

The geometry, structure and material constants of the sample model were already introduced in Section 3.6. The construction of the room is again of heavy weight type (the standard includes a light weight type as well) and the single zone model is adiabatically connected to the rest of the building. Deviations from the definitions of the Tables 3.2 to 3.5 are indicated in the text.

The results presented in the VDI standard [12] which are used in this context were computed with the five simulation tools DOE-2 (release 2.1E), DS-THERM (release 3.26), GEBSIMU (release 4.32), TAS (release 8.0) and TRNSYS (version 14.2). It should be noted that the sequence used in the figures below does not correspond to the alphabetic order of the mentioned tools (see also [10]). The VDI 6020 provides test examples capturing dynamic room effects

with respect to internal loads, set point changes and solar radiation, and integral performance results of a whole year simulation.

### 12.3.1 Transient responses during 60 day period

It is assumed that after a 60 day period reasonable solutions are obtained, i.e. that the continuous oscillations are independent of the choice of the initial conditions. *Example 1* of the VDI Standard 6020 [12] addresses this type of transient response in terms of simulating free floating temperatures.

In the set-up, the window is modeled as opaque component without thermal mass (no solar heat gains). The internal heat gains are set to 1000W which is supplied via convection. The infiltration rate is set to zero. Temperatures are initialized at 22°C.

The iZone results are shown in Figures 12.1 and 12.2. The comparison with the *Beuken model* [9, 10] as published in the standard [12] indicates the same dynamic behavior. However, the converged air temperature (right hand side of Figure 12.2) is clearly underestimated by the model. This effect is due to the fact that iZone uses the empirical formulation of ALAMDARI & HAMMOND [2] for computing the convective heat transfer functions and not the fixed value

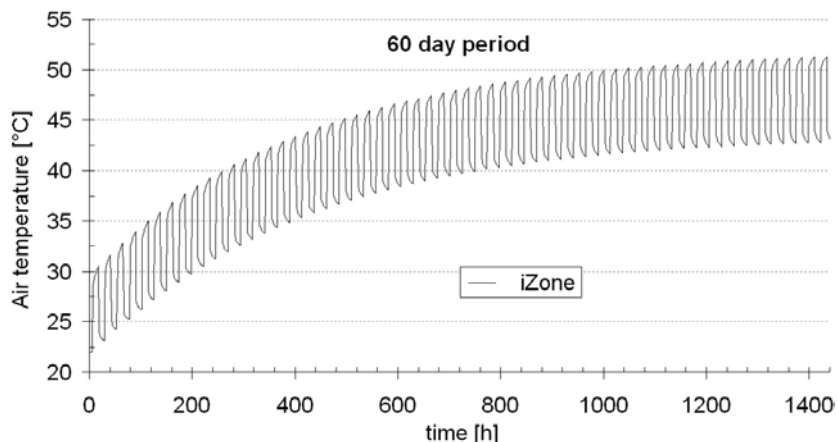


Figure 12.1: Transient response of the air temperature captured by the dynamic model during a 60 day period.

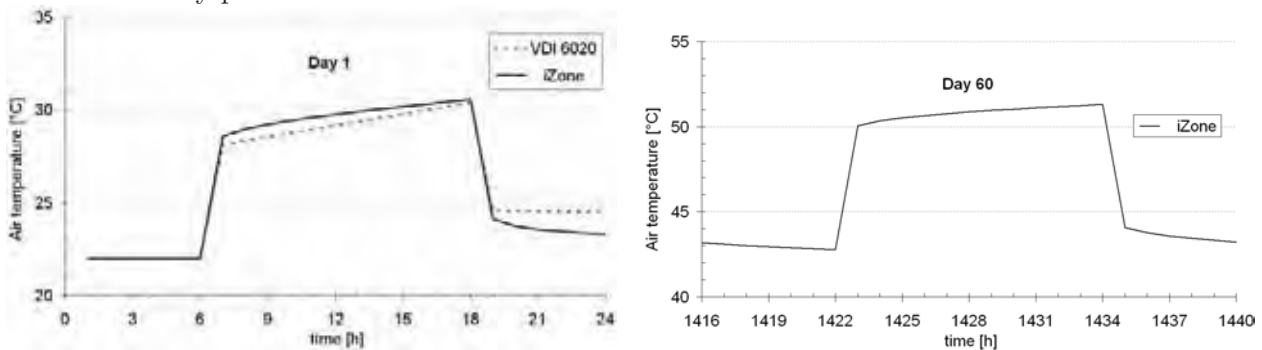


Figure 12.2: Details of the air temperature profile of the days 1 and 60 of Figure 12.1.

as requested by the standard. As the internal loads are the only heat source and as the latter are provided solely by convection, the effect is clearly significant.

### 12.3.2 Plant performance for solar radiation and zero capacity

*Example 8* of the VDI Standard 6020 [12] addresses the transformation of the irradiation data and the angular dependency of the transmission of short wave radiation through a multi-layered window system.

In order to maximize the solar effects, the thermal capacitance of the massive components is minimized by choosing the overall thickness to  $0.001\text{ m}$ , the capacity to  $0.1\text{ kJ/(kg}\cdot\text{K)}$ , and the density to  $1\text{ kg/m}^3$ . At the same time, the heat conductivity is increased to  $9.999\text{ W/(m}^2\text{K)}$  and the absorption coefficient is set to 100%. The sun shading device is switched off, the internal heat loads are zero. The cooling system supplies energy by convection only, the cooling performance is not limited. The test reference year TRY5 supplies the outside weather conditions. Again, the empirical formulae [2] are used for computing the convective heat transfer

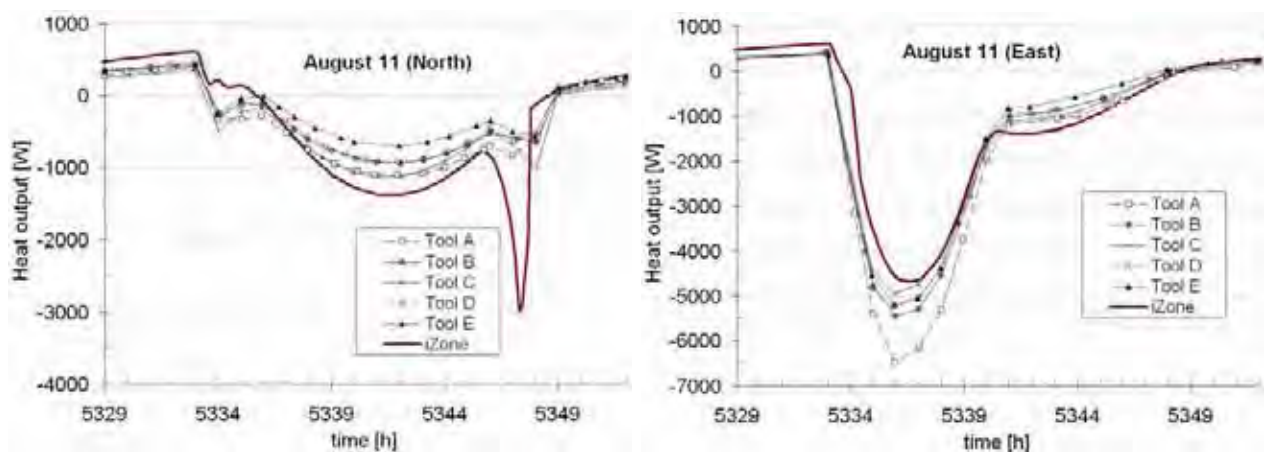


Figure 12.3: Simulation of plant output for August 11 (sunny day), window due north and east.

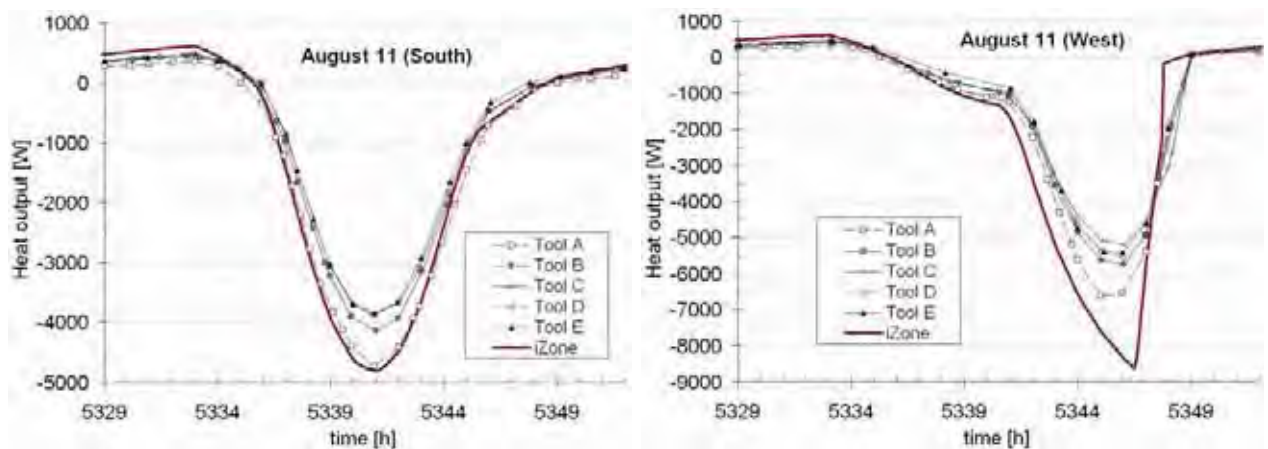


Figure 12.4: Simulation of plant output for August 11 (sunny day), window due south and west.

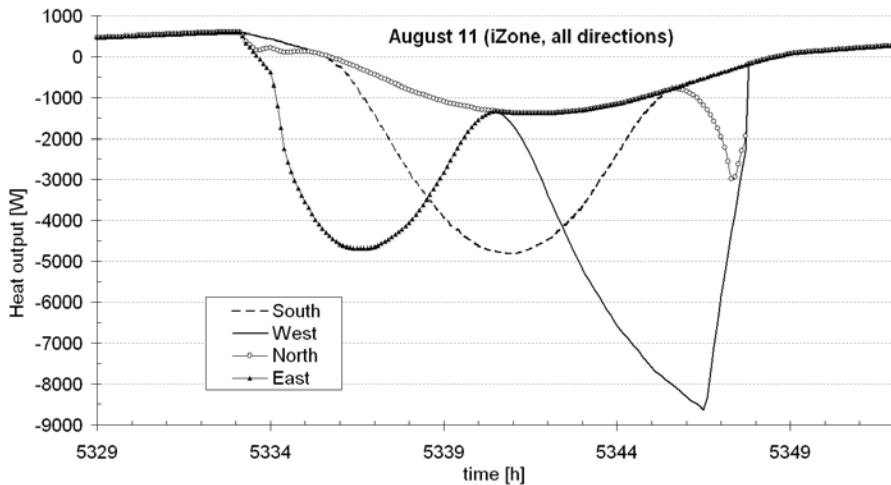


Figure 12.5: Zonal heating/cooling load obtained by iZone for August 11 (sunny day).

functions, which differs from the benchmark settings.

In the following, four cases are considered for the two days August 11 and August 21 of the test reference year. The window surface ( $10.5\text{ m}^2$ ) is thereby oriented towards the four directions north, east, south and west by rotating the zone (i.e. changing the azimuth angle). August 11 is a sunny day, while August 21 is characterized by no direct radiation, i.e. a completely cloudy day.

As the thermal capacity is effectively zero, very small timesteps of  $3.6\text{ s}$  had to be used in the simulation in order to obtain a well-converged solution (cf. Section 10.5).

The results shown in Figures 12.3 and 12.4 are in good agreement with the benchmark solutions, except for two occasions. Due to the detailed geometric treatment of solar radiation in iZone and the fairly small timesteps, a peak response of the plant output is obtained for the north orientation if the sun passes the building. For the west side, the incident radiation is

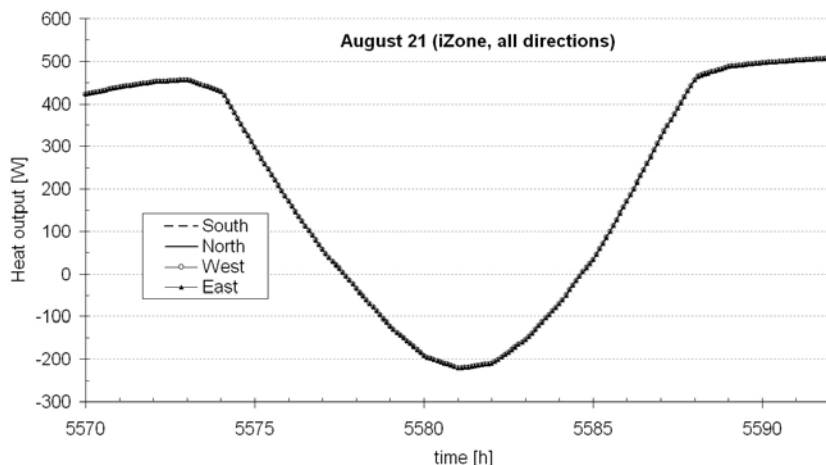


Figure 12.6: Zonal heating/cooling load obtained by iZone for August 21 (cloudy day).

overestimated during three hours of the respective day.

Figure 12.5 combines the graphs of the iZone model of the Figures 12.3 and 12.4 into a single diagram (still for the sunny day). It is interesting to note that all curves are bounded with respect to the amount of the diffuse radiation entering the zone. The effect becomes visible from Figure 12.6 for the case of August 21, which is a cloudy day *without* direct radiation. All curves are equal in this case indicating the isotropic distribution of the diffuse radiation.

### 12.3.3 Annual heating and cooling performance

In the next example, in the VDI Standard 6020 [12] referred to as *Example 13*, the scope is extended to a whole year. Material properties, components and plant operation schedule are

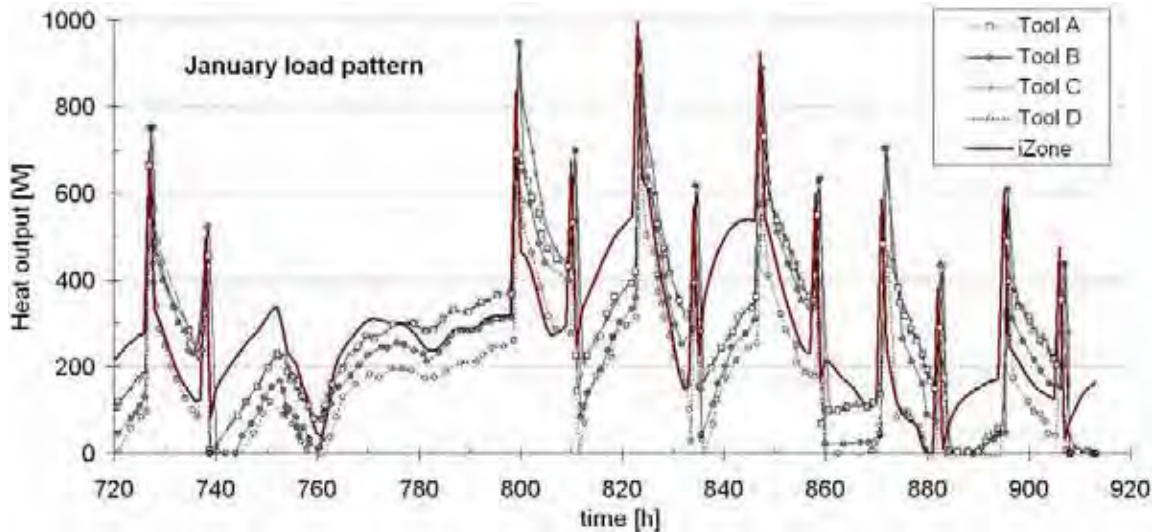


Figure 12.7: January load pattern obtained with iZone compared with the other codes.

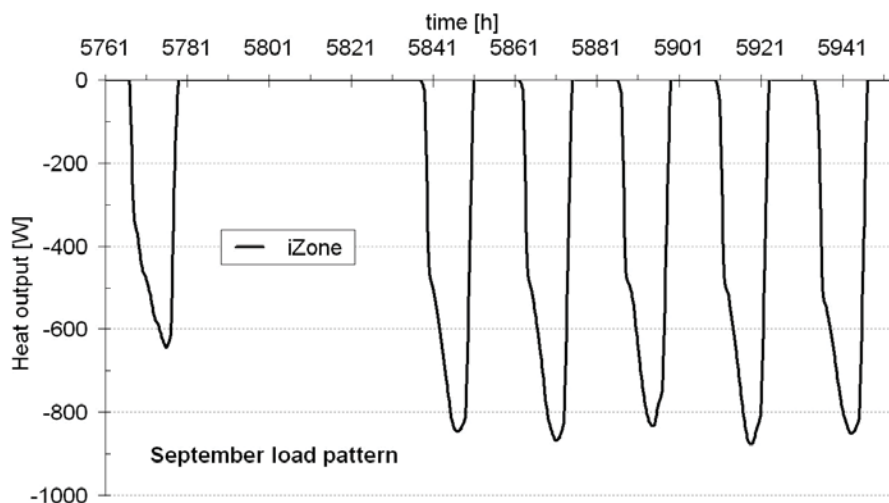


Figure 12.8: Load pattern from Aug 29 to Sept 5 computed with iZone.

	Max. heating performance [W]	Total heating energy [kWh]
Tool A	692	49.5
Tool B	944	45.0
Tool C	920	36.0
Tool D	676	45.4
Tool E	812	41.2
<b>iZone</b>	<b>994</b>	<b>54.6</b>

Table 12.1: Results for Jan 31 to Feb 7.

	Max. cooling performance [W]	Total cooling energy [kWh]
Tool A	716	37.4
Tool B	743	37.5
Tool C	638	35.1
Tool D	693	36.5
Tool E	630	31.3
<b>iZone</b>	<b>875</b>	<b>42.9</b>

Table 12.2: Results for Aug 29 to Sept 5.

defined according to Section 3.6. The outside weather conditions are specified by the test reference year TRY5. The artificial illumination is switched off.

The window is south-facing and the shading is activated if the global irradiation on the transparent surface exceeds  $150 \text{ W/m}^2$ . In this case, only 15% of the beam radiation and 30% of the diffuse radiation pass the external shading device towards the window.

In the test case, two periods of 8 days are considered, period one (winter case) from Friday, January 31 to Friday, February 7 and period two (summer case) from Friday, August 29 to Friday, September 5.

Figure 12.7 shows the load patterns obtained for January in comparison with the other tools. The results agree with the benchmark solution, especially the dynamics and peak loads are well captured. In Figure 12.8, the September load pattern is displayed. In this case, the cooling performance is predicted several watts above the reference values. Tables 12.1 and 12.2 further summarize the results for both periods in terms of the maximum heating and cooling performances and the total heating and cooling energy.

The corresponding air temperature distribution of both periods is given in the left and right

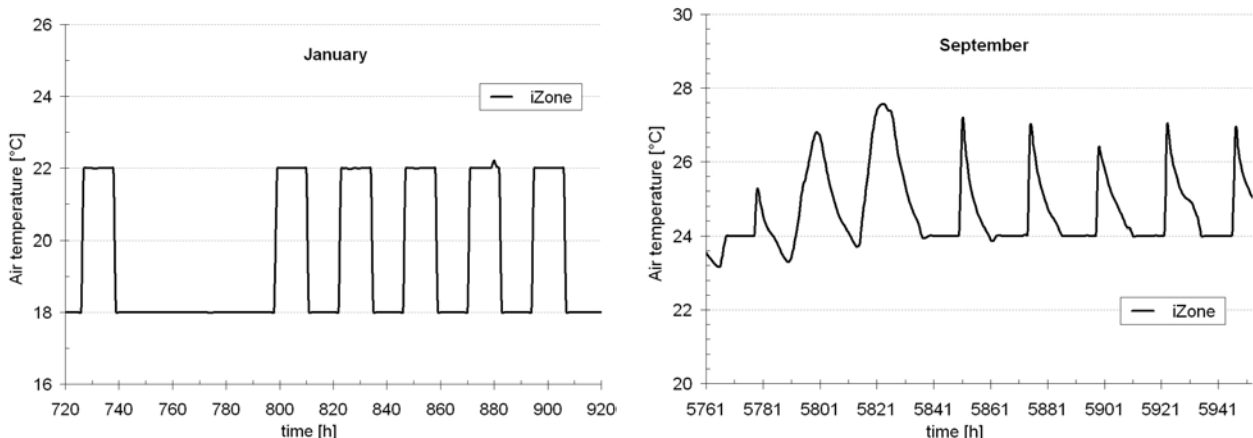


Figure 12.9: Air temperature for the simulation sequences shown in Figures 12.7 and 12.8.

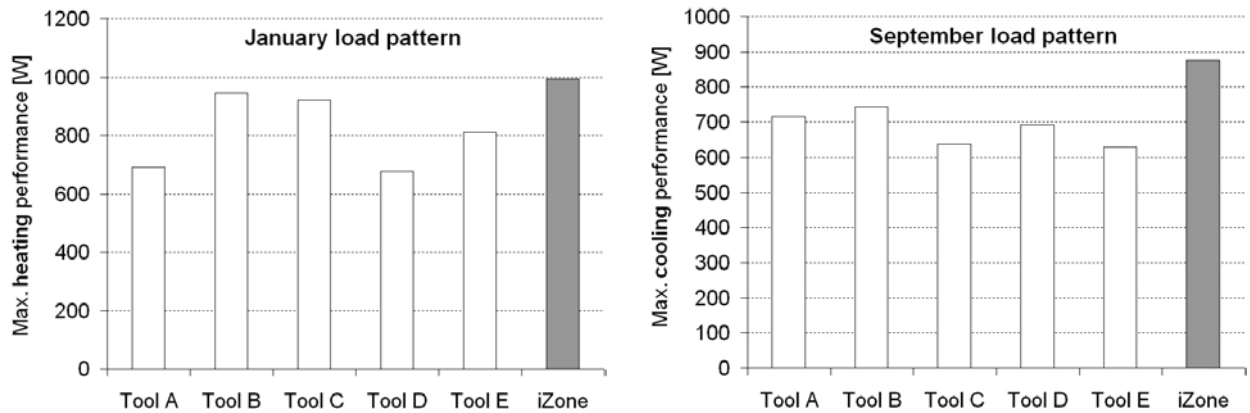


Figure 12.10: Comparison between the maximum heating and cooling performances and the total heating and cooling energy according to Tables 12.1 and 12.2.

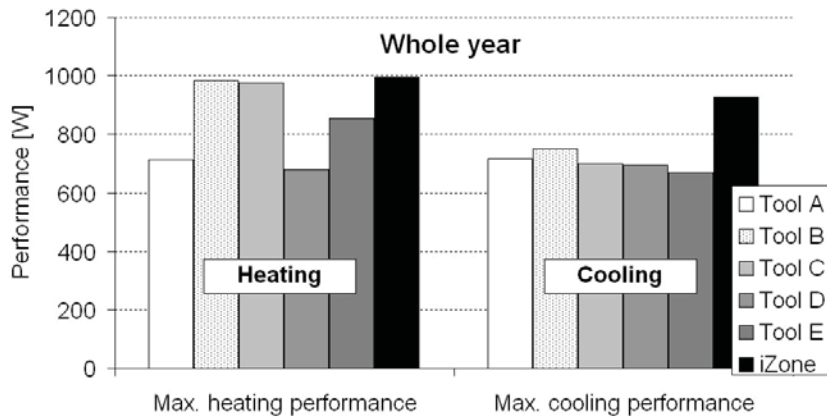


Figure 12.11: Comparison of the different tools regarding the heating (left) and cooling (right) performances for the whole year simulation.

hand picture of Figure 12.9. The spikes at the beginning and the end of the plant operation time, which can be seen in the left hand Figure 12.9, result from the necessity of heating the room for a single hour without internal heat sources from the occupants or the equipment. This effect is due to differences in the working and plant operating schedule (defined by the standard). Otherwise the graph follows the schedule in terms of the set point and set back temperature.

The maximum heating and cooling performances given in Tables 12.1 and 12.2 are visualized in Figure 12.10 for January and September, respectively.

Figure 12.11 finally summarizes the heating (left) and cooling (right) performances with respect to the different tools. For the heating performance, the iZone results are within the range of the other data, whereas the cooling performance exceeds the other values by 20 per cent. Table 12.3 further details the latter performances and the energy demands for the whole year simulation of the TRY5.

	Max. heating performance [W]	Max. cooling performance [W]	Total heating energy [kWh]	Total cooling energy [kWh]
<i>Tool A</i>	713	716	604.4	469.3
<i>Tool B</i>	983	749	504.4	498.4
<i>Tool C</i>	975	699	381.6	554.0
<i>Tool D</i>	681	693	505.1	482.4
<i>Tool E</i>	855	668	477.0	470.0
<i>Mean value</i>	841	705	494.5	494.8
<b>iZone</b>	<b>994</b>	<b>928</b>	<b>618.7</b>	<b>701.8</b>

Table 12.3: Comparison of the results for the whole year simulation.

## 12.4 References

- [1] ASHRAE Standard 140. *Standard Method of Test for the Evaluation of Building Energy Analysis Computer Programs (ANSI Approved)*. American Society of Heating, Refrigerating and Air-Conditioning Engineers, 2007.
- [2] F. Alamdari and G.P. Hammond. Improved data correlation for buoyancy-driven convection in rooms. SME/J/83/01, Applied Energy Group, Cranfield Institute of Technology, 1983.
- [3] I. Bryn and P.A. Schiefloe (editors). Atrium models for the analysis of thermal comfort and energy use. Report of Task 12, Project A.3, Atrium Model Development, International Energy Agency (IEA), 1996.
- [4] EN 15255. *Energy performance of buildings – Calculation of energy needs for space heating and cooling using dynamic methods – General criteria and validation procedures*. 2007.
- [5] EN 15265. *Energy performance of buildings – Sensible room cooling load calculation – General criteria and validation procedures*. 2007.
- [6] P. Heiselberg, S. Murakami, and C.-A. (editors) Roulet. Ventilation of large spaces in buildings. Report of Annex 26, Energy Efficient Ventilation of Large Enclosures, International Energy Agency (IEA), 1998.
- [7] R. Judkoff and J. Neymark. *International Energy Agency building energy simulation test (BESTEST) and diagnostic method*. National Renewable Energy Laboratory, U.S. Department of Energy, 1995.
- [8] J. Neymark and R. Judkoff. *International Energy Agency building energy simulation test and diagnostic method for heating, ventilation and air-conditioning equipment models (HVAC BESTEST)*. National Renewable Energy Laboratory, U.S. Department of Energy, 2002.
- [9] L. Rouvel and F. Zimmermann. Ein regelungstechnisches Modell zur Beschreibung des thermisch dynamischen Raumverhaltens, Teil 1. *Heizung Lüftung/Klima Haustechnik*, 48(10), 1997.

- [10] L. Rouvel and F. Zimmermann. Ein regelungstechnisches Modell zur Beschreibung des thermisch dynamischen Raumverhaltens, Teil 2. *Heizung Lüftung/Klima Haustechnik*, 48(12), 1997.
- [11] A. Schälin, A. Moser, J. van der Maas, and D. Aiulfi. Application of air flow models as design tools for atria. In *Roomvent*, Yokohama, Japan, 1996.
- [12] VDI 6020 Part 1. *Requirements for methods of building performance simulation, part 1: buildings*. VDI Verein Deutscher Ingenieure, Beuth Verlag, 2001.
- [13] VDI 6020 Part 2. *Requirements for methods of building performance simulation, part 2: HVAC system*. VDI Verein Deutscher Ingenieure, Beuth Verlag, 2001.

# Chapter 13

## Thermal quality performance assessment in buildings

### 13.1 Indoor thermal quality performance prediction

The indoor thermal quality and the air quality influence health, productivity and thermal comfort as well as the energy consumption of a building with respect to the cooling and heating demands. Concerning the indoor air quality, engineers are confronted with complex thermal, physical, chemical and microbiological phenomena with mutual influences potentially resulting in sick building syndrome [15, 65, 92]. This chapter will focus on the issue of the indoor thermal quality performance.

Standards give recommendations for reasonable ranges of parameters affecting the thermal environment in buildings in terms of both comfort and system layout. Among the most significant changes in standards over the last decade is the consideration of people's adaptations in naturally ventilated spaces due to conscious actions in order to improve the thermal situation by themselves.

Temperature sensation and perception of thermal comfort are related to the thermal state of the human body, to the efforts for regulating body temperature [8] and to the moisture sensation at the skin [38, 40]. Core and skin temperatures, as well as their variation over time, influence several thermophysical and thermoregulatory processes of the body, which aim to keep a thermal neutral state or to acclimatize due to physiological adaptations [28, 39, 38, 93].

In building simulation, thermal sensation and comfort are expressed by voting scales and are usually considered in terms of steady state, uniform conditions for the body as a whole. The approach is based on the pioneering empirical work of FANGER [28] which considers the heat balance of the human body as a whole and statistically relates the predicted mean vote of peoples' satisfaction with the thermal environment to the ambient conditions. The method is implemented in several international as well as country specific standards. Comfort zones define the acceptable ranges of temperatures in buildings with respect to the operative temperatures such as the ISO Standard 7730 [23] or the ASHRAE Standard 55 [1]. The standards further take into account the air humidity for a selected clothing insulation and level of activ-

ity. The comfort zone can be drawn on a psychrometric chart, as shown in ASHRAE 55 and as introduced in Section 3.3. The standards also recommend tolerance limits for local effects such as draught risk, temperature stratification and asymmetric radiation. In transient conditions, cyclical temperature changes and drifts or ramps should be restricted to small fluctuations. Adaptive models further take into account the behavioral adaptation of people in naturally ventilated buildings and relate the acceptability of thermal conditions to the current outside weather conditions [16, 21].

The mentioned methods are well suited for predicting the indoor thermal quality performance of buildings. However, the models are focussing on the body as a whole when close to thermal neutrality and are limited usable for inhomogeneous environments and are not applicable to transient thermal conditions. The ergonomic requirements of the local thermal environment can be obtained by measurements and experiments with subjects which are exposed to locally specific conditions. Non-uniform scenarios can be correlated to a uniform environment using the concept of equivalent temperatures. Figure 13.1 shows a typical setup of such an experimental analysis. With a thermal manikin equipped with heated sensors, surface temperatures are measured which are correlated to the individual votes of the subjects [67].



Figure 13.1: Thermal manikin DRESSMAN measuring resultant surface temperature values (courtesy of Fraunhofer Institute for Building Physics, Germany) [67, 105].

It is difficult to predict human responses for non-uniform conditions with high resolution by experiments [76, 114, 117], i.e. to resolve for individual local effects and their relevance with respect to an overall thermal vote. Non-uniform conditions may affect both convective and radiative heat transfer in practice. Personalized ventilation [111] or radiant cooling or heating systems are examples where local effects may dominate the overall thermal vote.

Besides activities in measuring and modeling local human responses under various conditions, e.g. [95], current research also focuses on the numerical simulation, in detail on the integration



*Figure 13.2:* Large-eddy lattice Boltzmann simulation of turbulent convective air flow in separator room. The model contains 295,899 facettes and  $24 \cdot 10^6$  degrees of freedom [107]. In cooperation with the Flensburger Schiffbaugesellschaft (FSG), Germany.

of thermal manikin models [34, 35, 57, 93, 96] into numerical simulation tools.

It should be reiterated at this point, that simulation approaches in building performance simulation range from steady-state monthly and annual balances (coarse level) over dynamic multizone models up to computational methods modeling fluid flow and radiative heat transfer in detail (fine level). For assessing the indoor thermal quality of a building in terms of comfort, descriptive integral quantities are required such as the frequency of temperatures exceeding a certain limit during an annual period. For this, the zonal methods discussed in this book are suitable. For a detailed analysis with the above mentioned thermal manikin models, however, a high resolution is required. This may include the use of a flow and a thermal radiation solver, a thermal manikin modeling the heat exchange between body and environment and the human thermoregulation, as well as a model relating the local thermal sensation votes. Chapter 14 will give some typical application examples.

In other industrial areas, the analysis can become fairly complex. For example, Figure 13.2 shows the CFD analysis within a part of a machinery room of a ferry boat which contains four hot separator devices (surface temperature up to  $60^\circ\text{C}$ ). In terms of the occupational safety assessment, appropriate working conditions must be maintained in the room if the devices are cooled by fresh air (and not by water cooling in this case to reduce costs). The figure shows streamlines of the averages velocity field for the case of turbulent natural convection ( $\text{Ra} \approx 10^{10}$ ).

## 13.2 The energy balance equation

According to FANGER [31, 28] the thermal exchange between the human body and the environment can be described with the energy balance equation (13.1). In the equation, the net heat production equals the total metabolic rate  $M$  minus the produced heat which is converted to external mechanical power  $W$ . The metabolic activity is expressed in terms of the heat production per unit skin area, unit [met], where  $1\text{met} = 58\text{W/m}^2$  for a resting adult. Typical values for the metabolic heat generation for different levels of activity can be found in the EN ISO Standard 8996 [25], ISO 7730 [23] or ASHRAE Standard 55 [1].

$$\underbrace{M - W}_{\text{net heat production}} = \underbrace{(Q_{conv} + Q_{cond} + Q_{rad} + E_{skin})}_{\text{skin heat losses}} + \underbrace{(C_{resp} + E_{resp})}_{\text{respirative heat losses}} + \underbrace{S}_{\text{heat storage}} \quad (13.1)$$

The terms involving heat loss and storage are on the right hand side of Equation (13.1). The sensible heat losses from the skin are due to convection and radiation,  $Q_{conv}$  and  $Q_{rad}$ , heat conduction by contact  $Q_{cond}$ , and latent heat losses by evaporation of sweat and moisture diffusion  $E_{skin}$ .  $C_{resp}$  and  $E_{resp}$  are the sensible and latent heat losses of the respiratory system.  $S$  denotes the change in internal energy due to the thermal capacity and the rate of change in transient conditions.

Instead of considering the body as a whole, the model can be further refined by decomposing the body into two thermal compartments, skin and core, using the two-node model of GAGGE [38] or in a more detailed way by a multi-segment model as proposed by STOLWIJK [93]. The latter includes models for blood circulation and physiological responses of the body.

In order to describe the heat transfer between the body and the environment, linearized heat transfer coefficients or detailed numerical methods can be applied. Basic methods addressing convective and radiative heat transfer are summarized in text books such as BEJAN [6] and MODEST [72], respectively. DE DEAR ET AL. [13], for example, summarize heat transfer coefficients for individual human body segments. The heat balance is usually established at the surface which is exposed to the environment, i.e. the outer clothing or the skin surface, where the sensible and latent heat losses can be expressed relative to the parameters skin temperature (with respect to clothing insulation, if relevant) and skin wettedness with respect to the independent environmental variables air temperature, air velocity, mean radiant temperature and ambient water pressure. For a detailed description of the terms in the heat balance equation it is referred to [2, 28, 33].

## 13.3 Human thermoregulation in detail

### 13.3.1 Regulation mechanisms and thermal stimuli

The thermal state of the body is a composite result of several thermophysical and thermoregulatory processes. The heat gains and losses from/to the environment due to convection and radiative heat transfer, heat conduction, evaporation and respiration must be compensated by

the metabolism, in order to maintain a constant body core temperature over a wide range of ambient conditions. The total metabolic rate thereby consists of the internal heat production due to conscious and unconscious muscle activity and by a basal metabolic rate.

The thermoregulatory reactions of the central nervous system (CNS) are based on multiple signals from core and peripheral sensors. Furthermore, local changes of the skin temperature may cause local autonomic reactions such as modifying the sweating rate or the local vasodilatation [34, 35]. For example, the cold perception when the skin temperature is actively falling is different from observations when the temperature remains at a constant cold level [2]. Significant indicators are

- the mean skin temperature  $T_{sk,m}$  and
- its variation over time  $\partial T_{sk,m}/\partial t$ , and
- the hypothalamus (core) temperature  $T_{hy}$ .

Calorimetric phenomena such as heat fluxes are not well suited for describing these effects [33].

Cutaneous (skin) thermoreceptors are inhomogeneously distributed over the body and show local different sensitivities which requires weighting if integral values are requested [33]. Warmth and cold receptors operate in different but overlapping ranges and cold receptors are more densely distributed than warm receptors; it is distinguished between receptors sensing warmth, cold and pain. As suggested by STOLWIJK, the mode of operation of the warmth and cold receptors allows to formulate thermoregulation models in terms of set-point deviations from the state of thermal neutrality [93]. Both types of receptors show a dynamic overshoot in their response frequency if skin temperatures change over time [52]. Thermosensitive neurons in the body core are mainly concentrated in the hypothalamus region. The hypothalamus plays a central role in the information processing. It can also be stimulated by local warming or cooling which causes dilatation and sweating or constriction and shivering, respectively.

The mentioned stimuli can be correlated with the responses of the CNS in order to form a detailed thermoregulation model in terms of  $f(T_{sk,m}, \partial T_{sk,m}/\partial t, T_{hy})$ . In essence, human thermoregulation involves four essential autonomic regulation mechanisms which control the heat exchange with the environment (physiological adaptations):

- The skin blood flow can be changed by *vasoconstriction* and *vasodilatation*;
- evaporative heat loss is achieved by *sweating*, while
- *shivering* produces heat by increased metabolism in the muscles.

Also *behavioral adaptations* are important to mention. These are conscious reactions such as (locally) changing clothing, performing exercises, changing the current ambient conditions by opening a window or having a cold drink, for example.

### 13.3.2 Human thermoregulation models

In the past, several human thermoregulation models have been proposed in the literature. These models usually consider the heat exchange between body and environment with a *passive system* where the body is decomposed into segments, each segment consisting of layers with well defined physical and physiological properties which are in thermodynamic contact with each other and with the ambient microclimate. The models include sub-models for clothing and models for blood circulation. The task of an *active thermoregulation system* is the integration of the thermal stimuli from the various receptors and the formulation of proper reactions to the simultaneous and partially contradicting signals from core and skin with respect to the above mentioned regulation mechanisms concerning the peripheral vasomotion, sweating and shivering [93].

The model of GAGGE, for example, consists of the two compartments: skin and core [38]. Most work related to multi-segment models is based on the early work of STOLWIJK [93]. The segment model of Stolwijk has been enhanced by several authors, for example, by GORDON [46], HUIZENGA [57], WERNER [108], WISSLER [109], FIALA [33, 34, 35] and TANABE with a 65-node model [96]. The history of these developments is summarized by HOLMÉR in [56].

With these models, the dynamic responses of the human metabolism can be simulated for transient and uniform conditions over a wide range of thermal boundary conditions. Applications of this approach in practice and ongoing developments are reported in [37, 63, 64, 77, 78, 79, 83, 91, 94, 106, 115, 116, 117], for example. In the following subsection, the model of FIALA [35] will be further detailed which has been developed at the De Montfort University (UK).

### 13.3.3 The model of Fiala

Based on the STOLWIJK model [93], FIALA divides the body into fifteen cylindrical and spherical elements [33, 34, 35] to form the passive system. Some of these segments are further subdivided into *anterior*, *posterior* and *inferior* sectors as schematically shown in Figure 13.3 for the implementation of the FIALA-FE model [36] by PAULKE [83] using the finite element-based tool THESEUS-FE [97]. The concentric layer model decomposes elements and sectors into layers of different thickness, representing bone, muscle, fat and skin layers. In the special case of the FIALA-FE model, clothing is treated as additional layer which differs from the original model. Figure 13.4 details the structure. The subdivision of the elements is important in many cases of asymmetric and non-uniform environments as occurring in vehicles and buildings as for example shown by MELIKOV ET AL. [71].

As depicted in Figure 13.4, metabolic heat is transported via blood circulation and by radial conduction to the body surface where it is transferred to the environment by convection, radiation, evaporation and, if applicable, respiration and conduction. The heat transfer within the tissue can be described by the *bioheat equation* (13.2) proposed by PENNES [84]:

$$k \left( \frac{\partial^2 T}{\partial r^2} + \frac{\omega}{r} \frac{\partial T}{\partial r} \right) + q_m + \rho_{bl} w_{bl} c_{bl} (T_{bl,a} - T) = \rho c \frac{\partial T}{\partial t} \quad (13.2)$$

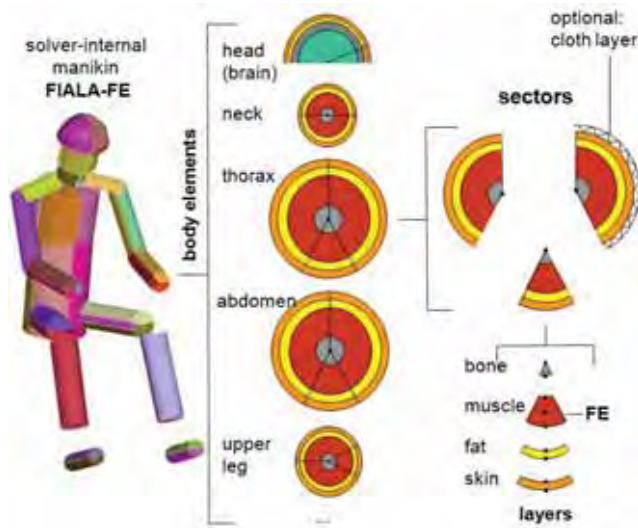
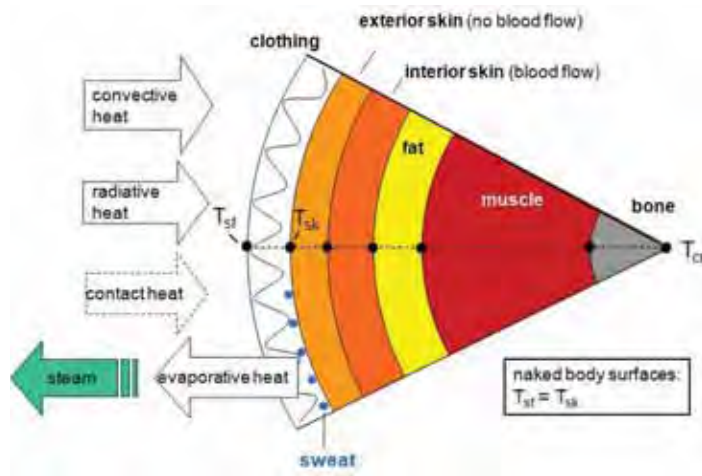


Figure 13.3: Solver internal shell model of the FIALA-FE manikin [36]. Courtesy of P+Z Engineering, Munich [83].

The differential equation models the heat transfer in human tissues with a cylindrical model where  $k$  represents the tissue conductivity ( $\text{W} \cdot \text{m}^{-1} \cdot \text{K}^{-1}$ ),  $T$  the tissue temperature ( $^{\circ}\text{C}$ ),  $r$  the radius (m) and  $\omega$  a dimensionless geometric factor ( $\omega = 1$  for cylinders,  $\omega = 2$  for spheres).  $q_m$  denotes the metabolism ( $\text{W}/\text{m}^3$ ) which consists of a basal value plus the local autonomic thermoregulation while shivering or performing external work. The last term on the left hand side of Equation (13.2) represents blood perfusion, where  $\rho_{bl}$  stands for the density ( $\text{kg}/\text{m}^3$ ),  $w_{bl}$  for the perfusion rate ( $\text{s}^{-1}$ ),  $c_{bl}$  for the heat capacity ( $\text{J} \cdot \text{kg}^{-1} \cdot \text{K}^{-1}$ ) and  $T_{bl,a}$  for the arterial blood temperature ( $^{\circ}\text{C}$ ). The right hand side of the equation denotes the heat storage within the tissue. For the blood circulation a central blood pool is assumed by modeling a countercurrent exchange within the arterial and venous vascular system and by neglecting the heat storage within the vascular system. The metabolism  $q_m$  and blood perfusion rate  $w_{bl}$  are thereby influenced by the active control system. Only radial heat conduction is considered as the surface areas of the interfaces between two sectors are insignificant compared to the surface areas of the sectors themselves and as in internal tissue layers metabolism and blood circulation dominate. With respect to the skin moisture evaporation a partial differential equation is used to describe the moisture accumulation and sweat production as predicted by the active system. For the respirative exchange, which again depends on the metabolism, it is distinguished between dry and latent heat exchange which is distributed along the pulmonary tract [33, 105].

The model is, however, calibrated for an average human adult with the physiological properties as detailed in [35]. Recently, individualized models with respect to individually tuned physiological properties are reported in literature [103].

Following the concept of Stolwijk's afferent signal analysis, responses are formulated in the active system in terms of the deviation of the hypothalamus temperature  $T_{hy}$  and the mean skin temperature  $T_{sk,m}$  with respect to their state at thermal neutrality (the setpoint) and the time derivation of the mean skin temperature  $\partial T_{sk,m} / \partial t$ . With an experimental regression analysis based on a literature survey, Fiala [35] derived source terms for the vasoconstriction



*Figure 13.4:* A single sector of the concentric FIALA-FE layer model [36] including layers for modeling bone, muscle, fat, the two skin layers and clothing. *Courtesy of P+Z Engineering, Munich [83].*

and dilatation ( $W/K$ ), the sweat production ( $g/min$ ) and the increased muscle action in terms of shivering ( $W$ ). The model is thus applicable over a wide range of ambient conditions. In Chapter 14, the application of the model will be demonstrated.

## 13.4 Conditions for thermal comfort

### 13.4.1 What is thermal comfort?

With the above introduction to human thermoregulation in mind, the definition of the term *thermal comfort* of BENZINGER [7] sounds straightforward. He defines thermal comfort as "the absence of driving impulses from cutaneous and hypothalamic receptors" which would cause the body to counteract with physiological adaptations. For a resting and unclothed individual such thermoneutral conditions occur at approximately  $30^\circ C$  ambient temperature [39] where conscious actions are not required for influencing the thermal state. The ASHRAE Standard 55 [1] defines thermal comfort as the "condition of mind that expresses satisfaction with the thermal environment".

According to the latter definition, the level of thermal comfort is a subjective measure. Several voting scales have been proposed in the literature. The differences between these scales is that some scales exclusively refer to thermal sensation (hot, warm, cool, cold, etc.), others combine thermal sensation and comfort (pleasant, unpleasant, etc.) in terms of acceptability. A significant problem in practice is that differences in language and in subjective observations may cause misinterpretations of the experimental data. Furthermore, it is not straightforward to translate one scale into another as it is difficult to include the acceptability vote at a later stage if individuals were not explicitly asked for this during the experiment.

For votes in terms of acceptability, GAGGE [39] suggested an unpleasantness scale with the levels *{pleasant, indifferent, slightly unpleasant, unpleasant}*. Another sequence for describing

the level of (dis)comfort is  $\{\text{comfortable}, \text{slightly uncomfortable}, \text{uncomfortable}, \text{very uncomfortable}\}$ .

The BEDFORD scale [5] uses a mixed formulation for combining thermal sensation and comfort perception. Bedford found that the relationship between comfort votes and equivalent temperatures can be described in a linear manner and that humidity plays a minor role for temperatures below  $24^{\circ}\text{C}$ . The 7-point scale (from 1 to 7) is defined by the sequence  $\{\text{much too warm}, \text{too warm}, \text{comfortably warm}, \text{comfortable}, \text{comfortably cool}, \text{too cool}, \text{much too cool}\}$ . The neutral element is 4 in this case, which may not advantageous for questionnaires.

The most well known scale is the 7-point ASHRAE thermal sensation scale [1] proposed by ROHLES ET AL. [89] which is shown in Figure 13.5. Rohles et al. [89] found linear correlations between comfort level, dry bulb temperature, humidity, sex and length of exposure in a large field study [2]. As shown in Figure 13.5, 0 corresponds to neutral. The scale, however, does not distinguish between comfortable and uncomfortable votes. Usually the range between  $\{-1, \dots, +1\}$  is considered as comfortable.

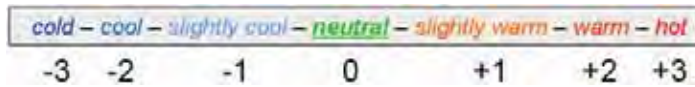


Figure 13.5: The ASHRAE 7-point thermal sensation scale [1].

Like the ASHRAE scale, the mean thermal vote (MTV) scale [77, 110] has zero as the neutral element. The scale additionally distinguishes between acceptable and not acceptable ratings which is well suited for questionnaires. The sequence is similar to the Bedford scale but counts from  $-3$  to  $+3$  for the sequence  $\{\text{much too cold}, \text{too cold}, \text{cold but comfortable}, \text{neutral}, \text{hot but comfortable}, \text{too hot}, \text{much too hot}\}$ .

### 13.4.2 Linking temperature sensation and comfort

With a thermoregulation model, the dynamic responses of the human body to ambient conditions can be predicted at a fairly high resolution. Detailed information concerning skin, surface and core temperatures is obtained. In order to assess the impact of these conditions to the individual, further models are required which relate these variables with the temperature sensation and comfort perception.

Section 13.3.1 indicated the types of cutaneous thermoreceptors and their inhomogeneous distribution over the skin surface and different sensitivities. Local thermal sensation is governed by skin temperatures [73], but if integral or mean values are questioned, the mentioned asymmetry must be reflected [33, 69]. CABANAC ET AL. [11] and ISSING & HENSEL [61] report that local (dis)comfort depends on the general comfort perception.

ZHANG ET AL. [113, 114] confirmed these observations and quantified in experimental studies how both local temperature sensation and local comfort perception depend on the overall thermal state of the body. The authors further showed the influence of the individual body parts [113]. The found relationships between the deviation of the skin temperatures from their

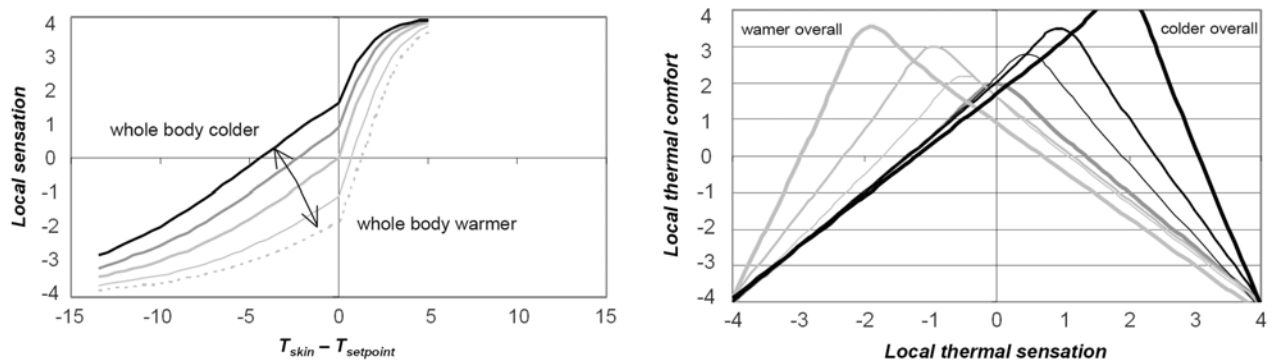


Figure 13.6: Left: Local thermal sensation votes plotted against the setpoint deviation from thermal neutrality. Right: Local thermal comfort plotted against the former local sensation. Both graphs depend on the overall thermal state of the body. Reprinted from [114] with permission from Springer.

respective set points at thermal neutrality and the local thermal sensation are shown on the left hand side of Figure 13.6. Negative values thereby correspond to cold and positive values to warm sensations. It can be seen from the figure that the responses to negative (cooler) and positive (warmer) deviations from the setpoint are non-symmetric and that these responses depend on the overall thermal state of the body [114]. In the right hand side of Figure 13.6, the obtained local thermal sensation votes are plotted against the acceptability. The sensation at which a neutral level is perceived depends on the overall thermal state and is shifted in terms of the overall feeling. If, for example, the core temperature is low, a warm stimulus may be perceived as more pleasant than a cold one [113, 114].

Local effects may dominate the overall thermal sensation in asymmetric environments. Likewise, parts of the body may feel uncomfortable, even if the whole body is. It is accordingly not possible to apply the concept of neutral thermal sensation without further modification.

The effort of the body for regulating its temperatures is as well significant [8]. Recently, a number of dynamic sensation models have been proposed in the literature. For example, with the dynamic thermal sensation (DTS) index, FIALA [33] introduces a dynamic comfort model for the whole body based on physiological effects which is applicable over a wide range of ambient conditions. In order to account for dynamic responses to transient conditions, a derivative (such as the change of skin temperature and the influence of the core temperature) needs to be included into the regression equations for modeling the experienced transient sensations as the signals contain a static and a dynamic part [52, 87].

In terms of the acceptability of the thermal conditions of the surrounding microclimate it is accordingly to be distinguished between the terms *skin temperature*, *thermal sensation*, and *thermal comfort*. However, in building performance studies it is reasonable, to correlate the thermal comfort perception directly to the ambient thermal conditions, i.e. to circumvent and omit the detailed modeling of the dynamics of the human body. FANGER showed that the level of comfort can be related to the disequilibrium in the energy balance equation (13.1) [28]. The method, which will be detailed in Section 13.5.1, refers to uniform and steady state conditions

near thermal neutrality for the body as a whole and is reasonable for typical applications of building performance simulation if dynamic effects and details of the human thermoregulation are not required.

### 13.4.3 Environmental and personal parameters affecting comfort

**Primary environmental and personal parameters.** The relevance of the environmental and personal parameters affecting thermal comfort is evident from the energy balance equation (13.1) as an imbalance in this equation can be related to the level of comfort [28]. The parameters further affect local effects such as asymmetric radiation, draught or vertical temperature gradients which are significant indicators for describing discomfort [29].

- The primary *environmental parameters* are air temperature [28, 70] and (relative) velocity [90], mean radiant temperature of the surrounding surfaces [27] and relative humidity [90].

Furthermore, the degree of turbulence is also relevant [2]. The influence of thermal radiation is perceivable, particularly if the surrounding surfaces are colder than the environment [53].

- *Personal parameters* include level of activity, clothing insulation level and clothing moisture permeability which can both be influenced by an individual.

The thermal resistance of clothing is expressed in [*clo*] where  $1\text{clo} = 0.155(m^2K)/W$ . The clothing insulation and vapor permeability of fabrics and clothing ensembles can be obtained from measurements and are given in standards such as EN ISO Standard 9920 [26] or ASHRAE Standard 55 [1]. Values for the metabolic rates at different activities are, for example, detailed in EN ISO Standard 8996 [25] and in ASHRAE 55 [1].

It is interesting to note, that researchers found in experiments that the comfort perception is statistically uniform provided the same environmental and personal parameters are applied. People do not prefer other thermal environments due to physiological adaptation [32]. This observation is independent of cultural diversities and climate region [2, 10, 16, 28]. However, there is a difference between physiological and behavioral adaptations. People tend to show different expectations and thermal preferences in buildings. With behavioral adaptations people influence the thermal microclimate, for example, by changing clothing or by exploiting natural ventilation facilities [16]. High room air temperatures can thereby be compensated by increasing the ventilation rate [23].

**Skin wettedness.** According to GAGGE, GONZALEZ and others, the moisture sensation at the skin is also an important indicator as the skin moisture correlates with warm discomfort [8, 38, 40, 42, 45]. However, for moderate climates ( $20\% < rh < 70\%$ ), and if the operative temperature is within a reasonable range, humidity fluctuations tend not to show a considerable effect [42, 44, 74].

The effect is, however, significant if sweating occurs at high room temperatures where the comfort limit is reached [86] as the ambient humidity level influences the evaporation intensity. The *skin wettedness* expresses thereby the fraction of the skin covered with water.

At low humidity ratios, respiratory diseases occur more frequent as the mucous membranes dry out and there is more dust in the indoor air since particles do not sediment [2, 86].

**Scope dependent rational and empirical indicators.** A number of environmental indices are defined in standards for particular scopes with respect to the stress a thermal environment imposes on a human. These indices are useful in an industrial context regarding occupational safety and health criteria. EN ISO Standard 11399 [19] summarizes calculation procedures for hot, moderate and cold environments and for the case of (skin) contact problems.

For estimating the thermal stress in hot (industrial) environments, ISO Standard 7933 [24] suggests an analytical method in terms of calculating the *sweat rate*. The diagnostic method of EN ISO Standard 7243 [22] in turn is based on the *wet bulb globe temperature index (WBGT)* for predicting thermal comfort. The heat stress index (HSI) expresses the ratio of the total evaporative heat loss required for thermal equilibrium to the maximum possible evaporative loss for specific ambient conditions [2].

For cold conditions, the empirical wind chill index (WCI) [2, 19] and the required clothing insulation (IREQ) according to ISO 11079 [60] can be used.

The methods applicable to moderate climates and relevant to building simulation are detailed in the Sections 13.5.1, 13.5.2 and 13.5.3 below.

**Secondary factors affecting comfort.** It was already mentioned that physiological adaptations (not to be confused with behavioral adaptations) have only minor influence, if at all [32]. Comfort perception, health and productivity are affected by mutual dependencies with other effects such as the indoor air quality (concerning the air age, chemical and microbiological issues, or contamination), acoustical effects, light, electro-magnetic fields and other effects. Secondary effects are summarized in [2, 86] such as day-to-day variations (negligible according to FANGER [28]), sex (almost same preferences between men and women; women tend to have a lower metabolism), and age (influence due to lower activity level of elderly people).

## 13.5 Prediction of thermal comfort

### 13.5.1 Uniform and steady state conditions

The *predicted mean vote (PMV)* is a statistical index for a large group of people with identical activity level and clothing insulation expressing their satisfaction with the thermal environment in terms of the 7-point ASHRAE scale. The model is based on the pioneering work of FANGER [28] who found a correlation between people's thermal sensation votes and a disequilibrium in the energy balance equation of the human body.

The model is valid for moderate climates and for uniform and steady state conditions near thermal neutrality. Close to thermal neutrality the skin temperature and sweat rate are the main parameters influencing the heat balance of the human body [2]. The state of thermal neutrality thereby corresponds to  $PMV = 0$ . A disequilibrium between left and right hand

side of Equation (13.1) (corresponding to the square bracket [...] of Equation (13.3)) accordingly expresses the case if the heat flow differs from the flow which would be required for thermal neutrality regarding a specific level of activity and clothing insulation.

Fanger reduced his empirical correlations into a single equation for  $PMV$ :

$$\begin{aligned} PMV = & (0.303 \cdot e^{-0.036 \cdot M} + 0.028) \cdot \\ & \left[ (M - W) - 3.05 \cdot 10^{-3} [5733 - 6.99(M - W) - p_a] \right. \\ & - 0.42[(M - W) - 58.15] - 1.7 \cdot 10^{-5} M (5867 - p_a) - 0.0014 M (34 - T_{air}) \quad (13.3) \\ & \left. - 3.96 \cdot 10^{-8} f_{cl} [(T_{cl} + 273)^4 - (\bar{T}_r + 273)^4] - f_{cl} h_c (T_{cl} - T_{air}) \right] \end{aligned}$$

As the model is based on the (steady state) energy balance equation, it refers to the body *as a whole* and correlates thermal comfort perception directly with the six environmental and personal parameters mentioned in Section 13.4.3: mean air temperature  $T_{air}$  [ $^{\circ}C$ ], mean radiant temperature  $\bar{T}_r$  [ $^{\circ}C$ ], mean air velocity  $u_{ar}$  [ $m/s$ ], relative humidity in terms of water vapor pressure  $p_a$  [ $Pa$ ]; level of activity in terms of metabolism  $M$  minus external mechanical work  $W$  in [ $W/m^2$ ] (the latter is due to low mechanical efficiency usually close to zero) and clothing in terms of clothing insulation  $I_{cl}$  [ $m^2K/W$ ] and a clothing factor  $f_{cl}$  [–].

The calculation sequences are defined in the EN ISO Standard 7730 [23] and the ASHRAE Standard 55 [1]. Some equations thereby need to be solved iteratively such as the equations for obtaining the clothing surface temperature  $T_{cl}$  [ $^{\circ}C$ ] and for the convective heat transfer coefficient  $h_c$  [ $Wm^2/K$ ] which depends on the air velocity  $u_{ar}$ . For valid ranges of the parameters and further details it is referred to [1, 23].

With a thermal multizone model the relevant input parameters are available for this type of analysis, assuming that reasonable assumptions are made for the air speed and that the surface temperatures of the surrounding surfaces are known. For a detailed assessment, coupling with a CFD solver becomes necessary in order to obtain field values at a high(er) resolution in terms of  $f(x, y, z, t)$  for air temperature and local flow velocity [4, 104]. Dynamic responses and details of the human thermoregulation are not represented in the  $PMV$  model.

Parameter ranges of comfortable thermal conditions, so-called *comfort zones*, can be defined in terms of deviations from  $PMV = 0$ , such as such as the range " $-0.5 < PMV < +0.5$ ". If the personal and some of the environmental parameters are fixed (choosing a typical value for the relative humidity and assuming low local air velocities, for example), a corresponding range of operative temperatures is obtained based on the  $PMV$  limits. In standards, these ranges are usually defined in tables for winter ( $1.0clo$ ) and summer ( $0.5clo$ ) clothing ensembles and for typical scenarios such as light sedentary office work corresponding to  $1.2met$ . If, for example, the range of  $PMV$  is restricted to  $-0.2 < PMV < +0.2$ , the requirements for the operative temperatures are minimum  $21^{\circ}C$  in winter and maximum  $25.5^{\circ}C$  in summer [1, 21, 23]. EN ISO 7730 [23] indicates the relationship between clothing insulation and metabolic rate by diagrams with isolines of optimum operative temperatures for  $PMV = 0$ .

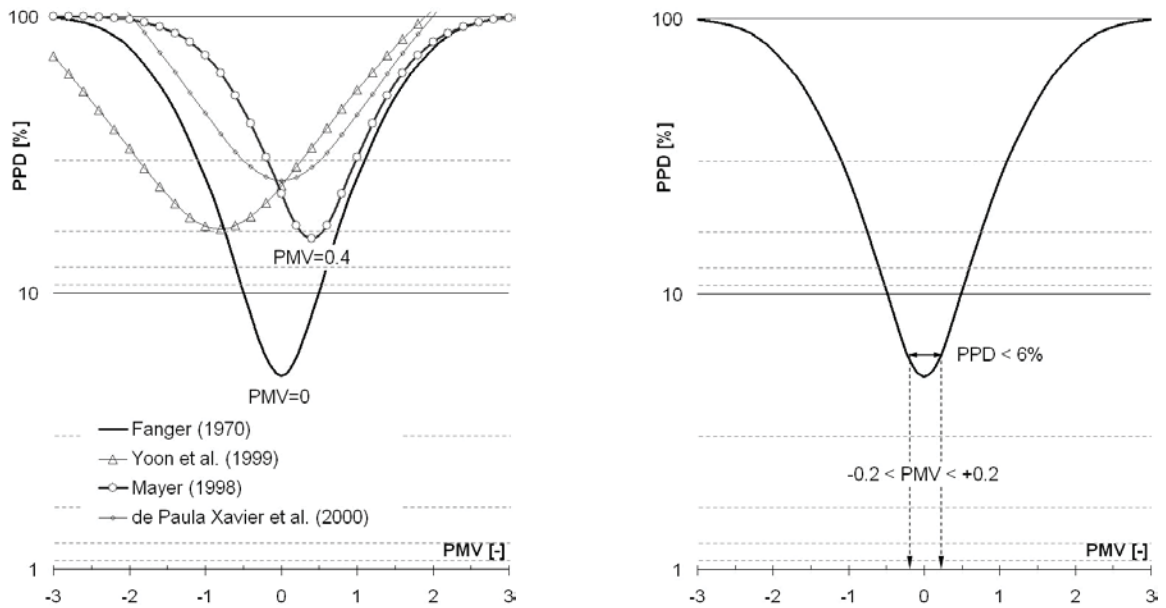


Figure 13.7: Correlations between PMV and PPD found by several authors (logarithmic y-axis). Formulae are summarized in [101]. The example on the right hand side shows the definition of a comfort zone in terms of PPD and the respective PMV range using Equation (13.4).

As the PMV model is representative for a large group of subjects exposed to the same thermal conditions, it is reasonable to relate PMV to a *percentage of people being dissatisfied (PPD)* via the algebraic expression (according to Fanger [28])

$$\text{PPD} = 100 - 95 \cdot e^{(-0.03353 \cdot \text{PMV}^4 - 0.2179 \cdot \text{PMV}^2)} . \quad (13.4)$$

The inverted hat-like function plotted in Figure 13.7 indicates the link between both indices in logarithmic scaling (for the y-axis). Limiting the acceptance rate to  $\text{PPD} < 6\%$ , for example, corresponds to the above mentioned range of  $-0.2 < \text{PMV} < +0.2$ . According to Fanger [28], it is not possible to have less than 5% dissatisfied of a large group of people with identical activity and clothing level.

Several authors report different settings for the state of thermal neutrality which are shown in Figure 13.7. VAN HOOF [101] summarizes further relationships which were found by MAYER [66], DE PAULA XAVIER et al. [17] and YOON et al. [112]. For example, Mayer derived  $\text{PMV} = +0.4$  ( $\text{PPD} < 16\%$ ) for thermal neutrality from experiments [66].

GAGGE [41] suggested another definition of the PMV index, the  $\text{PMV}^*$  index, which further takes the moisture sensation into account by replacing the operative temperature with the  $ET^*$  effective temperature (cf. Section 13.5.3 below for the definition of the term effective temperature).

### 13.5.2 Local thermal comfort for conditions near thermal neutrality

The PMV and PPD indices describe thermal comfort in terms of the acceptability for uniform conditions and for the body as a whole, statistically representative for a group of people with identical activity and clothing. However, in reality individuals wear different clothing and may not have the same activity level. Very often non-uniform or asymmetric effects are present which are not captured by the model. Local undesirable effects may dominate if parts of the body are cooled or heated differently from the rest of the body. Among these effects, local draught risk frequently occurs in practice because of cold down draught from (large) windows in winter. Local effects are especially noticeable if people perform light sedentary activities. People are less sensitive at higher activity levels [23].

According to FANGER [27] and others, the following indicators are significant:

- draught risk [30, 51, 68],
- asymmetric radiation [27, 29, 43],
- warm and cold floor surfaces [80, 81], and
- vertical temperature gradients [82].

In building design, the heating, ventilation and air-conditioning (HVAC) systems are usually designed in order to meet the heating and cooling demands for maintaining operative room temperatures at well defined levels – and not with respect to local effects affecting comfort. It is therefore reasonable in building simulation to combine the whole body related comfort assessment with the investigation of local effects for the design of HVAC components and other local heat exchanging devices – especially in the scope of energy efficient building design [49, 50, 85].

The standards ISO 7730 [23] and ASHRAE-55 [1] provide formulae and tools for assessing these local criteria in terms of PPD. The correlations are only valid for conditions near thermal neutrality. Other cases are detailed in Section 13.5.3.

- **Draught risk.** Draught occurs if parts of the body are cooled by a locally increased convective air flow. Local velocity fluctuations, i.e. the local degree of turbulence, influence the perception together with the mean air temperature and the mean velocity [30]. The draught risk (DR) can be estimated in terms of PPD [1, 23] by

$$DR = (34 - T_{air})(u_a - 0.05)^{0.62}(0.37 \cdot u_a \cdot Tu + 3.14) , \quad (13.5)$$

where  $u_a$  [ $m/s$ ] is the mean air speed ( $u_a < 0.5m/s$ ),  $T_{air}$  [ $^{\circ}C$ ] the mean air temperature and  $Tu$  [%] the degree of turbulence. For the ranges of parameters and further definitions it is referred to [1, 23]. The application of the model requires detailed information on the flow and temperature fields which can be obtained by CFD analysis. A thermal multizone model is not able to deliver this type of information. RECKNAGEL ET AL. [86] summarize simplified empirical formulae by FANGER [28], HEISELBERG [51] and

NIELSEN [75] for predicting the risk of cold down draught near window surfaces without CFD.

However, high ambient temperatures can be compensated by increasing the air flow which influences the convective heat exchange. The effect is quantified in the standards [1, 23] and can be utilized in naturally ventilated buildings to allow temperatures to rise above the comfort zone in summer.

- **Asymmetric radiation.** The asymmetric distribution of radiation due to different surface temperatures such as hot ceilings and/or cold surfaces can lead to uncomfortable situations [27, 29], especially if these surfaces are large. The standards [1, 23] provide diagrams indicating the effect of hot and cold vertical and horizontal surfaces in terms of PPD. With a thermal multizone model these effects can be captured if long wave radiation is modeled in detail with a geometric model.
- **Warm or cold floor surfaces.** The standards further indicate the comfort perception for the special case of warm or cold floor surfaces. In order to account for this in building performance simulation, the model must account for short and long wave radiation in a geometrical manner. Usually a large amount of the incident short wave radiation is absorbed at floor surfaces causing the temperature to rise. Radiant floor heating and cooling systems are discussed by OLESEN in [80, 81].
- **Vertical temperature gradients.** Vertical temperature gradients are usually measured between head and ankles, i.e. at 1.1m and 0.1m above the floor surface. ISO 7730 and ASHRAE-55 provide a diagram for assessing this effect. Temperature profiles can be predicted with CFD in full detail if appropriate boundary conditions are used. With a thermal multizone model a vertical temperature stratification can be predicted for large spaces. In case of a stratified temperature distribution, formulae for the natural stack effect may be applied to calculate the vertical temperature gradient, if applicable to the situation.

### 13.5.3 Inhomogeneous and transient conditions

The discussed methods are applicable for conditions near thermal neutrality where the level of comfort can be predicted, given the ambient microclimate. However, in some situations, local thermal sensation of non-uniform conditions and/or dynamic responses to transient conditions are of interest. For example, FANGER [27, 29] reports human responses to asymmetric conditions, GAGGE [39] and GRIFFITHS & MCINTYRE [47] evaluate transient uniform conditions. HENSEN [53] provides a literature review on thermal comfort in transient conditions. The investigation of human responses to non-uniform and transient conditions at the same time is subject to ongoing research [114].

The correlation between skin temperatures and local thermal sensation votes can be found by experiments as for example described by WYON et al. [110]. These experiments involve

thermal manikins which are equipped with heated sensors providing a constant heat flux for measuring resultant surface temperatures at a number of body segments [67]. In a survey, test subjects exposed to the same thermal conditions fill questionnaires with their respective thermal sensation votes for each segment of the body. The procedure is defined in EN ISO Standard 14505-2 [20].

**Equivalent temperature.** The non-uniform scenario from the above experiment can be correlated to a uniform environment using the concept of *equivalent temperatures* [9, 110]. EN ISO Standard 14505-2 [20] defines the equivalent temperature as "the uniform temperature of an imaginary enclosure with air velocity equal to zero in which a person will exchange the same dry heat by radiation and convection as in the actual non-uniform environment". This approach is also advantageous to relate thermal conditions to thermal sensation perceived by subjects assuming similar subjective responses irrespective of the combination of the heat transfer mechanisms (radiation and convection).

Regressions between the local thermal sensation votes and the local equivalent temperatures usually show a linear relationship. The correlations are therefore limited to the range of ambient conditions and the settings in terms of clothing and activity as defined by the experiment. Experiences in measuring and modeling human responses under various conditions are reported by BOHM et al. [9], HAN et al. [48], HOLMER [55], MAYER [67], NILSSON [77], STRØM-TEJSEN et al. [95], and ZHANG et al. [113, 114], for example.

As an example, Figure 13.8 shows a comfort zone for 16 segments in terms of equivalent

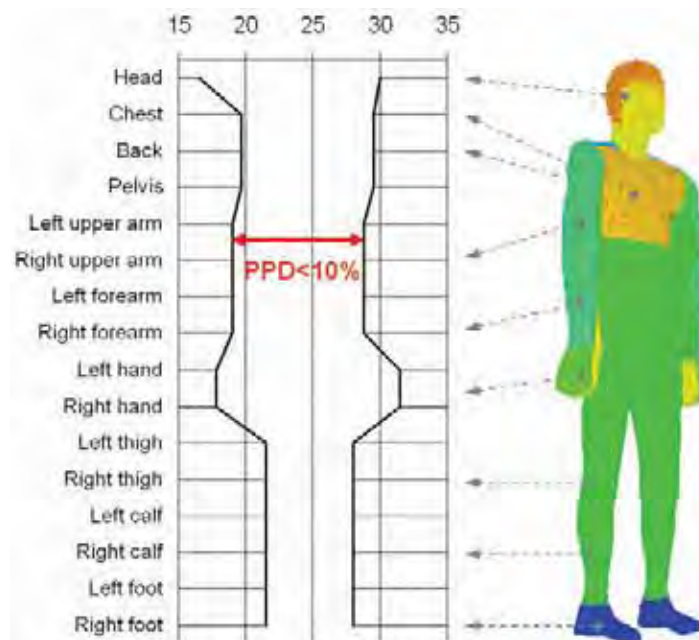


Figure 13.8: Comfort zone for PPD < 10% (90% acceptability) in terms of equivalent temperatures for 16 body segments, redrawn from the correlations found by BOHM et al. for the passenger cabin of a car [9, 48]. (For visualization, the manikin is displayed in an upright position.)

temperatures and 90% acceptability. The figure is redrawn from the results of BOHM et al. [9] which were obtained for a car from measurements of the vehicle climate with a thermal manikin.

**Operative/humid operative temperature and ET\*.** It is noted that equivalent temperatures refer to non-evaporative heat losses from the body. In order to further include the effect of skin wettedness, the *humid operative temperature* describes the operative temperature in an environment at a relative humidity of 100% that yields the same total heat loss from the skin as the actual environment. The *effective temperature (ET\*)* by GAGGE [42] is the same but for 50% relative humidity [2].

The definition of the *operative temperature* differs from the equivalent temperature. It is defined in ASHRAE Standard 55 [1] as "the temperature of a uniform environment with radiantly black enclosure that transfers dry heat by radiation and convection at the same rate as in the actual environment" and takes into account the mean radiant temperature and the air temperature *at the actual velocity*. If both values are close enough, the operative temperature can be taken as average between radiant and air temperature.

**Simulation of local thermal sensation votes and dynamic responses.** Section 13.3.2 introduced human thermoregulation models for the numerical simulation of dynamic physiological responses to transient thermal conditions and to predict the skin and core temperatures and their change over time. Skin temperatures can accordingly be transformed into equivalent temperatures for all segments of the manikin model. If a correlation between equivalent temperatures and local thermal sensation votes is known, local sensation votes can be visualized on the artificial skin of the virtual manikin as shown in Figure 13.8. Chapter 14 gives an example of such a numerical analysis using the model of Fiala [35].

However, it is extremely difficult to predict human responses for non-uniform conditions [76, 114, 117] experimentally. ZHANG et al. [113, 114] derived mathematical models for both non-uniform and transient conditions from a series of experiments with subjects addressing both the local and global temperature sensation and comfort perception. The researchers in Berkeley developed local sensation and comfort models for 19 individual body parts, as well as global sensation and comfort models for the whole body taking into account the weights of the different segments. The models are formulated in terms of skin and core temperatures and their rates of change over time in order to account for transient conditions.

FIALA also proposes a *dynamic thermal sensation model* in his thesis [33]. The empirical dynamic thermal sensation (DTS) model is formulated with a hyperbolic tangent function which relates to the change of skin temperature, the influence of the core temperature with respect to the thermal sensation and the dynamic changes. Skin and core temperature are thereby obtained from the thermoregulation model. As the model takes into account the physiological responses of the body, the DTS behavior clearly differs from the PMV which is directly related to the ambient microclimate.

### 13.5.4 People's expectation and behavioral adaptation

"People react in a way to restore their thermal comfort" in order to reduce physiological strain in conditions of thermal discomfort. This statement of HUMPHREYS & NICOL [59] is also confirmed by the observations of DE DEAR & BRAGER [16] who show that people evaluate the indoor thermal environment in a different way if the building allows for individually controlling the indoor climate. People can react in terms of opening windows, changing clothes (if not restricted by a dresscode), opening or closing roller blinds, using local fans, or having refreshments. Such reactions are referred to as *behavioral adaptation*.

De Dear and Brager [16] found that people in naturally ventilated ("free running") buildings accept a wider range of temperatures due to behavioral adaptations than predicted by the static comfort envelopes of ISO 7730 and ASHRAE-55. The observations are summarized in Figure 13.9. Both figures also show the regressions for the comfort temperature based on the PMV from De Dear and Brager's survey which are plotted against the mean outdoor air temperature. The PMV model (left hand side) predicts the observations well for buildings which fully controlled by an HVAC system. This is not surprising as HVAC components are designed according to the static comfort envelopes. Naturally ventilated (NV) buildings (right hand side) show a steeper gradient of the observed responses as people allow a wider range of thermal conditions.

The term *psychological adaptation* refers to people's expectation of the indoor climate which is related to the time history of the outside thermal conditions during the preceding days. VAN DER LINDEN et al. [99, 98] discuss a method to account for this effect by formulating comfort ranges in terms of the running mean outdoor temperature.

It is noted, that in principle the PMV model can cover behavioral adaptations as the model generally accounts for personal and environmental parameter. For example, modifying the clothing insulation impacts the energy balance equation of the human body and thus the

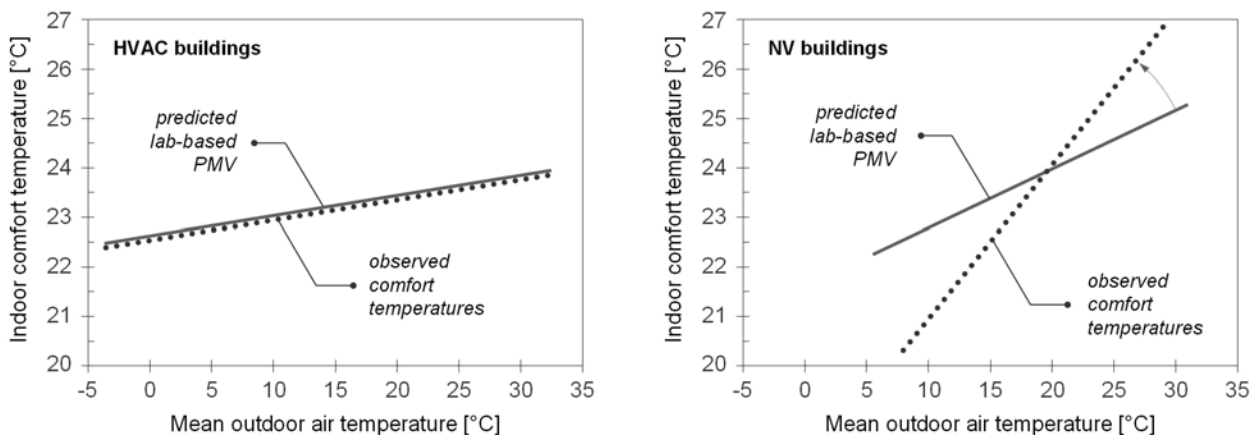


Figure 13.9: Observed and predicted comfort temperatures from a field study by DE DEAR & BRAGER [16] for buildings controlled by HVAC and for free running buildings. Redrawn from the values in [16].

predicted PMV. FANGER & TOFTUM [32] extended the PMV model to further account for people's expectations. A correction term, the so-called *expectancy factor e*, accordingly enlarges the range of thermal sensation votes of people in non-air conditioned buildings in warm climates. It is referred to the discussion of VAN HOOF & HENSEN [102, 101].

### 13.5.5 Overheating risk prediction

The above discussion revealed that people prefer a wider range of thermal conditions due to psychological and behavioral adaptations which are further influenced by the time history of the outdoor weather conditions. People tolerate a limited number of occasions if the indoor temperature exceeds the comfort temperature [3]. In order to account for the accumulation of such heat stress events, ROBINSON & HALDI [88] propose a mathematical model to predict the overheating risk in buildings for moderate climates.

The model is based on the analogy between charging and discharging of the tolerance to overheating stimuli to the principle of charging an electrical capacitor. The tolerance is accordingly the inverse of the probability of overheating. During a warm period, the overheating tolerance is discharged, and a series of cold days yields recharging. The dynamics of the model are determined in terms of the empirical time constants for charging and discharging.

In a field survey, Robinson and Haldi found out that the overheating is in fact caused by an accumulation of heat stress events and not primarily by single events.

According to BAKER & STANDEVEN [3] a series of adaptations cause the neutral temperature sensation to raise. The effect is called *adaptive increments*. Robinson and Haldi [88] also quantify the elevation of the neutral temperature in their work. The authors therefore relate comfort temperatures and their increments to specific actions and their conjugates. Furthermore, *probability functions* for these adaptive actions are suggested which are shown to be primarily correlated with the indoor temperatures. With the probability functions of adaptive actions in terms of the user behavior and the respective adaptive increments, Robinson and Haldi tested an explicit model which eliminates the adaptive increments. (The adaptability is implicitly given in the (dis)charging time constants of the model.) It is interesting to note that Robinson and Haldi [88] conclude that the adaptive effects can be interpreted as an aggregation of individual adaptive processes which can be isolated in terms of successive adaptive temperature increments which determine the *slope of the adaptive curve* of an adaptive comfort envelope to some extent.

## 13.6 Ergonomics of the thermal environment in buildings

A number of country specific standards define comfort envelopes with respect to acceptable ranges of temperatures. The indoor thermal quality performance of a building is usually classified in terms of *quality categories* with well defined limits of the percentage of dissatisfied for a selected type of clothing, level of activity and climate. The following sections will introduce

Category	Whole body-related discomfort		Local discomfort	
	PPD [%]	PMV [–]	PD in terms of draught risk [%]	asymmetric radiation PD [%]
A	< 6%	$-0.2 < \text{PMV} < +0.2$	< 10%	< 5%
B	< 10%	$-0.5 < \text{PMV} < +0.5$	< 20%	< 5%
C	< 15%	$-0.7 < \text{PMV} < +0.7$	< 30%	< 10%
else	> 15%	PMV < -0.7 or > 0.7	> 30%	> 10%

Table 13.1: Categories A, B and C according to EN ISO Standard 7730 [23].

the concept of such static and adaptive comfort envelopes.

It is thereby distinguished between mechanically and naturally ventilated buildings, and so-called "mixed-mode" buildings with hybrid ventilation. DE DEAR & BRAGER [16] show that occupants show different expectations for naturally ventilated buildings as people adapt themselves to warm conditions by changing clothes or by opening windows and doors. Adaptive comfort guidelines account for these effects by relating the individual expectation and local adaptation to the change of the ambient climate over time.

The indoor thermal quality strongly influences the heating and cooling demands of a building. The traditional and "perhaps" not the best way in terms of energy efficiency is to dimension an HVAC system in order to always meet the heating and cooling demand which would be required for maintaining the operative temperatures within defined limits. In existing buildings, the indoor thermal quality can be assessed by measurements and surveys during operation [21]. However, with simulation many details of the building performance and the indoor thermal quality become visible in advance. This makes it possible to exploit the full potential of active and passive measures in energy efficient building design, for example to save cooling energy if an adaptive comfort guidelines is applied for a building with natural ventilation in summer. If, in turn, the air temperature is strictly controlled by the HVAC system, the level of comfort is determined by the set point temperature of the control device, irrespective if occupants would accept other temperatures.

### 13.6.1 Static comfort envelopes

EN ISO Standard 7730 [23] defines the "ergonomics of the thermal environment" for moderate climates in terms of *three categories A, B and C* indicated in Table 13.1 which limit the percentage of the dissatisfied with respect to the whole body and to the four major local comfort criteria which were described in Section 13.5.2. The method is applicable to steady state conditions, cyclical temperature changes are restricted to 1K and drifts and ramps are limited to 2K per hour. Given the parameters for clothing insulation, activity, humidity and local air velocity, the allowed range of operative temperatures can be calculated from the specified PMV ranges.

In a similar manner, EN Standard 15251 [21] defines four categories for mechanically ventilated buildings regarding high expectations (I) of the indoor thermal quality, usual expectations (II), and moderate (III) and low (IV) expectations. Tables summarize the recommended temper-

ature ranges for designing heating and cooling devices with respect to a selected comfort category, type of clothing and level of activity. For the second category (II), for example, which is suggested for new or renovated buildings, it is recommended to keep PPD < 10% thus  $-0.5 < \text{PMV} < +0.5$ . For people working in an open plan office with sedentary light activity (1.2met) this means that within the heating period, the minimum operative temperature (winter clothing 1clo) should be maintained above  $20^\circ\text{C}$  and within the cooling period (summer clothing 0.5clo) below  $26^\circ\text{C}$ . Again, local thermal comfort criteria such as draught risk or radiation asymmetries must be met in terms of the ISO 7730 criteria.

EN Standard 15251 further includes an adaptive assessment method with respect to the dependence of the comfort temperature on the outside weather conditions in free running buildings.

### 13.6.2 ASHRAE summer and winter comfort zones

The assessment method of ASHRAE Standard 55 [1] "thermal environmental conditions for human occupancy" is similar to ISO 7730 [23] regarding the PMV model and the local conditions as indicated in Section 13.5.2. ASHRAE Standard 55 thereby defines its comfort zones with a *psychrometric chart* (see Section 3.3) in order to express satisfaction with the thermal environment for a deviation of  $\pm 0.5$  PMV from thermal neutrality.

In the chart, which is redrawn from [1] in Figure 13.10, the range of operative temperatures is given for 80% acceptability and further limits the wet bulb temperatures in terms of the humidity ratio (or the dew point temperature) for a *summer zone* for 0.5clo and a *winter zone* for 1.0clo. The activity levels are set to 1 or 1.3met, respectively. The air speed is  $< 0.2\text{m/s}$ . The 80% acceptability combine a limitation of  $\text{PPD} < 10\%$  for general comfort plus 10%

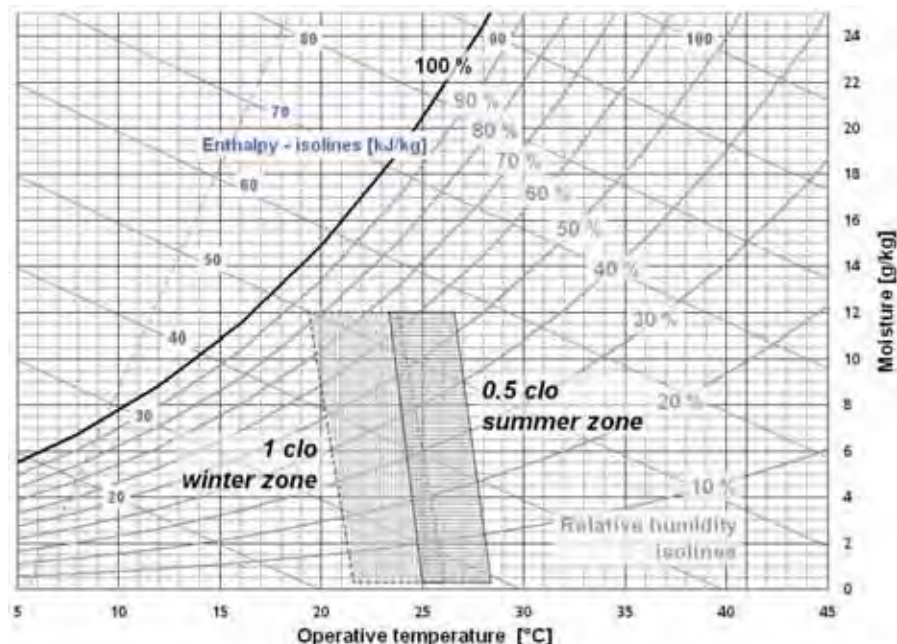


Figure 13.10: Psychrometric chart with summer and winter comfort envelope within the  $\pm 0.5$  PMV limits. Redrawn from the specifications in [1] using the diagram of Section 3.3.

for local effects. The humidity ratio is limited in its upper and lower bound as a high relative humidity causes discomfort due to skin wettedness [40] and increased skin friction, and a low humidity is responsible for dry skin, throat and eyes and may cause respiratory illness [2].

ASHRAE Standard 55 also provides an adaptive guideline for naturally ventilated buildings.

### 13.6.3 Adaptive comfort guidelines

Examples of *adaptive thermal comfort (ATC)* guidelines are EN ISO Standard 15251 [21], the Dutch ISSO Standard 74 [62] and ASHRAE Standard 55 [1]. The guidelines can be applied for naturally ventilated, i.e. non-air-conditioned, office type buildings or similar, which provide a high level of occupant control [54] and where people mainly perform light (sedentary) work. The adaptive comfort envelopes define acceptable indoor temperatures which vary in terms of the running outdoor temperatures<sup>1</sup>. The time history of the (averaged) the outside temperatures is evaluated in different ways in the standards. HUMPHREYS [58] suggests exponentially weighted running mean values over a seven day period, VAN DER LINDEN et al. [98] a four day period, and DE DEAR & BRAGER [16] take monthly mean values of the dry bulb outdoor temperature. The application of the ATC guidelines is straightforward in simulation, as the operative indoor temperature and the time history of the outdoor temperatures are the only inputs.

The permitted range of acceptable temperatures is centered around the comfort temperature which is defined by an ATC regression equation as published in the standards. The ATC envelope can then be derived for a respective PMV range as demanded by the acceptability in terms of a specified PPD design value. For example, de Dear and Brager [16] obtained the

<sup>1</sup>For example, also DIN Standard 1946 specifies room air temperature ranges in terms of ambient air temperatures [18].

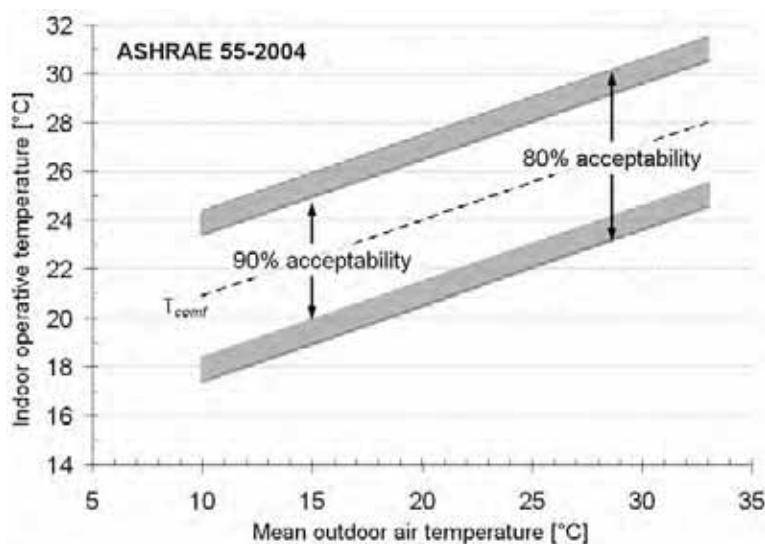


Figure 13.11: ASHRAE adaptive comfort envelope according to eq. (13.6) and [16] for 90% and 80% acceptability.

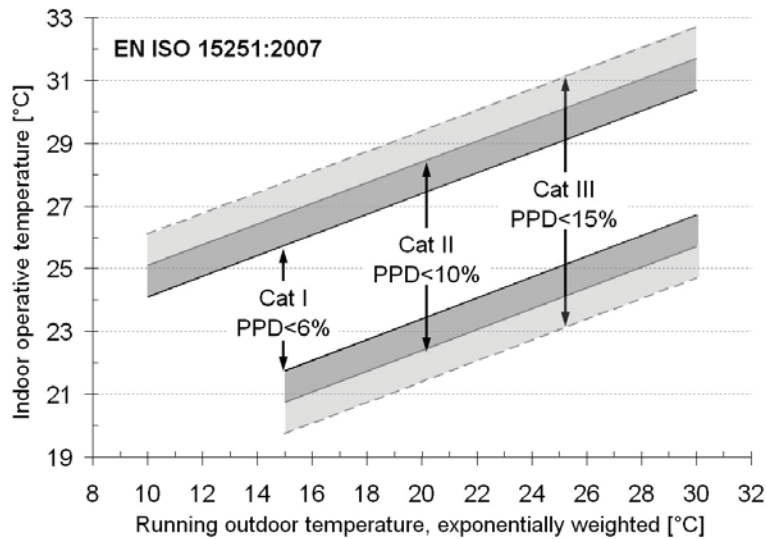


Figure 13.12: Adaptive comfort envelope according to EN ISO 15251 according to eq. (13.7) and [21] for the three categories I, II and III.

relation

$$T_{\text{comf}} = 0.31 T_{rm,out} + 17.8 \pm \Delta T \quad (13.6)$$

for the comfort temperature  $T_{\text{comf}}$  and the running mean outdoor temperature  $T_{rm,out}$  and suggest a bandwidth of  $\Delta T = 2.5K$  and  $3.5K$  for 90% and 80% acceptability, respectively, for the ASHRAE guideline. The comfort envelope is shown in Figure 13.11.

EN ISO Standard 15251 [21] defines the regression

$$T_{\text{comf}} = 0.33 T_{ew,out} + 18.8 \pm \Delta T \quad (13.7)$$

for the comfort temperature  $T_{\text{comf}}$  in naturally ventilated buildings without air-condition installed. The value  $T_{ew,out}$  is the exponentially weighted running daily outdoor temperature in this case. The standard suggests the temperature bandwidths  $\Delta T = 2K$ ,  $3K$  and  $4K$  for limiting the three categories I, II and III as shown in Figure 13.12. For outdoor temperatures below  $10^{\circ}\text{C}$  (upper bound) and  $15^{\circ}\text{C}$  (lower bound), the settings of the PMV model for mechanically ventilated buildings are applied.

In a similar manner, ISSO Standard 74 [62] defines its comfort ranges for PMV < 90%, 80% and 65% in terms of the classes A, B and C. The background of the guideline is again motivated by the research of de Dear and Brager [14]. It is distinguished between type Alpha buildings offering a high degree of occupant control and type Beta for centrally controlled HVAC systems. In the heating period for outdoor temperatures below  $10$  to  $12^{\circ}\text{C}$ , the same operative temperature limits are applied for type Alpha and for type Beta buildings.

Section 13.5.4 mentions, that the PMV model can be used to model behavioral adaptations, if these adaptations are explicitly accounted for in the model. In this way, the ATC method has been compared by VAN DER LINDEN et al. [100] with the PMV model. In their study,

the authors calculated acceptable ranges of operative temperatures with the PMV model for selected seasonal scenarios and other relevant input parameters for a moderate climate, which were compared with to the ATC guideline. Different settings for the humidity and air velocity were assumed for the winter and summer cases. In order to account for the clothing habits in the PMV model, the experimentally obtained correlations by DE CARLI et al. [12] between mean outdoor temperatures and clothing insulation for naturally ventilated buildings were included. The results indicate, that the adaptive ranges can be well explained for moderate climates in terms of the PMV ranges up to mean outdoor temperatures of 21°C.

In summary, for naturally ventilated buildings the ATC approach defines a wider range of acceptable conditions than the classical static comfort envelopes, if people can react in a way to respond to the local climate. VAN HOOF & HENSEN [102] quantified the energy reduction potential of the ATC method which can be estimated to about 10% for type Alpha buildings in the Netherlands.

### 13.6.4 Long-term thermal quality performance

Thermal multizone models make most of the data relevant for comfort prediction available in postprocessing. For the analysis of the large amount of simulation data, descriptive integral measures for evaluating the annual thermal quality performance are required as well as indicators for capturing the issue of local thermal comfort.

The standards ISO 7730 [23] and EN 15251 [21] define *long term indicators* for predicting the frequency of occurrence in terms of penalty functions if it is not adhered to the thermal quality during a whole year thermal simulation in terms of a defined acceptability level. The following indices are suggested:

- **Hourly performance index.** This index quantifies the number of hours per year (or the percentage of the time) if the comfort criteria are met or not in terms of a single indicator [21].
- **Degree hour criterion.** In this case, the time (without set-back times) is weighted by the degree hours if the operative temperature  $T_{op}$  drops out of a specified comfort range. The unit of the performance index is hours [21].

The weights  $w = T_{op} - T_{op,limit}$  are calculated in terms of exceeding temperatures, i.e. by the difference between the temperature of the upper or lower bound  $T_{op,limit}$  of the comfort zone, respectively. The product of the weighting factor  $w$  and the time  $t$  is summed up ( $\sum w \cdot t$ ) for characteristic periods, i.e. for the heating period if  $T_{op} < T_{op,limit}$ , or for the cooling period if  $T_{op} > T_{op,limit}$ .

- **PPD weighted performance index.** In a similar way, the PMV index can be weighted and summed up over a characteristic period. The weighting factor is now determined in terms of the ratio between the PPD value of the actual PMV based on the operative temperature and the PPD which corresponds to the PMV at the boundary of the comfort range if the actual PMV drops out of this range. Within the PMV range, the weight is zero [21].

The PMV based weighting factor is a sharper criterion than the index which is based on degree hours as more hours are obtained [21].

It is emphasized that these performance indicators do not accurately account for the *accumulation of heat stress events* that cause overheating [88]. See also the discussion in Section 13.5.5.

VAN DER LINDEN [98] et al. evaluate different prediction methods in terms of their expressiveness in simulation. A comparison of the Dutch TO/GTO methods (TO is based on exceeding temperatures and GTO means weighted excess hours) with the Dutch adaptive guideline [62] indicates that the ATC guideline is more rigorous than the degree hour method (TO/GTO). This is due to the fact that the quality category is downgraded if only a single value drops out of a specified range of acceptability for the ATC guideline.

## 13.7 References

- [1] ASHRAE. *Standard 55: Thermal Environmental Conditions for Human Occupancy*. American Society of Heating, Refrigerating and Air-Conditioning Engineers, Atlanta, 2004.
- [2] ASHRAE. *Handbook - Fundamentals (SI)*. American Society of Heating, Refrigerating and Air-Conditioning Engineers, 2005.
- [3] N. Baker and M. Standeven. Thermal comfort for free-running buildings. *Energy and Buildings*, 23:175–182, 1996.
- [4] I. Beausoleil-Morrison. *The adaptive coupling of heat and air flow modelling within dynamic whole building simulation*. PhD thesis, University of Strathclyde, Glasgow, 2000.
- [5] T. Bedford. The warmth factor in comfort at work. vol 76, MRC Industrial Health Board Report HMSO, London, UK, 1936.
- [6] A. Bejan. *Convection heat transfer*. John Wiley & Sons, Inc., 1993.
- [7] T.H. Benzinger. The physiological basis for thermal comfort. In P.O. Fanger and O. Valbjørn, editors, *Indoor Climate*, pages 441–476, Danish Building Research Institute, Copenhagen, 1979.
- [8] L.G. Berglund and D.J. Cunningham. Parameters of human discomfort in warm environments. *ASHRAE Transactions*, 92(2B):732–746, 1986.
- [9] M. Bohm, M. Brown, I. Holmer, P.V. Nilsson, and O. Noren. Evaluation of vehicle climate with a thermal manikin. Technical report, Swedish Institute of Agricultural Engineering, 1990.
- [10] J.F. Busch. A tale of two populations: Thermal comfort in air-conditioned and naturally ventilated offices in Thailand. *Energy and Buildings*, 18:235–249, 1992.

- [11] M. Cabanac and J.D. Hardy. Réponses unitaires et thermorégulatrices lors de réchauffements et réfroidissements localisés de la région préoptique et du mésencéphale chez le lapin. *J Physiol Paris*, 61:331–347, 1969.
- [12] M. de Carli, B.W. Olesen, A. Zarrella, and R. Zecchin. People's clothing behaviour according to external weather and indoor environment. *Building and Environment*, 42:3965–3973, 2007.
- [13] R. J. de Dear, E. Arens, Z. Hui, and M. Oguro. Convective and radiative heat transfer coefficients for individual human body segments. *Int J Biometeorology*, 40:141–156, 1997.
- [14] R.J. de Dear and G.S. Brager. Developing an adaptive model of thermal comfort and preference. *ASHRAE Technical Data Bulletin*, 14(1):27–49, 1998.
- [15] R.J. de Dear and G.S. Brager. Thermal adaptation in the built environment: A literature review. *Energy and Buildings*, 27(1):83–96, 1998.
- [16] R.J. de Dear and G.S. Brager. Thermal comfort in naturally ventilated buildings: revisions to ASHRAE Standard 55. *Energy and Buildings*, 34:549–561, 2002.
- [17] A.A. de Paula Xavier and R. Lamberts. Indices of thermal comfort developed from field survey in brazil. *ASHRAE Transactions*, 106:45–58, 2000.
- [18] DIN 1946 Teil 2. *Raumluftechnik, Gesundheitstechnische Anforderungen*. DIN Deutsches Institut für Normung e.V., Beuth, 1994.
- [19] EN ISO 11399. *Ergonomics of the thermal environment - Principles and application of relevant International Standards*. 1995.
- [20] EN ISO 14505-2. *Ergonomics of the thermal environment - Evaluation of thermal environment in vehicles - Part 2: Determination of the Equivalent Temperature*. 2004.
- [21] EN ISO 15251. *Indoor environmental input parameters for design and assessment of energy performance of buildings addressing indoor air air quality, thermal environment, lighting and acoustics*. 2007.
- [22] EN ISO 7243. *Hot environments - Estimation of the heat stress on working man, based on the WBGT-index (wet bulb globe temperature)*. 1989.
- [23] EN ISO 7730. *Ergonomics of the thermal environment – Analytical determination and interpretation of thermal comfort using calculation of the PMV and PPD indices and local thermal comfort criteria*. 2005.
- [24] EN ISO 7933. *Ergonomics of the thermal environment - Analytical determination and interpretation of heat stress using calculation of the predicted heat strain*. 2004.
- [25] EN ISO 8996. *Ergonomics of the thermal environment - Determination of metabolic rate*. 2004.

- [26] EN ISO 9920. *Ergonomics of the thermal environment – Estimation of thermal insulation and water vapour resistance of a clothing ensemble*. 2007.
- [27] P.O. Fanger. Thermal discomfort caused by radiant asymmetry, local air velocities, warm and cold floors, and vertical air temperature gradients. In J. Durrand and J. Rayuand, editors, *Thermal Comfort*, volume 75, pages 145–152. Editions INSERM, 1977.
- [28] P.O. Fanger. *Thermal comfort*. Robert E. Krieger, Malabar, 1982.
- [29] P.O. Fanger, B.M. Ipsen, G. Langkilde, B.W. Olesen, N.K. Christensen, and S. Tanabe. Comfort limits for asymmetric thermal radiation. *Energy and Buildings*, 8:225–236, 1985.
- [30] P.O. Fanger, A.K. Melikov, H. Hanzawa, and J. Ring. Air turbulence and sensation of draught. *Energy and Buildings*, 12:21–39, 1988.
- [31] P.O. Fanger, J. Ostergaard, O. Olesen, T. Madsen, and Lund. The effect on man's comfort of a uniform air flow from different directions. *ASHRAE Transactions*, 80:142–157, 1974.
- [32] P.O. Fanger and J. Toftum. Extension of the PMV model to non airconditioned buildings in warm climates. *Energy and Buildings*, 34:533–536, 2002.
- [33] D. Fiala. *Dynamische Simulation des menschlichen Wärmehaushalts und der thermischen Behaglichkeit*. Band 41, De Monfort University Leicester, HFT Stuttgart, 1998.
- [34] D. Fiala, K.J. Lomas, and M. Stohrer. A computer model of human thermoregulation for a wide range of environmental conditions: the passive system. *J Appl Physiol*, 87:1957–1972, 1999.
- [35] D. Fiala, K.J. Lomas, and M. Stohrer. Computer prediction of human thermoregulatory and temperature responses to a wide range of environmental conditions. *Int J Biometeorol*, 45:143–159, 2001.
- [36] FIALA-FE, 2008. Manikin model validation manual, release 2.0, <http://www.theseus-fe.de>.
- [37] A.J.H. Frijns, D. Limpens-Neilen, M.E.A. Schoffelen, and G.M.J. van Leeuwen. Simulation of the human thermal responses to local heating. In *Proc. IEA2006*, Maastricht, Netherlands, 2006.
- [38] A. Gagge. Rational temp. indices of man's thermal env. and their use with a 2-node model of his temp. reg. *Fed. Proc.*, 32:1572–1582, 1973.
- [39] A. Gagge, J. Stolwijk, and J. Hardy. Comfort and thermal sensation and associated physiological responses at various ambient temperatures. *Environ. Res.*, 1:1–20, 1967.
- [40] A.P. Gagge. The role of humidity during warm discomfort. In P.O. Fanger and O. Valbkorn, editors, *Indoor Climate*, pages 527–538. Danish Building Research Institute. Copenhagen, 1979.

- [41] A.P. Gagge, A.P. Fobelets, and P.E. Berglund. A standard predictive index of human response to the thermal environment. *ASHRAE Transactions*, 92(2B):709–731, 1986.
- [42] A.P. Gagge and R.R. Gonzalez. Physiological bases of warm discomfort for sedentary man. *Arch. Sci. Physiol.*, 27:A409–A424, 1973.
- [43] B. Glück. Zulässige Strahlungstemperatur-Asymmetrie. *Gesundheitsingenieur*, 115(6):285–344, 1994.
- [44] R.R. Gonzalez and L.G. Berglund. Efficacy of temperature and humidity ramps in energy conservation. *ASHRAE Journal*, 6:34–41, 1979.
- [45] R.R. Gonzalez and A.P. Gagge. Magnitude estimates of thermal discomfort during transients of humidity and operative temperature. *ASHRAE Transactions*, 79(1):88–96, 1973.
- [46] R. Gordon. *The response of human thermoregulatory system in the cold*. PhD thesis, Univ. of California, St. Barbara, CA., 1974.
- [47] I.D. Griffiths and D.A. McIntyre. Sensitivity to temporal variations in thermal conditions. *Ergonomics*, 17:499–507, 1974.
- [48] T. Han, L. Huang, S. Kelly, C. Huizenga, and H. Zhang. Virtual thermal comfort engineering. SAE technical paper series 2001-01-0588, 2001.
- [49] G. Hausladen, M. de Saldanha, and P. Liedl. *ClimaSkin, Konzepte für Gebäudehüllen, die mit weniger Energie mehr leisten*. Verlag Callwey, München, 2006.
- [50] G. Hausladen, M. de Saldanha, P. Liedl, and Sager. C. *ClimaDesign, Lösungen für Gebäude, die mit weniger Technik mehr können*. Verlag Callwey, München, 2005.
- [51] P. Heiselberg. Stratified flow in rooms with a cold vertical wall. *ASHRAE Transactions*, 100(1):1011–1023, 1994.
- [52] H. Hensel. *Thermal sensation and thermoreceptors in man*. Charles C. Thomas, Springfield, 1982.
- [53] J.L.M. Hensen. Literature review on thermal comfort in transient conditions. *Building and Environment*, 25(4):309–316, 1990.
- [54] S. Herkel, U. Knapp, and J. Pfafferott. A preliminary model of user behaviour regarding the manual control of windows in office buildings. In *Building Simulation 2005*, Montreal, Canada, 2005.
- [55] I. Holmér. Heated manikins as a tool for evaluating clothing. *Annals of Occupational Hygiene*, 39(6):809–818, 1995.
- [56] I. Holmér. Thermal manikin history and applications. *Eur J Appl Physiol*, (92):614–618, 2004.

- [57] C. Huizenga, Z. Hui, and E. Arens. A model of human physiology and comfort for assessing complex thermal environments. *Building and Environment*, 36:691–699, 2001.
- [58] M.A. Humphreys. Outdoor temperatures and comfort indoors. *Building Research and Practise*, 6:92–105, 1978.
- [59] M.A. Humphreys and J.F. Nicol. Understanding the adaptive approach to thermal comfort. *ASHRAE Transactions*, 104(1):991–1004, 1998.
- [60] ISO 11079. *Ergonomics of the thermal environment - Determination and interpretation of cold stress when using required clothing insulation (IREQ) and local cooling effects*. 2007.
- [61] K. Issing and H. Hensel. Static thermal sensation and thermal comfort. *Z Phys Med Baln Med Klim*, 11:354–365, 1981.
- [62] ISSO 74. *Thermische behaaglijkheid; eisen voor de binnentemperatuur in gebouwen*. publicatie 74, ISSO, Rotterdam, 2004.
- [63] S. Kato, H. Nagano, and L. Yang. A CFD manikin with a thermo physiology model. In *RoomVent2007*, Helsinki, 2007.
- [64] J.C. Kok, J. van Muijden, S. Burgers, H. Dol, and S.P. Spekreijse. Enhancement of aircraft cabin comfort studies by coupling of models for human thermoregulation, internal radiation, and turbulent flows. In P. Wesseling, E. Oñate, and J. Périaux, editors, *EC-COMAS CFD 06, European Conference on Computational Fluid Dynamics, September 5-8*, Egmond aan Zee, The Netherlands, 2006.
- [65] P. Kröling. Sick Building Syndrom: Symptome, Ursachen und Prophylaxe gebäudebedingter Gesundheitsstörungen. *Allergologie*, 21(5):180–191, 1998.
- [66] E. Mayer. Ist die bisherige Zuordnung von PMV und PPD noch richtig? *KI Luft- und Kältetechnik*, 12:575–577, 1998.
- [67] E. Mayer. Manfitted measurement of thermal climate by a dummy representing suit for simulation of human heatloss (DRESSMAN). In *Healthy Buildings*, volume 2, pages 551–556, Washington DC, 2000.
- [68] E. Mayer and R. Schwab. Untersuchungen der physikalischen Ursachen von Zugluft. *Gesundheitsingenieur*, 111(1):17–30, 1990.
- [69] D.A. McIntyre. *Indoor Climate*. Applied Science Publishers LTD, London, 1980.
- [70] P.E. McNall and J.C. Schlegel. The relative effect of convective and radiation heat transfer on thermal comfort. *ASHRAE Transactions*, 74:131–143, 1968.
- [71] A.K. Melikov, N.R.J. Janicas, , and M.C.G. da Silva. Segmental equivalent temperature determined by means of a thermal manikin: A method for correcting errors due to incomplete contact of the body with a surface. ROOMVENT 2004, Coimbra, Portugal, 2004.

- [72] M.F. Modest. *Radiative Heat Transfer*. Academic Press, USA, 2nd edition, 2003.
- [73] G.D. Mower. Perceived intensity of peripheral thermal stimuli is dependent of internal body temperature. *J Comp Physiol Psychol*, 90:1152–1155, 1976.
- [74] R.G. Nevins, R.R. Gonzalez, Y. Nishi, and A.P. Gagge. Effect of changes in ambient temperature and level of humidity on comfort and thermal sensations. *ASHRAE Transactions*, 81(2):169–182, 1975.
- [75] P.V. Nielsen. Luftströmninger i ventilerede arbejdslokaler. SBI-rapport 128, Statens byggeforskningsinstitut, 1981.
- [76] P.V. Nielsen, S. Murakami, S. Kato, C. Topp, and J.H. Yang. Benchmark test for a computer simulated person. Technical report, Aalborg University, <http://www.cfd-benchmarks.com>, 2003.
- [77] H. Nilsson. Comfort climate evaluation with thermal manikin methods and computer simulation models. Technical report, National Institut for Working Life, Stockholm, Schweden, 2004.
- [78] H.O. Nilsson, H. Brohus, and P.V. Nielsen. CFD modeling of thermal manikin heat loss in a comfort evaluation benchmark test. In *RoomVent2007*, Helsinki, 2007.
- [79] J. Niu and N. Gao. Personalized ventilation for commercial aircraft cabins. In *IndoorAir2008*, Copenhagen, Denmark, 2008.
- [80] B.W. Olesen. Radiant floor heating in theory and practise. *ASHRAE Journal*, 7:19–24, 2002.
- [81] B.W. Olesen. Radiant floor cooling systems. *ASHRAE Journal*, 9:16–22, 2008.
- [82] B.W. Olesen, M. Scholer, and P.O. Fanger. Discomfort caused by vertical air temperature differences. In P.O. Fanger and O. Valbjorn, editors, *Indoor Climate*. Danish Building Research Institute, Kopenhagen, 1979.
- [83] S. Paulke. Finite element based implementation of Fiala's thermal manikin in THESEUS-FE. In *EUROSIM 2007*, 2007.
- [84] H.H. Pennes. Analysis of tissue and arterial blood temperatures in the resting human forearm. *J. Appl. Physiol.*, 1(2):93–122, 1948.
- [85] J. Pfafferott, S. Herkel, D. Kalz, and A. Zeuscher. Comparison of low-energy office buildings in summer using different thermal comfort criteria. *Energy and Buildings*, 39:750–757, 2007.
- [86] Recknagel, Sprenger, and Schramek. *Taschenbuch für Heizung, Klima und Technik*. Oldenburg Verlag, München, Wien, 73 edition, 2007.
- [87] J.W. Ring and R.J. de Dear. Temperature transients: A model for heat diffusion through the skin, thermoreceptor response and thermal sensation. *Indoor Air*, 1(4):448–456, 1991.

- [88] D. Robinson and F. Haldi. An integrated adaptive model for overheating risk prediction. *J Building Performance Simulation*, 1(1):43–55, 2008.
- [89] F.H. Rohles and R.G. Nevins. The nature of thermal comfort for sedentary man. *ASHRAE Transactions*, 77(1):239–246, 1971.
- [90] F.H. Rohles, J.E. Woods, and R.G. Nevins. The effect of air movement and temperature on the thermal sensation of sedentary man. *ASHRAE Transactions*, 80:101–118, 1974.
- [91] J. Sano, S. Tanabe, K. Murakami, H. Nagayama, H. Oi, and T. Itami. Evaluation of thermal environments in vehicles by CFD coupled with numerical thermoregulation-model JOS. In *IndoorAir2008*, Copenhagen, Denmark, 2008.
- [92] J.A. Stolwijk. Sick-Building Syndrome. *Environmental Health Perspectives*, 95:99–100, 1991.
- [93] J.A.J. Stolwijk. A mathematical model of physiological temperature regulation in man. Contractor report NASA CR-1855, National Aeronautics and Space Administration, Washington D.C., 1971.
- [94] R. Streblow, D. Müller, and I. Gores. A coupled simulation of the thermal environment and thermal comfort with an adapted tanabe comfort model. In *IndoorAir2008*, Copenhagen, Denmark, 2008.
- [95] P. Strøm-Tejsen, D. Zukowska, A. Jama, and D.P. Wyon. Assessment of the thermal environment in a simulated aircraft cabin using thermal manikin exposure. In *RoomVent2007*, Helsinki, 2007.
- [96] S.-I. Tanabe, K. Kobayashi, J. Nakano, and Y. Ozeki. Evaluation of thermal comfort using combined multi-node thermoregulation (65MN) and radiation models and computational fluid dynamics (CFD). *Energy and Buildings*, 34:637–646, 2002.
- [97] THESEUS-FE, 2008. Theory manual, release 2.0, <http://www.theseus-fe.de>.
- [98] A.C. van der Linden, A.C. Boerstra, A.K. Raue, S.R. Kurvers, and R.J. de Dear. Adaptive temperature limits: A new guideline in The Netherlands. *Energy and Buildings*, 38:8–17, 2006.
- [99] K. van der Linden, A.C. Boerstra, A.K. Raue, and S.R. Kurvers. Thermal indoor climate building performance characterized by human comfort response. *Energy and Buildings*, 34:737–744, 2002.
- [100] W. van der Linden, M. Loomans, and J. Hensen. Adaptive thermal comfort explained by PMV. In *IndoorAir2008*, Copenhagen, Denmark, 2008.
- [101] J. van Hoof. Fourty years of Fanger's model of thermal comfort: comfort for all? *IndoorAir*, 18:182–201, 2008.
- [102] J. van Hoof and J.L.M. Hensen. Quantifying of relevance of adaptive thermal comfort models in moderate thermal climate zones. *Build. Environ.*, 42:156–170, 2008.

- [103] W.D. van Marken Lichtenbelt, A.J.H. Frijns, M.J. van Ooijen, D. Fiala, A.M. Kester, and A.A. van Steenhoven. Validation of an individualised model of human thermoregulation for predicting responses to cold air. *Int J Biometeorol*, 51:169–179, 2007.
- [104] C. van Treeck. *Gebäudemodell-basierte Simulation von Raumluftströmungen*. PhD thesis, Technische Universität München, 2004.
- [105] C. van Treeck, J. Frisch, M. Pfaffinger, E. Rank, S. Paulke, I. Schweinfurth, R. Schwab, R. Hellwig, and A. Holm. Integrated thermal comfort analysis using a parametric manikin model for interactive real-time simulation. *J Building Performance Simulation*, 2(4):233–250, 2009. DOI: 10.1080/19401490902914637.
- [106] C. van Treeck, P. Wenisch, A. Borrmann, M. Pfaffinger, N. Cenic, and E. Rank. Utilizing high performance supercomputing facilities for interactive thermal comfort assessment. In *Proc. 10th IBPSA Conf. Building Simulation*, Bejing, China, September 3-6 2007.
- [107] C. van Treeck, P. Wenisch, A. Borrmann, M. Pfaffinger, M. Egger, O. Wenisch, and E. Rank. Towards interactive indoor thermal comfort simulation. In P. Wesseling, E. Oñate, and J. Périaux, editors, *ECCOMAS CFD 06, European Conference on Computational Fluid Dynamics*, September 5-8, Egmond aan Zee, The Netherlands, 2006.
- [108] J. Werner and M. Buse. Temperature profiles with respect to inhomogeneity and geometry of the human body. *J. Appl. Physiol.*, 65(3):1110–1118, 1988.
- [109] E. Wissler. Mathematical simulation of human thermal behaviour using whole body models. In Eberhart Shitzer, editor, *Heat Transf. in Med. and Biol.*, volume 1, chapter 13, pages 325–373. 1985.
- [110] D.P. Wyon, S. Larsson, B. Forsgren, and I. Lundgren. Standard procedures for assessing vehicle climate with a thermal manikin. SAE technical paper 890049, pp. 1-11, 1989.
- [111] B. Yang, A. Melikov, and C. Sekhar. Cooling effect of ceiling mounted personalized ventilation systems. IndoorAir2008, Copenhagen, Denmark, 2008.
- [112] D.W. Yoon, J.Y. Sohn, and K.H. Cho. The comparison on the thermal comfort sensation between the results of questionnaire survey and the calculation of the PMV values. In G. Raw, C. Aizlewood, and P. Warren, editors, *Indoor Air*, volume 2, pages 137–141, Edinburgh, 1999.
- [113] H. Zhang. *Human thermal sensation and comfort in transient and non-uniform thermal environments*. PhD thesis, Univ. of California, Berkeley, 2003.
- [114] H. Zhang, C. Huizenga, E. Arens, and D. Wang. Thermal sensation and comfort in transient non-uniform thermal environments. *Eur J Appl Physiol*, 92:728–733, 2004.
- [115] Y. Zhang and T. Yang. Simulation of human thermal responses in a confined space. In *IndoorAir2008*, Copenhagen, Denmark, 2008.
- [116] S.W. Zhu, S. Kato, R. Ooka, and T. Sakai. Development of a computational thermal manikin applicable in a non-uniform thermal environment (part 1). *ASHRAE HVAC&R Research*, 13(4):661–679, 2007.

- [117] S.W. Zhu, S. Kato, R. Ooka, T. Sakoi, and K. Tsuzuki. Development of a computational thermal manikin applicable in a non-uniform thermal environment (part 2). *ASHRAE HVAC&R Research*, 14(4):545–564, 2008.

# Chapter 14

## Application examples

### 14.1 Applications in building performance simulation

Simulation offers a cost effective tool for a thorough investigation of the energy and indoor thermal quality performance of buildings. Chapter 13 detailed models for statistically correlating performance indicators of peoples' thermal satisfaction with the ambient environment. However, the expressiveness a thermal simulation in terms of a comfort analysis is determined by the accuracy and resolution of the simulation approach in space and time.

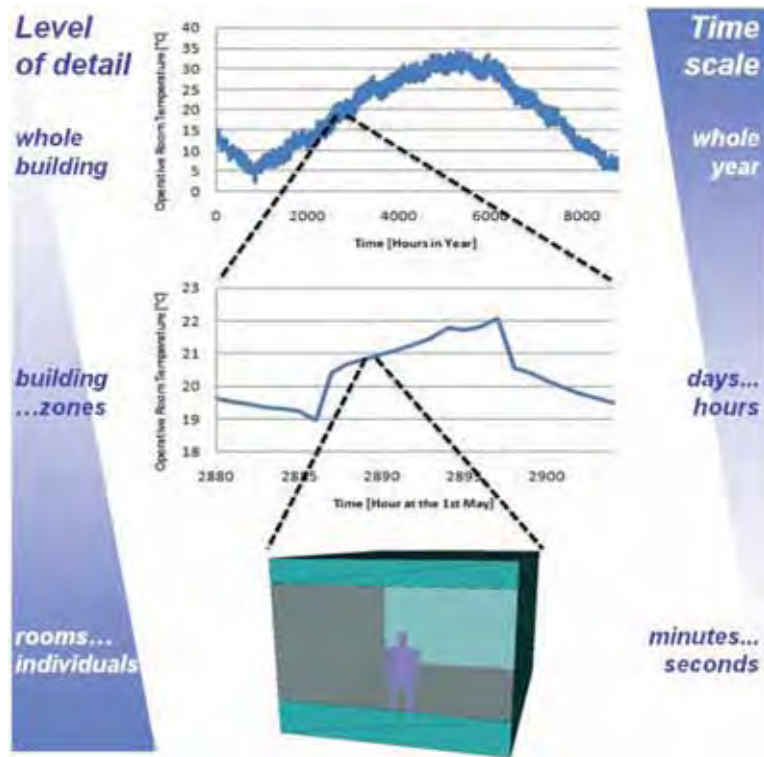


Figure 14.1: Level of detail dependent thermal analysis in space and time.

To capture the overheating risk within a building zone as indicated in Figure 14.1, the frequency of occurrence when operative room temperatures exceed a critical value must be predicted. Therefore, a whole-year simulation must be carried out. If such critical periods are

identified, the model can be further refined. For the analysis of radiation asymmetry, for example, a geometric radiation model must be available in order to determine the wall surface temperatures. In order to investigate local draught risk, a detailed computational fluid dynamics (CFD) simulation is necessary for getting insight into the room airflow. Due to the large computational overhead, the latter is clearly restricted to a few characteristic time steps within the overall analysis.

In this chapter, the application of three different simulation approaches for predicting the indoor thermal quality performance will be demonstrated. It should be noted that with increasing resolution in space and time also the simulation costs are elevated because of the time which is needed for creating or coupling the respective models. First of all, the comfort analysis with the thermal multizone model developed in this book is discussed. Different adaptive comfort envelopes are used to classify the thermal performance of the respective building. The second example addresses the local draught risk using a coupled CFD approach. In the last example, a thermal manikin model is applied for predicting the dynamic responses of the human body and the individually perceived local thermal sensation in detail.

### 14.1.1 Thermal comfort analysis using a multizone model

With a dynamic multizone model as sketched in Chapter 10 most of data become available which are relevant for predicting thermal comfort. By further assuming a well-stirred or stratified air temperature distribution with the methods discussed in Chapter 11, the operative temperatures, i.e. the mean air and mean radiant temperatures of the surrounding surfaces of a zone, are predicted with a high resolution in time for a whole year period.

The following results for the sample room of the VDI Standard 6020 [24] benchmark are post-processed in hourly intervals, which was already used in Section 3.6 for the static heat balancing method. (The simulation time step size was set to 3.6 seconds in order to obtain a well-converged solution.) In this context the room is considered as a naturally ventilated office space. The room and its components have the same properties as given in the Tables 3.2 to 3.5; the window surface is again oriented due south with appropriate shading devices.

As it is assumed that people in the room perform light sedentary activities and can individually control the window ventilation, an adaptive thermal comfort guideline can be applied. In the following Figures 14.2, 14.3 and 14.4, results are compared for the static comfort envelope of ISO Standard 7730:2005 [5] and two adaptive guidelines, the European Standard EN ISO 15251:2007 [4] and the Dutch ISSO Standard 74:2005 [10].

For the envelope of the ISO 7730, the operative temperatures are plotted against the daily mean ambient air temperature; for the ISO 15251 against the exponentially weighted running mean outdoor temperatures and for the ISSO 74 against the weighted running mean outdoor temperatures. To define the bounds of the static envelope, for summer and winter different clothing insulations (0.5 clo and 1.0 clo), values for the local air speed and the relative humidity are assumed. Details are given in ISO 7730. The figures only contain the daily minimum and maximum values in order to increase the readability.

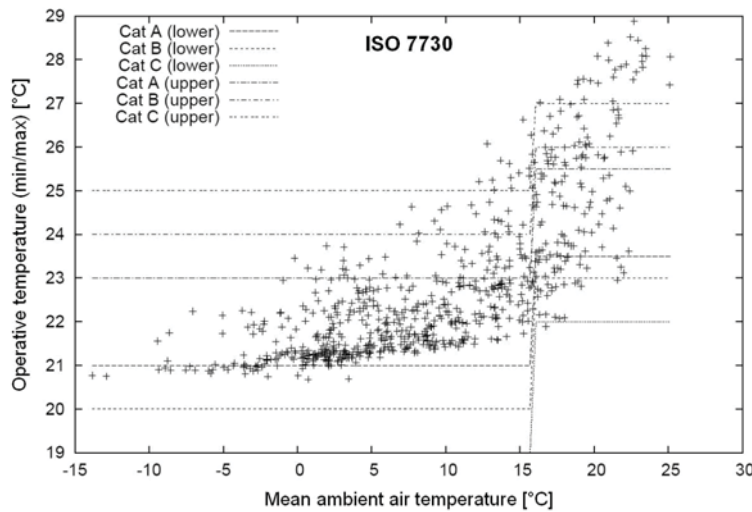


Figure 14.2: Operative room temperatures plotted against the daily mean ambient air temperatures for the comfort envelope of ISO 7730:2005.

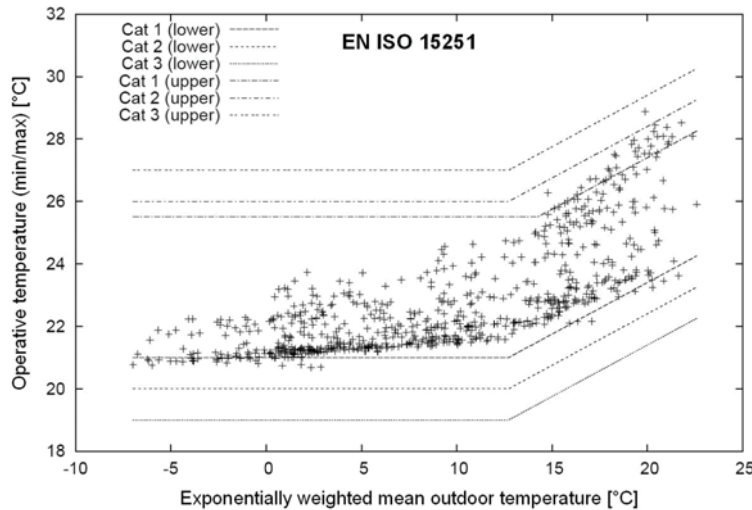


Figure 14.3: Operative room temperatures plotted against the exponentially weighted running mean outdoor temperatures for the comfort envelope of N ISO 15251:2007.

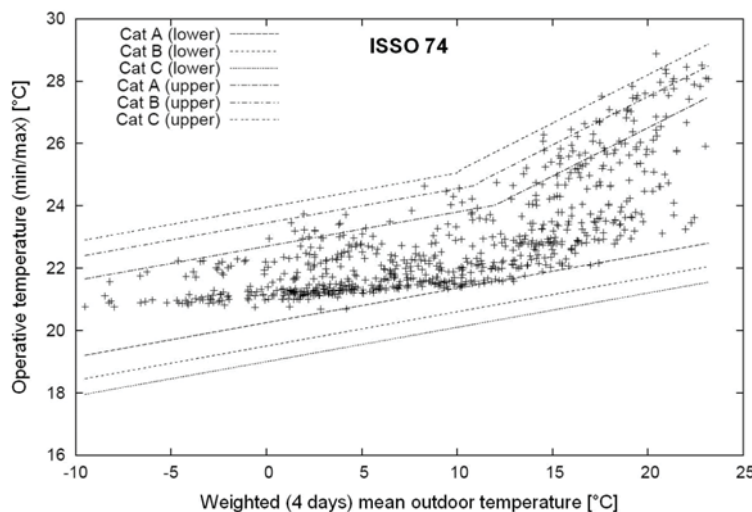


Figure 14.4: Operative room temperatures plotted against the weighted running mean outdoor temperatures for the comfort envelope of ISSO 74:2005.

<b>ISO 7730</b>	A	B	C	<b>else</b>
Acceptability	94%	90%	85%	< 85%
Frequency of occurrence	77.1%	14.4%	6.5%	2.0%

<b>EN ISO 15251</b>	I	II	<b>III</b>	IV
Acceptability	94%	90%	85%	< 85%
Frequency of occurrence	95.8%	4.2%	0.1%	0%

<b>ISSO 74</b>	A	B	C	<b>else</b>
Acceptability	90%	80%	65%	< 65%
Frequency of occurrence	95.7%	3.7%	0.6%	0.1%

Table 14.1: Comparison of the different comfort approaches and categories.

The comfort envelopes shown in Figures 14.2, 14.3 and 14.4 classify the thermal quality of the building. The frequency of occurrence if these criteria are met or violated are summarized in Table 14.1 (for all 8760 time steps). If only a single value drops out of a respective comfort range, the building is downgraded to the next lower category. This becomes obvious for cate-

Maximum values (DIN EN 15251 / CAT II / upper part)												
Jan	Feb	Mar	Apr	May	Jun	Jul	Aug	Sep	Oct	Nov	Dec	
1	0	0	0	0	0	0.044	0.51	0.466	0	0	0	
2	0	0	0	0	0	0	0	0.001	0	0	0	
3	0	0	0	0	0	0	0	0.001	0	0	0	
4	0	0	0	0	0	0	0	0.526	0	0	0	
5	0	0	0	0	0	0	0.1	0	0	0	0	
6	0	0	0	0	0	0	0.212	0	0	0	0	
7	0	0	0	0	0	0	0.118	0	0	0	0	
8	0	0	0	0	0	0	0	0	0	0	0	
9	0	0	0	0	0	0	0.218	0	0	0	0	
10	0	0	0	0	0	0	0	0	0	0	0	
11	0	0	0	0	0	0	0	0.684	0	0	0	
12	0	0	0	0	0	0	0	0.699	0.0	0	0	
13	0	0	0	0	0	0	0	0.169	0	0	0	
14	0	0	0	0	0	0	0.734	0.574	0	0	0	
15	0	0	0	0	0	0	0.236	0.306	0	0	0	
16	0	0	0	0	0	0	0.174	0	0	0	0	
17	0	0	0	0	0	0	0.408	0	0	0	0	
18	0	0	0	0	0	0	0	0.643	0	0	0	
19	0	0	0	0	0	0	0.007	0.409	0	0	0	
20	0	0	0	0	0	0	0	0	0	0	0	
21	0	0	0	0	0	0	0.224	0	0	0	0	
22	0	0	0	0	0	0	0.253	0	0	0	0	
23	0	0	0	0	0	0	0	0.605	0	0	0	
24	0	0	0	0	0	0	0	0	0	0	0	
25	0	0	0	0	0	0	0.046	0	0	0	0	
26	0	0	0	0	0	0	0	0	0	0	0	
27	0	0	0	0	0	0	0	0	0	0	0	
28	0	0	0	0	0	0	0	0.085	0	0	0	
29	0	0	0	0	0	0	0	0.31	0	0	0	
30	0	0	0	0	0	0	0.327	0	0	0	0	
31	0	0	0	0	0	0	0.794	0	0	0	0	

Maximum values (DIN EN 15251 / CAT III / upper part)												
Jan	Feb	Mar	Apr	May	Jun	Jul	Aug	Sep	Oct	Nov	Dec	
1	0	0	0	0	0	0	0	0	0	0	0	0
2	0	0	0	0	0	0	0	0	0	0	0	0
3	0	0	0	0	0	0	0	0	0	0	0	0
4	0	0	0	0	0	0	0	0	0	0	0	0
5	0	0	0	0	0	0	0	0	0	0	0	0
6	0	0	0	0	0	0	0	0	0	0	0	0
7	0	0	0	0	0	0	0	0	0	0	0	0
8	0	0	0	0	0	0	0	0	0	0	0	0
9	0	0	0	0	0	0	0	0	0	0	0	0
10	0	0	0	0	0	0	0	0	0	0	0	0
11	0	0	0	0	0	0	0	0	0	0	0	0
12	0	0	0	0	0	0	0	0	0	0	0	0
13	0	0	0	0	0	0	0	0	0	0	0	0
14	0	0	0	0	0	0	0	0	0	0	0	0
15	0	0	0	0	0	0	0	0	0	0	0	0
16	0	0	0	0	0	0	0	0	0	0	0	0
17	0	0	0	0	0	0	0	0	0	0	0	0
18	0	0	0	0	0	0	0	0	0	0	0	0
19	0	0	0	0	0	0	0	0	0	0	0	0
20	0	0	0	0	0	0	0	0	0	0	0	0
21	0	0	0	0	0	0	0	0	0	0	0	0
22	0	0	0	0	0	0	0	0	0	0	0	0
23	0	0	0	0	0	0	0	0	0	0	0	0
24	0	0	0	0	0	0	0	0	0	0	0	0
25	0	0	0	0	0	0	0	0	0	0	0	0
26	0	0	0	0	0	0	0	0	0	0	0	0
27	0	0	0	0	0	0	0	0	0	0	0	0
28	0	0	0	0	0	0	0	0	0	0	0	0
29	0	0	0	0	0	0	0	0	0	0	0	0
30	0	0	0	0	0	0	0	0	0	0	0	0
31	0	0	0	0	0	0	0	0	0	0	0	0



Figure 14.5: Calender type view indicating the deviation of the daily maximum operative temperatures from the categories of the EN ISO 15251:2007.

gory II of EN ISO 15251 (a single value outside cat. II) and for category C of ISSO 74 (two values outside the bounds). In this case, the building is accordingly classified by ISO 7730 as *worse than category C*, by ISO 15251 as *category III*, and by ISSO 74 as *worse than category C* in terms of acceptability.

The graphical representation and the evaluation of the frequency of occurrences of exceeding temperatures is a descriptive method for indicating the overall annual thermal performance. However, it is not clear from these figures *when* these overheating events are taking place. In order to identify these events, a calendar type view can be used which indicates the deviation of the daily maximum (or minimum) operative temperatures from the comfort zone. Figure 14.5 clarifies this for the upper parts of the category II and III of EN ISO 15251. This type of visualization therefore provides an efficient way to compare the effectiveness of model modifications.

### 14.1.2 Local draught risk analysis using CFD

The methods discussed in the previous section help to identify critical times of a whole-year simulation. The results are related to the body as a whole in terms of the user acceptability. It is, however, with these methods not possible to investigate local effects which are relevant if for example the position of the outlets of a HVAC shall be properly designed. In this section, a typical application scenario is demonstrated: the analysis of the local draught risk (DR) in terms of PPD using the formulae provided in ISO Standard 7730 [5] or ASHRAE-55 [1]. Therefore the field values of the mean air temperature, the air velocity and the degree of turbulence are required as input, which can be obtained by a CFD analysis.

As indicated in Chapter 11, the turbulent convective nature of the air flows implies the application of turbulence models and a refined mesh near the walls. Realistic boundary conditions

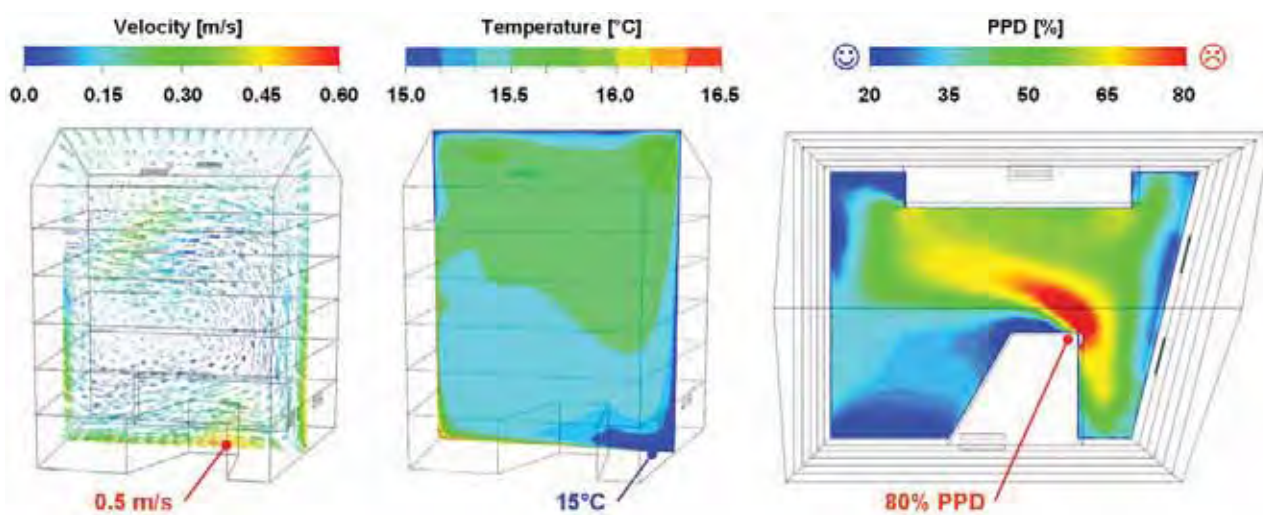


Figure 14.6: Draught risk analysis using ANSYS CFX where PPD (right-hand picture) is calculated from the averaged velocity field (left) and the temperature profile (center). The PPD is shown on a horizontal plane 0.4m above ground. Modified from [19].

are required such as in- and outflow conditions (velocity or pressure values) as well as temperatures (Dirichlet conditions) or heat fluxes (type Neumann conditions) at the surfaces bounding the flow domain. In this case, boundary conditions were obtained by coupling with a thermal multizone model as previously demonstrated in [19]. After supplying the geometric model with these boundary conditions, a surface and volume mesh of the flow domain is created.

The example in Figure 14.6 shows the simulation of the down draught from the cold glazing facade of a building atrium for the winter case. The building with inner courtyard was subject to a number of investigations which are detailed by SCHÄLIN ET AL. [15]. The facade of the atrium is oriented due south, the other sides are in contact with the office building. The top-most floor protrudes the surrounding building, the atrium height is 26m, vents are assumed closed in this case.

The percentage of dissatisfied is computed for a horizontal plane 0.4m above the floor surface. The figure indicates that the down draught from the cold facade produces high local velocities up to  $0.5 \text{ m/s}$  at  $15^\circ\text{C}$  air temperature, the acceptance is thus below 20%. A possible solution for this case could be the installation of small local radiators within the facade plane or to improve the glazing U-value.

The application of CFD is time consuming because of the effort for the mesh generation and the subsequent modifications for further parameter studies. The computational costs are also high. The use of CFD is therefore restricted in daily engineering practice.

### 14.1.3 Local and dynamic comfort analysis using a human model

Both sections 14.1.1 and 14.1.2 addressed thermal comfort assuming steady state conditions for the body as a whole and close to the state of thermal neutrality. As explained in Chapter 13, this approach is to a large extent reasonable for predicting the indoor thermal quality performance in buildings. It is the preferred method in practice. However, apart from the building sector, the prediction of thermal comfort is relevant for a number of other industrial areas such as automotive, rail, coach and aircraft industries where local and dynamic effects under transient and non-homogeneous conditions become significant. In this section the application of a multi-segment thermal model of a human is demonstrated for the local and dynamic thermal comfort analysis in uniform but transient conditions. Surface, skin and core temperatures are computed in order to express local thermal sensations as a response to the ambient conditions, and the dynamic responses of the human body are displayed. The developed model could be likewise applied to non-uniform and inhomogeneous conditions.

Opposed to models that consider the steady-state human heat balance for the body as a whole, a detailed numerical approach using a virtual manikin for the comfort assessment essentially consists of

- a flow and thermal radiation solver in order to compute the convective and radiative heat transfer between the human body and environment,
- a multi-segment thermal model of the human body taking the body heat exchange, physical and physiological properties, the blood circulation and the human thermoregulation

into consideration [6, 16, 17], and

- empirical correlations between skin temperatures and temperature sensation as well as a model for the local and global thermal comfort prediction [26].

With a thermal manikin the surface and skin temperatures for the respective body segments, the core temperatures and the change of these quantities over time can be predicted. As described in Chapter 13, the surface temperatures can be transformed into local equivalent temperatures which, in turn, can be related to experimentally obtained local thermal sensation votes. Figure 14.7 details this process. The figure shows the simulated skin temperatures  $T_{skin,i}$ , the local equivalent temperatures  $T_{eq,i}$  and the obtained local thermal sensation votes  $LTSV_i$  by the linear correlation  $LTSV_i = a_i \cdot T_{eq,i} + b_i$  for each body segment  $i$ . The regression coefficients  $a_i$  and  $b_i$  are derived by experiments with human subjects [20].

The following results were obtained with the thermoregulation model of FIALA ET AL. [7, 8] which can be used to predict human thermal reactions to a wide range of environmental conditions. A parametric manikin model was therefore developed by VAN TREECK, FRISCH and others [20] which interfaces with the THESEUS-FE [18] implementation FIALA-FE [9] of Fiala's model developed by PAULKE [14]. The sector-wise discretization with 19 (conflated 15) spherical and cylindrical elements is similar to the original Fiala model but makes use of a finite element based approach using shell elements in order to represent the concentric layer structure of the manikin. Some of these segments are further subdivided into anterior, inferior and posterior parts. The total model consists of 48 subsegments [20].

The subdivision of the elements is important in many cases of non-uniform environments as occurring in vehicles and buildings [12]. Clothing is represented by an additional layer [9]. The FIALA-FE model is further capable of modeling contact problems if local segments are in solid contact with the surrounding structure. Contact problems are, however, not considered in this context.

The solver provides an adaptive time integration method which remedies the restrictions of the fixed time stepping of Fiala's original model [9, 20]. In order to reduce the computational

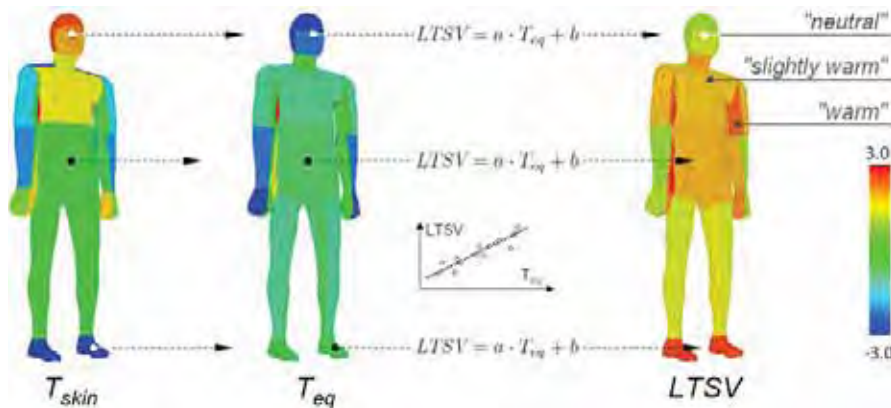


*Figure 14.7:* Simulated skin temperatures  $T_{skin}$ , transformation into local equivalent temperatures  $T_{eq}$  and mapping to local thermal sensation votes ( $LTSV$ ) for each segment.

overhead it is reasonable to use predefined view factors [6] (see also Section 7.1.4) and surface convection heat transfer coefficients such as the coefficients found by DE DEAR ET AL. [2]. Such correlations are usually obtained for manikin models placed within a rectangular cavity and can therefore be applied in the scope of building performance simulation with reasonable accuracy as interim solution.

Figures 14.8 and 14.9 give an example of the application of the developed parametric manikin model which is placed within a "virtual climate chamber" [20]. As depicted in Figure 14.8, the climate chamber is a rectangular box, precalculated view factors and heat transfer coefficients are used to reduce the computational effort. The simulation sequence corresponds to 30 minutes real time in intervals of 10 seconds. During the simulation, the boundary conditions of the climate chamber are adjusted, in detail the temperature of the surrounding surfaces, the air temperature and the mean air speed and the relative humidity.

In Figure 14.9, the dynamic thermal responses of the human body are shown with respect to changes in the ambient conditions, clothing and level of activity: Graph a) depicts the overall clothing insulation and the level of activity (boundary conditions), graph c) draws the mean hypothalamus, skin and surface temperatures, the mean equivalent temperature and the mean basal metabolic rate. The 3D images b), d) and g) indicate the skin temperatures, the local equivalent temperatures and the local thermal sensation votes for each body segment. In figure e) the whole-body related dynamic thermal sensation (DTS) and the predicted mean vote (PMV) are shown. The DTS index [6] takes the core and skin temperatures and their changes into account and is a comfort index of the dynamic responses of the whole body in uniform but transient conditions. It should be noted that the model was calibrated with respect to an average adult person; for a detailed discussion of the differences in the metabolism it is referred to [6]. Figure f) further details the local thermal sensation for the anterior part of the thorax, the anterior part of the right leg and for the head.

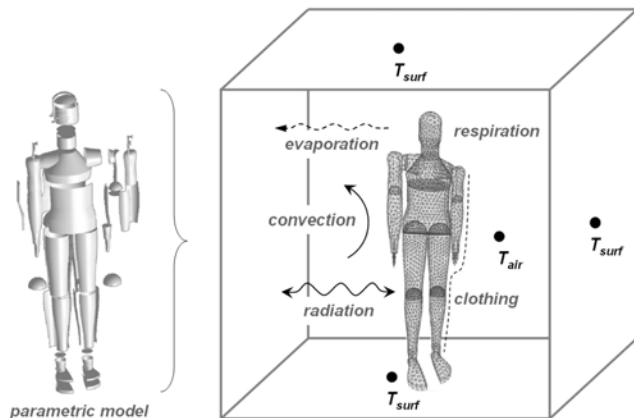


Figure 14.8: Parametric manikin model within the virtual climate chamber.

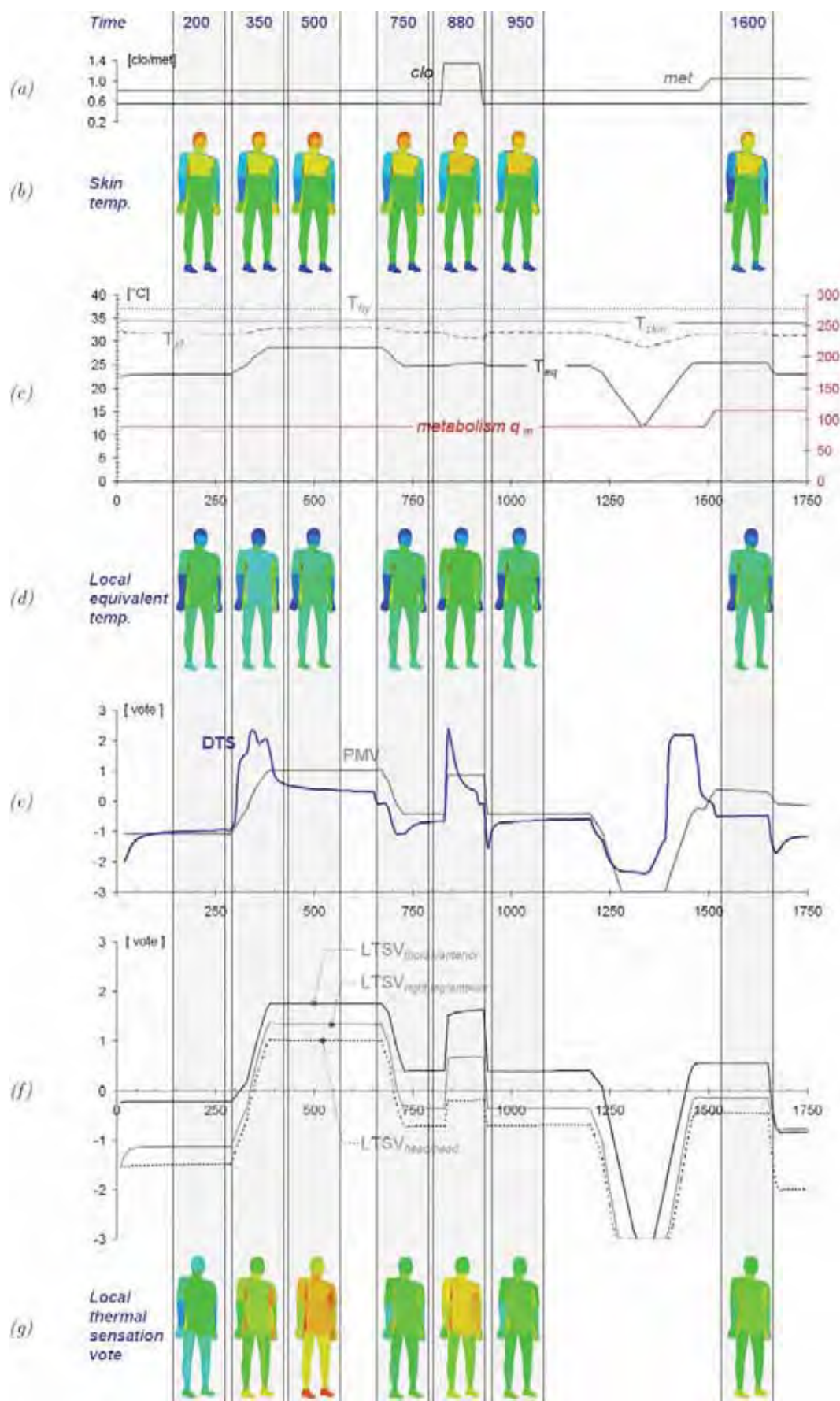


Figure 14.9: Dynamic thermal responses of the human body to changes in the ambient conditions, clothing and level of activity. Explanations see text.

## 14.2 Thermal flow analysis in an aircraft cabin

Apart from the building sector, the prediction of thermal comfort is relevant in a number of other industry branches such as the aircraft and vehicle manufacturing industry – and especially with respect to non-uniform and/or transient conditions. In a joint cooperation with the companies Askon (Germany) and Realix Technologies (France), the thermal flow in an aircraft passenger cabin was investigated in a pilot study in order to demonstrate the application of a CFD solver which was developed at the Technische Universität München [21].

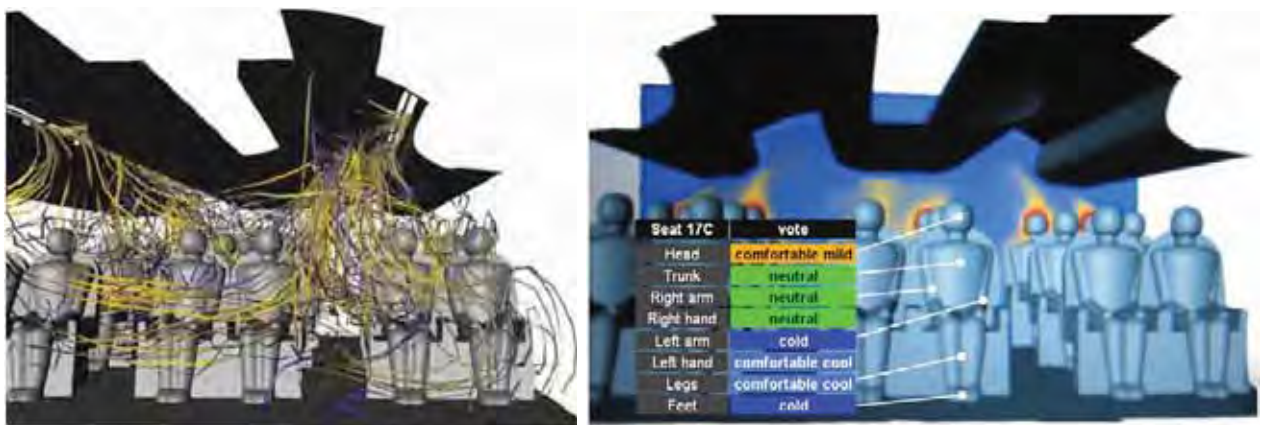


Figure 14.10: Turbulent mixed convection in an aircraft passenger cabin computed with a thermal lattice Boltzmann code [22]. Left: streamline plot of the averaged velocity field. Right: vertical plane with the averaged temperature field showing the thermal plumes above the heads of the subjects [21] and example of a comfort evaluation.

Segment	1A	1B	1C	1D	1E	1F
Head	comfortable	comfortable	comfortable	comfortable	comfortable	comfortable
Trunk	comfortable	comfortable	comfortable	comfortable	comfortable	comfortable
Right arm	comfortable	comfortable	comfortable	comfortable	comfortable	cold
Right hand	comfortable	comfortable	comfortable	comfortable	comfortable	comfortable cool
Left arm	cold	comfortable	comfortable	comfortable	comfortable	comfortable
Left hand	comfortable cool					
Legs	cold	comfortable cool				
Feet	cold	comfortable cool				

Segment	2A	2B	2C	2D	2E	2F
Head	comfortable	comfortable	comfortable	comfortable	comfortable	comfortable
Trunk	comfortable	comfortable	comfortable	comfortable	comfortable	comfortable
Right arm	comfortable	comfortable	comfortable	comfortable	comfortable	cold
Right hand	comfortable	comfortable	comfortable	comfortable	comfortable	comfortable cool
Left arm	cold	comfortable	comfortable	comfortable	comfortable	comfortable
Left hand	comfortable cool					
Legs	cold	comfortable cool				
Feet	cold	comfortable cool				

Segment	3A	3B	3C	3D	3E	3F
Head	comfortable	comfortable	comfortable	comfortable	comfortable	comfortable
Trunk	comfortable	comfortable	comfortable	comfortable	comfortable	comfortable
Right arm	comfortable	comfortable	comfortable	comfortable	comfortable	cold
Right hand	comfortable	comfortable	comfortable	comfortable	comfortable	comfortable cool
Left arm	cold	comfortable	comfortable	comfortable	comfortable	comfortable
Left hand	comfortable cool					
Legs	cold	comfortable cool				
Feet	cold	comfortable cool				

excessively cold	cold	comfortable cool	comfortable	comfortable mild	warm	excessively warm
------------------	------	------------------	-------------	------------------	------	------------------

Figure 14.11: Evaluation of the thermal sensation for 18 seats with an analytical 8-segment model of CORDIER using equivalent temperatures [21]. In cooperation with F. Hillion and A. Cordier, Askon (Germany) and Realix Technologies (France).

For the flow simulation, a parallelized CFD code was used which is based on a hybrid thermal lattice Boltzmann method [3, 11] with extensions for modeling turbulent convective flows of Boussinesq-incompressible fluids by a Smagorinsky subgrid scale turbulence model [22, 23]. Starting with a facette model from the manufacturer with approximately 600,000 faceted surface elements, a uniform cartesian voxel grid was created. The grid generator makes use of a spacetime-based algorithm [25] which is an efficient and robust method that allows for meshing the geometry in 7.4 seconds computing time without further modification of the triangulated model. The model with  $160 \cdot 10^6$  degrees of freedom was computed in 11 hours computing time (corresponding to resolving 90 seconds in real time) on 216+1 processors of the high performance computer SGI Altix 4700 at the Leibniz Computing Centre in Germany [13].

Based on the results for the configuration of turbulent mixed convection as shown in Figure 14.10, the surface temperatures were transformed into equivalent temperatures. The thermal performance was then evaluated by an analytical 8-segment model of CORDIER as depicted on the right hand side of Figure 14.10. Details of the thermoregulation were not considered in this case. The results in terms of the local thermal sensation votes, which were obtained for 18 seats, are displayed in Figure 14.11. For the evaluation, a scaling similar to the mean thermal voting (MTV) scale was used (see Section 13.4.1). For this configuration, the thermal sensation for the extremities which are exposed to the external surfaces was perceived between "comfortable cool" and "cold" as these positions were subject to locally high air speeds.

## 14.3 References

- [1] ASHRAE. *Standard 55: Thermal Environmental Conditions for Human Occupancy*. American Society of Heating, Refrigerating and Air-Conditioning Engineers, Atlanta, 2004.
- [2] R. J. de Dear, E. Arens, Z. Hui, and M. Oguro. Convective and radiative heat transfer coefficients for individual human body segments. *Int J Biometeorology*, 40:141–156, 1997.
- [3] D. d’Humières, I. Ginzburg, M. Krafczyk, P. Lallemand, and L.-S. Luo. Multiple-relaxation-time lattice Boltzmann models in three dimensions. *Phil. Trans. R. Soc. Lond. A*, 360:437–451, 2002.
- [4] EN ISO 15251. *Indoor environmental input parameters for design and assessment of energy performance of buildings addressing indoor air air quality, thermal environment, lighting and acoustics*. 2007.
- [5] EN ISO 7730. *Ergonomics of the thermal environment – Analytical determination and interpretation of thermal comfort using calculation of the PMV and PPD indices and local thermal comfort criteria*. 2005.
- [6] D. Fiala. *Dynamische Simulation des menschlichen Wärmehaushalts und der thermischen Behaglichkeit*. Band 41, De Monfort University Leicester, HFT Stuttgart, 1998.

- [7] D. Fiala, K.J. Lomas, and M. Stohrer. A computer model of human thermoregulation for a wide range of environmental conditions: the passive system. *J Appl Physiol*, 87:1957–1972, 1999.
- [8] D. Fiala, K.J. Lomas, and M. Stohrer. Computer prediction of human thermoregulatory and temperature responses to a wide range of environmental conditions. *Int J Biometeorol*, 45:143–159, 2001.
- [9] FIALA-FE, 2008. Manikin model validation manual, release 2.0, <http://www.theseus-fe.de>.
- [10] ISSO 74. *Thermische behaaglijkheid; eisen voor de binnentemperatuur in gebouwen*. publicatie 74, ISSO, Rotterdam, 2004.
- [11] P. Lallemand and L.-S. Luo. Theory of the lattice Boltzmann method: Acoustic and thermal properties in two and three dimensions. *Physical Review E*, 68(036706), 2003.
- [12] A.K. Melikov, N.R.J. Janicas, , and M.C.G. da Silva. Segmental equivalent temperature determined by means of a thermal manikin: A method for correcting errors due to incomplete contact of the body with a surface. ROOMVENT 2004, Coimbra, Portugal, 2004.
- [13] Leibniz Computing Centre of the Bavarian Academy of Sciences and Humanities, 2009. <http://www.lrz-muenchen.de>.
- [14] S. Paulke. Finite element based implementation of Fiala’s thermal manikin in THESEUS-FE. In *EUROSIM 2007*, 2007.
- [15] A. Schälin, A. Moser, J. van der Maas, and D. Aiulfi. Application of air flow models as design tools for atria. In *Roomvent*, Yokohama, Japan, 1996.
- [16] J.A.J. Stolwijk. A mathematical model of physiological temperature regulation in man. Contractor report NASA CR-1855, National Aeronautics and Space Administration, Washington D.C., 1971.
- [17] S.-I. Tanabe, K. Kobayashi, J. Nakano, and Y. Ozeki. Evaluation of thermal comfort using combined multi-node thermoregulation (65MN) and radiation models and computational fluid dynamics (CFD). *Energy and Buildings*, 34:637–646, 2002.
- [18] THESEUS-FE, 2008. Theory manual, release 2.0, <http://www.theseus-fe.de>.
- [19] C. van Treeck. *Gebäudemodell-basierte Simulation von Raumluftströmungen*. PhD thesis, Technische Universität München, 2004.
- [20] C. van Treeck, J. Frisch, M. Pfaffinger, E. Rank, S. Paulke, I. Schweinfurth, R. Schwab, R. Hellwig, and A. Holm. Integrated thermal comfort analysis using a parametric manikin model for interactive real-time simulation. *J Building Performance Simulation*, 2(4):233–250, 2009. DOI: 10.1080/19401490902914637.

- [21] C. van Treeck, F. Hillion, A. Cordier, M. Pfaffinger, and E. Rank. Flow and thermal sensation analysis in an aeroplane passenger cabin using a lattice boltzmann based approach (abstract). In *ICMMES 2007*, Munich, Germany, July 16-20 2007.
- [22] C. van Treeck, E. Rank, M. Krafczyk, J. Tölke, and B. Nachtwey. Extension of a hybrid thermal lbe scheme for Large-Eddy simulations of turbulent convective flows. *Computers and Fluids*, 35:863–871, 2006.
- [23] C. van Treeck, P. Wenisch, A. Borrmann, M. Pfaffinger, M. Egger, O. Wenisch, and E. Rank. Towards interactive indoor thermal comfort simulation. In P. Wesseling, E. Oñate, and J. Périaux, editors, *ECCOMAS CFD 06, European Conference on Computational Fluid Dynamics, September 5-8*, Egmond aan Zee, The Netherlands, 2006.
- [24] VDI 6020 Part 1. *Requirements for methods of building performance simulation, part 1: buildings*. VDI Verein Deutscher Ingenieure, Beuth Verlag, 2001.
- [25] P. Wenisch and O. Wenisch. Fast octree-based voxelization of 3D boundary representation objects. Technical report, Lehrstuhl für Bauinformatik, Technische Universität München, 2004.
- [26] H. Zhang, C. Huizenga, E. Arens, and D. Wang. Thermal sensation and comfort in transient non-uniform thermal environments. *Eur J Appl Physiol*, 92:728–733, 2004.

# Chapter 15

## Some future trends and aspects in building simulation

### 15.1 Simulation, integration and modeling trends

#### 15.1.1 Multi-physics simulation

As mentioned earlier, a drawback of the traditional zonal discretization method is, however, that multizone modeling starts already by definition with a *discrete* model. The continuous physical problem is described by partial differential and integro-differential equations. Several physical processes are approximated by linearization, and the mathematical-physical model is transformed into a set of difference expressions. However, the model still can be locally refined to improve the accuracy in terms of increasing the number of cells or grid points – but only with respect to the degrees of freedom ‘left’ by the discretization model. For example, an element degenerated to represent uniaxial heat conduction in terms of an RC-network cannot describe three-dimensional effects. Advanced numerical techniques such as adaptive mesh refinement in more than one direction may accordingly not be applicable.

State-of-the-art multi-physics software packages make use of a partitioned solution approach in order to treat the different thermodynamic domains in a separate manner. Examples are FEM-Lab [4] within the MATLAB/Simulink environment [19], and the MapleSim tool [14].

A possible solution is the development of scale-adaptive algorithms, where the selection of the numerical method, the discretization scheme and the solver is optimized to comply with both the physically required/constrained resolution and the resolution, which can be afforded in terms of the computational resources.

#### 15.1.2 Integrated product data management

Another important issue is the integration of computer simulation into information models, such as building information models (BIM) which provide access to an object-oriented and/or parametric description of a building in terms of the geometry, topology, semantics, and other information like the evolution of the model over time (also known as 4D modeling). Integration offers the possibility to derive computational models directly from CAD and, thus, to

reduce the effort for creating numerical models from scratch. Examples of such integrated environments are the link between Autodesk REVIT and Ecotect [1], or the DesignBuilder software [6] which is linked with EnergyPlus [21].

Integration comes along with the issue of data exchange and interoperability. The building industry very slowly adapts from the traditional draft-oriented design to the integrated model-based design using BIM. An associated problem is, that the disciplines involved in the planning process (HVAC engineer, lighting engineer, structural engineer, architect, etc.) have different views [25], which makes the interoperability task even more complicated. Although there are a few promising solutions, such as the Industry Foundation Classes (IFC) [9], a STEP-based building product model standard for the data exchange between applications, in practice we are still far away from collaboratively sharing data between applications.

Known software-related problems are the issues of checking for model consistency, collision detection, work flow management, automatic revision and access control (including check-out, check-in, permissions, spatial collision detection, etc.), collaborative engineering [3], trade-dependent model design, and the lack of interest of the software industry in platform-independent interfaces due to marketing their own proprietary products.

A few product model server products are already available, such as the EDM Server using the EXPRESS Data Manager (EDM) of Jotne EPM Technology [11], or the EuroSTEP server solution [8]. However, the development of product data management (PDM) systems has just started, for example, including the development of so-called spatial query languages [2] known from the geographical information systems (GIS) community.

A vision for the future would be, that engineers of the various disciplines involved in the design process will one day collaboratively work on the same model. Parts of the model may be checked out, modified and again committed. Engineers of other disciplines, who are affected by such changes, are notified by events and can modify their respective sub-models. The product model thereby serves as the basis for all subsequent engineering models.

### 15.1.3 Equation-based modeling

In addition to the powerful multi-physics simulation packages mentioned in Section 15.1.1 before, a new and very promising trend is the equation-based object-oriented multi-physics modeling. An example is the MODELICA modeling language, which is a non-proprietary language to model complex physical systems [16], or one of its predecessors such as the simulation language SMILE [18]. A number of simulation environments are available, such as Dymola [5], MapleSim [14], MathModelica, and OpenModelica [16].

For example, WETTER [31] developed an open-source component model library for building energy systems. LJUBIJANKIC & NYTSCH-GEUSEN [13] present a methodology, to combine different levels of detail in MODELICA, in this case in terms of coupling CFD with an equation-based HVAC plant simulation.

## 15.2 Computational steering – a new trend?

### 15.2.1 What is computational steering?

Finite volume-based methods as commonly applied in CFD simulations, or the finite difference (node) based discretization models discussed in this book are basically state-of-the-art approaches in engineering practice. Limited by the complexity of mesh generation and the effort for setting up numerical models, the investigative application of these detailed tools is clearly restricted, particularly if a coupling between these tools becomes necessary.

The idea of *Computational Steering* is to integrate the three steps of preprocessing, simulation and postprocessing into a single coherent process. The term therefore means "to interact with the simulation itself". One of the first statements from the scientific community addressing this issue goes back to the 1980s [10, 15]. Most related work in the subsequent years focussed on enhancing the postprocessing sequence in terms of interactivity [17, 22]. With the increasing access to parallel hardware and the development of parallel communication libraries the interaction with the computation itself became possible.



Figure 15.1: Basic principle of *computational steering*.

Figure 15.1 shows the basic idea of computational steering for an interactive flow simulation. The computational steering environment has been developed at the Technische Universität München and consists of a fast grid generator [30], a parallel CFD kernel and an integrated visualization component [24, 27, 30]. Interactions with the 3D scene in Virtual Reality (VR) are communicated with the master node of the computing kernel which is executed on a high performance computer. The master process distributes the problem by domain decomposition to a number of slave processes which exchange data at the respective domain interfaces via message passing. Results are collected and sent back for visualization; in this case to a holobench visualization device supporting stereoscopic projection. Performance optimizations and hierarchical grid generation techniques enable interactive sessions with immediate responses close to real-time [30].

Computational steering may accordingly serve as a helpful tool in the daily engineering practice in the near future as multi- and many-core processor architectures will become available



*Figure 15.2:* Experiment versus simulation. Left: Thermal manikin equipped with heated sensors measuring resultant surface temperatures (courtesy of Fraunhofer Institute for Building Physics, Germany). Right: Screenshot of an interactive CFD session with the computational steering environment developed at the Technische Universität München [28].

at low cost soon. TÖLKE ET AL., for example, demonstrate the implementation of a lattice Boltzmann type CFD kernel on a graphical processing unit (GPU) [20]. GPUs have originally been designed for processing large data sets for rendering in a very fast way. Recently, a number of researchers try to accelerate non-graphical computations with these low-cost devices. The number of floating point operations of GPUs is thereby about one order of magnitude above conventional multi-core processors. In the application of GPUs a number of problems are not yet resolved such as that the available GPU memory is limited, the programming requires an individual programming language and that application is only advantageous for specially adapted numerical methods.

However, even with high performance computing hardware the resolution of truly interactive CFD sessions remains restricted to low Reynolds numbers and time averaged quantities. A possible solution is a model-adaptive coupling of solvers which depends on the required level of detail in space and time and the available computing resources (laptop, cluster, high performance computer) [23].

### 15.2.2 Application scenarios

A typical application scenario of the computational steering technology is the interactive exploration of indoor air flows. Figure 15.2 compares the experimental setup of surface temperature measurements in the industrial context using a thermal manikin in order to assess the thermal quality performance in an aeroplane passenger cabin with a similar configuration in simulation. For the CFD simulation a hybrid thermal lattice Boltzmann method is used [7, 12, 26].

The interactive steering environment thereby enables to modify both the geometry and the boundary conditions at runtime. Changes of the results are immediately displayed and thus engineers become aware of the consequences if design patterns are changed. Computational steering is a tool for initial pre-simulation because it offers a tool for a-priori optimization

before a high-resolution simulation job is posted as batch process.

Figure 15.3 shows another challenging example, the steering of a flow simulation in a surgery room [29]. A sterile air stream is directed towards the patient’s wound during an operation in order to prevent infection through bacteria. Besides the indoor air quality also the metabolism and thermal comfort of patient and surgeon(s), respectively, are important issues in such scenarios. But these were not considered in this case.

The high level of interactivity is obtained at the expense of the accuracy and depends on the type of available hardware. However, this flexibility is not yet available in common CFD packages and still is subject to research.

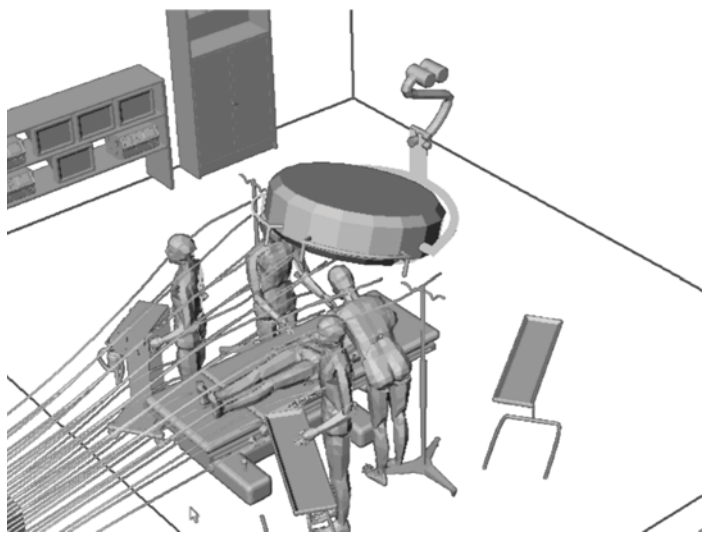


Figure 15.3: Steering of a flow simulation in a surgery room [29].

## 15.3 References

- [1] Autodesk, Inc. Autodesk Ecotect Analysis, 2009. <http://www.autodesk.com>.
- [2] A. Borrmann and E. Rank. Specification and implementation of directional operators in a 3D spatial query language for building information models. *Advanced Engineering Informatics*, 23(1):32–44, 2009.
- [3] A. Borrmann, P. Wenisch, C. van Treeck, and Rank E. Collaborative computational steering: Principles and application in HVAC layout. *Integrated Computer-Aided Engineering (ICAE)*, 13(4):361–376, 2006.
- [4] COMSOL AB. FEMLAB Multiphysics modelling and simulation tool, 2009. <http://www.femlab.com>.
- [5] Dassault Systems, Dynasim. Dymola Multi-Engineering Modeling and Simulation, 2009. <http://www.dynasim.se>.

- [6] DesignBuilder Software Ltd. DesignBuilder, 2009. <http://www.designbuilder.co.uk>.
- [7] D. d'Humières, I. Ginzburg, M. Krafczyk, P. Lallemand, and L.-S. Luo. Multiple-relaxation-time lattice Boltzmann models in three dimensions. *Phil. Trans. R. Soc. Lond. A*, 360:437–451, 2002.
- [8] EuroSTEP. EuroSTEP Share-A-space Server Solution, 2009. <http://www.eurostep.com>.
- [9] International Allicance for Interoperability (IAI). *IFC Release 2x Specification (online)*. <http://www.iai-ev.de/spezifikation/Ifc2x>, 2004.
- [10] C. Johnson, S. Parker, C. Hansen, G. Kindlmann, and Y. Livnat. Interactive simulation and visualization. *IEEE Computer*, 32(12):59–65, 1999.
- [11] Jotne EPM Technology. EXPRESS Data Manager (EDM), 2009. <http://www.epmtech.jotne.com>.
- [12] P. Lallemand and L.-S. Luo. Theory of the lattice Boltzmann method: Acoustic and thermal properties in two and three dimensions. *Physical Review E*, 68(036706), 2003.
- [13] M. Ljubijankic and C. Nytsch-Geusen. Combining different levels of detail in modelling for an improved precision of HVAC plant simulation. In *Proc. 11th IBPSA Conf. Building Simulation*, Glasgow, Scotland, 2009.
- [14] Maplesoft. MapleSim2 – High performance multi-domain modeling and simulation, 2009. <http://www.maplesoft.com>.
- [15] B.H. McCormick, T.A. DeFanti, and M.D. Brown. Visualization in scientific computing. *Computer Graphics*, 21(6), 1987.
- [16] MODELICA. Modelica Association, 2009. <http://www.modelica.org>.
- [17] J. D. Mulder, J. J. van Wijk, and R. van Liere. A survey of computational steering environments. *Future Gener. Comput. Syst.*, 15(1):119–129, 1999.
- [18] C. Nytsch-Geusen and G. Bartsch. An object-oriented multizone thermal building model based on the simulation environment SMILE. In *Proc. 7th IBPSA Conf. Building Simulation*, Rio de Janeiro, Brazil, 2001.
- [19] The Mathworks. MATLAB/Simulink, 2009. <http://www.matlab.com>.
- [20] J. Tölke and M. Krafczyk. TeraFLOP computing on a desktop PC with GPUs for 3D CFD. *Int J Computational Fluid Dynamics*, 22(7):443–456, 2008.
- [21] US Department of Energy (DOE). EnergyPlus Energy Simulation Software, 2009. <http://apps1.eere.energy.gov/buildings/energyplus/>.
- [22] R. Van Liere, J.D. Mulder, and J.J. van Wijk. Computational steering. In B.H.H. Liddell, A. Colbrook, and P. Sloot, editors, *High Performance Computing and Networking*, pages 696–702. 1996.

- [23] C. van Treeck, J. Frisch, M. Egger, and E. Rank. Model-adaptive analysis of indoor thermal comfort. In *Building Simulation 2009*, Glasgow, Scotland, 2009.
- [24] C. van Treeck, M. Pfaffinger, P. Wenisch, J. Frisch, Z. Yue, M. Egger, and E. Rank. Towards computational steering of thermal comfort assessment. In *IndoorAir2008*, Copenhagen, Denmark, 2008.
- [25] C. van Treeck and E. Rank. Dimensional reduction of 3d building models using graph theory and its application in building energy simulation. *Engineering with Computers*, 23:109–122, 2006.
- [26] C. van Treeck, E. Rank, M. Krafczyk, J. Tölke, and B. Nachtwey. Extension of a hybrid thermal lbe scheme for Large-Eddy simulations of turbulent convective flows. *Computers and Fluids*, 35:863–871, 2006.
- [27] C. van Treeck, P. Wenisch, A. Borrmann, M. Pfaffinger, N. Cenic, and E. Rank. Utilizing high performance supercomputing facilities for interactive thermal comfort assessment. In *Proc. 10th IBPSA Conf. Building Simulation*, Beijing, China, September 3-6 2007.
- [28] C. van Treeck, P. Wenisch, A. Borrmann, M. Pfaffinger, O. Wenisch, and E. Rank. ComfSim - Interaktive Simulation des thermischen Komforts in Innenräumen auf Höchstleistungsrechnern. *Bauphysik*, 29(1):2–7, 2007. DOI: 10.1002/bapi.200710000.
- [29] P. Wenisch. *Computational Steering of CFD Simulations on Teraflop-Supercomputers*. PhD thesis, Department for Computation in Engineering, Technische Universität München, 2007.
- [30] P. Wenisch, C. van Treeck, A. Borrmann, E. Rank, and O. Wenisch. Computational steering on distributed systems: indoor comfort simulations as a case study of interactive CFD on supercomputers. *Int. J. Parallel, Emergent and Distributed Systems*, 22(4):275–291, 2007.
- [31] M. Wetter. Modelica-based modelling and simulation to support research and development in building energy and control systems. *J Building Performance Simulation*, 2(2):143–161, 2009.